

TESIS DE LA UNIVERSIDAD
DE ZARAGOZA

2024 112

Esther Frecha Ferreiro

Catalytic conversion of cellulose using carbon nanostructures

Director/es

Suelves Laiglesia, Isabel
Pinilla Ibarz, José Luis

<http://zaguan.unizar.es/collection/Tesis>

ISSN 2254-7606



Premsas de la Universidad
Universidad Zaragoza



Universidad de Zaragoza
Servicio de Publicaciones

ISSN 2254-7606

Tesis Doctoral

**CATALYTIC CONVERSION OF CELLULOSE USING
CARBON NANOSTRUCTURES**

Autor

Esther Frecha Ferreiro

Director/es

Suelves Laiglesia, Isabel
Pinilla Ibarz, José Luis

UNIVERSIDAD DE ZARAGOZA
Escuela de Doctorado

Programa de Doctorado en Ingeniería Química y del Medio Ambiente

2022

CONSEJO SUPERIOR DE INVESTIGACIONES CIENTÍFICAS (CSIC)

INSTITUTO DE CARBOQUÍMICA (ICB)



DOCTORAL THESIS

**CATALYTIC CONVERSION OF CELLULOSE USING CARBON
NANOSTRUCTURES**

Esther Frecha Ferreiro

UNIVERSIDAD DE ZARAGOZA

DEPARTAMENTO DE INGENIERÍA QUÍMICA Y DEL MEDIO AMBIENTE

2021



**Universidad
Zaragoza**

CONSEJO SUPERIOR DE INVESTIGACIONES CIENTÍFICAS (CSIC)

INSTITUTO DE CARBOQUÍMICA (ICB)



**CATALYTIC CONVERSION OF CELLULOSE USING CARBON
NANOSTRUCTURES**

MEMORIA

Presentada por **Esther Frecha Ferreiro** en el Departamento de Ingeniería Química y Tecnología del Medio Ambiente para optar al grado de Doctor por la Universidad de Zaragoza.

Zaragoza, a 10 de diciembre de 2021

Los doctores **Dña. Isabel Suelves Laiglesia** y **D. José Luis Pinilla Ibarz**, Investigadora Científica y Científico Titular, respectivamente, del Instituto de Carboquímica del Consejo Superior de Investigaciones Científicas,

CERTIFICAN:

Que la presente memoria titulada:


**“CATALYTIC CONVERSION OF CELLULOSE USING CARBON
NANOSTRUCTURES”**

Corresponde al trabajo realizado por la Ingeniera Química **Dña. Esther Frecha Ferreiro** en el citado centro, de acuerdo al plan de investigación aceptado el 3 de junio de 2019 por la Comisión de Doctorado de la Universidad de Zaragoza, y autorizan su presentación para optar al grado de doctor en Ingeniería Química.

Y para que así conste, firman este certificado
en Zaragoza, a 10 de diciembre de 2021

Fdo: Dra. Dña. Isabel Suelves Laiglesia

Fdo: Dr. D. José Luis Pinilla Ibarz



“La vida es y seguirá siendo una ecuación sin solución, pero contiene algunos factores conocidos”.

Nikola Tesla

Agradecimientos

Quisiera dedicar las primeras líneas de esta Tesis a todas aquellas personas que han contribuido en su realización. En primer lugar a mis directores de Tesis, los doctores José Luis Pinilla e Isabel Suelves, por confiar en mí para hacer esta investigación y permitirme seguir, cuando todo parecía complicado e incierto. A los directores del Instituto, Luis de Diego e Isabel Suelves, y a María Jesús Lázaro como jefa del Grupo de Conversión de Combustibles.

Extender mi gratitud a todo el personal del Instituto de Carboquímica: servicio de análisis, administración, consejería, mantenimiento, gerencia y la plantilla de científicos titulares, investigadores y profesores de investigación que trabajan en el centro. Pero, sobre todo, a aquellas personas con las que he podido tener un trato más personal y cercano en el día a día. Los mismos que llenábamos el Café Nívola, antes de que las multitudes fuesen un problema sanitario (Laura D., Sandra, Sergio, Olga, Melani, Óscar, Iván, Patri, Iñaki, Antón, Giovanni, Anabel, David, Dani, Alberto, Isabel, Jorge, José Manuel, Sara, Javi, Cinthia, Nico, Laura A.) y que se redujo a mi grupo burbuja en tiempos de pandemia (Laura, Jesús y Claudia). Gracias por amenizarme el confinamiento y los últimos meses de redacción de esta Tesis. Probablemente, nunca iríamos de excursión a Peñaflores si no fuese por su emplazamiento al límite del cierre perimetral. Imposible no mencionar a Elba, por el tiempo compartido en el despacho, nave, cafés, cursos y congresos o a Javier Remón. Este trabajo lleva tu marca personal en todos los capítulos, desde el diseño de experimentos hasta la estancia en York. Hablar de York es agradecerle a Avtar la oportunidad de poder formar parte de su grupo durante 3 meses, y a Aryane, por mostrarme la cara más social y divertida de la ciudad (y de Dublín). Suman a la lista Allyn, Richard, Roxana, Parul, Xudong, Aashima, Tom, Florent y las incorporaciones más recientes al ICB (Clara, Edu, Miguel Ángel, José Miguel, Alberto Jr., Abraham, Jusbeli y Cía.).

A las personas que forman parte de mi vida desde mucho antes de 2016. Me refiero a mi familia, mis padres, mi hermana y los amigos de siempre. Especialmente a mis padres, el primer ejemplo de esfuerzo y dedicación al trabajo. Por estar detrás de todos estos años y poner sobre la

mesa los recursos que fuesen necesarios. Y si esta Tesis es algo así como el cuaderno de bitácora de los últimos cinco años, es justo registrar en ella a todos los que durante esta época hicieron tiempo y km de carretera para venir a visitarme: Lola, Pepe, Oli, Conchi, José, María, Mariló, Carmiña, Angela, Cris y Clara a York. Y al revés, los que me han abierto las puertas de su casa para que me pudiese escapar cualquier fin de semana: Susana en Madrid, Sandra en Hamburgo, etc. a parte de los que arriba se repiten. *Silvia, a ti non te inclúo porque no teu caso non foi unha vez senón moitas. Gracias por axudarme a desconectar en todos os viaxes e por estar sempre cerca, malia as mais de 10 h que nos separaban en tren. Eres a mellor irmán e a miña influencer.* Finalmente, acordarme de dos personas que se fueron sin mi despedida: Asunción y Manuela (a tía de Ortoño), y también de mi abuela Carmen, por vivir bajo los principios de sostenibilidad que años más tarde motivan esta Tesis.

... y a todos aquellos que de algún modo han dejado huella en mi recorrido académico y vital. Son muchos, pero algunos tienen nombre propio: Filomena, Pazos, Cristina, Bea, Menchu y Mikel, y otros nombre de lugar: Zaragoza y Santiago. Porque tal y como reza el mural que conmemora el bicentenario de los Sitios en un edificio del centro: “Ayer, hoy y siempre, a Zaragoza la defiende su gente”, y que de algún modo alude al carácter hospitalario y abierto que uno se encuentra al llegar. Y por supuesto a Santiago: principio, parada y final de la aventura.

INDEX OF CONTENTS

AGRADECIMIENTOS	9
RESUMEN.....	29
SUMMARY	34
CHAPTER 1.	41
INTRODUCTION, AIMS AND OUTLINE	
1.1 INTRODUCTION	41
1.1.1 FUELS AND CHEMICALS PRODUCTION FROM BIOMASS FEEDSTOCKS: AN INTRODUCTION TO CHEMISTRY, PROCESS AND ECONOMICS.....	42
1.1.1.1 Biomass as renewable carbon source for fuels and chemicals	42
1.1.1.2 Lignocellulose biomass composition.....	43
1.1.1.3 General approaches for lignocellulosic biomass conversion.....	44
1.1.1.4 Lignocellulosic biomass conversion to platform molecules via fractionation methods .	49
1.1.1.5 Carbohydrates conversion to platform molecules	52
1.1.2 CHEMOCATALYTIC APPROACHES FOR CELLULOSE VALORIZATION	53
1.1.2.1 Cellulose as raw material for biobased chemicals.....	53
1.1.2.2 Cellulose structure, molecular basis of their recalcitrance	54
1.1.2.3 Hydrolysis chemistry	55
1.1.2.4 Conversion through <i>one-pot</i> reactions.....	58
1.1.2.5 Pretreatments to improve the catalytic conversion of cellulose.....	60
1.1.3 CARBON-BASED CATALYSTS FOR CELLULOSE PROCESSING.....	63
1.1.3.1 Structural arrangement	64
1.1.3.2 Surface chemistry	65
1.2 THESIS FRAMEWORK	66
1.3 AIMS AND THESIS OUTLINE	68
1.4 LIST OF PUBLICATIONS	70

CHAPTER 2.	75
EXPERIMENTAL PROCEDURES, MATERIALS AND METHODS	
2.1 REAGENTS AND MATERIALS	75
2.1.1 GENERAL CONSIDERATIONS	75
2.1.2 CHEMICAL REAGENTS	75
2.1.2.1 Metal precursors	75
2.1.2.2 Oxidation agents and organic compounds	76
2.1.2.3 Analytic standards	76
2.1.2.4 Gases	77
2.1.3 SUSTRATES	78
2.1.3.1 Model compounds	78
2.1.3.2 Cellulose	78
2.1.3.3 Almond hulls	79
2.2 EXPERIMENTAL PROCEDURE	81
2.2.1 CATALYST PREPARATION	81
2.2.1.1 Synthesis of carbon nanofibers (CNF)	81
2.2.1.2 Purification and surface modification	83
2.2.1.3 Post-synthesis treatments	83
2.2.2 CELLULOSE PRE-TREATMENT	83
2.2.3 CATALYTIC TESTS	84
2.2.3.1 Conventional heating	84
2.2.3.2 Microwave heating	87
2.3 CHARACTERIZATION TECHNIQUES	89
2.3.1 Electron spectroscopy	89
2.3.1.1 X-ray photoelectron spectroscopy (XPS)	89
2.3.1.2 Atomic Emission spectroscopy (ICP-OES)	90
2.3.2 Electron microscopy	91
2.3.2.1 Scanning electron microscopy (SEM)	91

2.3.2.2 Transmission electron microscopy (TEM)	91
2.3.3 X-ray Diffraction (XRD).....	93
2.3.4 Thermal analysis.....	96
2.3.4.1 Elemental Analysis (EA)	96
2.3.4.2 Temperature programmed reduction (TPR).....	97
2.3.4 Chromatographic techniques	98
2.3.4.1 High Performance Liquid Chromatography (HPLC)	98
2.3.4.2 Gas-cromatography (GC)	100
CHAPTER 3.	105
CELLULOSE HYDROLYSIS INTO GLUCOSE USING LOW-DIMENSIONAL CARBON CATALYSTS	
Abstract	105
3.1 INTRODUCTION	107
3.2 EXPERIMENTAL	115
3.2.1 CATALYST PREPARATION	115
3.2.1.1 Oxidation in HNO ₃ (CNF _{600-ox})	115
3.2.1.2 Oxidative cutting of CNF _{600-ox} (modified Hummers method)	115
3.2.2 CATALYST CHARACTERIZATION.....	117
3.2.3 CATALYTIC TESTS.....	117
3.2.3.1 Cellulose pre-treatment.....	118
3.2.3.2 Hydrolysis reaction.....	118
a) Conventional heating	118
b) Microwave heating	118
3.2.4 PRODUCT ANALYSIS	119
3.3 RESULTS AND DISCUSSION	121
3.3.1 CATALYST CHARACTERIZATION.....	121
a) Oxidation degree of CNF	121
b) Exfoliation degree of CNF	123

3.3.2 CATALYTIC ACTIVITY	130
3.3.2.1 Conventional heating.....	130
a) Reaction conditions and surface chemistry	130
b) Correlation between graphene oxide structure and catalytic activity.....	133
3.3.2.2 Microwave heating	136
a) Delimiting the operational intervals under different heating sources	136
b) Influence of GO morphologies.....	140
3.3.2.3 Comparison between conventional and microwave heating.....	148
3.4 CONCLUSIONS	150
CHAPTER 4.	155
HYDROLYTIC HYDROGENATION OF CELLULOSE INTO SUGAR ALCOHOLS	
Abstract	155
4.1 INTRODUCTION	157
4.2 EXPERIMENTAL	163
4.2.1 CATALYST PREPARATION	163
4.2.1.1 Support synthesis.....	163
4.2.1.2 CNF-supported metal catalysts.....	163
a) Monometallic Ni catalysts.....	163
b) Bimetallic Ni-noble metal (Pt, Pd, Ru) catalysts	166
4.2.2 CATALYST CHARACTERIZATION.....	167
4.2.3 CATALYTIC ACTIVITY AND CELLULOSE PRE-TREATMENT.....	168
4.2.3.1 Cellulose pre-treatment.....	168
4.2.3.2 Catalytic tests.....	168
a) Monometallic Ni catalysts.....	168
b) Bimetallic catalysts	170
4.2.4 PRODUCT ANALYSIS	171
4.2.4.1 High Performance Liquid Chromatography (HPLC)	171

4.2.4.2 Gas chromatography.....	171
4.2.4.3 Conversion measurements and products yield.....	171
4.3 RESULTS AND DISCUSSION	173
4.3.1 HYDROLYTIC HYDROGENATION OF CELLOBIOSE: SCREENING OF CATALYSTS FOR SUGARS HYDROGENATION.....	173
4.3.1.1 Monometallic Ni catalysts	173
4.3.1.1.1 Catalyst characterization.....	173
4.3.1.1.2 Catalytic activity	181
4.3.1.2 Bimetallic Ni catalysts.....	186
4.3.1.2.1 Catalyst characterization.....	187
4.3.1.2.2 Catalyst performance.....	194
a) Support catalytic activity.....	194
b) Monometallic components.....	196
c) Bimetallic catalysts.....	198
d) Reaction pathway.....	202
4.3.2 HYDROLYTIC HYDROGENATION OF CELLULOSE	204
4.3.2.1 Effect of pre-treatment, time and temperature reaction on cellulose conversion and products distribution.....	204
4.3.2.2 Statistical analysis and model fitting	212
4.3.2.3 Effect of H ₂ pressure.....	219
4.4 CONCLUSIONS	222
CHAPTER 5.....	227
CATALYTIC VALORIZATION OF THE EFFLUENTS GENERATED DURING NANOCELLULOSE EXTRACTION FROM ALMOND HULLS: A BIOREFINERY APPROACH	
Abstract	227
5.1 INTRODUCTION	228
5.2 EXPERIMENTAL	233
5.2.1 RAW MATERIAL	235
5.2.2 SAMPLE PREPARATION	235

5.2.3 PROCESS SCHEME	236
5.2.3.1 Nanocellulose production	236
5.2.3.2 Downstream catalytic conversion technologies.....	237
a) Hydrolytic hydrogenation of sugars.....	237
b) MW-hydrolysate upgrading line: organic phase extraction and mild hydrotreatment.....	238
• Extraction process.....	238
• Pyrolysis of almond hulls	239
• Catalytic hydrotreatment for bio-oil stabilization.....	240
5.2.4 PRODUCT ANALYSIS	241
5.2.4.1 Effluents composition.....	241
5.2.4.2 Gas products	241
5.2.4.3 Bio-oil and organic phases characterization	241
5.3 RESULTS AND DISCUSSION	243
5.3.1 MAIN LINE: NANOCELLULOSE PRODUCTION AND PRODUCT PROPERTIES.....	243
5.3.2 HYDROLYTIC HYDROGENATION OF SUGARS	244
5.3.3 ORGANIC PHASE UPGRADING LINE	248
5.3.4 OVERALL MASS BALANCES	258
5.4 CONCLUSIONS	261
MAIN CONCLUSIONS	265
CONCLUSIONES PRINCIPALES.....	268
REFERENCES.....	273

LIST OF FIGURES AND SCHEMES

Figure 1.1 CO ₂ cycles for bio-based industry (left) vs. linear carbon flow of fossil-based industry (right).	42
Figure 1.2 Structure, composition and organization of lignocellulosic biomass	43

Figure 1.3 Synthesis of chemicals from fossil resources (left to centre) and biomass feedstocks.....	45
Figure 1.4 Alternative value chains for renewable chemicals and their compatibility with current petrochemical lines	47
Figure 1.5 Degree of processing of fossil and biomass feedstocks as a function of the effective H/C ratio.....	48
Figure 1.6 Fuels and chemicals production from crude oil.....	49
Figure 1.7 Overview of the approaches used for biomass fractionation as the primary steps for its selective valorization.	51
Figure 1.8 Plausible transformation scheme from cellulose to bulk chemicals, most of them included in	54
Figure 1.9 Representation of a cellulose structure fragment, H-bonding and labelling of the C-atoms	55
Figure 1.10 Mechanism of acid-hydrolysis of cellulose	56
Figure 1.11 Overview of cellulose pretreatment approaches.....	61
Figure 1.12 Different carbon nanostructures produced by catalytic decomposition of hydrocarbons	64
Figure 1.13 Main forms of carbon nanostructures	65
Figure 1.14 Typical catalytic sites in the graphene surface upon heteroatom incorporation.	66
Figure 2.1 Cellobiose as structural unit of cellulose.	78
Figure 2.2 XRD patterns of commercial cellulose (Avicel PH-101) as a function of milling time: non treated (a) and ball-milled at 600 rpm during 2 h (b) and 8 h (c). The crystalline index gradually decreased from 78.5 % to 37.5 % and amorphous state.....	79
Figure 2.3 SEM analysis of cellulose a) non-pretreated, b) intermediate crystallinity (ICr=37.5 %) and c) amorphous.....	79
Figure 2.4 Flow-chart for biomass preparation.....	80
Figure 2.5 Pilot plant used for the synthesis of CNF by CDB.	82
Figure 2.6 Planetary ball-mill (PM 100 CM).....	84
Figure 2.7 BR-40 Berghof reactor and BRC-3000 controller.	85
Figure 2.8 Parker Autoclave Engineers.	86

Figure 2.9 5500 Parr reactor.	86
Figure 2.10 CEM Discover SP microwave reactor.	88
Figure 2.11 CEM Mars 6 microwave reactor.	88
Figure 2.12 ESCAPlus OMICROM spectrometer.	90
Figure 2.13 Spectroblue from Ametek.	90
Figure 2.14 SEM EDX Hitachi S-3400 N.	91
Figure 2.15 a) X-ray crystal diffraction scheme and b) Instrument configuration according to Bragg-Brentano geometry and its main components.	94
Figure 2.16 D8 Advance Diffractometer (Bruker).	95
Figure 2.17 Representative XRD diffractogram of cellulose a) crystalline and b) in amorphous state.	96
Figure 2.18 Thermo Flash 1112 Elemental analyzer.	97
Figure 2.19 a) AutoChem II equipment (Micromeritics) and b) OmniStar TM mass spectrometer (Pfeiffer).	98
Figure 2.20 HPLC apparatus equipped with RI-detector, manual injector, oven and pump.	99
Figure 2.21 Typical chromatographic separation of some commercial standards.	99
Figure 2.22 GC, Perkin Elmer Instruments.	101
Figure 2.23 Varian CP4900 Micro Gas Chromatograph.	102
Figure 3.1 Conversion of cellulose into chemical and fuels via glucose.	107
Figure 3.2 Enhanced-adsorption mechanism for the hydrolysis of cellulose over carbonaceous acid catalysts.	109
Figure 3.3 Flowchart for the synthesis of various GO-derivatives catalysts.	116
Figure 3.4 Flowchart for hydrolysis tests, from cellulose pre-treatment to product analysis.	118
Figure 3.5 C1s XPS spectra before (left) and after (right) hydrothermal reduction.	125
Figure 3.6 S2p XPS spectra for the set of catalysts before (left) and after (right) hydrothermal reduction.	126
Figure 3.7 XRD diffraction patterns of the starting graphitic precursor (CNF _{600-ox}) and derived GO-based materials in the original form (a) and after hydrothermal reduction (b).	127
Figure 3.8 Graphical representation of different carbon nanostructures.	128

Figure 3.9 TEM images of GO and rGO materials: a-b) GONF, c-d) FLGO, e-f) GOQD, g-h) rGONF, i-j) rFLGO and k-l) rGOQD.	129
Figure 3.10 Time-resolved product profiles during amorphous cellulose hydrolysis over GOQD at 135°C.	131
Figure 3.11 Catalytic activity of GOQD as a function of the cellulose crystallinity index (CrI).....	134
Figure 3.12 Catalytic activity of different graphene oxide mix-milled with cellulose for 10 min (a) and 120 min (b). Reaction conditions: 135 °C, 24h.	135
Figure 3.13 Structural evolution of GONF during ball-milling stage.	135
Figure 3.14 Kinetic profiles of hydrolysis from a starting suspension of 0.25 wt. % in cellulose and using GONF as the catalyst a) cellulose conversion and b) glucose yield.	137
Figure 3.15 Kinetic profiles of cellulose hydrolysis over GOQD as catalyst from a starting suspension of 0.25 wt. % in cellulose.	138
Figure 3.16 Catalytic results as a function of the concentration of the initial suspension over GONF (a) and GOQD (b) as the catalysts (Holding time of 60 min).	139
Figure 3.17 Time-course of cellulose conversion in hydrolysis reaction using different GO-derivatives at several temperatures a) 135 °C, b) 150 °C and c) 165 °C. (2.0 wt. % of cellulose in the initial solution).	141
Figure 3.18 Kinetic curves of sugars production over different GO-morphologies at 135°C (a), 150°C (b) and 165 °C (c). (2.0 wt. % of cellulose in the initial solution)	142
Figure 3.19 Temporal evolution of levulinic acid at 165 °C.	143
Figure 4.1 Sorbitol as platform molecule.	158
Figure 4.2 Typical steps for the synthesis of Ni catalysts following colloidal-deposition approaches.	164
Figure 4.3 TG-H ₂ profile for NPs Ni/CNF _{ox} after removing the organic surfactants.	165
Figure 4.4 Details for catalyst reduction a) Reduction reactor, b) Typical temperature program used for metal catalyst preparation and c) TPR-H ₂ profile for Ni/CNF prepared by dry impregnation (10 wt. %).	166
Figure 4.5 TEM images of CNF before and after purification.	174
Figure 4.6 XRD pattern of raw CNF (a) and oxidized CNF (b).	175

Figure 4.7 C1s XPS spectra for oxidized CNF.	175
Figure 4.8 HRTEM images and derived particle size histograms a) NPs Ni/CNF,	176
Figure 4.9 X-ray diffraction pattern for the set of Ni/CNF catalysts	178
Figure 4.10 Ni 2p 3/2 core level spectra a) NPs Ni/CNF, b) Ni/CNF _{DI} and c) 7.3 % Ni/CNF _{DP} and d) 14 % Ni/CNF _{DP}	180
Figure 4.11 Catalytic results for hydrolytic hydrogenation of cellobiose (Reaction conditions: 190°C, 3 h, 4 MPa H ₂ (RT)).....	181
Figure 4.12 HPLC chromatogram resulting from blank test (Reaction conditions: 190°C, 3 h, 4 MPa H ₂ (RT)).	183
Figure 4.13 Representatives TEM micrographs of raw CNF with occluded metal nanoparticles. ...	184
Figure 4.14 Effect of Ni loading on hydrogenation performance over Ni/CNF.	186
Figure 4.15 Comparison between TPR-H ₂ profiles of mono- and bimetallic catalysts a) Pd, Ni and Ni-Pd, b) Pt, Ni and Ni-Pt and c) Ru, Ni and Ni-Ru, d) CNF gasification.	189
Figure 4.16 HRTEM images and derived histograms of the metal particle size of a) Ni/CNF, b) Pd/CNF, c) Pt/CNF, d) Ru/CNF, e) Ni-Pd/CNF, f) Ni-Pt/CNF and g) Ni-Ru/CNF.	191
Figure 4.17 Chemical composition of arbitrary bimetallic nanoparticles determined by EDX analysis:	192
Figure 4.18 X-ray diffraction patterns of supported catalysts a) pure and b) alloy metals.	194
Figure 4.19 Performance of the support (CNF) in the hydrolytic hydrogenation of cellobiose. (Reaction conditions: 180 °C, 0-3 h, 4.0 MPa H ₂ (RT)).....	195
Figure 4.20 Evolution of the cellobiose conversion and products distribution using Ni/CNF as catalyst. (Reaction conditions: 180 °C, 0-3 h, 4.0 MPa H ₂ (RT)).....	196
Figure 4.21 Evolution of cellobiose conversion and products distribution for noble metal-based monometallic catalysts and bimetallic compositions: a) Ru/CNF, b) Pd/CNF and c) Pt/CNF, d) Ni-Ru/CNF, e) Ni-Pd/CNF and f) Ni-Pt/CNF. (Reaction conditions: 180 °C, 0-3h, 4.0 MPa H ₂)	199
Figure 4.22 Comparison between XRD signal of fresh and spent Ni-Pt/CNF catalysts before and after the reaction	201
Figure 4.23 HRTEM micrographs and derived histogram for spent Ni-Pt/CNF catalyst.	202

Figure 4.24 Temperature effect on product distribution using Ni-Pt/CNF: a) 190 °C and b) 200 °C.	203
Figure 4.25 Catalytic results as a function of reaction temperature, time and cellulose crystallinity a) 190 °C and b) 230 °C.....	206
Figure 4.26 Influence of cellulose crystalline degree on catalytic	209
Figure 4.27 Influence of reaction temperature on the catalytic conversion of.....	211
Figure 4.28 Conversion profile of cellulose (CrI=37.5 %) at 210 °C.....	211
Figure 4.29 Response surface for cellulose conversion from samples with different crystallinities.	215
Figure 4.30 Response surface and contour plot of hexitols yield obtained from cellulose with different crystallinities.	216
Figure 4.31 Response surface for the production of C2-C5 polyols obtained from cellulose samples with different crystallinities.	218
Figure 4.32 Effect of H ₂ pressure on catalytic results.....	220
Figure 5.1 Hierarchical structure of cellulose fibers.....	229
Figure 5.2 Process flowchart of the nanocellulose biorefinery concept from almond hulls	234
Figure 5.3 Parts of almond fruit	235
Figure 5.4 Experimental set-up for bio-oil extraction.....	239
Figure 5.5 Product distribution for E-1 downstream valorization by hydrolytic	245
Figure 5.6 Hydrolytic hydrogenation of E-2 stream	250
Figure 5.7 Chemical structure and relative distribution of various 3-hydroxypyridine-derived compounds.....	252
Figure 5.8 Sankey diagram for nanocellulose biorefinery concept from almond hulls.	259
Scheme 1.1 Catalytic conversion of cellulose into hexitols	58
Scheme 3.1 Reaction network for the conversion of cellulose into glucose and products degradation.	130
Scheme 3.2 Reactions network from cellulose to levulinic acid.	143
Scheme 4.1 Catalytic conversion of cellulose into hexitols	157

Scheme 4.2 Reaction network involved in the cellobiose hydrolysis.....	183
Scheme 4.3 Reaction network involved in the hydrogenation step.....	197
Scheme 4.4 Alternative reaction pathways in the cellobiose conversion into sorbitol.....	202
Scheme 4.5 Sorbitol degradation pathways at high temperature and in the presence of metal catalysts	208
Scheme 4.6 Reaction routes for glucose degradation in presence of hydrogen and metal catalysts	210
Scheme 4.7 Major reaction pathways of sorbitol hydrogenolysis	212
Scheme 5.1 Main reaction routes involved in the catalytic hydrogenation of E1-A.	246

LIST OF TABLES

Table 1.1 2004 DOE Top chemical opportunities from biorefinery carbohydrates.....	52
Table 1.2 Cellulose catalytic conversion to polyols in water.....	59
Table 2.1 Almond hulls characterization	80
Table 2.2 Synthesis conditions of CNF.....	82
Table 3.1 Comparison of catalytic performance of different carbon-based materials in the MW-assisted hydrolysis of cellulose.....	111
Table 3.2 Bulk and surface catalyst composition.....	123
Table 3.3 Chemical state of oxygen and sulphur species determined by XPS.....	126
Table 3.4 Structural parameters determined by XRD from (002) and (002)* peak position: interplanar spacing, d; crystallite size, Lc and number of layers, n.	128
Table 3.5 Catalytic results for the hydrolysis of amorphous cellulose (ball milled for 8h at 600 rpm) over different GO-based materials. Reaction conditions: 135 °C, 24h.	132
Table 3.6 Changes on structural parameters induced by ball-milling.	135
Table 3.7 Cellulose conversion and products distribution for the MW-assisted hydrolysis, GONF as catalyst (starting solution of 0.25 wt.%).	137
Table 3.8 Cellulose conversion and products distribution for the MW-assisted hydrolysis, GOQD as catalyst (starting solution of 0.25 wt.%).	138

Table 3.9 Cellulose conversion and products distribution for the MW-assisted hydrolysis using GONF as catalyst and a starting solution of 2.0 wt. %	144
Table 3.10 Cellulose conversion and products distribution for the MW-assisted hydrolysis, using FLGO as catalyst and a starting solution of 2.0 wt. %	145
Table 3.11 Cellulose conversion and products distribution for the MW-assisted hydrolysis using GOQD as catalyst and a starting solution of 2.0 wt. %	146
Table 3.12 Kinetic parameters for MW-assisted hydrolysis reaction at the beginning of the reaction.	148
Table 3.13 Summary chart of catalytic hydrolysis results under different heating sources.	149
Table 4.1 Experimental conditions for each run. (Inlet solution: 300 mg of substrate, 150 mg of catalyst (Ni/CNF _{DI}) and 30 mL of H ₂ O).....	169
Table 4.2 Physicochemical properties of various CNF-supported Ni catalysts.	177
Table 4.3 Cellobiose conversion and products distribution using Ni-based catalysts.....	181
Table 4.4 Metal content and average crystallite size determined by ICP-OES, XRD and TEM, respectively.	190
Table 4.5 Cellobiose conversion and products yields during the hydrolytic hydrogenation tests on CNF.....	195
Table 4.6 Cellobiose conversion and products distribution over monometallic catalysts.....	198
Table 4.7 Cellobiose conversion and products distribution over bimetallic catalysts.....	200
Table 4.8 Cellobiose conversion and products distribution over Ni-Pt/CNF catalyst after 3 h of reaction at various temperatures.	203
Table 4.9 Catalytic conversion of cellulose over Ni/CNF _{DI} under 4.0 MPa H ₂	205
Table 4.10 Analysis of variance for response surface model.....	214
Table 4.11 Theoretical optimization: objectives, relative importance (from 1 to 5) and the optimal solution predicted by the model (operational conditions and response variables).....	218
Table 4.12 Influence of H ₂ pressure on cellulose conversion and products distribution after 26 h at 190 °C.	220
Table 5.1 Details of reaction conditions for each run	238
Table 5.2 Compositional analysis of E-2 by GC/MS and HPLC.	249

Table 5.3 Chemical extraction of E-2.	250
Table 5.4 Chemical composition of organic extracts.	251
Table 5.5 Elemental analysis and derived bio-oil properties.	253
Table 5.6 Chemical composition of hydro-treated samples based on the analysis of volatile compounds.	255
Table 5.7 Chemical characterization of hydro-treated samples.	257

NOTATION AND GLOSSARY

Abbreviations

A

AC: Activated Carbon

ATR-IR: Attenuated Total Internal Reflectance Infrared Spectroscopy

B

BE: Binding Energy

BTX: Benzene, Toluene, Xylene

C

CCF: Box Wilson Face Centered

CDB: Catalytic Decomposition of Biogas

CNF: Carbon Nanofibers

CNT: Carbon Nanotubes

CrI: Crystallinity Index

D

DAP: Dilute Acid Pre-treatment

DI: Dry impregnation (DI)

DOD: Degree of Deoxygenation

DoE: Department of Energy

DP: Degree of Polymerization

DP: Deposition-Precipitation

E

EA: Elemental Analysis

EDX: Energy Dispersive X-Ray

EO: Ethylene Oxide

F

FCC: Fuels Conversion Group

FCC: Face-Centered Cubic

FEG: Field Emission Gun

FID: Flame Ionization Detector

FLGO: Few-Layers Graphene Oxide

FT: Flow-Through mode

FWHM: Full Width at Half Maximum

G

GC: Gas Chromatography

GCCE: Green Chemistry Centre of Excellence

GC-MS: Gas Chromatography-Mass Spectroscopy

GO: Graphene Oxide

GONF: Graphene Oxide Nanofibers

GOQD: Graphene Oxide Quantum Dots

GQD: Graphene Quantum Dots

Gr: Grafite

GVL: γ - valerolactone

H

HHV: Higher Heating Value

HMDS: Hexamethyldisilazane

HPLC: High-Performance Liquid Chromatography

HWP: Hot Water Pre-treatment

I

ICCD: International Centre for Diffraction Data

ICP-OES: Inductively Coupled Plasma-Optical Emission Spectroscopy

INA: Institute of Nanoscience of Aragón

L

LMA: Advanced Microscopy Laboratories

M

MC: mesoporous carbon

MFC: Microfibrilated Cellulose

MMC: meso- and macroporous carbon

MW: microwave energy

MW-HT: Microwave Hydrothermal Treatment

N

NIST: National Institute of Standards and Technology

P

PE: Polyethylene

PID: Proportional Integral Derivative Controller

PP: Polypropylene

PTFE: Polytetrafluoroethylene

R

RCF: Reductive Catalytic Fractionation

rFLGO: reduced Few-Layers Graphene Oxide

rGONF: reduced Graphene Oxide Nanofibers

rGOQD: reduced Graphene Oxide Quantum Dots

RID: Refractive Index Detector

RT: Room Temperature

S

SBC: Sulfonated Bamboo Carbon

SEM: Scanning Electron Microscopy

SEP: Steam Explosion Pre-treatment

T

TAPPI: Technical Association of Pulp and Paper Industry

TCD: Thermal Conductivity Detector

TEM: Transmission Electron Microscopy

TEMPO: 2,2,6,6-tetramethylpiperidine-1-oxyl radical

TMCS: Trimethylsilyl chloride

TPR: Temperature Programmed Reduction

U

US: United States

X

XPS: X-ray photoelectron spectroscopy

XRD: X-ray diffraction

Z

ZSM-5: Zeolite Socony Mobil-5

List of variables

d : inter-planar spacing of the crystal (\AA)

\bar{d}_s : number of surface area-weighted diameter

d_M : mean size particle

E_a : activation energy (KJ/mol)

I : Intensity of diffraction

k : kinetic constant (min^{-1})

K : constant for the Debye-Scherrer equation

L_c : average crystallite size

n_i : number of particles with a given diameter d_i

S_{Ni} : nickel specific surface area

n : integer referred to the order of reflection

n : number of layers

R^2 : correlation coefficient

T_R : reduction temperature

x_i : independent variables

X: conversion of cellulose

Y: product Yield

y: response variable

β : full width of diffraction line at half maximum (in radians)

β_0, β_i : independent term and the regression coefficients

θ : diffraction angle (degrees)

λ : radiation wavelength (\AA)

ρ : density (g/cm^3)

σ_M : standard deviation

Resumen

La celulosa, un polímero natural presente en las paredes celulares de las plantas, está llamada a ser una de las materias primas renovables más importantes para la síntesis de energía y productos químicos en la futura biorefinería. En el centro de este esquema se encuentra la ruptura hidrolítica de sus enlaces glucosídicos (reacción de hidrólisis) para formar azúcares simples, que constituyen las moléculas plataforma para su posterior transformación en productos de alto valor añadido. Uno de los aspectos clave para asegurar la sostenibilidad del proceso es el uso de sistemas catalíticos heterógenos en fase acuosa, en resonancia con los principios de la Química Verde. Sin embargo, el diseño de catalizadores ácidos sólidos para la hidrólisis de celulosa es todavía un gran reto, debido a las limitaciones difusionales impuestas por una extensa red de enlaces intra- e intermoleculares. En las últimas décadas se han propuesto un gran número de estrategias para superar esta barrera física, tales como el uso de técnicas de pre-tratamiento mecánico para romper la estructura cristalina o el ajuste de las propiedades catalíticas.

Conceptualmente, un catalizador sólido ideal para la hidrólisis de celulosa debe contener centros ácidos, alta afinidad por el sustrato (puntos de adsorción) y características estructurales compatibles con la matriz de celulosa. En este contexto, las nanoestructuras de carbono proporcionan un material de partida único para la ingeniería del catalizador, con morfologías que abarcan desde 0D a 3D y una química superficial que se puede modificar a través de diversos métodos de funcionalización y relacionarse específicamente con su tamaño. Como un ejemplo ilustrativo de este potencial, en esta Tesis se evaluaron las implicaciones catalíticas de reducir las dimensiones del óxido de grafeno (GO), en términos de transporte difusional, facilidad de funcionalización y distribución de grupos funcionales. Para ello se partió de nanofibras de carbono (NFC) de tipo *fishbone* como material precursor de una serie de morfologías de GO, incluyendo nanofibras (GONF), láminas de pocas capas (FLGO) y puntos cuánticos (GOQD), y su actividad catalítica se comparó en la reacción de hidrólisis de celulosa.

El análisis químico y estructural de los materiales se realizó mediante análisis elemental (EA), espectroscopía fotoelectrónica de rayos X (XPS), difracción de rayos X (XRD) y microscopía electrónica de transmisión (TEM). La fracción con el dominio grafénico de menor tamaño, basada en GOQD, mostró la mejor actividad catalítica y la densidad más alta en grupos funcionales (54.7 % O and 6.1 % S). Con todo, los resultados catalíticos estuvieron condicionados por las características cristalinas del sustrato inicial, alcanzando niveles de glucosa del 60.1 % tras la conversión del 83.9 % de celulosa amorfa a 135 °C durante 24 h, mientras que a partir de celulosa cristalina sólo se despolimerizó un 17.8 % en glucosa. Además, la presencia de grupos funcionales oxigenados de carácter débilmente ácido se hizo indispensable para facilitar la aproximación de la celulosa a la superficie del catalizador, tal y como se constató con una caída en los porcentajes de glucosa (43.9 %) y conversión (71 %) sobre muestras parcialmente reducidas (rGOQD). Estas observaciones experimentales evidencian una transformación controlada por el grado de interacción molecular entre la celulosa y el catalizador. Por consiguiente, los resultados mejoraron de forma notable cuando este contacto se forzó a través de la molienda conjunta del catalizador (GOQD) y celulosa durante 10 min, logrando conversión completa y un 83.5 % de glucosa. En condiciones análogas, las fracciones basadas en FLGO y GONF resultaron en un 71.3 % y 60.4 % de glucosa, respectivamente.

Aprovechando las propiedades dieléctricas de los materiales de carbono, en la segunda parte de esta Tesis se exploraron los beneficios de la radiación microondas en la hidrólisis de celulosa amorfa catalizada por GO. Un barrido inicial de condiciones permitió identificar las variables más influyentes en la velocidad de reacción. En el análisis se incluyeron los efectos de la temperatura de reacción (135-180 °C), tiempo de irradiación (0-120 min), morfología del catalizador y la concentración de celulosa en la disolución de partida (0.25-2.0 % en masa). Después, el estudio se complementó con una optimización paramétrica de la reacción para cada morfología de óxido de grafeno, con un doble propósito: maximizar la producción de glucosa y describir cuantitativamente la influencia del diseño estructural del GO en la función hidrolítica.

En general, la reactividad del óxido de grafeno siguió una correlación directa con su grado de oxidación/exfoliación, según la secuencia: GOQD > FLGO > GONF. Por otro lado, la activación de la reacción mediante energía microondas permitió reducir considerablemente la escala de tiempo de 24 h (propio de sistemas de calentamiento convencional) hasta 20 min, alcanzando niveles de azúcares similares a las condiciones de operación más idóneas para cada tecnología (63.7, 42.4% and 44.7 % a partir de GOQD, FLGO y GONF, respectivamente). La reducción de los tiempos de tratamiento en un orden de magnitud, así como la posibilidad de procesar disoluciones más concentradas (2.0 % en masa en lugar del 0.25 % usada en sistemas de calentamiento convencional) representan una contribución significativa a la intensificación de la reacción.

Las condiciones hidrotermales pueden también mejorar la solubilidad de la celulosa y reducir las limitaciones de transporte. Una estrategia para controlar la degradación térmica de la glucosa en estas condiciones es la hidrogenación hidrolítica en una sola etapa (conversión *one-pot*). La reacción combina la despolimerización de celulosa con la hidrogenación *in-situ* de los azúcares a compuestos más termostables (sorbitol), en presencia de partículas metálicas y atmósfera reductora. La efectividad de esta transformación se encuentra en primer lugar condicionada por la capacidad de hidrogenación del catalizador, donde parámetros de diseño tales como la composición metálica y su fracción en peso, tamaño de partícula y los efectos de transferencia de materia (cristalinidad de celulosa y presión de H₂) juegan un papel importante. Por otro lado, entender las relaciones entre la cristalinidad de la celulosa, temperatura y tiempos de reacción es asimismo fundamental para limitar la extensión de varias reacciones paralelas y consecutivas y asegurar la selectividad del producto. Los dos mecanismos de degradación más importantes incluyen reacciones retro-aldólicas de los azúcares intermedios y el craqueo de los hexitales a polialcoholes de menor peso molecular vía hidrogenólisis. Para racionalizar todos estos puntos, en esta Tesis se emplearon catalizadores de Ni soportadas sobre NFC sobre una serie de reacciones control. Los aspectos de diseño del catalizador sobre la actividad de hidrogenación y distribución de productos se han abordado a través de la conversión de compuestos modelo.

Para ello se han empleado técnicas de caracterización como TPR, XRD, TEM, XPS y espectrometría de emisión atómica (ICP-OES). En la preparación de catalizadores se incluyeron composiciones mono- y bimetalicas, dentro de un rango amplio de tamaños de cristal (2.1-20.4 nm) y concentración en peso (3-14 % de Ni y 0.5 % de metal noble: Pt, Pd o Ru). Se encontró una solución de compromiso entre el área superficial de Ni ($3.89 \text{ m}^2/\text{g}$) y su resistencia a la oxidación para un tamaño de cristal intermedio ($\sim 11.3 \text{ nm}$) y cargas del 10.7 %, permitiendo la hidrogenación de un 81.2 % de celobiosa en sorbitol tras 3h a $190 \text{ }^\circ\text{C}$ y 4.0 MPa H_2 . La tendencia natural de las partículas de Ni más pequeñas a la desactivación por oxidación superficial imposibilitó el uso de catalizadores altamente dispersados para disminuir los requerimientos de contenido metálico. Esta tendencia pudo en cierta manera revertirse tras el dopaje del Ni con pequeñas cantidades de un metal noble (Ni:metal noble = 3:0.5 % en peso). En este caso, se encontró un efecto sinérgico importante para las combinaciones basadas en Ni-Pt/CNF y Ni-Pd/CNF, cuyo rendimiento a productos de hidrogenación (96.0 and 61.2 %, incluyendo celobitol y sorbitol) excedió la suma de actividad de sus constituyentes en solitario (32.9, 0.44 and 25.9 % para el Ni/CNF, Pd/CNF y Pt/CNF, en cada caso) a las condiciones de reacción de 3h, $180 \text{ }^\circ\text{C}$ y 4.0 MPa H_2 . En cambio, el catalizador de Ru/CNF permitió la hidrogenación de celobiosa prácticamente en su totalidad, haciendo innecesaria la formación de la aleación Ni-Ru.

De cara a identificar las mejores condiciones para el procesamiento de celulosa, el trabajo se completa con un estudio detallado sobre la influencia de la duración del pre-tratamiento (0-8 h), tiempo (3-26 h) y temperatura de reacción ($190\text{-}230 \text{ }^\circ\text{C}$), planificado e interpretado según la metodología del diseño de experimentos. En estos ensayos, se aplicó una presión fija de 4.0 MPa de H_2 sobre un catalizador de Ni/CNF. El efecto de la presión de H_2 ($6.0\text{-}8.0 \text{ MPa}$) se consideró finalmente sobre las condiciones de reacción óptimas. El mejor rendimiento a sorbitol (61.5 %) se ha alcanzado tras un tratamiento de celulosa amorfa a $190 \text{ }^\circ\text{C}$ y 8.0 MPa H_2 durante 24 h, incorporando una etapa de mix-milling adicional de 30 min.

En última instancia, las transformaciones catalíticas más prometedoras deben formar parte de esquemas de procesamiento de muestras de bioma real, incluyendo la recuperación de corrientes secundarias en la estrategia de valorización global y trabajando en simbiosis con otras economías (por ejemplo, utilizando subproductos de las industrias agroalimentarias como materia prima). Para ilustrar este aspecto, esta Tesis incluye una propuesta de aprovechamiento integral de pericarpios de almendra, donde los efluentes generados a partir de un proceso previamente optimizado para la extracción de nanocelulosa, basado en un pre-tratamiento etanosolv seguido de un proceso hidrotermal asistido por microondas, fueron objeto de valorización catalítica mediante diferentes tecnologías de hidrotratamiento y extracción. En este caso, la fracción hemicelulósica recuperada durante el proceso etanosolv puede ser utilizada para la producción de azúcares alcohólicos (sorbitol y xilitol) tras reacción con un catalizador de rutenio (Ru/CNF, 0.4 wt. %) a 165 °C y 5.0 MPa H₂ durante 3h, obteniendo rendimientos relativamente altos (47.4 %). Por otro lado, la estrategia de valorización propuesta para la corriente de hidrolizado procedente del tratamiento hidrotermal asistido por microondas se basa en la extracción de un producto orgánico rico en moléculas bioactivas basadas en 3-hidroxipiridinas. La fracción oligomérica de esta fase fue estabilizada químicamente mediante un hidrotratamiento catalítico (230 °C, 60 min, 4.0 MPa H₂), pudiendo ser utilizada como fuente de productos químicos de alto valor añadido, tales como ácido dietil succínico, o como biocombustible tras un posterior tratamiento de desoxigenación e hidrocraqueo más severo. Comparado con el esquema de producción inicial basado únicamente en la producción de nanocelulosa, esta propuesta de biorefinería introduce una mejora en la eficacia de recuperación del material de partida del 21.8 al 37.8 % en masa.

Por tanto, en esta Tesis se ha demostrado la viabilidad del uso de catalizadores basados en nanoestructuras de carbono para la conversión selectiva de celulosa en productos químicos de interés industrial, contribuyendo así al desarrollo del concepto de biorefinería.

Summary

Cellulose, a natural polymer present in plant cell walls, is called to be one of the most important renewable feedstock for the production of fuels and commodity chemicals in the future biorefinery. At the heart of this process is the hydrolytic cleavage of their glycosidic bonds (hydrolysis reaction), yielding simple sugars that are the platforms for subsequent transformations. Out of many catalytic proposals, the use of heterogeneous systems in aqueous phase is worth being considered, in resonance with the ethos of Green Chemistry principles. However, designing solid acid catalysts for the hydrolysis of cellulose remains a big challenge because it needs to overcome its robust crystalline structure, where the ubiquitous intra- and inter molecular hydrogen network blocks the accessibility to the inner ether linkages from a granular catalyst for their scissoring. Various strategies have been explored in the last decades to cope with this physical barrier, including the use of mechanical pre-treatments to disrupt the crystalline assembly or the fine tuning of the catalyst properties.

Conceptually, a good solid catalyst for the hydrolysis of cellulose should bring strong acid sites, high affinity for the substrate (adsorption sites) and structural features compatible with the matrix bulkiness. In this field, carbon nanostructures provide an ideal playground for catalyst engineering, with morphologies that range from three- to zero-dimensionalities and surface moieties that can be incorporated through numerous functionalization approaches and specifically related to their size. As a first evidence of this potential, the present Thesis discusses the catalytic implications of gradually downscaling on graphene oxide (GO) morphologies, in terms of diffusional transport, ease of functionalization and distribution of functional groups. To this end, *fishbone* carbon nanofibers (CNF) were used as material precursor of a series of GO-derivatives, including nanofibers (GONF), sheets of few-layers (FLGO) and quantum dots (GOQD), and their catalytic behavior was compared in the hydrolysis of cellulose. Chemical and structural analyses of GO materials were performed by elemental analysis (EA), X-ray photoelectron spectroscopy (XPS), X-ray diffraction (XRD) and

transmission electron microscopy (TEM). The fraction based on GOQDs, as the smallest one, exhibited the best catalytic activity and the highest density of functional groups (54.7 % O and 6.1 % S). Still, catalytic results were largely conditioned by the crystalline features of the starting substrate, yielding to 60.1 % of glucose and 83.9 % of conversion in 24 h at 135 °C from amorphous cellulose but only 17.8 % when converting crystalline raw samples. In addition, the presence of weakly acid oxygen functionalities was essential for cellulose adsorption, as reflected by a marked decrease on the glucose yield (43.9 %) and cellulose conversion (71 %) over partially reduced counterparts (rGOQD), denoting a transformation primarily governed by the molecular collision between the cellulose and the catalyst. An effective interaction between both solid reactants was achieved when this contact was forced in advanced through a short mix-milling of the cellulose with the catalyst (GOQD) for 10 min, rendering complete conversion and 83.5% of glucose. In comparison, 71.3% and 60.4% of glucose was obtained from their sister counterparts: FLGO and GONF, respectively.

Seeking to harness the excellent dielectric properties of carbon materials, a follow-up study explored the benefits of MW radiation on the GO-catalyzed hydrolysis of amorphous cellulose. Firstly, a preliminary experimental work was undertaken to figure out those variables controlling the reaction rate. The influence of reaction temperature (135-180 °C), holding time (0-120 min), catalyst morphology and cellulose-to-water ratio (0.25-2.0 wt. %) was assessed and compared with traditional heating mode. Then, a more detailed parametric optimization was performed for each GO-catalyst toward a dual purpose: maximize the glucose yield and discerning how and to what extent the graphene morphology impact on the target reaction. Overall, the reactivity of the GO-catalyst followed the order of the oxidation/exfoliation degree, decreasing in the sequence: GOQD > FLGO > GONF. Regarding the heating mechanism, MW system dramatically reduced the processing time from typical 24 h in conventional heating down to 20 min. Under the best operation conditions of each technology, similar sugars yields were attained (63.7, 42.4% and 44.7 % for GOQD, FLGO and GONF at 165 °C). A significant reduction on the reaction time length, together with the processing of solutions with a rather

higher concentration ratios (2.0 wt. %), constitute an important step towards the process intensification.

Hydrothermal conditions can also improve the cellulose solubility and greatly reduce mass-transfer limitations. A promising route to control the chemical reactivity of sugars under such conditions relies on combining hydrolysis with simultaneous hydrogenation of glucose into more thermostable sugar alcohols (sorbitol) in presence of metal centres and reductive atmosphere (*one-pot* conversion). The effectiveness of this process is first conditioned by the catalyst hydrogenation ability, determined by design paramets such as metal composition, weight loading and particle size as well as mass-transfer effects (cellulose crystallinity and H₂ pressure). Further on, understanding the intricancies between cellulose crystallinity, reaction time and temperature becomes mandatory to limit the extent of a large panel of parallel and consecutive side-reactions and ensure the hexitol selectivity. The former includes retro-aldol pathways of sugar intermediates and cracking chain of hexitols to low molecular weight polyols via hydrogenolysis. To shed more light to these points, a series of controlled reactions was performed using various Ni containing catalysts supported on CNF. Initially, mechanistic insights into catalyst design for superior activity was addressed on the hydrolytic hydrogenation of model compounds. Relationships between catalysts properties and their reactivity have been delineated using characterization techniques such as temperature programmed reduction (TPR), XRD, TEM, XPS and inductively coupled plasma-optical emission spectroscopy (ICP-OES). The screening of catalysts included mono- and bimetallic compositions within a wide range of sizes (2.1-20.4 nm) and weight metal fractions (3-14 wt. % of Ni and 0.5 wt. % of noble metals, Pt, Pd or Ru). A fair compromise between Ni surface area (3.89 m²/g) and its resistance against oxidation was found for intermediate crystallite sizes (~11.3 nm) loaded at 10.7 wt. %, affording the hydrogenation of 81.2 % of cellobiose to sorbitol after 3h of reaction at 190 °C and 4.0 MPa H₂. The ease oxidation of Ni at smaller particles sizes hampered the use of highly dispersed catalysts to reduce the metal content requirements. This tendency could be somewhat reverted by doping it with small quantities of noble metals (Ni:noble metal=3:0.5 wt. %). Thus,

a remarkable synergic effect was noticed for the Ni-Pt/CNF and Ni-Pd/CNF combinations, since the yields to hydrogenation products after 3h at 180 °C and 4.0 MPa H₂ (96.0 and 61.2 %, including cellobitol and sorbitol) exceeded the sum of the activity of their pure constituents (32.9, 0.44 and 25.9 % for Ni/CNF, Pd/CNF and Pt/CNF, respectively). In turn, the Ru/CNF catalyst enabled the practically total hydrogenation of cellobiose, making unnecessary the Ni-Ru alloy formation.

To match the best reaction conditions for cellulose processing, a detailed study on the influence of ball-mill duration (0-8 h), reaction time (3-26 h) and temperature (190-230 °C) was later described following the methodology of experimental design. For such tests, a fixed H₂ pressure of 4.0 MPa on a Ni/CNF catalyst was used. The effect of H₂ pressure (6.0-8.0 MPa H₂) was finally assessed under the optimised reaction conditions. The highest sorbitol yield (61.5 %) was reached after treating amorphous cellulose at 190 °C for 26 h under 8.0 MPa H₂, including an additional stage of mix-milling for 30 min.

At last, the most promising catalytic routes should be part of an integrated process for raw biomass conversion, with optimal recovery of secondary products from side-streams and working in symbiosis with other economies (i.e., using feedstocks wasted from agro-food industries). In this line, this Thesis applied a process for the extraction of nanocellulose from almond hulls, involving an etanosolv pre-treatment followed by MW-assisted hydrothermal reaction, to explore various valorization strategies of the garnered effluents based on hydrotreatment technologies. For instance, the hemicellulose fraction recovered during the ethanosolv process was used as inlet stream for the production of sugar alcohols (sorbitol and xylitol) with relatively high yield (47.4 %) on a 0.4 % Ru/CNF catalyst (165 °C, 3h, 5.0 MPa H₂). A suited valorization approach for the MW-hydrolysate stream was combine solvent extraction with mild hydrotreatment. In this manner, an organic oil product rich in bioactive molecules based on 3-hydroxypyridines was directly extracted from this effluent. The oligomeric portion of this phase was chemically stabilized through a catalytic hydrotreatment (230 °C, 60 min, 4.0 MPa H₂) to produce additional chemicals (diethyl succinic acid) and fuel

intermediates. As compared with the early production scheme based on the single production of nanocellulose, this multi-product layout introduces a significant enhancement on the resource recovery from 21.8 to 37.8 wt. %.

Therefore, this Thesis has demonstrated the feasibility of using catalysts based on carbon nanostructures for the selective conversion of cellulose into chemical products of industrial interest, thus contributing to the development of the biorefinery concept.



Chapter 1.

Introduction,
aims and outline



Chapter 1.

Introduction, aims and outline

1.1 Introduction

In the past, mankind was largely reliant on plant biomass to meet its energy needs. Over the last two hundred years, wood fuels were progressively overtaken by carbon fossil resources (coal, oil and natural gas), with Industrial Revolution in the 18th century and the discovery of crude oil in the 19th century as the main drivers of these changes. The use of these highly available and inexpensive carbon sources helped to industrialize the world and improved the living standards [1]. Nowadays, with dwindling oil supplies and the rise on environmental issues, biomass is gaining a renewed momentum as a renewable carbon source [2]. The Roadmap for Biomass Technologies predicts a gradual shift back to a carbohydrate-based economy by 2030 where 25% of chemicals and 20% of transportation fuels in the U.S. will be derived from biomass [3, 4]. In Europe, it is projected that renewable resources reduce at least 30% the intensity of fossil consumption in the chemical manufacture by this time [5]. However, several technical barriers should be addressed before realizing these ambitious targets. Major challenges in this transition relate to a new manufacture paradigm, adapted to the polymeric and multifunctional nature of biomass, differing in many aspects from fossil feeds in today's oil refining (mainly based on hydrocarbons). This places new requirements in the process engineering, not only in terms of conversion strategies and catalysis but also in terms of end-final products that can be derived, which eventually may lead to a complete re-design of the value chain [6]. In this scenario, carbon nanostructures show a series of promising catalytic opportunities to respond to this change. Before describing the potential of carbons in this field, it is important to briefly introduce the most highlighted aspects faced by the forthcoming biorefinery for the efficient conversion of biomass feedstock.

1.1.1 FUELS AND CHEMICALS PRODUCTION FROM BIOMASS FEEDSTOCKS: AN INTRODUCTION TO CHEMISTRY, PROCESS AND ECONOMICS

1.1.1.1 Biomass as renewable carbon source for fuels and chemicals

Biomass is a collective term to describe the biogenic organic matter, typically formed from CO_2 and H_2O using sunlight as the energy source [7]. The use of biomass as building material technically converts atmospheric CO_2 into energy and chemicals, bearing the potential to achieve carbon neutral value chains (Figure 1.1). This is because CO_2 emissions released from biomass utilization can be counterbalanced by the CO_2 taken from the atmosphere during plant growth via photosynthesis [6, 8, 9]. A better quantification of net savings in CO_2 emissions relies on considering the impacts for the full cycle of production based on life-cycle assessment methodologies, as the use of biomass does not necessary means sustainability [10]. A case in point is the production of ethanol from corn crops, whose farming and production processes approximately consume 60-75 % of its energy content [11]. At any rate, closed carbon cycles could be virtually realized when efficient conversion processes are developed [1]. The combustion and utilization of fossil fuels, in turn, transfers geologic carbon into the atmosphere, which is invariably associated to a net increase in greenhouse gas levels.

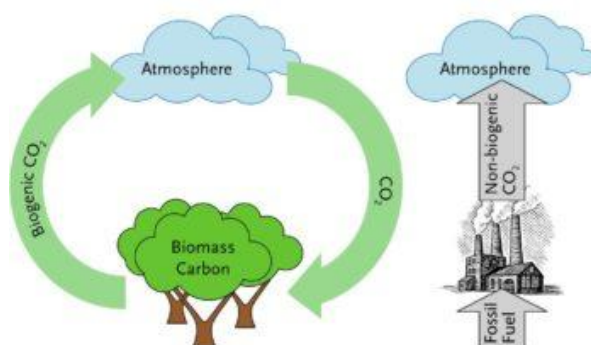


Figure 1.1 CO_2 cycles for bio-based industry (left) vs. linear carbon flow of fossil-based industry (right). (Image taken from reference [12]).

Among various sources of biomass (starchy, triglyceride and lignocellulose feedstocks), lignocelluloses is the most abundant class. It comprehends 70 % of all biomass produced by nature (*ca.* 170-200 billion metric tons per year) [13]. In addition, its industrial utilization is

preferred over edible biomass because it does not conflict with the food supply nor disrupt the land use unduly [7, 14].

1.1.1.2 Lignocellulose biomass composition

Lignocellulose is the fibrous material that constitutes the plant cell walls. It is made-up of three major components, namely, cellulose (25-55 %), hemicelluloses (24-50 %) and lignin (10-35 %) and minor fractions of extractives and mineral matter (terpenes, tannins, waxes, fatty acids, proteins and flavonoids) [11, 15]. This distribution may vary depending on the botanic species, tissues and plant cells maturity. In nature, cellulose strands are interlaced with hemicelluloses forming the structural backbone while lignin fills the spaces between them by ether and ester linkages (Figure 1.2). Such assembly constructs an inner structure with hydrolytic stability, structural robustness and resistance to microbial degradation, a feature commonly referred as recalcitrance [16].

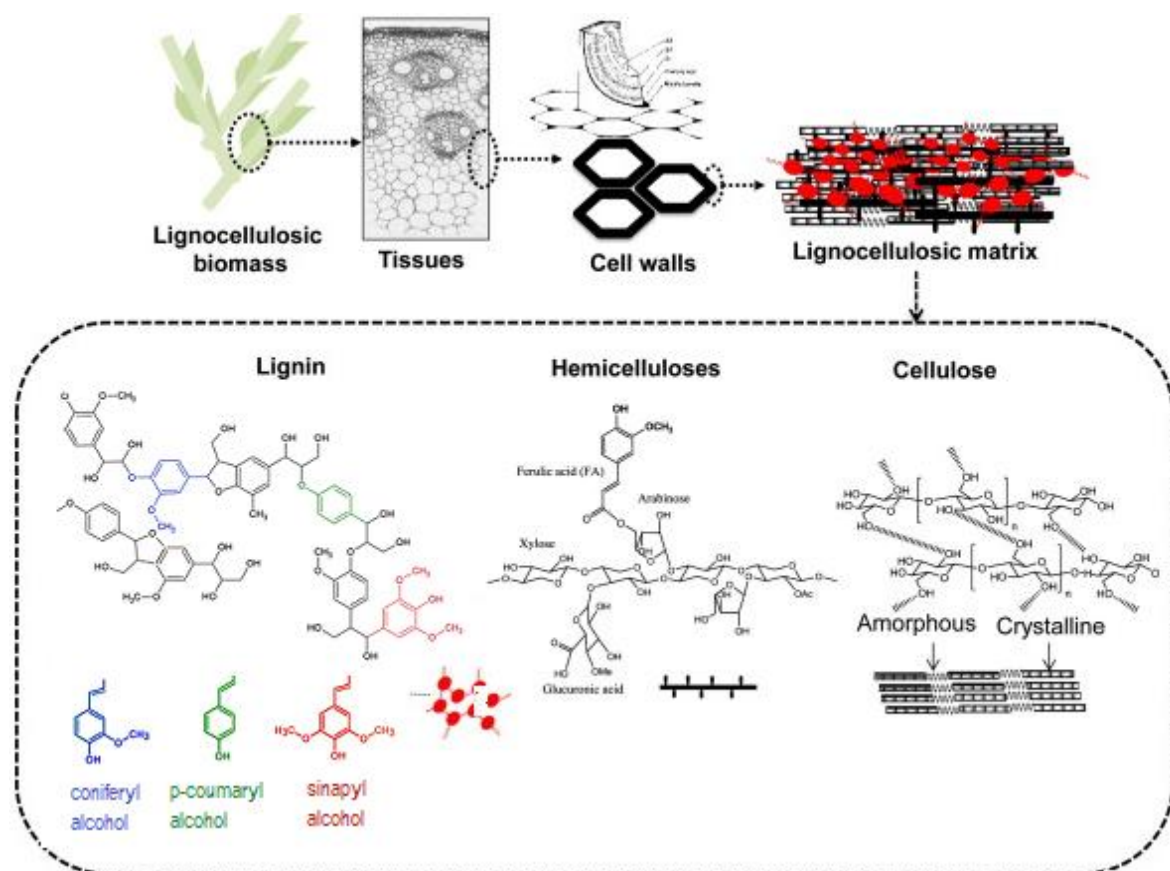


Figure 1.2 Structure, composition and organization of lignocellulosic biomass (Adapted from [17]).



Chemically, cellulose is a homopolymer composed of D-glucopyranose units linked by β -1,4-glycosidic covalent bonds. The average number of anhydroglucose units in native cellulose may reach 10,000 [18]. Hydroxyl groups of cellulose interact to each other through an extensive hydrogen network and Van der Waals forces, forming rigid microfibrils in a semi-crystalline array [19]. Hemicellulose is a polysaccharide of pentoses (xylose, arabinose) and hexoses (glucose, mannose and galactose) linked by β -1,4- or β -1,3-glycosidic bonds. Its heterogeneous structure also contains some acids (D-glucuronic, D-galacturonic and acetic acids) and acetyl moieties as side-chain groups [20]. Unlike cellulose, a typical chain of hemicellulose is amorphous, branched and shorter (polymerization degree of 500–3000 sugar units) and thus more easily soluble and hydrolysable [21, 22]. On the other hand, lignin is an aromatic polymer build-up of phenylpropane units (coniferyl, p-coumaryl and sinapyl alcohols) connected through C-C and C-O-C linkages [23, 24]. The three structures can be visualized in Figure 1.2.

1.1.1.3 General approaches for lignocellulosic biomass conversion

On a global picture, the conversion of lignocellulosic biomass into chemical and fuels mirrors the operation scheme of current oil industry (Figure 1.3). Therein, crude oil is fractionated and refined into a small set of products or cuts such as methanol, aromatics (benzene, toluene, xylene, BTX) and light olefins (ethylene, propylene, 1,3-butadiene) that are the primary basis for the synthesis of a broad range of products and fuels. Following an analogous work path, a future biorefinery could achieve the conversion of renewable resources into a multitude of chemicals, fuels and energy but starting from the biomass building up compounds.

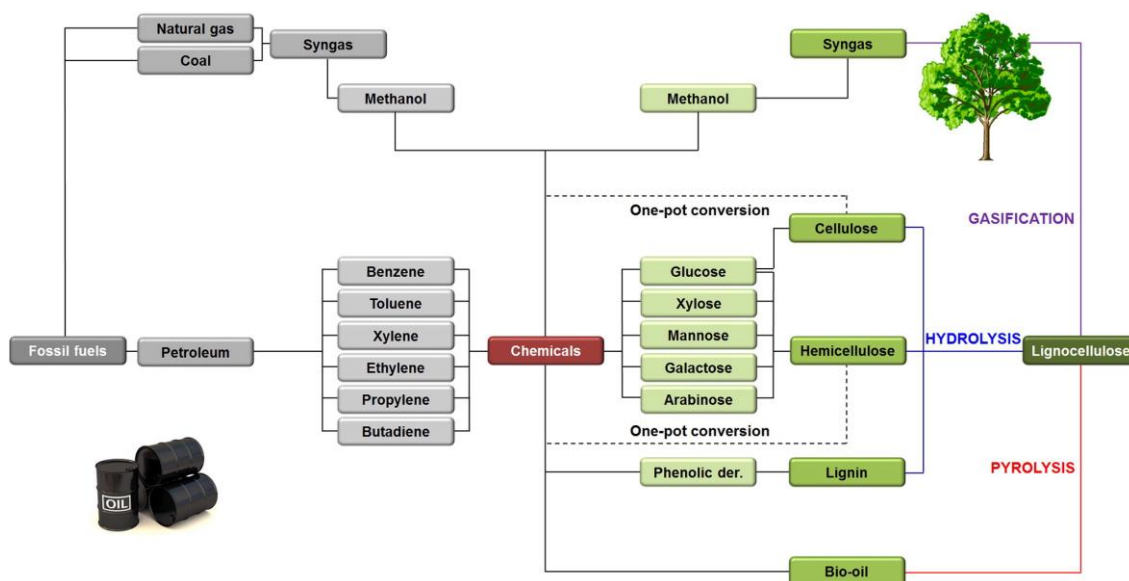


Figure 1.3 Synthesis of chemicals from fossil resources (left to centre) and biomass feedstocks (right to centre). Image taken from [25].

Biomass degradation into upgradable platforms can be nominally divided into two primary routes, involving thermochemical and hydrolysis pathways. In the first one, biomass is deconstructed at high temperature through various processes to yield fractions like synthesis gas (CO/H_2) by gasification (600-1300 °C) and bio-oil from pyrolysis (450-650 °C) or liquefaction (250-400 °C) [1]. The syngas can be further introduced in the value chain for the synthesis of methanol, dimethyl ether or hydrocarbons via Fischer-Tropsch technologies [26, 27]. Meanwhile, bio-oil finds utility for heat and power generation, as fuels upon upgrading or as chemicals precursor from selected fractions [28]. Due to their own nature, gasification, liquefaction and pyrolysis directly convert the whole biomass. However, thermal techniques often suffer from low chemical selectivity and high energy inputs. As an alternative, the second processing option is based on the biomass fractionation into its main constituents, *viz.*, cellulose, hemicelluloses and lignin, followed by the hydrolysis of the individual fractions into their respective monosaccharides (hexoses and pentoses from carbohydrates and phenolic derivatives from lignin). Afterwards, the monomeric units can be transformed to a plethora of products through various biological or chemical approaches. Overall, biomass valorization via hydrolysis based strategies adds complexity to the biorefinery process. However, they also offer selective



processing options to platform intermediates unavailable from thermal technologies in which the chemical polyfunctionality intrinsic of biomass is preserved. This point can be exploited as source of new chemicals [29].

One important consideration when designing biomass value chains is the ease of integration of the biorefinery process in current petrochemical infrastructure. There are two main philosophies: i) duplicate bio-derived products that already exist from fossil sources (drop-in solution) and ii) the production of novel molecules from biorefinery building blocks (emerging strategy). These overall scenarios, schematically illustrated in Figure 1.4, were introduced by Vennestrom *et al.* to assess their economical feasibility in terms of the market competition with their fossil counterparts [30]. In short, the “drop-in strategy” converts the biomass into an intermediate molecule that is fully compatible with the existing petrorefinery facilities. A common example of this path is the synthesis of ethanol by fermentation and subsequent dehydration to ethylene. In this manufacturing line, sugars source for ethanol production come from the saccharification of biomass whereas the ethylene is an intermediate that can be blended with petroleum streams and further co-processed in standard refinery units (e.g., polymerization, oxidation, halogenations and alkylation reactions). The main advantage of this path grounds on the use of the technology developed for current petrochemical industry (reaction units, catalysts and process) from certain step of the transformation train onwards. On the downside, the bio-derived processes will be struggling to compete economically with their fossil analogues, obtained from mature routes that were object to a steady optimization for more than 100 years [31, 32]. On the contrary, the “emerging strategy” represents a brand new route, releasing products that lacks of petrochemical correspondence. This route enlarges the range of products that can be derived from biomass while exploiting their inherent functionality in a more rational manner [33].

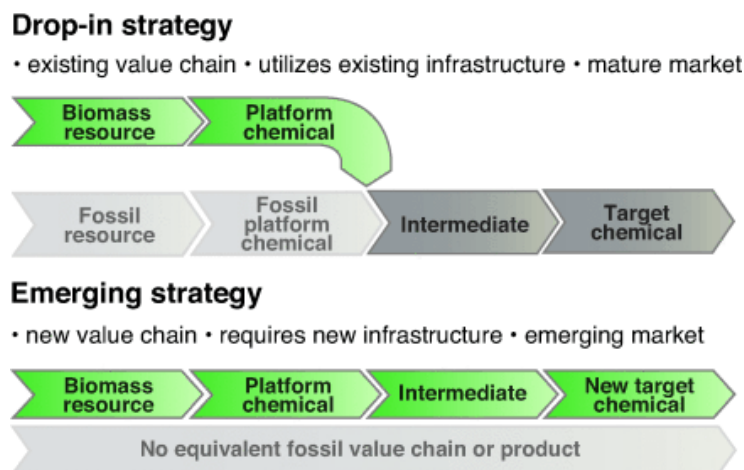


Figure 1.4 Alternative value chains for renewable chemicals and their compatibility with current petrochemical lines (Image taken from ref [30]).

Doubtlessly, the high density of functional groups in biomass becomes a winning opportunity for the synthesis of novel and valuable compounds [34]. In fact, the synthesis of oxygen-rich molecules appears more efficient from the view point of atom economy than its conversion to fuels, taking into account the chemical composition of biomass. This is in sharp contrast to fossil resources, whose low functionalization is best suited for fuel uses. A qualitative indication of processing degree based on the stoichiometric composition of the starting material is the van Krevelen diagram, where different feedstock, target compounds, platform molecules or intermediates are plotted according to their effective H/C ratio (Figure 1.5). This term is defined as the ratio between hydrogen and carbon atoms in the molecule corrected by the oxygen content, e.g., $(H-O)/C$. In such maps, trends along horizontal lines denote structural similarities among groups of compounds. A gap distance on the effective H/C ratio between the resource and a target product means a deeper chemical transformation and higher number of modifications steps. Besides, the second vertical lines lend additional information about the energy content per carbon atom [35]. It can be seen that the effective H/C ratio to ensure high energy density of transportation fuels, in the range of 1-2.3, is comparable to that of crude oil (purple box). This feature makes fossil resources ideal feedstocks for liquid fuels purposes, allowing its almost straightforward utilization upon minimal adjustments of the molecular weights, structure, octane and cetane numbers by means of reactions like cracking, alkylation

and isomerization. Conversely, the manufacture of commodity chemicals from hydrocarbon fossil resources often requires previous functionalization stages at high-temperature and gas-phase, aimed to activate highly volatile compounds characterized by a hydrophobic and inert character. Such activation step becomes unnecessary for biomass-derived platform molecules, which bears the same chemical functionalities as the targeted end-products *per se*. Hence, oxygen-rich compounds such as sorbitol, levulinic acid or γ -valerolactone are some of the molecules that can be derived from biomass more efficiently than fossil resources pathways (blue box).

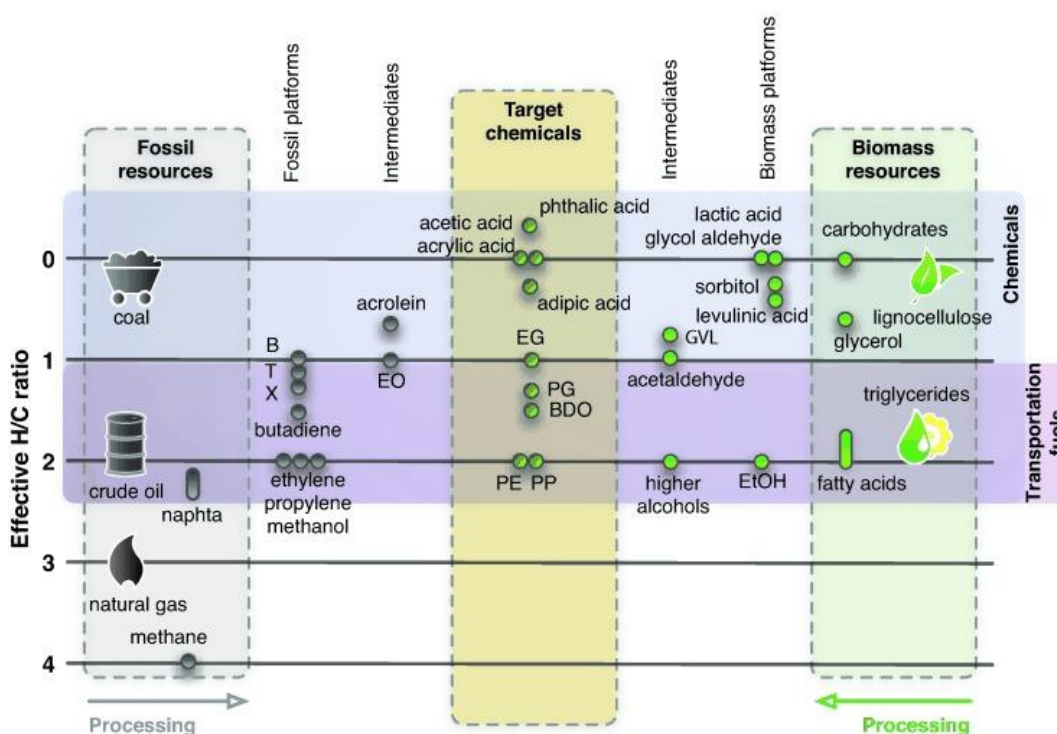


Figure 1.5 Degree of processing of fossil and biomass feedstocks as a function of the effective H/C ratio. Abbreviations: B= benzene, T=toluene, X=xylene, EO= ethylene oxide, EG=ethylene glycol, PG=propylene glycol, BDO= 1,4-butanediol, PE=polyethylene, PP=polypropylene, GVL= γ -valerolactone (Source: [30]).

As a final remark, utilizing biomass for the manufacture of commodity chemicals also offers superior economic prospects than its use as fuels since the former commands higher prices than the latter. This point has been well exemplified by the operation of petroleum refineries. Presently, fuels production accounts for *ca.* 70.6 % of the crude oil that is consumed in North America (pie chart of the Figure 1.6). This distribution is roughly similar across the world and it generates annual profits at around US\$ 385 billion. Albeit only 3.4 % of crude oil is converted



into chemicals, this creates monetary returns nearly close to the market fuel (US\$ 375 billion) [14].

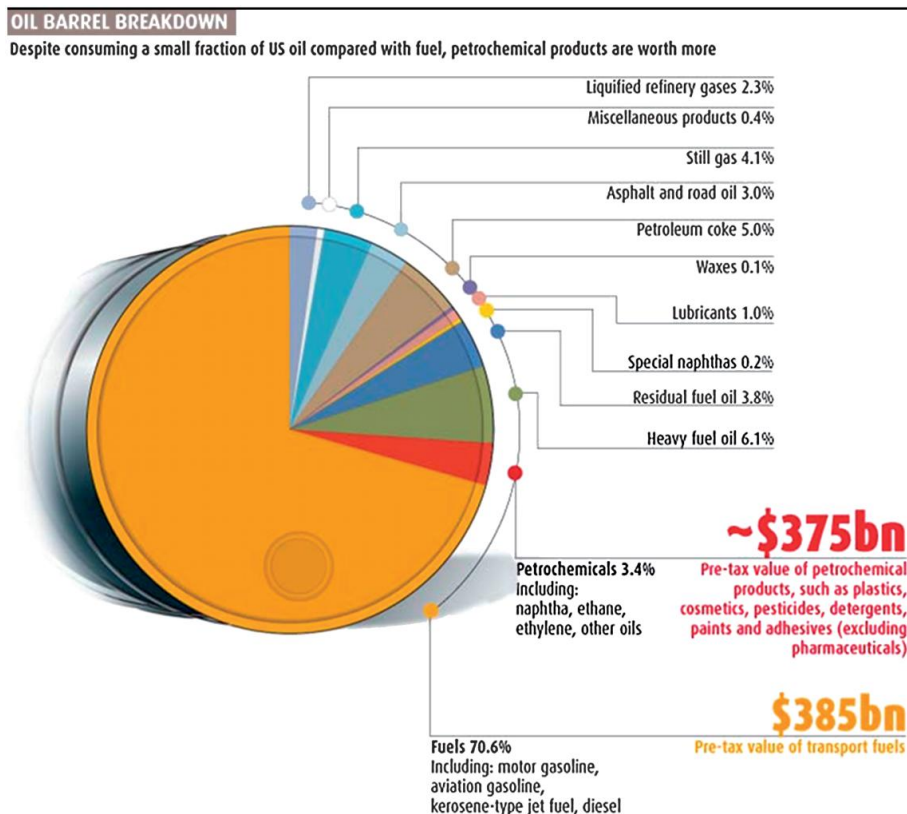


Figure 1.6 Fuels and chemicals production from crude oil (Image taken from ref [14]).

1.1.1.4 Lignocellulosic biomass conversion to platform molecules via fractionation methods

Following the preceding discussion, promising biorefinery concepts are built around the strategy via platform molecules. The former entails a stepwise process whereby biomass is first pre-treated and separated into its three major fractions, followed by depolymerization and upgrading. In this sequence, the primary fractionation step aims to reduce heterogeneity and the structural recalcitrance of raw material [15, 36]. A general approach towards fractionating is the selective solubilisation of lignin and/or hemicelluloses from the rigid matrix, leaving the cellulose fibers unaltered [15, 36, 37]. Potential delignification routes are graphically overviewed in Figure 1.7, ranging from classical alkaline and acid solvolysis to more contemporary innovations. Alkaline fractionation methods were traditionally championed by



wood paper industry, in which various pulping methods (Kraft, sulphite and soda pulping) are used to dissolve the lignin while the (hemi)cellulose fraction is recovered as a delignified pulp. Common alkaline solutions used in these methods include NaOH, Ca(OH)₂ and ammonia.

The solubilisation of lignin may also take place under hydrothermal conditions, including liquid hot water and steam explosion pre-treatments (HWP and SEP, respectively). The main intention of these methods is the splitting of hemicellulose but additionally has repercussion on lignin [38]. More unfortunately, the solubilised lignin in acid/hydrothermal solution tends to condensate and redeposit on the biomass surface. This effect can be partially ameliorated by working in flow-through mode (FT) that reduces the residence time within the reactor [39, 40]. In the former processes, the acidity of the system stems from the increased dissociation of water at elevated temperature as well as some organic acids released from the biomass (e.g., acetic acid from acetate groups). A variant of such pre-treatment consist on the external addition of dilute organic acids (H₂SO₄, HCl) in flow-through systems (FT-DAP). Besides, some other alternative strategies have been proposed to overcome acid-catalyzed re-polymerization of lignin such as the formaldehyde-assisted fractionation and the reductive catalytic fractionation (RCF). The first method makes use of formaldehyde for the chemical stabilization of lignin during its solvolytic extraction by a dioxane/water mixture acidified with HCl [41]. The RCF method, on the other hand, combines delignification with reductive stabilisation by hydrogenation to produce a phenol-rich lignin oil [42].

Another approaches widely applied for biomass delignification and/or hemicelluloses solubilisation rely on the use organic acid solvents through various organosolv pulping methods or the ionic liquid dissolution. The ionic liquid dissolution may lead to the complete dissolution of biomass or either the selective extraction of lignin and hemicelluloses, within the process coined as ionosolv pulping. Finally, the isolation of wood lignin can also be achieved upon the extensive ball-milling of biomass at room temperature and subsequent extraction with organic solvents.

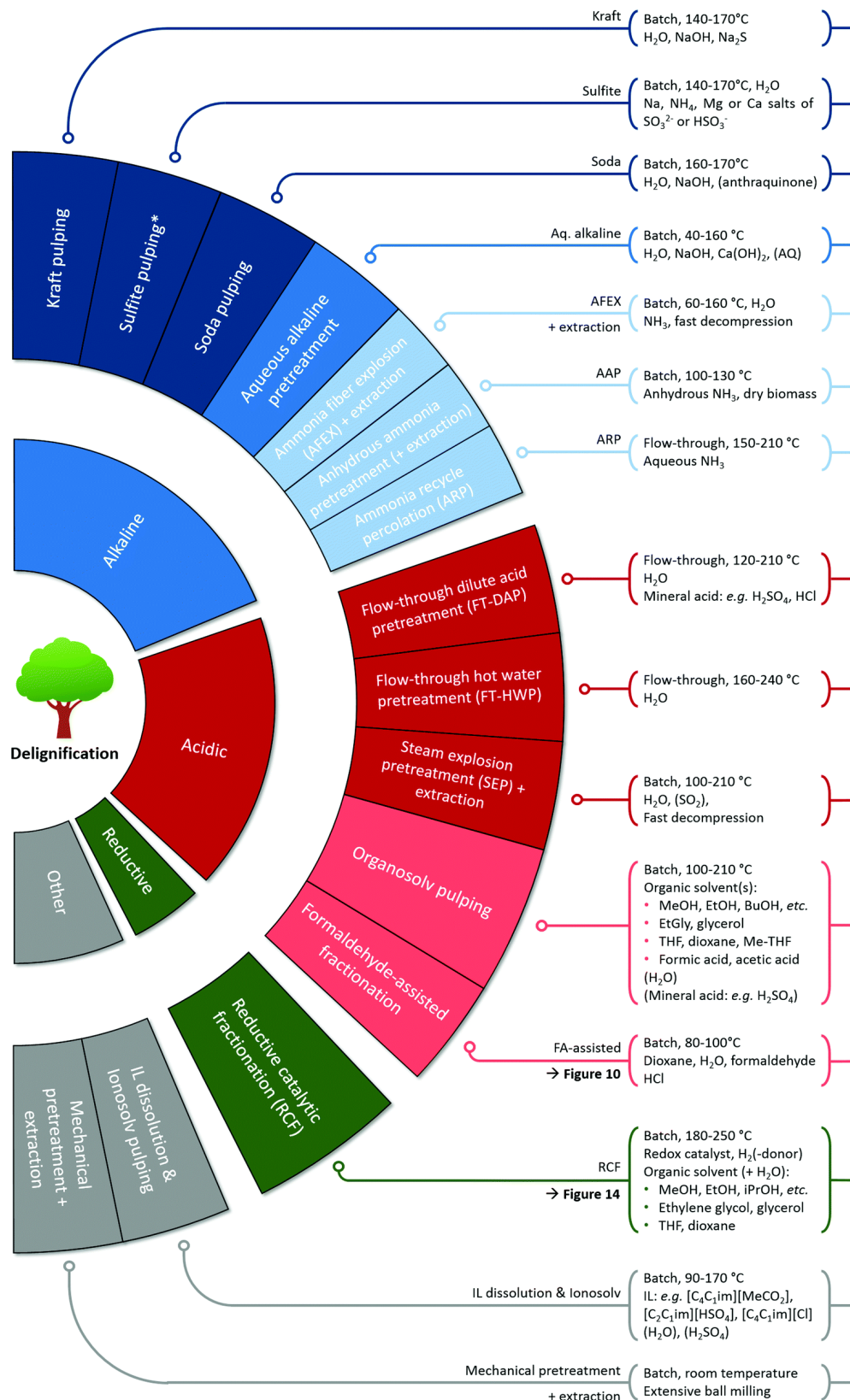


Figure 1.7 Overview of the approaches used for biomass fractionation as the primary steps for its selective valorization. (Image taken from [36]).



1.1.1.5 Carbohydrates conversion to platform molecules

Carbohydrates fraction ranges between 75-85 wt. % of lignocellulose, and thus, its effective utilization is one of the first targets in the field of biorefinery [43]. Out of many processing schemes, the syntheses of chemicals through platform molecules are among the most widely envisioned approaches. The former suggests the conversion of the carbohydrates stream into a limited set of chemical structures that serves as the intermediates for product diversity. This conversion strategy allows for the selective and flexible design of tailor-made downstream pathways starting from individual products. Thereto, it is essential to know the whole conversion potential of a given sugar platform molecule and identify catalysts and conditions that favor the specific transformation on purpose. Owing the huge number of chemical routes at stake, a rational pre-selection of schemes that offer the best prospects for research investment could be a valuable guidance. As part of this effort, the U.S Department of Energy (DoE) reported in 2004 a list of twelve building block compounds that could be obtained from carbohydrates with potential commercial success [44]. The final Top 12 chemicals, detailed in Table 1.1, was the result of a screening of more than 300 candidates attending to economic criteria, readiness of technology, industrial feasibility, market size and the compounds utility as platform molecules in the overall evaluation. The original report was revisited in 2010 by Bozell and Petersen [45].

Table 1.1 2004 DOE Top chemical opportunities from biorefinery carbohydrates[44]

1,4-diacids (fumaric, succinic and malic)
2,5-furan dicarboxylic acid
3-hydroxypropionic acid
glucaric acid
itaconic acid
glutamic acid
aspartic acid
3-hydroxybutyrolactone
levulinic acid
Sorbitol
xylitol/arabinitol
Glycerol



For any such platforms, the first step for carbohydrates conversion is their depolymerization into soluble oligosaccharides and sugars through the hydrolytic cleavage of the glycosidic bonds [46]. This stage is particularly troublesome for cellulose, whose crystalline structure makes it robust towards the chemical transformations. Such chemical inertness of cellulose has long been considered as the main bottleneck for an eventual biorefinery realization based on carbohydrates [47-49]. As a matter of fact, many research works are specifically devoted on the effective conversion of this biomass component. In these studies, it is started from commercially available cellulose samples for a better understanding of its crystallinity and reactivity and/or the development of novel cellulose-derived materials such as nanocellulose [50, 51]. The two most well-known forms of cellulose are Avicel microcrystalline cellulose, produced from pure bacterial cellulose and α -cellulose, extracted from wood with alkali solutions [52, 53].

1.1.2 CHEMOCATALYTIC APPROACHES FOR CELLULOSE VALORIZATION

1.1.2.1 Cellulose as raw material for biobased chemicals

As briefly outlined below, the industrial application of biorefinery waits for further enhancement on cellulose conversion, the major component of biomass. Possible valorization schemes pre-identified by the Department of Energy for the synthesis of potential bulk chemicals from cellulose are depicted in Figure 1.8. As it can be seen, the hydrolysis reaction into its monomeric units (glucose) is at the onset in every catalytic value chain, either carried out separately or in *one-pot* processes. However, the low reactivity of cellulose, arisen from a chemically stable structure and its poor solubility in common solvents, makes the breakdown process rather perplexing. Such difficulties are further exacerbated in heterogeneous conditions, whose use is prioritized in green chemistry.

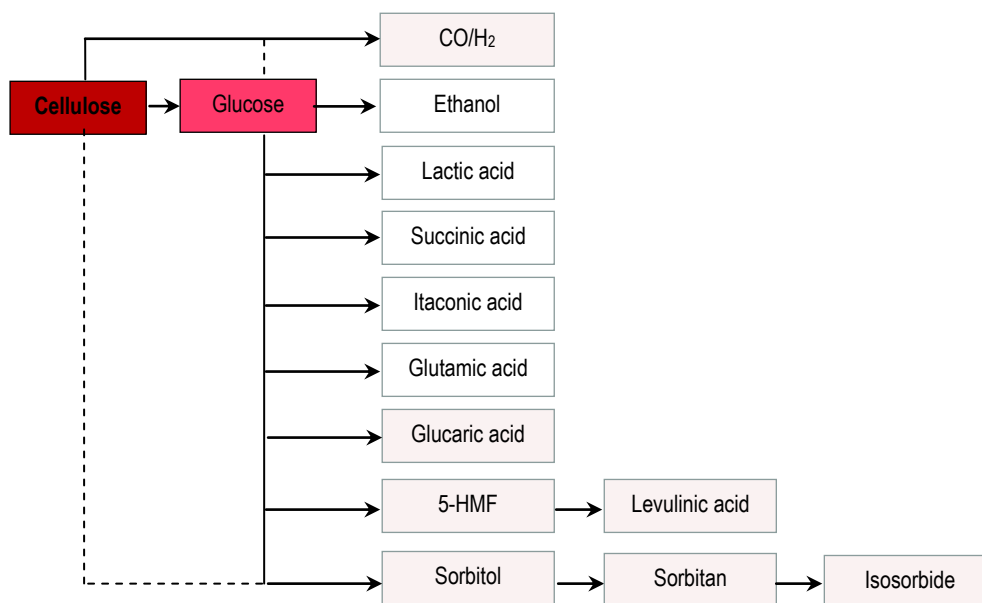


Figure 1.8 Plausible transformation scheme from cellulose to bulk chemicals, most of them included in the DoE Top chemical opportunities. Mainly available from biological paths (white) or chemocatalytic approaches (light pink).
Image adapted from [54]

1.1.2.2 Cellulose structure, molecular basis of their recalcitrance

Naturally, cellulose exhibits a series of structural protection mechanisms, devised for keeping the structure of plant cells, that restricts the access of the acid sites to the ether linkages [55]. The structure of this biopolymer was first described by Staudinger in 1920 [56]. At a molecular level, cellulose is an homopolymer of anhydrous D-glucose units connected by β -(1,4)-glycosidic bonds, in which every glucose unit is rotated 180° with respect to its neighbor (Figure 1.9). The number of repeating units defines the degree of polymerization (DP) and it is largely source-dependent [47, 57]. Relevant examples of DP values encountered in the literature is about 800-1100 for α -cellulose, 7000 for cotton and no greater than 350 in microcrystalline cellulose [15]. Each glucose unit contains three hydroxyl groups in the equatorial position (secondary on C2, C3 and primary on C6), which are involved in H-bonding with the oxygen of adjoining ring and neighboring -OH groups (intra- and inter-chain). In this structure, the symmetric position of the anomeric configuration is essential to stabilize the linkage and minimizes flexibility [57, 58]. To more clearly appreciate this role, it is useful to compare

cellulose to other polysaccharides like amylose (starch). Both are polymers of glucose connected through C1 and C4 carbon atoms with the major difference that glucose units in amylose are interlinked in a α -(1,4) fashion instead of β -(1,4). These changes on the chemical bonds have a dramatic impact on their structure and reactivity: amylose assumes a helical conformation with hydrolysable α -glycosidic linkages whereas cellulose glucans are organized in linear chains, leaving the hydroxyl groups available for H-bonding [50, 57]. Linear glucan chains are then piled-up in flat sheets, hold together by an array of physical and chemical interactions: van der Waals, π - π and hydrophobic forces and interchain H-bonds [59]. This tight internal packaging creates a rigid supramolecular structure, resistant to hydrolysis and insoluble in most solvents (water included) [60, 61] even though its amorphous regions are more reactive than those highly crystalline [62, 63].

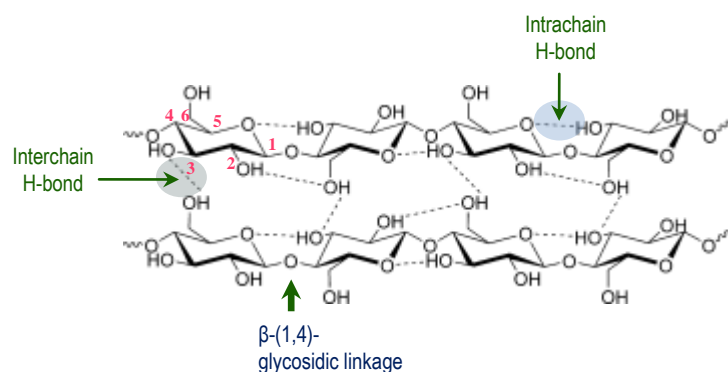


Figure 1.9 Representation of a cellulose structure fragment, H-bonding and labelling of the C-atoms (Adapted from [46])

1.1.2.3 Hydrolysis chemistry

The reaction of cellulose hydrolysis involves the breakage of β -1,4 glycosidic bonds into smaller polysaccharides [52]. It can either be performed under alkaline or acidic conditions. The alkaline degradation of cellulose leads to C1-C6 carboxylic acids as products, but this approach often lacks of high yield and selectivity [64]. The acid-catalyzed transformation, on the other hand, goes through the electrophilic attack of acidic sites (H^+) to yield oligomers and glucose [65]. Mechanistically, the reaction is initiated with the protonation of either the glycosidic

oxygen (path 1) or the pyran ring oxygen (path 2) to form a conjugated acid as it is illustrated in Figure 1.10. The ensuing cleavage of the C-O bond results in a positively charged acyclic or cyclic intermediate (carbocation), which further reacts with water to reestablish the anomeric center and release H_3O^+ species [47].

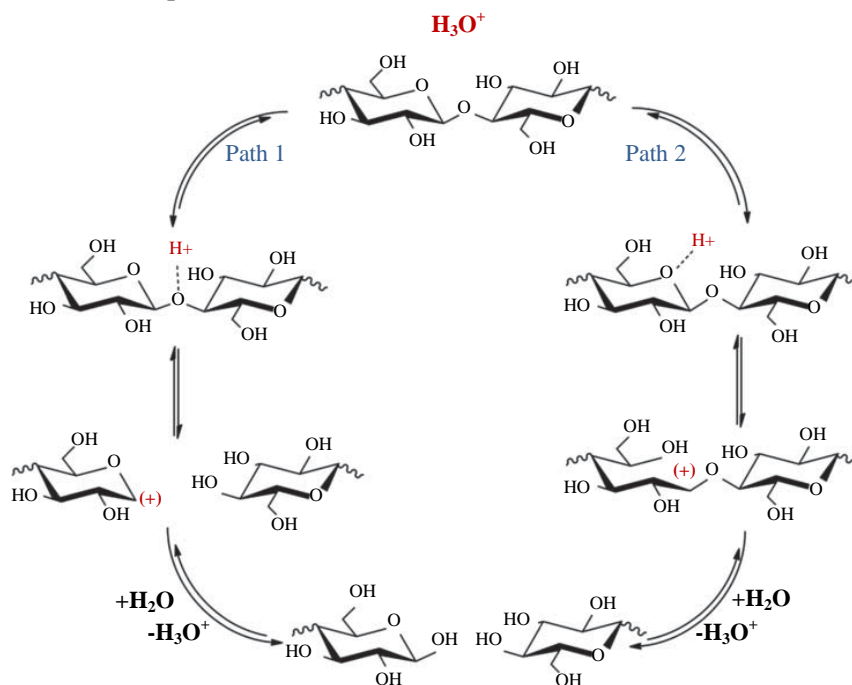


Figure 1.10 Mechanism of acid-hydrolysis of cellulose
(Adapted from [47, 55])

Acid-conversion of cellulose to sugars units has a rather long history. Seminal studies using mineral acids have been performed since 1940s [66, 67]. A large body of work has been focused on the use mineral acid such as sulfuric (H_2SO_4), hydrochloric (HCl), hydrofluoric (HF), nitric (HNO_3) and organic acids (oxalic, maleic, fumaric), applied in more or less concentrations at either low and high temperatures [52, 64, 65, 68]. Typically, high concentrations of mineral acids (31-70 wt. % H_2SO_4 or 15-16 N HCl) utilize low reaction temperature (20-50 °C) whereas more dilute solution (pH 1.5-2.5) requires more severe conditions (200-230 °C) to compensate the weaker acid strength [22]. In most cases, concentrated acids processes afford high hydrolysis rates with minimal degradation of sugars due to the use of mild temperatures [64]. The use of dilute acids, although advantageous from the standpoint of acid reagent costs and corrosion equipments, often suffers from glucose degradation at high temperature. This last



issue can be somewhat controlled through short residence times. One may cite, for instance, the successful study of Grethlein and Thompson, who achieved 50% of glucose from cellulose using 1 wt. % H_2SO_4 at 240 °C on a plug flow reactor at a residence time of 0.22 min [69].

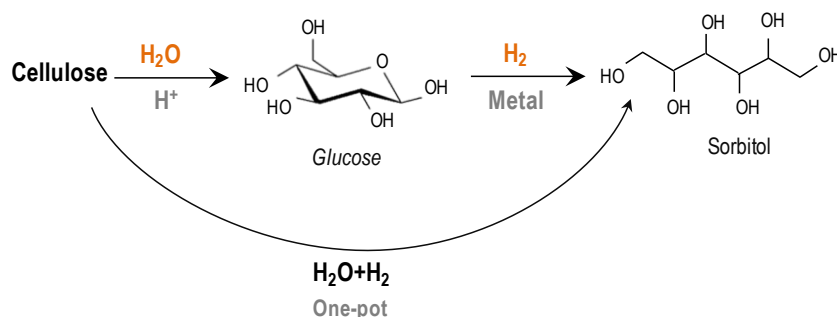
Despite its proved effectiveness, the hydrolysis of cellulose under homogeneous conditions always faces environmental and operational issues related to product separation, catalyst recycling, additional downstream neutralization steps, high costs of reagents and expensive construction materials [70]. For instance, lots of wastes are generated as gypsum during the neutralization of H_2SO_4 effluents with calcium salts (a mixture of CaO/CaSO_4) [71]. In order to sort out these drawbacks and develop environmentally friendlier processes, its replacement by solid acid catalysts are worthwhile considered, mainly due to their easy separation and reusability [52]. However, designing solid acid catalysts for the hydrolysis of cellulose in aqueous phase conditions is not a trivial task. First, most solid acids tend to deplete acid strength in water due to the formation of a solvation layer around acid sites via H-bonding. A second major issue relates with the insoluble nature of cellulose in water solutions, excluding from the facile diffusion of the acid sites from a granular catalyst to the internal ether linkages sites of the crystal for its scissoring [72]. In the last decades, many strategies have been developed to cope with such mass transfer resistances and limited solid-solid interactions through a better catalysts design. The latter contemplates changes on the chemical surface of the catalysts (e.g., acid site density and strength, physical adsorption of the substrate onto the catalyst surface) but also on their textural properties (porosity, surface area and so on). In this field, carbon-based materials offer a unique tool-box to tailor the specific catalysts features, showing morphologies that range from three-to zero dimensionalities and acid moieties that can be tuned as per the reaction needs through various functionalization methodologies [73]. Equally important, the hydrophobic nature of carbon materials may help to prevent the acid sites deactivation from hydration [74, 75].

At the same time, several auxiliary methods have been proposed to maximize the catalytic process efficiency. Some of them involve the pre-treatment of cellulose to reduce its

crystallinity and promote the accessibility to catalyst, the use of ionic liquids, subcritical water and microwave radiation [52].

1.1.2.4 Conversion through *one-pot* reactions

Depolymerization of cellulose can also be coupled with consecutive catalytic reactions like oxidation or reduction to yield valuable chemicals in a single stage (*one-pot* conversion) [9]. Making use of the synergies established between different chemical routes (tandem-reactions) as well as the operation of more compact plants, without intermediate separation steps, are some of the advantages of this multi-step pathways [76]. An example of this transformation is the direct synthesis of sorbitol from cellulose (Scheme 1.1). The reaction combines an initial hydrolysis step with the metal-catalyzed reduction of the resulting sugars (hydrolytic hydrogenation), where various enzymatic, homogeneous and heterogenous catalysts possibilities may be involved. A promising option based on the integration of hydrothermal hydrolysis with catalytic hydrogenation on supported metal nanoparticles. In this system, the acidity is ascribed to the H^+ ions generation from hot water dissociation that easily diffuse inside the cellulose molecule and facilitate its depolymerization [77] while the simultaneous hydrogenation of soluble sugars into sorbitol permits the stabilization of glucose against thermal decomposition.



Scheme 1.1 Catalytic conversion of cellulose into hexitols
(Adapted from reference [78])



An overwhelming number of catalytic systems and experimental conditions have been applied on purpose, resulting in a wide spectrum of products (hexitols and shorter polyols). Some of the most representative studies were compiled in Table 1.2.

Table 1.2 Cellulose catalytic conversion to polyols in water.

Entry	Substrate (CrI)	Catalyst	Temp. (°C)	Time (h)	P H ₂ (MPa)	Conv. (wt. %)	Products Yield (wt. %)			Ref.
							Hexitols	Shorter polyols	Others	
1	MCC	2.5 % Pt/ γ -Al ₂ O ₃	190	24	5.0	46	34	9	2	[79]
2	MCC	4.0 % Ru/C	245	0.5	6.0	85.5	39.3	41.5	4.8	[80]
3	MCC	1% Ru/CNT	185	24	5.0	n.r.	40.0	6.0	n.r.	[81]
4	Acid-treated (33 %)	1% Ru/CNT	185	24	5.0	n.r.	73	10	n.r.	[81]
5	Acid-treated (33 %)	1% Ru/Al ₂ O ₃	185	24	5.0	n.r.	25.0	14.0	n.r.	[81]
6	Acid-treated (33 %)	1% Ru/MgO	185	24	5.0	n.r.	< d.l	16.0	n.r.	[81]
7	Acid-treated (33 %)	1% Ru/CeO ₂	185	24	5.0	n.r.	7.0	13.0	n.r.	[81]
8	Acid-treated (33 %)	1% Ru/SiO ₂	185	24	5.0	n.r.	8.0	< l.d.	n.r.	[81]
9	MCC	20 % Ni/MC	245	0.5	6.0	84.5	42.1	23.3	19.1	[82]
10	MCC	20 % Ni/AC	245	0.5	6.0	61.9	19.7	22.7	19.5	[82]

^a n.r.= not reported

Among the variety of platinum group metals (Pt, Rh, Ru, Os, Pd, Ir), Ru and Pt stand as the most effective candidates [78, 81, 83]. For instance, 2.5 wt. % Pt/ γ -Al₂O₃ catalyzed the conversion of 46% microcrystalline cellulose to 25 % of sorbitol and 6 % of mannitol at the reaction conditions of 24 h, 190 °C and 5.0 MPa H₂ (Entry 1) [79]. Apart from the support intrinsic acidity, it was proposed that hydrogen spillover effect from the metal to the support surface may increase the pool of protonic acid sites and contribute to the hydrolysis of cellulose [79, 84]. An analogous effect was reported by Luoe *et al.* from H⁺ ions generated from hot water dissociation at elevated temperatures (245 °C). Nearly 40 % yield of sorbitol was reached within 30 min in the presence of a supported ruthenium clusters (4% Ru/C) as hydrogenation catalyst and under 6.0 MPa of H₂ pressure (Entry 2) [80]. The same hexitols productivity (40 %)



was reported by Deng *et al.* after treating commercial cellulose (85 % of crystallinity) for 24 h at 185 °C and 5.0 MPa H₂ onto a 1.0 % Ru/CNT (Entry 3) [81]. This result was significantly enhanced to 73 % (69% sorbitol; 4.0 % mannitol) when the cellulose was pre-treated in phosphoric acid (85% H₃PO₄, 50 °C, 40 min) to reduce its crystallinity (33 %). Both the metal and catalytic support influenced on the product yield, since other transition metals (Fe, Co, Ni, Pd, Pt, Rh, Ir, Ag, Au) and support materials (SiO₂, CeO₂, MgO, Al₂O₃) resulted in rather low percentages of sorbitol (in the range of 0-25.0 %, Entries 5-8). Although no information about cellulose conversion was included, the superior H₂ adsorption and spillover ability of Ru/CNT catalyst was clearly pointed out from the H₂-TPD characterization, with an outstanding amount of H₂ desorbed species of 100 μmol/g, twice than Ru/Al₂O₃ and more than 20-fold for the other examined catalysts (Ru supported on SiO₂, CeO₂, MgO).

Likewise, many other studies highlight the influence of support material on the hexitols productivity [82, 83, 85]. For instance, a MC supported Ni catalyst (20% Ni/MC) was much more efficient for the transformation of cellulose microcrystalline than the AC supported counterpart (20 % Ni/AC), Entries 9 *vs* 10. To be specific, a sorbitol yield of 42.1 % was attained after 30 min at 245 °C and 6.0 MPa H₂, which is comparatively higher than that obtained from the 20% Ni/AC (19.7 %) [82]. In this case, the better behavior of 20 % Ni/MC was attributed to its mesoporous architecture. On the other hand, the sugar alcohols productivity obtained from this catalytic system, in the same order of Ru and Pt catalysts when reacting raw cellulose (*vide supra*), opens the door for the substitution of noble metals by rather less-expensive Ni-based catalysts, which were traditionally considered less selective for the synthesis of sugar alcohols, alluding to their hydrogenolysis activity.

1.1.2.5 Pretreatments to improve the catalytic conversion of cellulose

As previously discussed, the resistance of cellulose to chemical transformations under heterogeneous conditions is primarily dictated by the low accessibility to ether bonds. To disassemble the polymeric structure of and make it more reactive, cellulose has been subjected

to a wide range of pre-treatments, including physical, chemical and biological approaches or combinations of various. These methods, summarized in Figure 1.11, enhance the accessibility of cellulose through changes on the structural features (particle size, porosity, polymerization degrees and crystalline index) or the disruption of the internal cohesion by swelling effects. The pros and cons of each proposals have been recently reviewed in the literature [15].

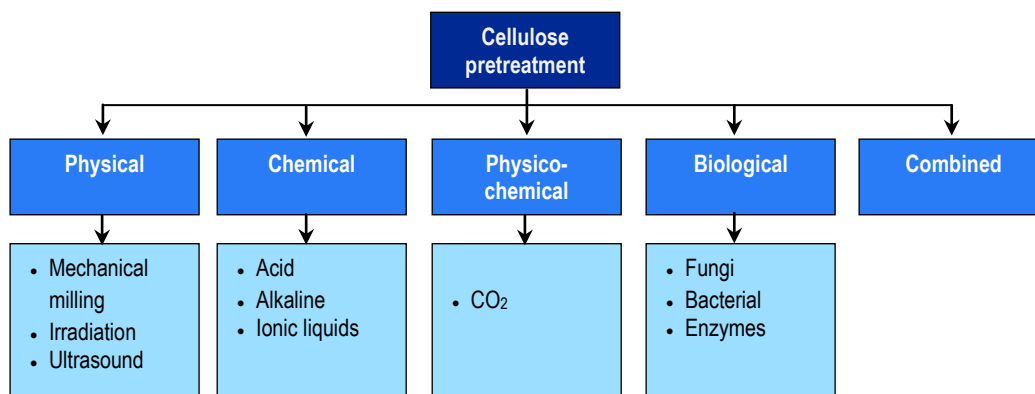


Figure 1.11 Overview of cellulose pretreatment approaches
(Adapted from [15])

Out of them, mechanical methods by ball-milling are extensively applied in research prior to catalytic degradation studies until complete amorphization of cellulose. The crystalline-to-amorphous transition evidences a weakening on the cellulose H-bonding network upon this treatment. Also, a concurrent reduction on the degree of polymerization (DP) and particle size further contribute to increase the external surface area and the accessibility of cellulose. A detailed account of these changes was provided by Ribeiro *et al.* as a function of the milling time and frequency. In their study, the crystallinity of commercial cellulose gradually reduced from 92 % to 33 % after 48 h of rotation at 10 Hz, which went on parallel to a slight decline on the DP from 221 to 191. Meanwhile, the average diameter decreased from 68 nm to 28 nm during the first 8 h of treatment and then rose to 37 nm, likely due to the particle agglomeration [86]. The foregoing changes overall resonate on a greater number of catalytic interactions and a better catalytic efficiency. An example of the positive influence of cellulose ball milling on the hydrolysis reaction was reported by Benoit *et al.* who noted an enhanced glucose yield from



below 1% to 13 % once the substrate was pre-treated. The comparison was performed under MW-assisted hydrothermal conditions (150 °C, 3 h, 250 W) using a ion-exchange resin (Amberlyst 35) as solid catalyst [87]. Noteworthy, catalytic results were shown not only influenced by the pre-treatment method applied but also by the ball-milling pattern. Thus, a drastic improvement in the hydrolysis was reported by Kobayashi *et al.* when the cellulose and a weakly-acid carbon catalyst (K26) were ball-milled together. This practice, termed as “mix-milling”, was significantly more effective than the single-milling of cellulose or using trace amounts of hydrochloric acid in the reaction media [88]. In quantitative terms, the yield of glucans (*viz.*, the sum of glucose and oligosaccharides) after 20 min at 180 °C was 7 and 2.4-fold higher than that of the individually-milled one treated in neat and slightly acidic water, respectively [89]. Such differences in catalytic activity were later explained from the effective interaction between the cellulose and the functional groups of the solid acid. To elucidate this effect, the authors performed a series of model reactions, using soluble substrates (cellobiose) or catalyst (benzoic acid as representative soluble compound of the weakly acid active sites), in which no important differences on product yield were noted upon mix-milling. These results indicate that the promotional role of mix-milling relies on better physical contact between both solid reactants since no obvious impact was observed on liquid-solid reactions [89].

Significant improvements on the hydrolytic hydrogenation of cellulose were also highlighted after using pre-treated substrates by ball-milling or mix-milling [83, 86, 90]. This topic was first researched by Kobayashi *et al.* on a carbon black supported platinum catalysts (5.0 MPa, 463 K, 24 h). By ball-milling the cellulose for 48 h, the conversion raised from 65.6% to 81.9 % while the yield of hexitols reached 43.1 % and 57.7 %, respectively [83]. The beneficial effect of mix-milling on catalytic results was clearly evidenced by Ribeiro *et al.*, who observed an enhanced on the sorbitol production from ball-milled cellulose (45 %) after 5 h of reaction at 205 °C and 5.0 MPa H₂ whereas only 14.4 % of sorbitol was obtained from untreated samples. This value was further increased to 72 % when the Ru/AC catalyst was ball-milled together with cellulose [86].



1.1.3 CARBON-BASED CATALYSTS FOR CELLULOSE PROCESSING

Heterogeneous catalysts systems for hydrolyzing cellulose can be broadly subcategorized as solid acids or as supported metal catalysts via hydrolytic hydrogenation. In either case, carbon-based materials could play a leading role over other alternatives like metal oxides, H-form zeolites or functionalized silicas [91-93]. The first of these applications makes use of the intrinsic catalytic properties of surface functionalities (carbocatalysis) whereas in the latter, the role of carbon is to provide a scaffold for metal decoration and maybe in the best cases, facilitates the approach of reagents to surface catalyst. In addition, it is also possible to combine various active sites in the same catalysts to achieve a multifunctional behavior.

To date, a broad variety of carbons have been studied for biomass processing. The array of structures extends from crystalline to amorphous within a range of allotropic forms. In many cases, the use of carbon nanostructures enjoy a series of catalytic advantages over their disordered contenders (often more heterogeneous in their nature). They possess well-defined morphology, resistance to acid and base media, high thermal and electrical conductivity, mechanical strength, high surface area (80-200 m²/g) and easily tuned mesoporosity [94]. One of the most singular properties relies on their peculiar mesoporosity, where the absence of microporous reduces mass transfer limitations [95, 96].

All these attributes offer numerous perspectives for adsorption and dispersion of metal phase, which often results in superior features in terms of molecular diffusion of reactants, hydrogen spillover and resistance against metal leaching [91]. This is because they not only provide a large surface area but also behave as heat and electrical conductors. The high thermal conductivity, for instance, minimizes the catalyst damage by hot spots formation whereas the electron conductivity facilitates stronger metal-supports interactions [97]. However, carbon nanostructures are not only envisaged as promising catalytic supports but also as catalyst on their own upon surface modification. The following paragraphs aim to illustrate the versatility of carbon nanostructures regarding their structural, chemical and synthesis possibilities, which

put together, open an unmatched number of options for the rational design of novel catalysts for cellulose processing.

1.1.3.1 Structural arrangement

Carbon nanofilaments are classically produced by catalytic decomposition of hydrocarbons. Depending on the metal catalyst, growth temperature and other synthesis parameters, an assorted arrangement can be generated. The two most renowned forms are carbon nanotubes (CNT) and nanofibers (CNF). Both contain sp^2 -hybridized carbon atoms but they differ from the alignment of the graphene sheets. As sketched in Figure 1.12, CNT exhibit tubular morphology (with one or multiple concentric layers) whereas the CNF orient their graphene planes at an angle with respect to the fiber axis. Various types of CNF can also exist according to the graphene layers line-up: parallel to the growth axis in ribbon-like CNF, leaning obliquely in fishbone structures and perpendicular in CNF platelets [98].

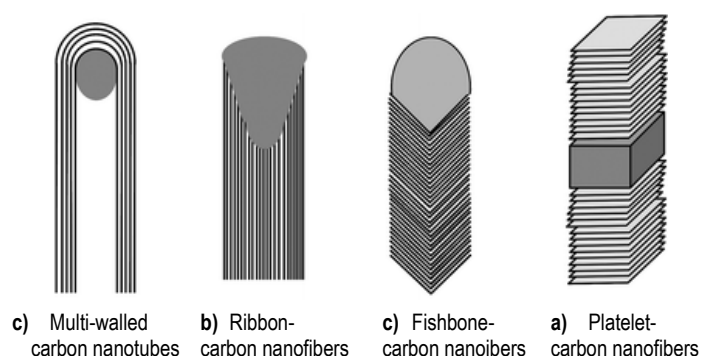


Figure 1.12 Different carbon nanostructures produced by catalytic decomposition of hydrocarbons (Image taken from [95]).

The possibility of adjust the edge-to-basal plane ratio on CNF through the orientation of the graphene layers points to an interesting feature for controlling the number of exposed edges [97, 99]. The number of edges has clear implications on the degree of CNF functionalization, as later will be discussed, which ultimately influences on the properties of CNF and the metal nanoparticles that are supported on them [100, 101]. Afterwards, the density of edges sites may be further increased using low dimensional carbons (Figure 1.13), generated upon the

exfoliation into two-dimensional graphene and then shrinking into smaller domains (carbon dots). This turns carbon nanostructures an ideal platforms for the synthesis of opens novel catalysts with engineered morphology and functionalities, with graphitic arrays that ranges from three to zero dimensions and bearing surface moieties specifically related to their size [86].

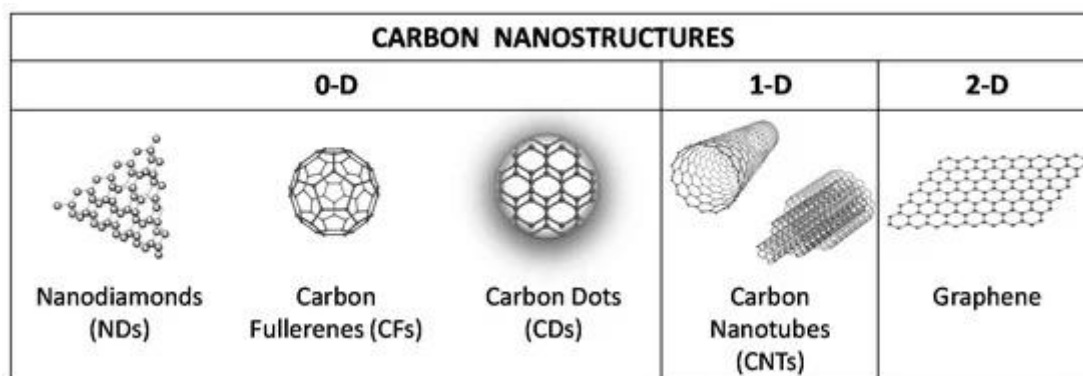


Figure 1.13 Main forms of carbon nanostructures
(Image taken from [102]).

1.1.3.2 Surface chemistry

The surface of carbon nanostructures is inert in origin. A broad range of methodologies is available for its surface modification and confer it intrinsic reactivity, either applied during the same carbonization procedures or through various post-synthesis approaches. The carbon reactivity will be essentially defined by the nature of the active sites, their concentration and accessibility [103]. Many of these controlling aspects are also size-dependent.

Oxygen is the most obvious functionality, although docking other heteroatoms such as sulphur and nitrogen is possible too. Figure 1.12 gives a graphical overview of different types of chemical moieties that can be grafted onto the carbon backbone by surface oxidation and/or chemical doping. A number of oxidation methods can be applied to tune the identity of surface oxygen groups and thus the acid-base or redox properties of carbons. Typically, oxidation with acids (HNO_3 , mixtures of $\text{HNO}_3/\text{H}_2\text{SO}_4$) introduces quinones, carboxyl and aldehyde groups whereas the treatment in air partially yields basic groups. Relative large amounts of basic phenol groups can also be generated by steam/plasma oxidation [97]. The amount and nature of

these groups are also influenced by the microcrystalline structure of the carbon and their size. For instance, small crystallites expose more edges, which are known as the preferred sites for anchoring perispherical species such as carboxylic acids [104].

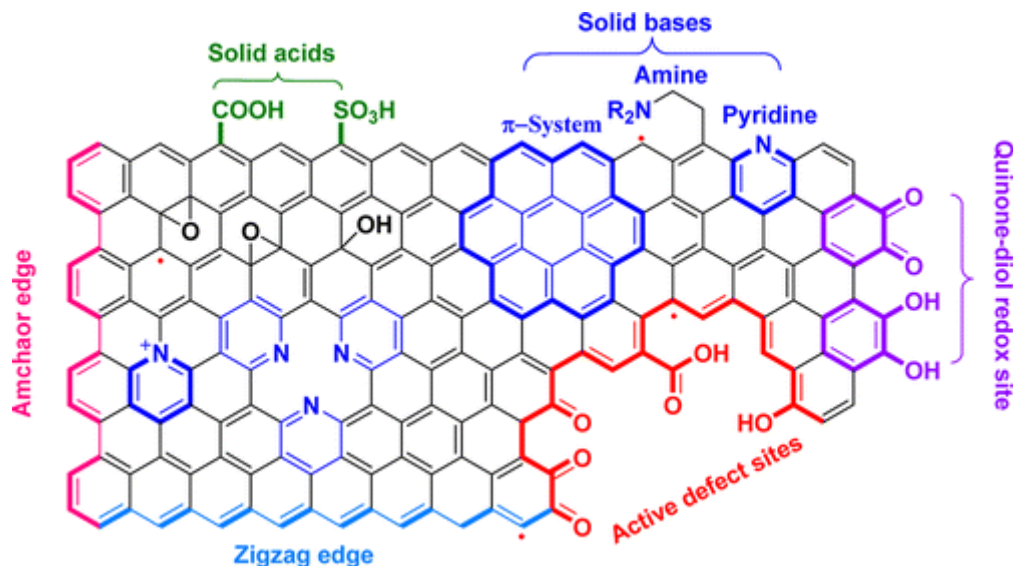


Figure 1.14 Typical catalytic sites in the graphene surface upon heteroatom incorporation. (Image taken from [104]).

The presence of these oxygenated species might be useful as active sites in different catalytic transformations and also allows carbon to mediate with reactants and metal precursors through a more hydrophilic surface [105]. Additionally, the surface modification with sulphur entities, mainly based on sulfonic groups ($-\text{SO}_3\text{H}$), is frequently used to impart stronger acidity. The SO_3H -functionalized carbons, termed colloquially as sulfonated carbons, have received a great deal of attention as water-tolerant solid acids for a variety of biomass transformations, including the hydrolysis of cellulose, with a Brønsted acidity on par to concentrated H_2SO_4 [106-108].

1.2 Thesis framework

The present work has been carried out within the Fuels Conversion Group (FCC) at the Institute of Carboquímica (CSIC) as part of a project entitled “Development of biorefinery catalytic processes based on renewable nanostructured carbons for the synthesis of biofuels” supported by the Spanish Ministry of Science and Innovation (CARBIOREF, ENE2017-83854- R).



This research line follows the logical chronology of the work performed by the group in the last years, trying to find cutting-edge applications to carbon nanostructures generated by catalytic decomposition of hydrocarbons. This process is a promising alternative to steam methane reforming, the most wide-spread technology for hydrogen production. It decomposes methane-rich streams in carbon nanostructures, in a variety of morphologies depending on the catalyst and process conditions, and a hydrogen-rich gas stream (60-90 vol. %). The gas stream can be used to power a combustion engine or fed to fuel cells upon proper purification, as previously demonstrated in an earlier research project (Catalytic Decomposition of natural gas: an integrated process for the production of mixtures for alternative internal combustion engines and carbon materials with energy applications, ENE2008-06516-C03).

An interesting advance in this technology was the use of renewable hydrocarbons as hydrogen source. In this field, the group was pioneer on using biogas streams as feed under the context of the project ENE2011-28318-C03, "Catalytic decomposition of biogas to produce hydrogen-rich gases suitable for ignition engines and carbon materials for energy storage". By this means, similar nanostructures to those prepared by methane decomposition could be obtained, but with the renewable origin as the hallmark. The scaling up and process optimization was addressed through the design and set-up of semi-pilot plants based on rotary and fluidized bed reactors, rendering productions of carbon nanostructures in the order of hundreds of grams per day.

The challenges and opportunities for successful commercialization of the catalytic decomposition of hydrocarbons come from the application of not only the hydrogen but also and mainly the carbon nanostructures. A number of potential applications have been studied, including their use in electrochemical devices for energy conversion and storage applications, in advanced catalytic systems for biorrefinery processes as well as graphenic materials precursors. This last development was addressed within the scope of the Thesis "Carbon nanofilaments obtained by catalytic decomposition of methane-rich streams as graphene materials precursors" [109]. The transformation involves an oxidative treatment by a modified Hummers method and the subsequent ultrasonic exfoliation. Variations on the oxidation ratio and the type of carbon



nanofilaments (nanofibers and nanotubes) afforded the synthesis of several graphene oxide morphologies, spanning from graphene oxide nanofibers, sheets of few-layers and quantum dots. These products were effectively fractioned in size through the implementation of a degressive differential centrifugation process and minutely characterized. The rich surface chemistry of these materials, combined with their unique morphological features, offer intriguing catalytic properties for many biomass conversion reactions (carbocatalysis) [103].

Regarding the biorrefinery applications, an extensive work has been carried out under the framework of the research project “Biofuels upgrading by means of advanced catalytic systems based on carbon nanomaterials” (ENE2014-52189-C2-1-R), focused on the catalytic upgrading of pyrolysis liquids using carbon nanofibers supported molybdenum carbide (Mo_2C). Initially, the synthesis of catalysts supported on carbon nanostructures (Mo_2C , Cerium-modified Mo_2C and Pd-based catalysts) to deoxygenate model compounds of different types of biomasses (guaicol and stearic acid as representative units of lignocellulosic and oleaginous biomass, respectively) was studied and the main conclusions were compiled in the Thesis “Deoxygenation of lignocellulosic and oleaginous biomasses using catalysts based on carbon nanomaterials” [110]. More recently, the catalytic upgrading of different bio-oils is being more deeply studied in a continuous mode operation reactor with funds provided by the above mentioned project (ENE2017-83854-R), with emphasis on the long-term catalyst stability and the optimal reaction conditions.

Before concluding, it is interesting to note that part of the work described in this Thesis has been conducted in the Green Chemistry Centre of Excellence (GCCE), Department of Chemistry at York University during a 3 months-research stay (September-December, 2019) thanks to a grant-in-aid from Ibercaja bank entity (CB 7/19) and the financial support from the Government of Aragon for the funding to Grupo de Investigación Conversión de Combustibles (T06_20R).

1.3 Aims and Thesis outline



The primary focus of this Thesis is to develop effective catalytic strategies for the selective conversion of cellulose into high-value added products using carbon nanostructures as catalysts.

Specific objectives on this overall goal include:

- a) Designing highly active catalysts for cellulose conversion through various processing options: acid carbons for the hydrolysis reaction and metal supported catalysts with high hydrogenation capability for direct transformation of cellulose into sugar alcohols (*one-pot* operation).
- b) To understand the reaction mechanism and the molecular interaction between cellulose (insoluble) and the solid catalysts as well as the interrelationships between cellulose crystallinity, catalyst activity and reaction conditions.
- c) Processes intensification throughout the use of alternative heating sources (MW-radiation).
- d) To evaluate biorefinery strategies from natural resources (preferably with a local character), enabling the valorization of untreated biomass with optimal recovery of secondary products from side-streams.

To contribute to the abovementioned objectives, the study is divided into three main blocks. The first part of the work (Chapter 3) aims to provide an *ad-hoc* designed catalyst for the hydrolysis of cellulose into their monomeric units, using *fishbone*-type carbon nanofibers as the starting material, whose structural and chemical features were subsequently modified *as per* the reaction requirements. To this end, a subset of graphene oxide (GO) materials, differing structurally in morphology and oxidation degree, was prepared, characterized and tested for the hydrolysis of cellulose with various indexes of crystallinity. Optimization of reaction conditions was conducted using two alternative heating sources: conventional and MW-radiation

In a second approach (Chapter 4), a series of Ni-based catalysts supported on carbon nanofibers was applied for direct transformation of cellulose into sorbitol (*one-pot* conversion). In this system, the role of carbon is the dispersion of metals on a large surface whereas the H^+ species



in situ generated from water at hydrothermal conditions facilitate the hydrolysis of cellulose. A quantitative description on the influence of catalyst design details (metal composition, mass content, crystallite size), process severity (temperature and time) and structural features of cellulose on catalytic results (cellulose conversion and product distribution) was depicted. The impact of each parameter is discussed on the basis of the reaction mechanism

Finally, in the third part of the Thesis (Chapter 5), a process for extracting nanocellulose from almond hulls was used as the reference to assess various waste management possibilities. Thereto, a broad-set of soluble products was recovered from the spent liquor effluents and further upgrading via catalytic hydrogenation reactions.

1.4 List of publications

The main results of this Thesis have been published as follows:

a) Published articles:

- E. Frecha, D. Torres, A. Pueyo, I. Suelves, J.L. Pinilla. Scanning different Ni-noble metal (Pt, Pd, Ru) bimetallic nanoparticles supported on carbon nanofibers for one-pot cellobiose conversion, *Applied Catalysis A*, General 585 (2019) 117182.
- E. Frecha, D. Torres, I. Suelves, J.L. Pinilla, Custom-sized graphene oxide for the hydrolysis of cellulose, *Carbon* 175 (2021), 429-439.

b) Articles under preparation:

- Revisiting the influence of graphene oxide morphology on the hydrolysis of cellulose under MW-radiation.
- Understanding the factors which control the hexitols selectivity on one-pot cellulose conversion using Ni catalysts.



- An integrated scheme for nanocellulose extraction from almond hulls and simultaneous recovery of sugar alcohols, 3-hydroxypyridines and fuel precursors.

c) Related contributions:

- J. Remón, R. Sevilla, E. Frecha, J.L. Pinilla, I. Suelves. Direct conversion of almond waste into value-added liquids using carbon-neutral catalysts: hydrothermal hydrogenation of almond hulls over a Ru/CNF catalyst, *Journal of Environmental Management* (under revision).



Chapter 2.

Experimental procedures,
materials and methods



Chapter 2.

Experimental procedures, materials and methods

This Chapter refers to all the chemical reagents, general methods for the catalysts preparation and their respective characterization procedures. A detailed description of the experimental set-up used for the catalytic tests (reaction units and feedstock pre-treatments) and the instrumental techniques used in the products analysis is also included.

2.1 Reagents and materials

2.1.1 GENERAL CONSIDERATIONS

Commercial reactants were used as received without further purifications. Catalysts synthesis and reaction tests were carried out using Milli-Q water (conductivity=0.055 $\mu\text{S/s}$), dispensed by a Millipore filtration system (Siemens, Ultra Clear). The list shown below provides a complete account of chemical reagents used in this work, substrates and their preparation methods.

2.1.2 CHEMICAL REAGENTS

2.1.2.1 Metal precursors

- Aluminium (III) nitrate nonahydrate ($\text{Al}(\text{NO}_3)_3 \cdot 9\text{H}_2\text{O}$, Supelco)
- Cobalt (II) nitrate hexahydrate ($\text{Co}(\text{NO}_3)_2 \cdot 6\text{H}_2\text{O}$, 98%, Alfa Aesar)
- Nickel (II) nitrate hexahydrate ($\text{Ni}(\text{NO}_3)_2 \cdot 6\text{H}_2\text{O}$, 98 %, Alfa Aesar)
- Nickel (II) acetate tetrahydrate ($\text{Ni}(\text{ac})_3 \cdot 4\text{H}_2\text{O}$, 99.8%, Sigma Aldrich).



- Hydrogen hexachloroplatinate (IV) solution ($\text{H}_2\text{PtCl}_6 \cdot \text{H}_2\text{O}$, 8 wt. % in H_2O , Sigma Aldrich)
- Palladium (II) chloride (PdCl_2 , 99.999 %, Acros Organics)
- Ruthenium (II) chloride ($\text{RuCl}_2 \cdot \text{H}_2\text{O}$, Reagent Plus[®], Sigma Aldrich)

2.1.2.2 Oxidation agents and organic compounds

- Nitric acid (HNO_3 , 65 wt. %, Panreac)
- Sulfuric acid (H_2SO_4 , 95-97 %, Panreac)
- Potassium permanganate (KMnO_4 , 99 %, Panreac)
- Hydrochloric acid (HCl , 37 wt. %, Honeywell)
- Ammonium hydroxide solution (NH_4OH , 30 vol. %, Panreac)
- Hydrogen peroxide solution (H_2O_2 , 33 %, Panreac)
- Borane triethylamine ($\text{Et}_3\text{N} \cdot \text{BH}_3$, 95 %, Fluka)
- Oleylamine (OAm, 70 %, Aldrich)
- Oleic acid (OA, 99.5 %, Aldrich)
- Analytical grade ethanol (EtOH , 96 %, Panreac)
- Chloroform (CHCl_3 , 99.8 %, Scharlau)
- n-Hexane (95 %, Panreac)
- Ethyl acetate (EtOAc , 99,5 %, Honeywell)
- Toluene (99.8 %, Supelco)
- Methanol (99.8 %, Sigma Aldrich)
- Silylation agent (HMDS:TMCS:Pyridine, 3:1:9, Sylon[™] HTP, Superlco)

2.1.2.3 Analytic standards

- D-cellobiose (> 98 %, Sigma Aldrich)
- D-glucose (99.5 %, Sigma Aldrich)
- Fructose (99 %, Alfa Aesar)



- 5-hydroxymethylfurfural (5-HMF, 99 %, Sigma Aldrich)
- Levulinic acid (98%, Fluka)
- D-sorbitol (98 %, Sigma Aldrich)
- D-mannitol (99 %, Sigma Aldrich)
- Xylitol (99 %, Sigma Aldrich)
- Erythriol (99 %, Sigma Aldrich)
- Propylenglycol (98 %, Sigma Aldrich)
- Glycerol (99.5 %, Sigma Aldrich)
- Ethylene glycol (EG, 99 %, Sigma Aldrich)
- Hydroxycetone (90 %, Aldrich)
- 1,2 butanediol (98 %, Aldrich)
- 1,2-pentanediol (96 %, Aldrich)
- Propanoic acid (99.5 %, Sigma Aldrich)
- 2-hydroxy-3-methylcyclopentenone (99 %, Aldrich)
- Acetic acid (99 %, Fluka)
- Phenol (99 %, Sigma Aldrich)
- 3-hydroxy pyridine (98 %, Aldrich)

2.1.2.4 Gases

All gases employed along the different stages (synthesis of materials, reaction tests and product analysis) were of high purity: Hydrogen Premier Plus X50S (99,9992%, Air Liquid), synthetic air premier (20.9% O₂ ±1%, 99.995%, Air Liquid) as well as Nitrogen, Helium and Argon premier (99,9992%, Air Liquid). The gases used for the synthesis of carbon nanofibers were CH₄ from Messer (99.5 %) and CO₂ premier (99.995 %, Carbueros Metálicos S.A.). Finally, a mixture gas of 1% O₂ in N₂, (0.9983% O₂ ±0.5%, 99.000 ±0.05% vol./vol.) supplied by Carbueros Metálicos, S.A was used to passivate the metal catalysts.

2.1.3 SUSTRATES

2.1.3.1 Model compounds

D-(+)-cellobiose (purity > 98%, Sigma Aldrich[®]), a glucose dimer connected through the β -(1,4)-glycosidic bond, was used as representative compounds of cellulose structure (Figure 2.1). The moisture content of this reactant (at around 3 wt. %) was taken into account in the mass balance.

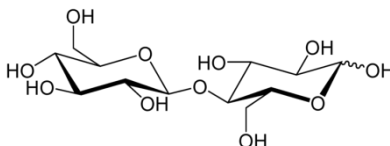


Figure 2.1 Cellobiose as structural unit of cellulose.

2.1.3.2 Cellulose

For cellulose conversion tests, either commercial cellulose (Avicel[®] PH-101, Fluka, moisture content ca. 5 wt. %) or pre-treated samples with various crystalline features were used. The index of crystallinity (CrI) was reduced by ball-milling and estimated from the XRD pattern (see details in Section 2.2.2 and 2.3.3). As it is observed in Figure 2.2, the CrI of raw cellulose, at around 78.5 %, was progressively decreased to 37.5 % until a final amorphous state after 2 and 8 h of rotation at 600 rpm, respectively. This pre-treatment not only disrupts the hydrogen bond network but also modifies the particle size and the morphology [62, 83].

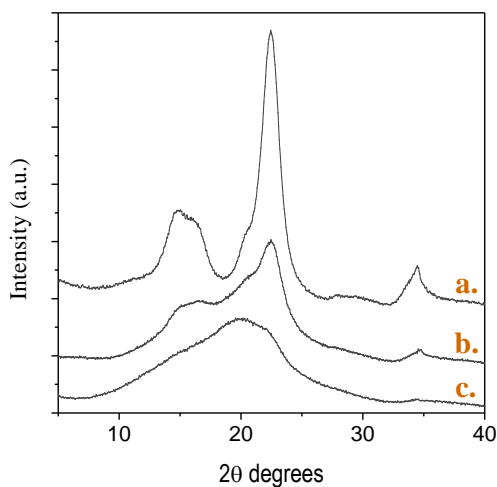


Figure 2.2 XRD patterns of commercial cellulose (Avicel PH-101) as a function of milling time: non treated (a) and ball-milled at 600 rpm during 2 h (b) and 8 h (c). The crystalline index gradually decreased from 78.5 % to 37.5 % and amorphous state.

SEM images gave more evidence on some of the morphological changes induced by ball-milling (Figure 2.3). Initially, microcrystalline cellulose was present as assemblies of fibrils with a mean size of 50 μm in length (Figure 2.3-a). A closer inspection of the crystallites reveals that cellulose strands remained stiffly aligned into parallel arrays along the longitudinal axis. The fibers were broken down into smaller fragments as cellulose crystalline features were partly lost ($\text{CrI}=37.5\%$ after 2 h of pre-treatment), but still owning certain similarities to the original sample (Figure 2.3-b). After 8 h of ball milling, the total disruption of cellulose backbone was finally noted on its amorphous state (Figure 2.3-c), forming a crumbled solid with a fairly smooth surface.

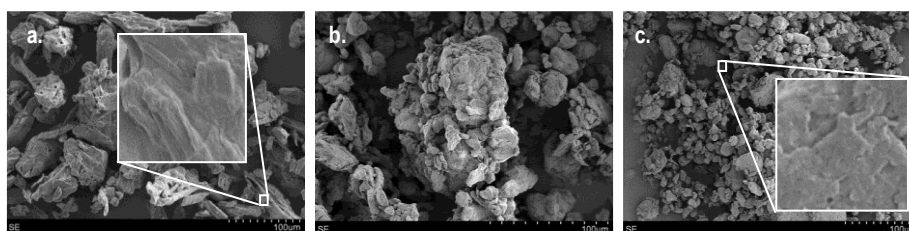


Figure 2.3 SEM analysis of cellulose a) non-pretreated, b) intermediate crystallinity ($\text{ICr}=37.5\%$) and c) amorphous. Scale bar=100 μm .

2.1.3.3 Almond hulls

Almond hulls (variety Marcona) originated from almond tree (*prunus dulcis*), were harvested from a local farmland (Ricla, Zaragoza, Spain) in season 2019 once they were separated from the edible kernel. As-received, the biomass sample was first sterilized by spraying ethanol (96 %, Panreac) and air-dried. The material was then ground to a particle size less than 0.5 mm using in sequence a RetschTM GM 300 grinder (2500 rpm, 30 s, 2 cycles), a coffee mill and a 50-mesh sieve (Endecotts, London). Figure 2.4 shows the scheme of this procedure.

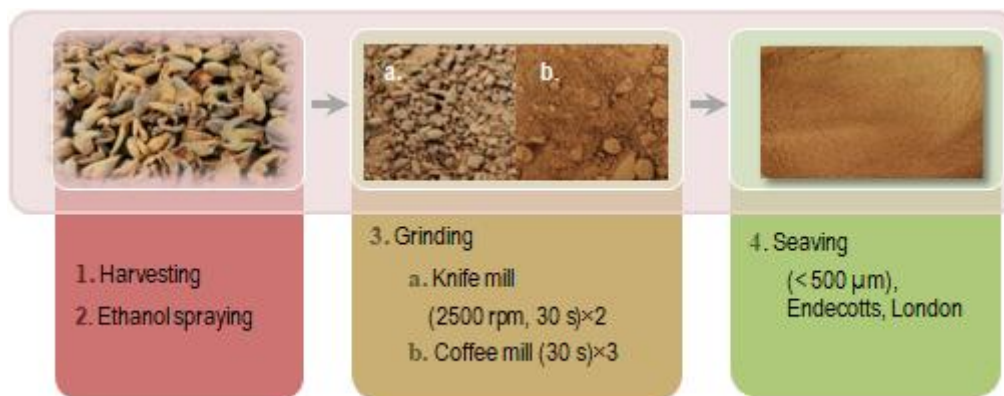


Figure 2.4 Flow-chart for biomass preparation.

The fine material was characterized following standard methods issued by the Technical Association of Pulp and Paper Industry (TAPPI). The three main components of the biomass (cellulose, hemicelluloses and lignin) were determined by chemical titration as reported by Hu *et al.* [111]. The overall content of each fraction, together with other relevant properties of the raw material, are tabulated in Table 2.1.

Table 2.1 Almond hulls characterization

FIBRE ANALYSIS (wt. %)	
Cellulose	12.60
Hemicellulose	19.40
Lignin	25.10
Proteins	7.81
Ash	11.80
Others	16.57
PROXIMATE ANALYSIS (wt. %)	
Moisture	6.72 ±2.87
Ash	11.80±0.37
Volatiles	62.72±1.93
Fixed carbon	18.77±0.57
ELEMENTAL ANALYSIS	
% C	44.23±1.38
% H	4.65±0.21
% N	1.25±0.07
% O ^[a]	49.88±1.52
HHV (MJ/kg) ^[b]	15.74±0.50

^[a] oxygen determined by difference

^[b] calculated from Channiwala formula [112]

For proximate analysis, the content of moisture, ash and volatile carbon was estimated according to the standards ISO-289-1981, ISO-1171-1976 and ISO-5623-1974, respectively. Elemental composition was performed using the Thermo Flash 1112 analyzer as it will be referred in Section 2.3.4.1.

2.2 Experimental procedure

2.2.1 CATALYST PREPARATION

2.2.1.1 Synthesis of carbon nanofibers (CNF)

Fishbone-type carbon nanofibers (CNF) were grown in a rotary bed reactor by catalytic decomposition of biogas (CDB), a synthetic mixture of $\text{CH}_4:\text{CO}_2$ at the same volumetric proportions (1:1 vol./vol.). A digital image of the experimental set-up is shown in Figure 2.5. Early studies on the synthesis of nanofibers set the influence between the process parameters (nature of the catalyst, composition of reactant gases and reaction temperature) and the physical and morphological features of CNF [113]. Herein, two experimental conditions were selected to prepare CNF with different graphitic order, as detailed in Table 2.2. Both exhibit a similar stacking arrangement (fishbone morphology) except that samples prepared at lower temperatures (CNF_{600}) show greater structural disorder than the CNF_{650} . A more elaborated discussion on the influence of temperature on the graphitic character of nanofibres can be found in previous works of the group, based on their structural and textural characterization by crystallography (XRD), physisorption and Raman spectroscopy [114].



Figure 2.5 Pilot plant used for the synthesis of CNF by CDB.

Table 2.2 Synthesis conditions of CNF.

	CNF ₆₀₀	CNF ₆₅₀
Catalyst:	Ni/Al ₂ O ₃	NiCo/Al ₂ O ₃
Feed (L/h)	150	150
Feed stream (vol./vol.)	(CH ₄ :CO ₂ ; 1:1)	(CH ₄ :CO ₂ ; 1:1)
Reaction time (min)	180	240
DCB Temperature (°C)	600	650
Weight hourly space velocity (L/(g _{cat} ·h))	30	30
CNF production (g/batch)	40.4	39.5
Catalyst content on raw CNF (Ni(Co)Al ₂ O ₃ , wt. %) ^[a]	7.9	9.3

^[a] Determined from Al, Ni and Co measurements by ICP-OES.

Catalysts for CNF synthesis were prepared by the fusion method, based on the physical mixture of metal nitrates (Ni:Co:Al molar composition of 2:0:1 for Ni/Al₂O₃ catalyst and equal to 1:1:0.98 for the bimetallic NiCo/Al₂O₃), followed by air calcination at 450 °C (heating rate of 5 °C/min) for 8 h. In a typical batch, 5.0 g of the fresh catalyst was placed in the reactor and reduced *in-situ* by flowing H₂ gas (80 mL/min) for 1 h at 600 °C. Next, reactor was fed by a mixture of CH₄:CO₂ stream (1:1, vol./vol., 150 mL/min) working under the experimental conditions summarized in Table 2.2. On average, a CNF yield of 40.0 g per batch was obtained, including the metal particles of Ni (NiCo alloy) and Al₂O₃. Such metal percentage accounted for

7.9-9.3 wt. %. Additional details about the catalyst preparation, reactor configuration and the characterization of final CNF can be found in previous works of the research group [115-117].

2.2.1.2 Purification and surface modification

Raw CNF were commonly functionalized through a two-step procedure. In a first stage, CNF were purified in HCl (37 wt. %, Fluka, 50 mL/g_{CNF}) under ultrasonic vibration for 4 h at 60 °C. This treatment leached most part of the metal content from the carbon nanostructure. A second oxidation in concentrated HNO₃ (65 wt. %, Panreac, 25 mL/g_{CNF}) at reflux conditions (130 °C) for 1 h helped to remove metal catalyst remnants while it incorporated different oxygenated functional groups onto the carbon surface. These species (i.e. carboxylic groups, lactones, phenols, carbonyls and ethers) serve as anchoring points for metal precursors and substrate interaction [118]. In both cases, CNF were separated from the acid solution by vacuum filtration, rinsed with deionized water to neutral pH, and dried at 70 °C overnight. The oxidized carbon nanofibers were denoted as CNF to simplify.

2.2.1.3 Post-synthesis treatments

CNF were further submitted to a series of post-synthesis treatments to incorporate additional functionalities (acid moieties and/or metal nanoparticles) according to the reaction needs. Such methodologies are specifically described in the next Chapters of the Thesis.

2.2.2 CELLULOSE PRE-TREATMENT

Prior to the reaction, commercial cellulose (Fluka, Avicel[®] PH-101, particle size, 50 µm; microcrystalline) was pre-treated by ball-milling using a planetary mill (PM 100 CM, Retsch, Germany) depicted in Figure 2.6. In practice, 6.75 g of cellulose were charged in a zirconia jar (50 mL) with balls inside (Ø = 10 mm, n=10, ZrO₂). The container was rotated at a speed of 600

rpm (10 Hz), including cool-down intervals of 10 min after every 50 min of run. Operation time was varied from 10 min to 8 h, according to the desired crystalline features. Mix-milled samples were similarly performed but entering cellulose and the catalyst as feed at a prefixed mass ratio.



Figure 2.6 Planetary ball-mill (PM 100 CM).

2.2.3 CATALYTIC TESTS

Catalytic tests were performed in batch mode using various bench-scale reactors, either heated by conventional means or by microwave energy. In general, Instituto de Carboquímica-CSIC (Zaragoza) allowed access for conventional heating reactors whereas microwave systems were operated at the experimental facilities of Green Chemistry Centre of Excellence (GCCE, Chemistry Department of York University).

2.2.3.1 Conventional heating

a) Equipment

Three optional conventional heating reactors were used for the catalytic tests, selected according to the reaction goals, the available sample volume and operation requirements. The

experimental set-up of each system is described below whereas their individual uses are explained in the corresponding Chapter.

- **Berghof autoclave.** High-pressure reactor (Berghof Products, BR-40 series, 45 mL) equipped with a temperature controller (BTC-3000) and a magnetic stirring (Figure 2.7). A filling volume of 15-20 mL is typically used.



Figure 2.7 BR-40 Berghof reactor and BRC-3000 controller.

- **Parker Autoclave Engineers.** Stainless steel high-pressure autoclave (Parker Autoclave Engineers, 100 mL) fitted with a temperature and stirring control (B-50) and magnetic drive. The reactor was externally heated by an electric furnace. The temperature of the furnace was regulated by a PID controller using two k-type thermocouples. One monitored the temperature of the outer mantle while the other measured the temperature inside the reaction solution. Figure 2.8 presents a digital image of this system.

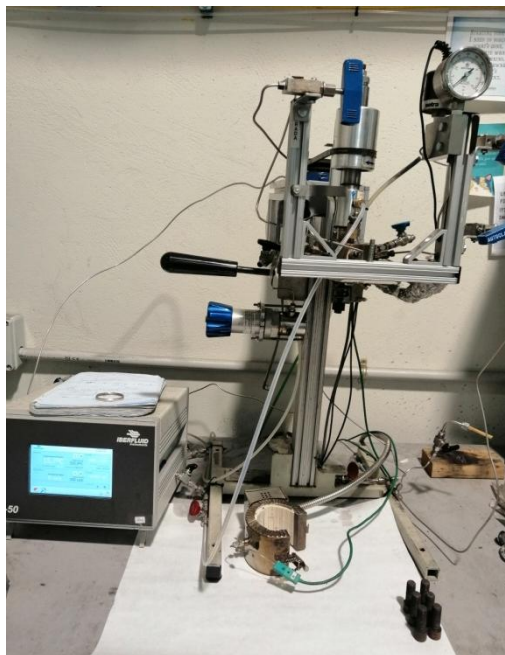


Figure 2.8 Parker Autoclave Engineers.

- **Parr reactor.** Stainless steel reactor lined with Teflon inserts (Parr Instruments Co., Series 5500) provided with temperature and stirring control (Mod. 4836). The nominal internal volume was 300 mL and it was filled with 150 mL. The reactor, schematically illustrated in Figure 2.9, was equipped with a thermocouple, pressure gauge and a dip tube, enabling the periodical withdrawal of samples (~ 5 mL) for analysis. Baffles were inserted into the reactor to facilitate the liquid mixture.

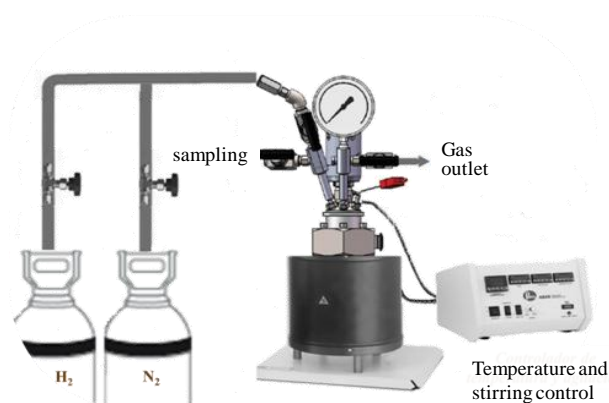


Figure 2.9 5500 Parr reactor.

b) Work-up procedure

In a typical set-up, an aqueous suspension of the substrate and the catalyst were placed inside the reaction vessel. The system is then sealed and inertized by filling the headspace with ~ 4.0



MPa of N₂ gas and flushing it repeatedly. In hydrolytic hydrogenation tests, N₂ volume was then displaced to H₂ gas, applying an identical purge protocol and finally pressurized between 4.0-8.0 MPa H₂ (RT). Prior to the reaction, a leak test was performed. Afterwards, the reactor was heated to the desired temperature under mild stirring (300 rpm). Zero time was considered when the set-point temperature was reached and then the stirring rate was raised to 1000 rpm. At the end of the test, the reaction was stopped by immersion in a tap water bath. Once at room temperature, the system was depressurized and opened. The insoluble fraction, containing the spent catalyst and the unconverted substrate, was recovered by vacuum filtration (glass microfibre, 1.0 µm, Whatman®), dried (60 °C) and weighted. The solution pH was monitored using a pH electrode GLP 21⁺ (Crison).

2.2.3.2 Microwave heating

Two different equipments activated by microwave irradiation were employed, namely, CEM Discover and CEM Mars 6, whose main features are described as follows:

- ***CEM Discover.***

CEM Discover SP microwave reactor (CEM Corporation, Matthews, USA) is a heating platform with a maximum inlet power of 300 W. The system, schematically illustrated in the Figure 2.10, accommodates vessel size of both 10 and 35 mL (pressure rated vessels of Pyrex with silicone lids) that are magnetically stirred at a variable speed. Temperature, time and power settings are controlled from SynergyTM software and/or on-board key pad. Reaction temperature is measured from a floor mounted infrared sensor. In addition, an integrated cooling system with air compressed allows for the rapid reaction quenching once it is completed.

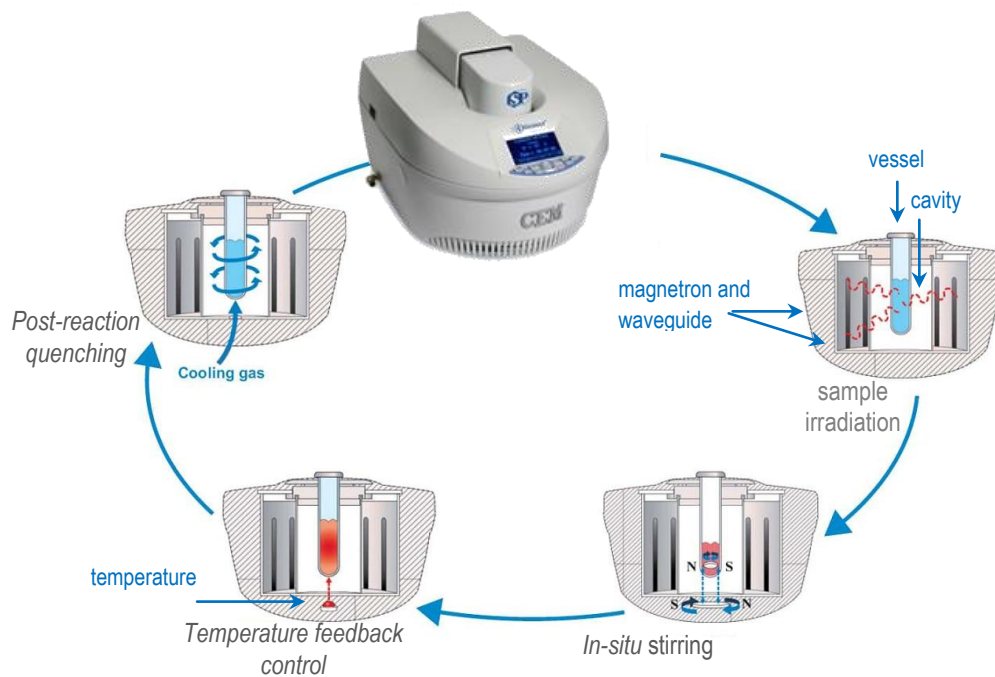


Figure 2.10 CEM Discover SP microwave reactor.

- **CEM Mars 6**

CEM Mars 6 microwave reactor (CEM Corporation, North Carolina, US) operates at a maximum power inlet of 600 W. As it is depicted in Figure 2.11, the sample is treated inside EasyPrep Plus[®] sealed vessels (Teflon, 100 mL) which are placed on the rotor tray using a pair number of them. The vessels are provided with a vent tube cap that prevents from an eventual over-pressure and work under magnetic stirring. The temperature is monitored using a dual infrared and fiber optic technology controlled from sensors located on a reference vessel.

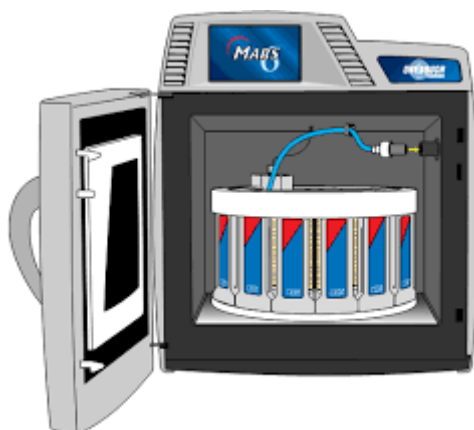


Figure 2.11 CEM Mars 6 microwave reactor.

2.3 Characterization techniques

This section describes the characterization techniques used along the Thesis. Specific procedures and conditions used for substrates and catalysts characterization as well as for the identification and quantification of the reaction products are included.

2.3.1 Electron spectroscopy

2.3.1.1 X-ray photoelectron spectroscopy (XPS)

XPS is a surface-sensitive technique that makes use of the photoelectric effect to describe qualitatively and quantitatively the chemistry of a material at the first 2-3 nm subsurface. Qualitative information is derived from chemical shifts of the binding energy whereas elemental composition can be quantified from the signal intensities [119]. Besides, it is a useful analytic tool to study surface phenomena such as segregation, cleaning and chemical functionalization as well as the valence state and electronic environment of each element present within the material under examination [120].

Surface characterization of solid catalysts by XPS was carried out in an ESCAPlus OMICROM System, equipped with a hemispherical electron energy analyser, Al/Mg dual anode and a detector with 7 channeltrons (Figure 2.12). The spectrometer was operated at 225 W (15 mA and 15 KV), using a non-monochromatic Mg $Al\alpha$ radiation ($K\alpha=1253.6$ eV) as excitation source. Survey scans were acquired at constant pass energy of 50 eV in the range of 1000 and 0 eV and 20 eV for higher resolution spectra of individual elemental regions. The base pressure in the chamber was maintained below 5×10^{-9} Torr. For the spectra processing, it was used the Casa[®]XPS software fitting the signal with a Voigt Gaussian- Lorentzian (GL60) line shape and a Shirley type background. Binding energy values were calibrated with reference to the graphitic C1s position (284.6 eV) within ± 0.2 eV accuracy. The escape depth corrected sensitivity factors were supplied by the instrument manufacturer.



Figure 2.12 ESCAPlus OMICROM spectrometer.

2.3.1.2 Atomic Emission spectroscopy (ICP-OES)

ICP-OES is a multi-component analysis technique that uses an inductive coupled plasma source to provoke excitation of electrons at higher energy levels. After the excitation, the electrons return to their original state emitting light in a characteristic wavelength for each element. The intensity of the emitted light is proportional to the atoms number of elements present. One of the main applications of the ICP-OES is the knowledge of metal composition of catalysts and their possible leaching to the reaction solution.

For these analyses, a Spectroblue-EOP-TI FMT26 (Ametek) spectrometer was employed (Figure 2.13) that allows determinations for most of the elements at the periodic table. Sample was digested according to the fusion method by sodium peroxide (Na_2O_2).



Figure 2.13 Spectroblue from Ametek.

2.3.2 Electron microscopy

Electron microscopy uses a system of electromagnetic lenses to focus an electron beam on the sample specimen, where the electrons interact with it and then are deflected. It can be performed in two modes: by scanning of an electron beam over the surface of the sample or in transmission-arrangement.

2.3.2.1 Scanning electron microscopy (SEM)

In scanning electron microscopy (SEM analysis), bounced beam electrons off the sample are collected by a secondary and retro-dispersive detector and converted into an image of the topography of the sample surface at high magnifications. In this case, SEM observation was employed to study the morphology of cellulose samples with different crystalline features. The microscope (Hitachi 3400N, Figure 2.14), was provided with an EDX Röntec XFlash de Si(Li) analyzer and operated in low vacuum mode and different electron acceleration voltages, emitting in a range from 1 to 30 kV. Cellulose sample were sputtered with gold before measurements.



Figure 2.14 SEM EDX Hitachi S-3400 N.

2.3.2.2 Transmission electron microscopy (TEM)

Transmission Electron Microscopy (TEM) is an imaging technique useful for size characterization and morphology of nanomaterials. Unlike SEM, the electron beam travels



across the specimen and information is obtained by looking at beam electrons transmitted by the sample. The microscopy works were conducted in the Advanced Microscopy Laboratories (LMA) at the Institute of Nanoscience of Aragón (INA). TEM micrographs were taken with a Tecnai F30 (FEI company) microscope, performed in both TEM and STEM (Scanning-Transmission) modes, with an accelerating voltage of 300 kV. The instrument is equipped with a Field Emission Gun (FEG) and SuperTwin[®] lenses, which allows a maximum point resolution of 1.5 Å. A coupled energy dispersive X-Ray spectrometer (EDS Microanalysis, Oxford Instruments Inca) provides additional details of local elemental composition. Prior to the analysis, the samples were ultrasonically dispersed in ethanol (metal catalysts) or water (graphene oxide samples). A droplet of this suspension was deposited onto a holey cooper grid coated with a lacey carbon film.

Particle size distribution analysis was performed from TEM measurements using the ImageJ software. At least 150 metal nanoparticles were counted to get meaningful information on the mean size particle (d_M), according to the Equation 2.1 [121]:

$$d_M = \frac{\sum d_i \cdot n_i}{\sum n_i} \quad [2.1]$$

where n_i is the number of particles with a given diameter d_i .

In order to assess how the observed distribution befits to the true population, the standard deviation (σ_M) was calculated by means of the mathematical expressions 2.2:

$$\sigma_M = \frac{\sum d_i^2 \cdot n_i - n d_M^2}{n^2} \quad [2.2]$$

The specific surface area of nickel (S_{Ni}) was determined from the metal particle size distribution profiles taking into consideration the particles geometry, the Ni density ($\rho_{Ni}=8.9 \text{ g/cm}^3$) and the number of surface area-weighted diameter (\bar{d}_s) [122, 123], following the expressions 2.3-4:



$$S_{Ni} = \frac{6}{\rho_{Ni} \cdot \bar{d}_s} \quad [2.3]$$

$$\bar{d}_s = \frac{\sum_i n_i \cdot d_i^3}{\sum_i n_i \cdot d_i^2} \quad [2.4]$$

On the assumption of a spherical form, a shape factor of 6 was fixed for Equation 2.3.

2.3.3 X-ray Diffraction (XRD)

X-ray scattering is routinely used for phase identification of a crystalline material and establish their lattice parameters. It is based on the constructive interference of monochromatic X-ray diffracted by a crystalline sample. The former takes place when the interaction between the incident rays and the sample satisfies the Bragg's Law (Equation 2.5):

$$n\lambda = 2d \sin \theta \quad [2.5]$$

where

- n is an integer referred to the order of reflection
- λ is the wavelength of the X-ray (Å)
- d is the inter-planar spacing of the crystal (Å)
- θ is the diffraction angle (degrees).

The expression relates the wavelength of the X-rays to the diffraction angle and the lattice spacing of the crystalline sample (Figure 2.15-a). Experimentally, X-rays are generated by a cathode ray tube, filtered to obtain a monochromatic radiation and collimated before being directed to the sample. The interaction between the incident rays with the specimen creates a series of diffractions which are recorded by a Lynx eye detector. For a typical powder patterns, data are collected at an angular position (2θ) of the incident X-ray beam between 10 and 80 °. The geometry of the diffractometer is such that the sample rotates at an angle of θ in the path of the collimated beam while the X-Ray detector collect the diffracted X-rays at an angle of 2θ (Figure 2.15-b). The conversion of the diffraction peaks to their corresponding d -spacing allows

to identify the crystal and elemental structure by comparison with that of standards reference patterns [124].

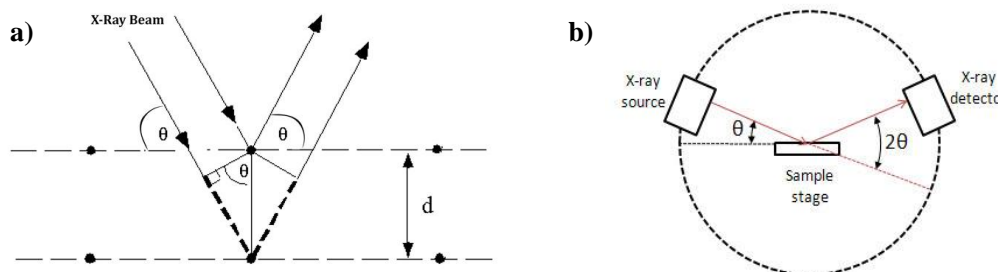


Figure 2.15 a) X-ray crystal diffraction scheme and b) Instrument configuration according to Bragg-Brentano geometry and its main components.

At the same time, the XRD line broadening (β) gives indication for the average crystallite size (L_c) according to the Debye-Scherrer equation (Eq. 3.6) [125, 126]. The technique has a limit detection of *ca.* 5 nm.

$$L_c = \frac{K\lambda}{\beta \cos \theta} \quad [3.6]$$

where

- K is a constant close to unit (0.89)
- λ is the radiation wavelength (\AA)
- β is full width of diffraction line at half maximum (in radians)
- θ is the diffraction angle of a line maximum (in radians).

XRD pattern were acquired on a Bruker diffractometer (Model D8 Advance, Series 2) in the 2θ range of $5\text{--}80^\circ$ at a scan speed of 4s/step and a step size= 0.05° using a copper anode ($\lambda = 1.54056 \text{\AA}$, 40 kV, 20 mA) and a secondary graphite monochromator as radiation source. XRD data processing was carried out by the Rietveld method with EVA and TOPAS software (Bruker) following the UNE-EN 13925 (1-2-3) rules. The ICDD database was used for phase assignments.



Figure 2.16 D8 Advance Diffractometer (Bruker).

The crystalline features of cellulose were also evaluated by XRD. The so called *index of crystallinity* (CrI) provides an empirical measure for changes in the cellulose structure after ball-milling, enabling the rapid comparison of samples. This value can be estimated according to the peak height method developed by Segal *et al.* [127]. By this method, CrI is defined as the difference in intensity between the (002) reflection and that of amorphous part ($I_{002}-I_{AM}$) divided by the total intensity (I_{002}) reflection (Equation 2.7):

$$\text{CrI} = \left(\frac{I_{002} - I_{AM}}{I_{002}} \right) \cdot 100 \quad [2.7]$$

Herein, I_{002} ($2\theta = 22.6^\circ$) includes contributions from both crystalline and amorphous cellulose whereas I_{AM} stands for only the amorphous region ($2\theta = 18^\circ$) and it corresponds to the height of the valley between the (002) and the (101) lattice peaks. The Miller indices of Avicel PH-101 cellulose are schematically illustrated in Figure 2.17-a. Upon amorphization, the intensity of (002) diffraction is clearly decreased and broadened (bottom of the Figure 2.17) [128].

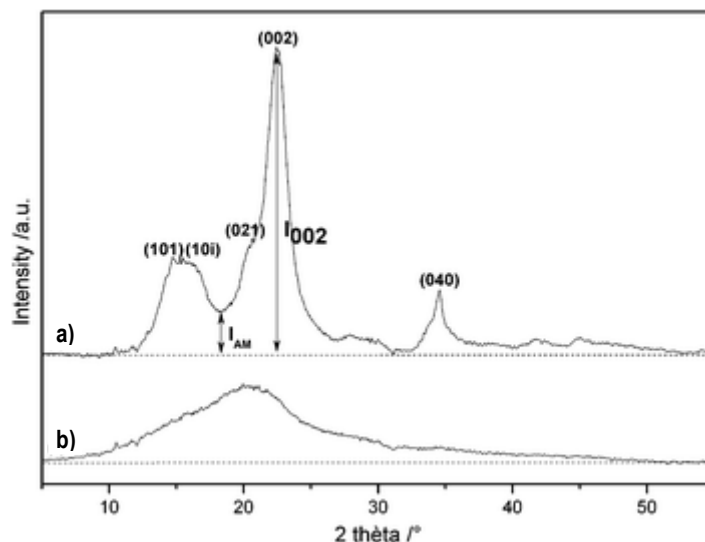


Figure 2.17 Representative XRD diffractogram of cellulose a) crystalline and b) in amorphous state (Imagen taken from the reference [49]).

2.3.4 Thermal analysis

2.3.4.1 Elemental Analysis (EA)

The weight percentage of C, O, H and S was determined by elemental analysis (FlashEA[®] 1112 Analyzer, Thermo Scientific, Figure 2.18). The technique is based on the dynamic flash combustion method, where target compounds of the sample are completely converted into CO₂, H₂O, N₂ and SO₂ and further quantified by chromatography. In practice, *ca.* 8 mg of sample were weighted in crucibles and introduced into the combustion reactor from a Thermo Scientific MAS 200 autosample. The oxidation was achieved at 900 °C using a helium stream temporally enriched in oxygen and V₂O₅ as promoter. Afterwards, reaction gases passed through a layer filled with copper, which removed the unreacted oxygen and reduced the nitrogen oxides to elemental nitrogen (N₂). The resulting mixture was separated into the individual gases onto a Poropak PQD chromatographic column and detected by a Thermal Conductivity Detector in the range of 0.05-99.95 wt. %. Data acquisition and report was carried out using the Eager Experience software. The amount of oxygen was estimated by subtraction of the different

elements mass to the total mass. The equipment calibration was performed using sulfanilamide as standard of reference. Every sample was assessed by duplicate.



Figure 2.18 Thermo Flash 1112 Elemental analyzer.

The higher heating value (HHV) of organic phases was theoretically estimated from CHN/O data using the modified form of Channiwala's formula (Equation 2.8) [112].

$$\text{HHV (MJ/kg)} = 0.3491 \cdot \text{C} + 1.1783 \cdot \text{H} + 0.1005 \cdot \text{S} - 0.1034 \cdot \text{O} - 0.0151 \cdot \text{N} \quad [2.8]$$

In this equation, C, H, S, O and N stand for carbon, hydrogen, sulphur, oxygen and nitrogen contents, expressed in mass percentages of material on dry basis.

2.3.4.2 Temperature programmed reduction (TPR)

Temperature programmed reduction (TPR) analysis depicts the reduction behavior of a catalyst. A closer observation of the TPR profile lends useful information about chemical changes resulting from promoters or metal/support interactions. In this work, TPR-H₂ experiments were performed on AutoChem II 2920 station by Micromeritics (Figure 2.19-a). In a typical essay, fresh catalyst (200-250 mg), previously stabilized at 110 °C by an inert gas, was submitted to a progressive heating (10 °C/min) from 45 to 500 °C under a H₂ stream (H₂/Ar, 10:90 vol./vol., 50 cm³/min) while a thermal conductivity detector (TCD) recorded variations on the outlet gas stream composition. Hydrogen consumption peaks were related to the metal reduction regions.

In some instances, the TPR-H₂ profile was acquired on a NETZSCH TG 209 F1 Libra thermal analyser coupled with mass spectroscopy. The analysis was performed on an initial sample mass

of *ca.* 8 mg, which is submitted to a gradient temperature (heating program from 30 to 600 °C at a rate of 10 °C/min) in a reductive controlled environment (10% vol/vol., H₂/N₂ using a constant H₂ flow of 50 mL/min). The outcoming gas was continuously monitored by a mass spectrometer (quadrupole OmniStar TM, Pfeiffer), shown in Figure 2.19-b.

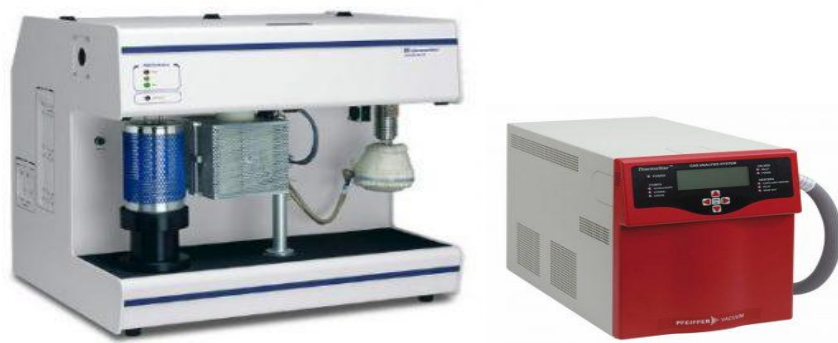


Figure 2.19 a) AutoChem II equipment (Micromeritics) and b) OmniStar TM mass spectrometer (Pfeiffer).

2.3.4 Chromatographic techniques

2.3.4.1 High Performance Liquid Chromatography (HPLC)

Reactor effluent composition was usually analyzed by High-Performance Liquid Chromatography (HPLC). The separation was achieved by isocratic elution of a volume sample using two optional systems. Technical specifications of both instruments and measurement conditions are summarized in the next paragraphs:

- a) HPLC apparatus (Jasco, LC-2000 Plus Series) at ICB-CSIC facilities uses a semi-micro HPLC pump PU-2085, refractive index detector (Jasco RID-2031) and a strong cation-exchange resin column (ReproGel Pb, 9 µm, 8×300 mm, ReproGel[®], Maisch). The main parts of the instrument can be identified in Figure 2.20. The column, preceded by a guard-column, was operated at 80 °C using ultrapure H₂O (0.055 µS/cm) at a flow rate of 0.5 mL/min as eluent. Sample separation was complete within a run time of 56 min. Cell

temperature was set to 30 °C while an injection loop of 50 μL was selected. Figure 2.21 shows an example of compounds separation.

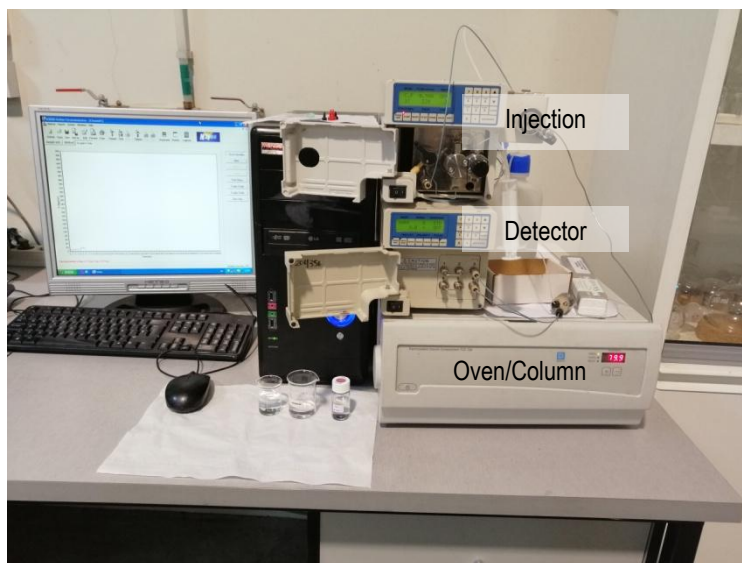


Figure 2.20 HPLC apparatus equipped with RI-detector, manual injector, oven and pump.

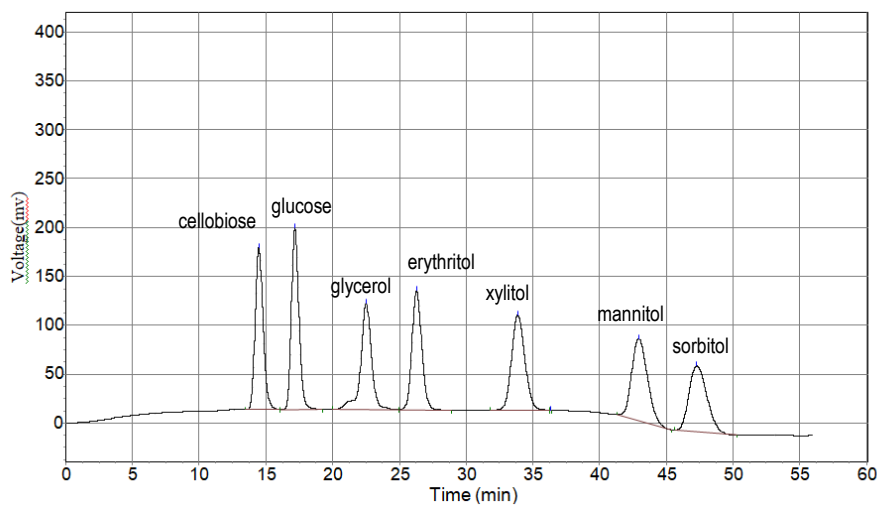


Figure 2.21 Typical chromatographic separation of some commercial standards.

- b) Agilent 1260 Infinity HPLC apparatus (USA). The chromatograph, housed at GCCE facilities, is equipped with ultraviolet-visible (254 nm) and refractive index detectors and a Hi Plex H column (7.7 \times 300 mm, particle size 8 μm , Agilent Technologies[®], USA). The separation was achieved by isocratic elution of a volume sample (5 μL), using 0.6 mL/min



of 5 mM H₂SO₄ as the mobile phase. The column and cell temperatures were hold at 60 °C and 55 °C, respectively.

Routinely, the solution was re-filtered before the injection through a 0.45 µm PTFE syringe filter. The identity and quantification of products were based on the retention time and the calibration curves of commercial analytical standards.

The products yield (Y) was calculated on their mass ratio basis with respect to the initial substrate (Equation 2.9):

$$Y (\%) = \left(\frac{\text{mass of product}}{\text{mass of fed substrate}} \right) \cdot 100 \quad [2.9]$$

2.3.4.2 Gas-cromatography (GC)

a) Silylation and GC-FID.

In certain cases, the analysis of products by gas chromatography was performed from their silylated analogues. In short, the derivatization procedure was as follows: sample aliquots (3 mL) were first evaporated to dryness under vacuum (75 °C) and then converted to their trimethylsilylether counterparts using an overstoichiometric proportion (1 mL per 10 mg of solid) of commercial silylation agent (HMDS:TMCS:Pyridine, 3:1:9, SylonTM HTP, Superlco). The reaction proceeded at 60 °C for 30 min under sonication. Before the injection, pyridine was evaporated with a N₂ flow line. The remaining solid was then re-dissolved in toluene and filtered through a 0.45 µm PTFE filter. A similar methodology was applied for the analytical standards used in the quantification.

In order to determine all those volatile compounds (i.e., EG, ethanol...) which could be lost during sample drying, an aliquot of the filtered sample was diluted in methanol (1:4) and directly injected.

The apparatus (GC, Perkin Elmer Instruments, Clarus[®]580) is equipped with an autosampler, a splitter injection port and flame ionization detector (FID), Figure 2.22. Separation of products (0.5 μ L of sample, split ratio of 1:11) was performed on an Elite-5 column (Crossbond 5% diphenil-95% dimetyl polioxane, 250 μ m \times 30 m) with helium (10 mL/min, 99,9992%, Air Liquid) as carrier gas. Oven temperature program was initially hold at 40 $^{\circ}$ C for 2.5 min, ramped to 330 $^{\circ}$ C at 10 $^{\circ}$ C /min, and kept at this point for 1 min, while injection and detection temperatures were fixed at 275 $^{\circ}$ C and 330 $^{\circ}$ C, respectively.



Figure 2.22 GC, Perkin Elmer Instruments.

b) Gas Chromatography coupled to Mass Spectroscopy (GC/MS)

Gas Chromatography-Mass Spectroscopy (GC/MS) was employed to complement the analysis of reaction products and/or gain structural information of unknown products via in-source fragmentation. For this purpose, a GC-MS Agilent 7890 Instrument equipped with auto-sample and a capillary HP-FFAP column (Agilent) was used. The GC column was first heated from 60 $^{\circ}$ C (holding time of 4 min) to 80 $^{\circ}$ C at a ramp rate of 1.5 $^{\circ}$ C/min and kept for 4 min. The temperature was then rose at 3.5 $^{\circ}$ C/min to 100 $^{\circ}$ C and maintained at this point for 10 min and finally ramped to 240 $^{\circ}$ C at a rate of 1.8 $^{\circ}$ C/min with an isothermal period of 5 min.

Chromatographic separation line was followed by Agilent single quadrupole with an atmospheric pressure chemical ionization source. Ion mass spectrum was identified using the preinstalled National Institute of Standards and Technology (NIST) reference database.



For quantification purposes, the products were calibrated in the range of 1-5 wt. % using commercial pure chemicals, including hydroxycetone, glycerin, propanoic and acetic acids, 2-hydroxy-3-methyl, 2-cyclopenten-1-one, phenol, 3-hydroxy pyridine, and a series of 1,2 alkanediols compounds (propylene glycol, 1,2 butanediol and 1,2-pentanediol). The concentration of some other products was estimated assuming a response factor equal to their closest chemical analogues.

c) *Gas chromatography-TCD*

The formation of gaseous products (CO_2 , CO , CH_4) was included in the mass balance from outlet gas samples analysis, carried out by a Micro GC (Varian CP4900) equipped with two packed columns (Molecular Sieve and Porapack) and a TCD detector (Figure 2.23). Calibration of compounds was daily made by interpolation from area peaks of known concentration using pure gases (100 vol. %) and a reference gas containing 15 % CO_2 , 20 % CH_4 , 30 % CO and 35 % H_2 (expressed in vol. %).



Figure 2.23 Varian CP4900 Micro Gas Chromatograph



Chapter 3.

Cellulose hydrolysis into glucose using low-dimensional carbon catalysts



Chapter 3.

Cellulose hydrolysis into glucose using low-dimensional carbon catalysts

Abstract

Carbon nanostructures have received a great deal of interest in cellulose hydrolysis reaction. In this Chapter, the influence of the oxidation/exfoliation degree of *fishbone* carbon nanofibers (CNF) on the catalytic activity was addressed. Various oxidative treatments, with increasing severity conditions, were applied to unravel the nature of the active sites and modulate their acid density and strength. These included the immersion in nitric acid (HNO_3) and the chemical treatment by the modified Hummers method. The oxidative exfoliation by Hummers' method afforded the highest degree of functionalization. Numerous O- and S-moieties (-OH, -COOH, - SO_3H) were covalently attached on the CNF backbone, whose relative proportions were in some instances tuned by a hydrothermal stage (180 °C, 6 h). By this method, a fraction of graphene oxide nanofibers (GONF) were de-laminated into sheets of few-layers (FLGO) and further disrupted into zero-dimensional domains (quantum dots, GOQD), allowing access to a wider portfolio of GO-morphologies, initially derived from CNF. The three fractions were size-separated by degressive differential centrifugation (DDC) and used as reference materials to disclose whether smaller dimensionalities can be translated into superior catalytic properties in terms of diffusion transport and functionalization degree. The study was conducted under different reaction conditions and heating sources (conventional and microwave radiation). Collectively, catalytic results obtained in this section shape a useful guide-line for the structural design of different GO-derivatives when their use as carbocatalysts for cellulose depolymerization is targeted. Besides, the use of auxiliary techniques such as ball-milling and microwave energy became essential for a better exploitation of surface functionalities and

reaction efficiency, either through a more intimate contact between the catalyst and the bulk cellulose or a significant reduction on the reaction timescale. The synergetic effect between microwave radiation and our catalytic system was studied during a short research stay in Green Chemistry Centre of Excellence (GCCE) at the University of York (UK).

3.1 Introduction

Acid depolymerization reaction to simple sugars constitutes the most common entry point into the biorefining schemes for cellulose valorization [47, 129-131]. The primary hydrolysis product, glucose, is a versatile intermediate from which a broad variety of chemicals can be derived (Figure 3.1) [132, 133].

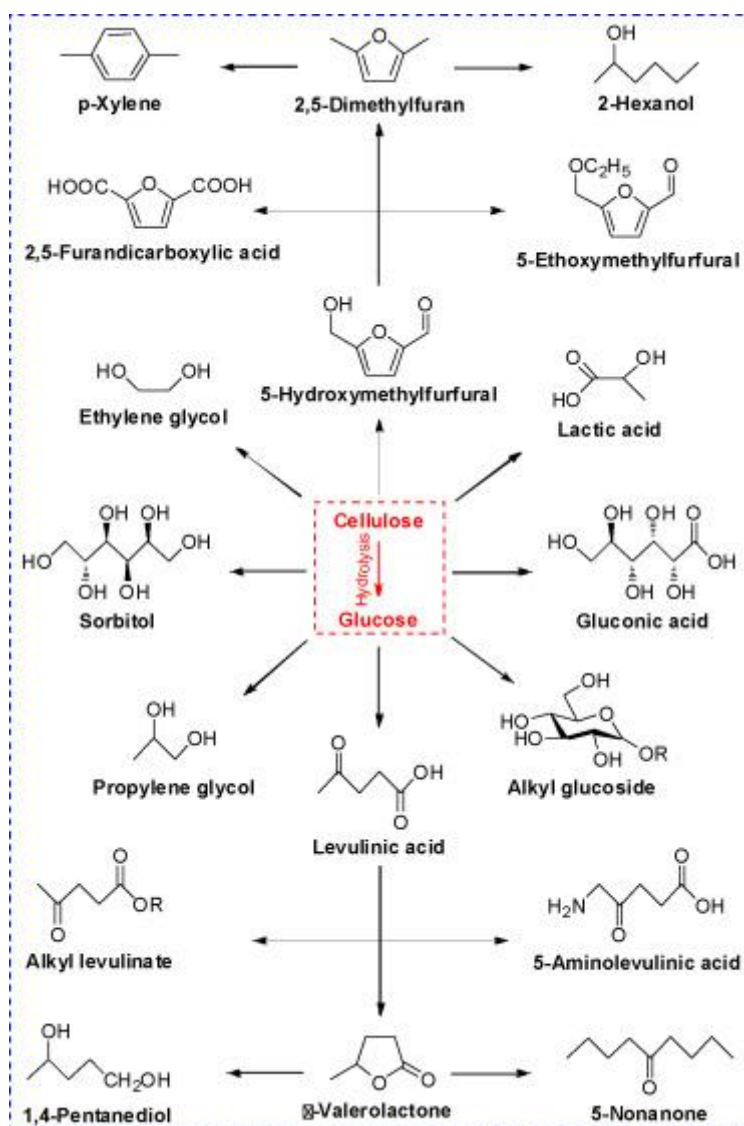


Figure 3.1 Conversion of cellulose into chemical and fuels via glucose. Image taken from [48].

Many catalytic processes have been explored in this field. Homogeneous systems, although attractive in terms of mass transfer and reaction efficiency, suffer from several operational and environmental drawbacks (i.e., equipment corrosiveness, catalyst recovery and waste disposal)

that discourage their usage at large scale. In search for more sustainable approaches, various solid acid catalysts were proposed [134-136]. However, the reaction between the active sites of a granular catalyst and the β -1,4-glycosidic bonds of cellulose entails a specific solid-solid interaction, usually controlled by the steric hindrance and mass transport limitations [48, 135, 137]. For this reason, heterogeneous process schemes often include an additional pre-treatment step, aiming at decrease the structural rigidity of crystalline cellulose and make the glucan chains more accessible [17, 138]. Techniques like activation by swelling, mechanical comminution, ball-milling or the immersion in diluted acids are among the most commonly referred methods on this goal [15, 139, 140].

Supramolecular effects of cellulose have also sparked a large number of catalysts designs directed to stretch its affinity for the substrate and ensure the exposure of the active sites [49, 141]. In this line, Suganuma *et al.* prepared an amorphous carbon bearing $-\text{SO}_3\text{H}$, $-\text{OH}$ and $-\text{COOH}$ groups by sulfonation of a partially carbonized organic precursor for the saccharification of crystalline cellulose [75]. The catalytic performance of this material (64% of soluble β -1,4 glucans; 4% of glucose) exceeded other conventional acid solids like H-mordenite, niobic acid, Nafion and Amberlyst-15. Moreover, its apparent activation energy value (110 kJ/mol) was estimated inferior than sulfuric acid (170 kJ/mol), which was ascribed to a stronger adsorption ability for the substrate and the co-existence of both hydrophilic sites and hydration-tolerant sulfonic groups [75], as briefly was introduced in Chapter 1. A cellulose-mimetic catalytic system, comprising binding domains and hydrolyzing centers, was proposed to understand the cooperative effect of different surface functionalities (Figure 3.2). In this scheme, oxygen-containing groups such as alcohols, epoxides or carboxylic acids help to disrupt the hydrogen bond network between cellulosic chains, increasing the accessibility of the β -(1 \rightarrow 4)-glycosidic bonds for its scission by Brønsted acidic groups ($-\text{SO}_3\text{H}$) [48].

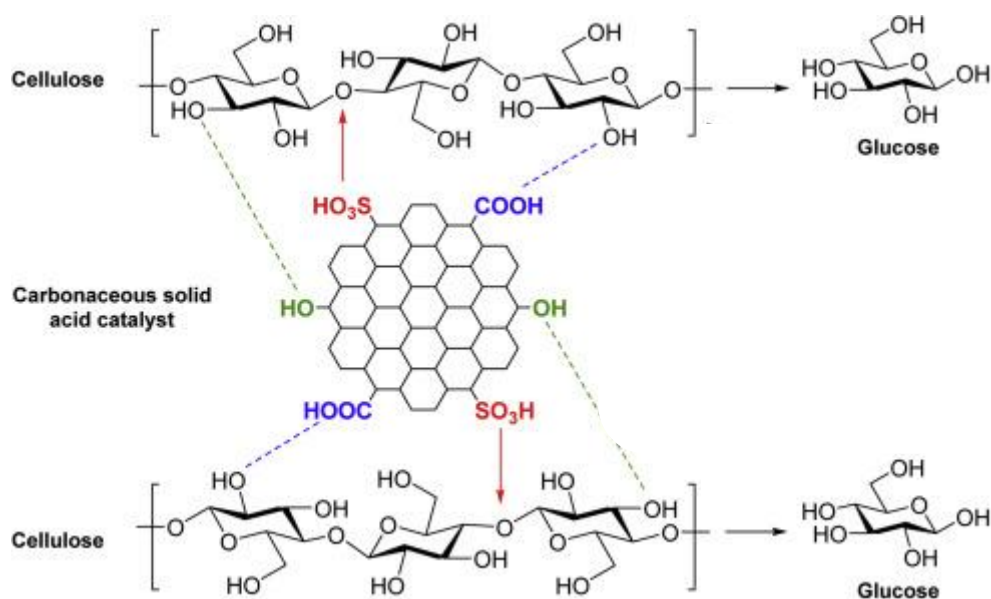


Figure 3.2 Enhanced-adsorption mechanism for the hydrolysis of cellulose over carbonaceous acid catalysts.

Source: [48]

This catalytic concept has inspired many other authors in their catalyst formulations [142-145], suggesting that design parameters such as the acid site density and their acid strength, surface area and the accessibility of active sites may also influence the catalyst performance [49, 135, 146, 147]. A correlation between the acid density of carbon materials and the hydrolysis activity was reported by Pang *et al.* In that work, the glucose yield was greatly enhanced from 7.1 % to 61.0 % upon rising the sulfonation temperature of a carbon active (AC) from 150 °C to 250 °C due to a higher loading of sulfonic species (0.19 and 0.24 mmol $-\text{SO}_3\text{H}/\text{g}$, respectively) [147]. More severe conditions (>250 °C), on the contrary, caused the decomposition of sulfonate (0.20 mmol $-\text{SO}_3\text{H}/\text{g}$ at 300 °C) with deleterious impact on the glucose yield (36.7 %). Apart from the treatment conditions, the extent of sulfonation also depended on the carbon source and the carbonization procedure. For instance, the amount of sulfur was 0.63 and 2.01 mmol $-\text{HSO}_3/\text{g}$ when an ordered mesoporous carbon (CMK-3) and a cellulose-derived carbon (cell-carbon), respectively, were sulfonated at 250 °C. In order to take full advantage of these functionalities, however, textural properties like porosity and surface area should be rationally tailored [148, 149]. Thus, yields of glucose as high as 74.5 % were attained from the above mesoporous



CMK-3 catalyst (412 m²/g) whereas it was only 35 % from the cell-carbon (6 m²/g) despite of having more acid functionalities [147].

As far as catalyst morphology concerns, it is generally considered that mesoporous architectures facilitate the diffusion transport of large molecules to the active sites of a porous material [14, 150]. The inverse approach of this assembly consists on the entanglement of carbon filaments (CNF) arranged around the cellulosic matrix [151]. The mesoporosity of CNF, arisen from its own cross-linking, can therefore be regarded as the inverse replicate of conventional supports wherein all the active sites become exposed [152, 153]. But the physical boundary of an unhindered interface between the reagents and the catalytic sites is likely depicted by their exfoliated version, based on graphene-like structures [154-156]. This morphology is best described as planar sheets of one-atom thickness organized into a honeycomb pattern. The usefulness of graphene on the hydrolysis of cellulose was disclosed by Zhao *et al.* over a lamellar lattice of graphene oxide (GO), decorated with abundant oxygen-functionalities that were directly grafted during the synthesis process [146]. Therein, the full exposure of the catalytic centers was attained only once the carbon sheets were completely separated into single layers (49.9% of glucose and 58.6% of cellulose conversion after 24 h and 150 °C vs. 39.4% of glucose and 51.1% of cellulose conversion from the oxide graphite parent) [146]. Also remarkable, the flexibility of graphene sheets was proposed to facilitate the close proximity of different groups to work synergistically [157].

Just on the limit of miniaturization of heterogeneous catalysts, novel nanoforms such as graphene quantum dots (GQD) could be similarly applied in the biomass conversion with promising prospects. This carbon allotrope can be defined as small planar pieces of graphene with nanometer lateral dimensions (below 100 nm) and monolayer thickness (less than ten layers) [158]. Structurally, graphene oxide quantum dots (GOQD), in their oxidized form, represent an ideal catalytic template for cellulose hydrolysis, providing large surface area, abundant active sites (edges, functional groups, etc.) and tunable surface chemistry [159]. Their excellent aqueous dispersibility, along with the opportunity of reuse, allows them to work on the

borderline between the homogeneous and heterogeneous conditions. This *quasi*-homogeneous behavior was recently highlighted by Chen *et al.* for the one-pot conversion of carbohydrates into 5-hydroxymethylfurfural (5-HMF) [160]. The aforementioned work is, to the best of our knowledge, the first catalytic application of GOQD in biomass conversion reactions, whose unique features promise to surpass other carbon materials reported thus far. More tentatively, a possible permeation inside the cellulosic matrix could be expected from its dimensionless character, aiding to suppress mass transfer limitations and enhancing the catalytic efficiency.

An added value of graphene materials and their GO-relatives are their MW-absorption features. This last property may be cleverly exploited to achieve further enhancement on the hydrolysis efficiency in terms of reaction rate, glucose selectivity and/or the collision chances between the catalyst and the cellulose. Some of the most relevant works previously reported in this area were summarized in Table 3.1. As a first example, Wu *et al.* studied the MW-assisted hydrolysis of microcrystalline cellulose catalyzed by a biomass char sulfonic acid (BC-SO₃H), noting a 3.8-fold higher yield of reducing sugars after 60 min at 90 °C (16.7 % of glucose and 7.4 % of cello-oligosaccharides, Entry 1) than that obtained from conventional heating sources [161]. To illustrate the positive influence of MW-systems on glucose selectivity, Sangib *et al.* compared the hydrolysis performance of a sulfonated bamboo-derived catalysts (SBC) under different heating means [162]. After the proper parametric optimization, the maximum yield of glucose (43.5 %) was found at 180 °C and 60 min of irradiation time (Entry 2) [162]. Similarly, Horikoshi *et al.* achieved 56 % of glucose upon MW-heating at 200 °C for 30 min over a sulfonated activated carbon (AC-SO₃H) (Entry 3) [163].

Table 3.1 Comparison of catalytic performance of different carbon-based materials in the MW-assisted hydrolysis of cellulose.

Substrate (S)	Catalyst (C)	Ratio (S/C)	Temp. (°C)	Holding time (min)	Conv. (%)	Glucose yield (wt. %)	Ref.
Crystalline cellulose (13.3 wt. %)	Sulfonated biomass (BC-SO ₃ H)	(2:1)	90	60	n.r. ^a	16.7	[161]
MCC (2.5 wt. %)	Sulfonated Bamboo Carbon (SBC)	(1:1)	180	60	~60	43.5	[162]



Cellulose (0.25 wt. %), (CrI=n.r)	Sulfonated activated carbon (AC-SO ₃ H)	(1:1)	200	30	n.r. ^a	56.0	[163]
MCC (2 wt. %)	Reduced graphene oxide (rGO2)	(1:1)	240	5	78.3	65.5	[164]
MCC (2 wt. %)	Graphite (Gr)	(1:1)	240	5	23.9	12.9	[164]
MCC (2 wt. %)	Carbon nanotubes (CNF)	(1:1)	240	5	40.7	27.4	[164]
MCC (2 wt. %)	Graphene oxide (GO)	(1:1)	180	60	n.r. ^a	61.0	[165]
Ball-milled cellulose (24h, 500 rpm), (0.67 wt. %)	Carbon-based solid (CSC)	(2:1)	200	60	n.r. ^a	31.1	[166]
Mix-milled cellulose (2h, 500 rpm)	Carbon-based solid (CSC)	(2:1)	200	60	n.r. ^a	62.7	[166]

^a n.r.= not reported

The origin of MW enhancement stems from a series of thermal effects such as the suppression of wall effects or the rapid and selective heating of reaction components, according to their dielectric properties [167-169]. MW energy might also participate in the activation of cellulose throughout specific interactions [161, 165, 170, 171]. The underlying mechanism was discussed by Fan *et al.* over a wide range of temperatures (160-260 °C). Above 180 °C, polar hydroxyl groups of cellulose (CH₂OH) experienced localized rotations. Such changes on the spatial orientation may distort and open the H-bonded network, enabling the rupture of β-1,4-glycosidic bonds. The highest selectivity to glucose (75%) was achieved for a microcrystalline cellulose conversion of 14% after 1 min at 220 °C [170].

Water as solvent is also a good microwave absorber [172]. The dipolar motion of their molecules, trying to align with the electromagnetic field, creates a friction which is dissipated into surroundings as heat [164, 173, 174]. However, water tends to become MW-transparent with temperature [175-178]. This characteristic holds back the use of high severity conditions, which is not only helpful in cellulose activation but also provide an environment rich in ionic species (H₃O⁺) that catalyze the hydrolysis [77, 134]. To compensate for the drop in the dielectric constant of water, Mission *et al.* employed a reduced graphene oxide as a MW sensitizer material. By this approach, a glucose yield of 66 % was attained after 5 min at 241 °C

vs. 11.5% in the absence of a catalyst (Entry 4) [164]. To more clearly understand this function, the adsorbing behavior of the catalyst should be considered. Carbon materials react to MW energy by interfacial polarization, which is usually associated with micro-plasma formation (hotspots) and a local surface overheating [163, 168, 179, 180]. The occurrence of high-temperature domains on the carbon surface could amplify the water dissociation equilibrium nearby the catalyst, yielding a pool of additional protonic sites to assist in the reaction [181].

In the latter example, most part of the oxygen/sulphur entities were thermally desorbed from the catalyst surface through a MW-assisted hydrothermal treatment at 200 °C and further annealing at 300 °C with the aim to restore the sp^2 -network and favor the electron mobility, which is essential for the rapid heating of the system [164]. In fact, a greater degree of π -electron mobility on graphenic network compared with other carbon nanostructures such as graphite (Gr) and multiwall nanotubes (CNT) might be behind their better outcome (12.9% of glucose from Gr and 27.4 % from CNT, Entries 5, 6). The synergistic effect between MW radiation and the functional groups of GO, primarily composed by oxygen and minus amounts of sulfur (0.6 wt. %), was addressed by the same research group in another study [165]. Interestingly, the authors claimed that, together with their intrinsic reactivity, MW-absorbing features of these functionalities may find certain roles as molecular radiators. Yields of glucose as high as 61 % was obtained after only 60 min at 180 °C (Entry 7) [165]. These promising results, among the highest values reported to date, leave still room for a further level of control in the GO-surface features such as the graphene domain size or the presence of HSO_3 in quantitative proportions.

Before concluding this section, it is worth mentioning to note that a vast majority of the studies listed in Table 1.1 started from untreated cellulose, harnessing the inherent contribution of MW-energy to cellulose decrystallization. However, a recent study published by Wang *et al.* demonstrated that catalytic results obtained from a carbon-based solid (CSC) were dependent on the pretreatment conditions. Thus, the glucose yield achieved after 60 min at 200 °C from the mixed ball-milling of CSC and MCC (62.74 %) was significantly higher than that of single ball-milled (31.34 %) or no ball-milled samples (hardly 4 %) (Entries 8-9).



To sum it up, this short introduction illustrates the huge potential of carbon nanostructures in catalysis for cellulose conversion. Opportunities abound when they are used as MW-absorber or the structural features are considered as part of the catalyst design. Although additional advantage seems to be unfolded as gradually downscaling from bi- to zero-dimensional morphologies, a systematic study in this field is still missing. In this Chapter, *fishbone* carbon nanofibers are used as the starting reference material for tailoring their surface functionalities and nano-engineering their morphology and size. For the first time, the potential of GOQD, initially derived from CNF, is explored and compared with other paradigmatic structures of GO, such as sheets of few layers (FLGO) and graphene oxide nanofibers (GONF). Altogether, the results provide small pieces of evidence on the importance of dimensionality and surface chemistry of GO, putting the rational basis for their use in the hydrolysis of cellulose. To maximize the catalytic efficiency, the collaborative effect of MW-energy and cellulose ball-milling was in parallel applied.

3.2 Experimental

3.2.1 CATALYST PREPARATION

To meet specific acid and hydrophilic properties, carbon nanofibers (CNF) prepared by CDB were functionalized by several post-synthesis methodologies, using various chemical reagents and oxidizing conditions. For this aim, CNF₆₀₀ were used as the initial material (see details in Chapter 2, section 2.2.1.1).

3.2.1.1 Oxidation in HNO₃ (CNF_{600-ox})

Initially, 16.0 g of raw CNF were soaked in concentrated HNO₃ (65 wt. %, Panreac, 25 mL/g_{CNF}) and reflux at 130 °C for 30 min. Samples were then filtered, rinsed with deionised water to neutral pH and oven-dried at 70 °C an overnight. The resulting samples were labeled as CNF_{600-ox}.

3.2.1.2 Oxidative cutting of CNF_{600-ox} (modified Hummers method)

GONF, FLGO and GOQD were obtained from the oxidative cutting of CNF, ultrasonic exfoliation and final fractioning in size. This synthesis protocol was previously optimized by Fuels Conversion Group [109]. In practice, 3.0 g of CNF CNF_{600-ox}, previously activated with HNO₃, and 3.0 g of NaNO₃ (Sigma Aldrich, purity ≥ 99.0%) were suspended in 128 mL of H₂SO₄ (Panreac, 96%) and placed in an ice bath. While stirring, 29.9 g of KMnO₄ (Panreac, 99%, KMnO₄/C=10) were carefully added (T^a<20 °C). The oxidation proceeded for the next 2 h at 30±5 °C and at room temperature overnight. Afterward, 240 mL of deionized water was drop-wised (<70 °C). The mixture was aged for 60 min before being diluted in another 600 mL of deionized water. At this point, the reaction was terminated with 29.9 mL of H₂O₂ (Panreac, 33%). The resulting material was exfoliated for 1 h in an ultrasonic bath and then washed with dilute HCl (10 vol. %, Panreac) through three successive centrifugation cycles (9500 rpm, 40 min, 4 °C). The final precipitate was re-dispersed in deionized water and separated into different

fractions according to a degressive differential centrifugation (DDC process). The flow sheet diagram describing the catalyst preparation is shown in Figure 3.3. Briefly, GOQD were separated from the parent suspension after 4 cycles of 100 min at 9500 rpm and 4 °C. First, the graphene material was thrice water suspended and centrifuged. Every supernatant was collected and directly submitted to a new centrifugation step (without H₂O-addition or shaking), recovering the GOQD as supernatants. Likewise, the precipitate was divided into GONF and FLGO at a rotary speed of 4500 rpm. For this purpose, the material was two-time suspended in water and centrifuged (4500 rpm, 20 min, 4 °C). Both supernatants liquids were then consecutively centrifuged (4500 rpm, 30 min, 4 °C). The bottom and upper layers belong to GONF and FLGO, respectively. The three GO-based fractions were concentrated in a rotary evaporator (56 °C), oven-dried (60 °C) and powdered.

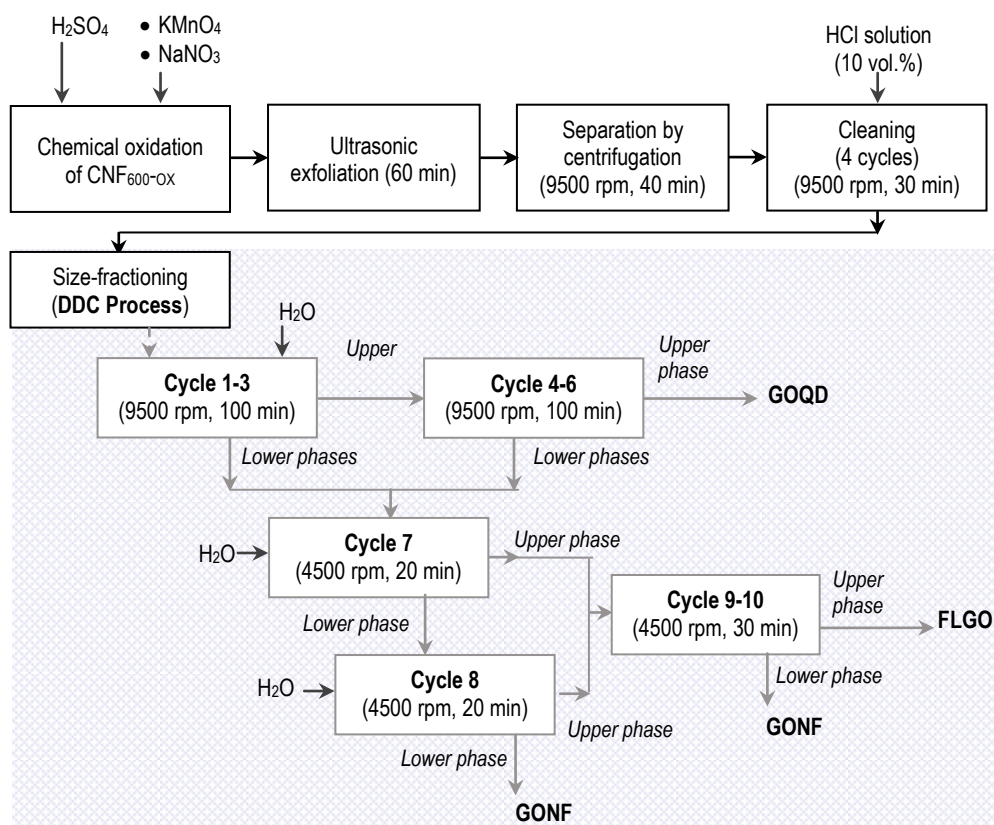


Figure 3.3 Flowchart for the synthesis of various GO-derivatives catalysts.

For some tests, GONF, FLGO and GOQD were partially reduced by hydrothermal treatment in a stainless steel autoclave (600 mL) with Teflon lining. To this effect, a 1 g sample was

dispersed in 400 mL of deionized water inside a PTFE cylinder by sonication for 30 min. The colloidal suspension was treated at 180 °C for 6 h and then it was evaporated to dryness at 60 °C, following the abovementioned methodology. Final samples were denoted as rGOQD, rFLGO and rGONF.

3.2.2 CATALYST CHARACTERIZATION

A set of instrumental techniques was used in the physicochemical characterization of each fraction: X-ray diffraction (XRD) and transmission electron microscopy (TEM) for structural information, X-ray photoelectron spectroscopy (XPS) and elemental analysis (EA) for surface chemistry and bulk composition, respectively. The analytical procedure used for each technique can be found in the preceding Chapter (section 2.3). Structural parameters such as mean crystal size (L_c) and interlayer distance (d -spacing) were estimated from XRD patterns applying the Scherrer formula and Bragg's Law to the (002) peak fit. The number of graphenic layers (n) was then calculated as $[(L_c/d_{002})+1]$.

3.2.3 CATALYTIC TESTS

The overall experimental set-up for the hydrolysis study is depicted in Figure 3.4, involving a first pre-treatment step, hydrolysis reaction under different heating sources and the product analysis.

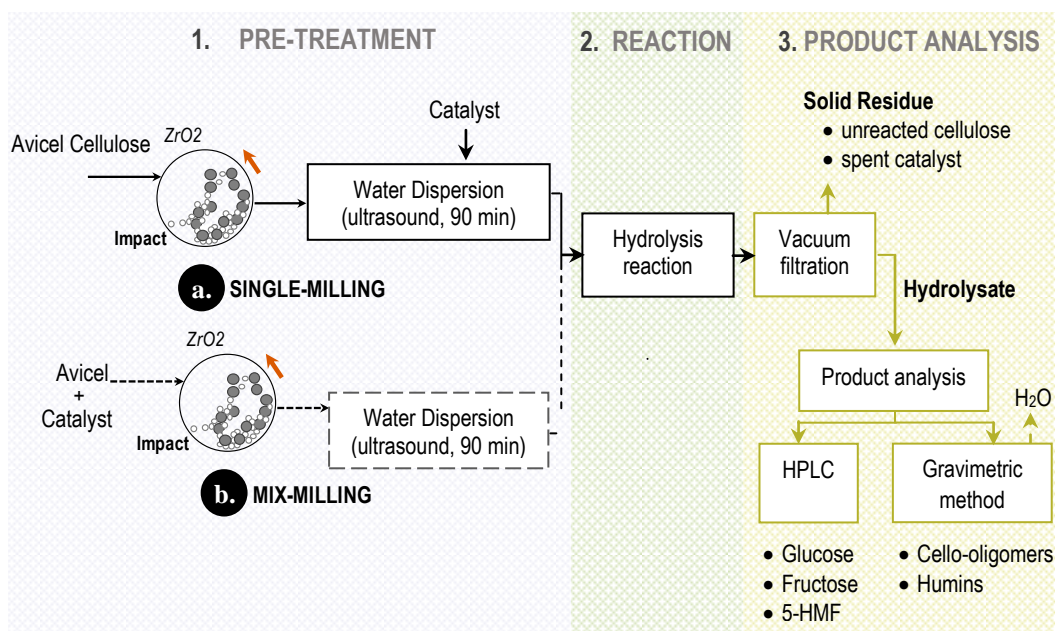


Figure 3.4 Flowchart for hydrolysis tests, from cellulose pre-treatment to product analysis.

3.2.3.1 Cellulose pre-treatment

Prior to hydrolysis, commercial cellulose (Avicel PH-101, Fluka) was pre-treated in a planetary ball-mill (PM 100 CM, Retsch) at a variable rotation time (10-480 min, 600 rpm). In mix-milled samples, catalyst was jointly milled with cellulose. The crystalline index (CrI) of cellulose was estimated from its XRD pattern by the peak height method as explained in Chapter 2.

3.2.3.2 Hydrolysis reaction

a) *Conventional heating*

Catalytic activity tests using conventional heating were carried out in batch high-pressure reactor (Berghof Products, BR-40 series, 45 mL). In a typical run, cellulose (50 mg), catalyst (50 mg) and water (20 mL) were placed inside the reaction vessel and ultrasonically dispersed for 90 min. The system was then sealed and repeatedly fluxed with N₂ gas. The hydrolysis reaction took place under stirring (1400 rpm) and autogenous pressure at temperatures in the range of 135-150 °C (± 3 °C) and a time-length between 18-30 h. Zero-point was considered when the set-point temperature is reached. At the end of the test, the reaction was rapidly stopped by quenching the system in a cool water bath. Unconverted cellulose and the catalyst were recovered by vacuum filtration (glass microfibre, 1.0 μ m, Whatman®), dried (60 °C) and weighted. The pH of the final solution was measured by employing a pH electrode GLP 21⁺ (Crison).

b) *Microwave heating*

MW-assisted hydrolysis tests were performed in a CEM Discover SP microwave reactor (CEM Corporation, Matthews, USA) with magnetic stirring and power control features (see details in Chapter 2). Experiments were run in a dynamic mode, with a maximum power input of 40 W. In a typical setup, an aqueous suspension (3 mL) containing the pre-treated cellulose



(solid/water ratio = 0.25- 2.0 wt. %) and the catalyst (mass catalyst to cellulose ratio equal to unit) was first ultrasonically dispersed for 90 min inside a Pyrex glass vessel (10 mL). After that, it was isothermally irradiated between 135-180 °C for a variable holding time (0-180 min). At the end of the reaction, the sample was air-chilled to 40 °C and diluted in 10 mL of deionized water. The insoluble fraction, containing a mixture of the solid catalyst and unreacted cellulose, was separated by vacuum filtration (glass microfiber, 0.22 µm, Whatman[®]), oven-dried (60 °C) and weighted. This part of the study was developed at the experimental facilities of Green Chemistry Centre of Excellence (GCCE, York University).

3.2.4 PRODUCT ANALYSIS

The hydrolysate composition was analyzed by High-Performance Liquid Chromatography (HPLC) using a LC-2000 Plus System (Jasco) and an Agilent 1260 Infinity HPLC apparatus for the samples generated from conventional and dielectric heating runs, in each case. Technical specifications of both instruments were given in Chapter 2 (section 2.3.5.1).

Products yield (Y) was calculated on its mass ratio basis with respect to the initial cellulose as expressed in equation 3.1:

$$Y (\%) = \frac{\text{mass of product}}{\text{mass of fed cellulose}} \cdot 100 \quad [3.1]$$

The formation of high molecular mass compounds, including partially hydrolyzed oligosaccharides and humins from sugars degradation routes, was estimated through an indirect gravimetric method. To this end, 5 mL of the filtrate solution was oven-dried at 60 °C to constant mass. The mismatch between this value (accounting for the total of non-volatile substances) and the sum of chromatographic products above the water boiling point was ascribed to this type of macromolecular complexes. The conversion of cellulose (X) was expressed as the total yield of the soluble products (Eq. 3.2):



$$X (\%) = \frac{\sum \text{mass of soluble products}}{\text{mass of fed cellulose}} \cdot 100 \quad [3.2]$$

Results were reproducible within a standard deviation of 4 %. The moisture content in the substrate was individually considered and taken into account in the mass balance (4.8 % as mean value).

3.3 Results and discussion

3.3.1 CATALYST CHARACTERIZATION

a) *Oxidation degree of CNF*

Controlling the surface chemistry of CNF becomes essential for defining their reactivity. Pristine CNF are inert and hydrophobic in nature [182]. The covalent attachment of oxygen and sulphur moieties, following routine activation procedures, turns the graphitic material into a more hydrophilic surface with certain acid features that can be potentially active in the hydrolysis of cellulose [81, 183]. One of the most conventional approaches is the wet oxidation in nitric acid [94]. Therein, nitronium ions (NO_2^+) attack the aromatic framework, which is probably the initial step in the introduction of different oxygenated species [183]. Next, the oxidation degree varies with the severity of the treatment (mainly reaction time) [184]. By this means, the overall amount of oxygen species on CNF_{600} upon reacting it with HNO_3 at $130\text{ }^\circ\text{C}$ for 30 min accounted to 3.12 wt. % of the bulk composition (Table 3.2, Entry 1).

Together with oxygen, surface modification with sulphur entities has been widely considered to increase their acid strength and hydrophilicity, mainly due to the incorporation of additional sulfonic acid groups ($-\text{SO}_3\text{H}$) [52, 107, 185, 186]. Sulfonation reaction is usually carried out in H_2SO_4 at elevated temperatures ($\sim 80\text{-}250\text{ }^\circ\text{C}$) according to a mechanism of electrophilic substitution: $\text{Ar-H} + \text{H}_2\text{SO}_4 \rightarrow \text{Ar-SO}_3\text{H} + \text{H}_2\text{O}$. Typically, heating at higher temperature, increase the acid strength of the sulfonation agent and/or the hydrophilic character of the parent material positively influence on the sulfonation extent [107, 187]. For instance, Zhang *et al.* showed that the $-\text{SO}_3\text{H}$ density of an activated carbon increased from 0.19 to 0.24 mmol/g upon raising the sulfonation temperature from $150\text{ }^\circ\text{C}$ to $250\text{ }^\circ\text{C}$. Above $250\text{ }^\circ\text{C}$, the thermal decomposition of the $\text{C-SO}_3\text{H}$ bonds was documented (0.20 mmol $-\text{SO}_3\text{H/g}$ at $300\text{ }^\circ\text{C}$) [147]. A notorious improvement on the acid density (0.44 mmol/g) was reported when the former sample was pre-oxidized in nitric acid and then treated in H_2SO_4 at $250\text{ }^\circ\text{C}$ [147]. This better outcome can be interpreted from various chemical viewpoints. By one hand, hydrophilic surface facilitate the



interaction between the carbon and the polar acid solution [185, 188]. On the hand, phenolic-like functionalities (-OH) are known as electron-donating species, facilitating electrophilic substitution reactions on the aromatic ring. A second strategy to increase the acid density of carbons is the use of fuming H_2SO_4 (15 % SO_3) [75]. It is believed that SO_3 species consumes the H_2O released from sulfonation reaction to form H_2SO_4 , forcing the reaction equilibrium towards the incorporation of SO_3H [189]. This effect has been clearly evidenced by Okamura *et al.*, who noted that a carbon sulfonated with fuming H_2SO_4 at 150 °C for 15 h exhibited twice acid density (1.34 mmol/g) than the analogous sample treated in concentrated H_2SO_4 (0.74 mmol/g) [189].

Based on the above experiences, a series of preliminary tests were performed for sulfonation of CNF_{600} under different oxidation/sulfonation conditions. However, the simple treatment of CNF with H_2SO_4 yielded invariably a modest acid density, either in terms of sulphur or oxygen content. After considering the main variables that influence on the functionalization efficiency, the total number of functional groups on acid-treated CNF_{600} remained considerably lower than other sulfonated carbons reported in the literature for the hydrolysis of cellulose [107, 185, 190], even working on the operational limits of the treatment (250 °C for 16 h) or using fuming H_2SO_4 (15 % SO_3) as a stronger acid source. The reason behind this poor degree of sulfonation/oxidation could be tentatively ascribed to the inherent properties of CNF , including an almost defect-free sp^2 network and their high structural ordering, as compared with other carbonaceous materials. It is remarkable to note that a vast majority of the former methods were applied for treating highly porous and structurally disordered carbons like activated carbons, much easier to be functionalized than the nanostructured ones [183, 191].

As a more severe route for functionalization, the chemical oxidation of $\text{CNF}_{600\text{-ox}}$ by a mixture of KMnO_4 with NaNO_3 in H_2SO_4 (modified Hummers method) was investigated. This treatment, previously optimised by Fuel Conversion Group, enabled the extensive oxidation of the carbon backbone, amounting to 45.6 % of O and 1.9 % of S (0.600 mmol $-\text{SO}_3\text{H/g}$) of the bulk composition. The resulting material, denoted as graphene oxide-derived nanofibers (GONF),

reserves the original layered structure of CNF, but showing an expansion in the interlayer distance to host the large variety of -O and -S moieties. More intriguingly, a further level of control on these functionalities in terms of chemical nature, distribution and surface density could be realized through the morphological modulation of the GONF-derivatives (ratio of edge to basal planes ratio, planar size, thickness and layered structure). This topic is specifically addressed in the next section.

b) *Exfoliation degree of CNF*

During the oxidative exfoliation of CNF_{600-ox}, a fraction of GONF was de-laminated into sheets of few-layers (FLGO) and progressively shrank their size into zero-dimensional graphene quantum dots (GOQD). Oxidized/exfoliated products were size-fractioned, each one presenting distinctive structural features and surface functionalities specifically related to their size.

As it is revealed from combustion chemical analysis, a gradual increase on the oxygen and sulphur content was noticeable as scaling down on carbon nanostructures from GONF to GOQD (Table 3.2). The oxygen percentage per weight of catalyst accounted up to 45.6, 47.2 and 54.7% in GONF, FLGO and GOQD and 1.92, 2.10 and 6.09% of sulphur, respectively. In comparison, CNF_{600-ox} used as graphenic precursor was primarily composed of carbon (95.6 wt. %) and small amounts of oxygen (3.1 wt. %), as previously commented. Minute amounts of metal residue (0.76 wt. %, determined by ICP-OES) remained still embedded onto the carbon filamentous upon the acid washing stage.

Table 3.2 Bulk and surface catalyst composition.

	EA (wt. %)				XPS (at. %)		
	C	O	S	H	C	O	S
CNF _{600-ox} *	95.6	3.12	0.02	0.34	94.05	5.95	---
GONF	50.1	45.63	1.92	2.35	70.49	27.01	2.46
FLGO	48.4	47.17	2.10	2.33	76.03	22.43	1.37
GOQD	36.4	54.67	6.09	2.84	66.51	27.83	5.56
rGONF	67.4	28.20	3.08	1.32	78.08	18.59	3.27
rFLGO	64.3	31.45	2.90	1.39	73.81	20.91	5.19
rGOQD	43.5	45.46	8.59	2.45	67.13	24.59	8.27

*Containing 0.76 % of metal residue (i.e. 0.17% of Ni and 0.31% of Al in the Al₂O₃ form) by ICP-OES.



All the samples underwent partial reduction after the hydrothermal treatment, removing the less stable oxygen groups with no obvious loss of sulphur. As a result of such compositional changes, the reduced samples are enriched in S and C (Table 3.2).

In general terms, the analysis of surface composition by XPS followed the same trend as the bulk, with the major difference shown on FLGO (Table 3.2). This fact might be ascribed to the exfoliation process of GONF, giving rise to a higher atomic fraction of C near the surface (76.0 vs. 70.5 at. %) at the expense of a lower relative peak intensity of O 1s and S 2p signals. The identity of surface functionalities was then inspected from XPS spectra deconvolution (Figure 3.5). The shape and broadness of C1s core level profile reflect the presence of various coordination environments for carbon atoms. This region was deconvoluted showed into five main components: an asymmetric peak at 284.6 eV combining aromatic (C=C, sp^2) and aliphatic carbon (C-C, sp^3); C-O bonds (hydroxyls/epoxides, 286.5 eV), C=O bonds (carbonyl/carboxylic groups, 288.5 eV), C-S linkages (285.2 eV) and the $\pi-\pi^*$ shake-up feature (291.0 eV) [192, 193]. Hydroxyl and epoxide groups will be preferentially located on the basal plane whereas lactones species, carboxylic acids and ketones would predominate on the edges, according to the Lerf-Klinowski model [194-196]. The three fractions shared similar C1s envelope, but showing different contributions from each species (quantified in Table 3.3 in atomic percentage). In principle, a higher fraction of both C-C/C=C bonds could be noted for lower dimensionalities, coming from hidden layers which are exposed upon the aperture of graphenic planes. In turn, the relative proportion of in-plane oxygenated groups (C-O-C/C-OH) species could be overshadowed by a larger number of edge functionalities (C=O, O=C-OH), concomitant to a higher edge to basal planes ratio. The edge to basal planes ratio inversely increased with the size of GO, so that the proportion of oxygenated out-plane groups become more significant at smaller graphene domain sizes. Irrespective of the sample, the speciation of S2p XPS spectra (spin-orbit splitting of 1.1 eV, intensity ratio $I_{1/2}/I_{3/2}=1:2$) was described by a major component at around 168.4 and 169.5 eV, signature of $-\text{HSO}_3$ groups, and minor portions of sulphur at lower oxidation state (S=O, 167.3 eV) as seen in Figure 3.6 [197, 198]. The

presence of C-S chemical bonds, arisen at C1s core-level, was indicative that S species were covalently linked onto the carbon lattice rather than forming $-O-SO_3H$ connections via etherification with oxygen atoms [157]. After reduction, the loss of most labile oxygen functionalities decreased the peak signals correspondent to (C-O), while the sp^2 -conjugated graphene network (and its inner $\pi-\pi^*$ transition) was restored. More resilient toward the hydrothermal stage seems sulphur and carboxylic species, remaining mostly unaffected.

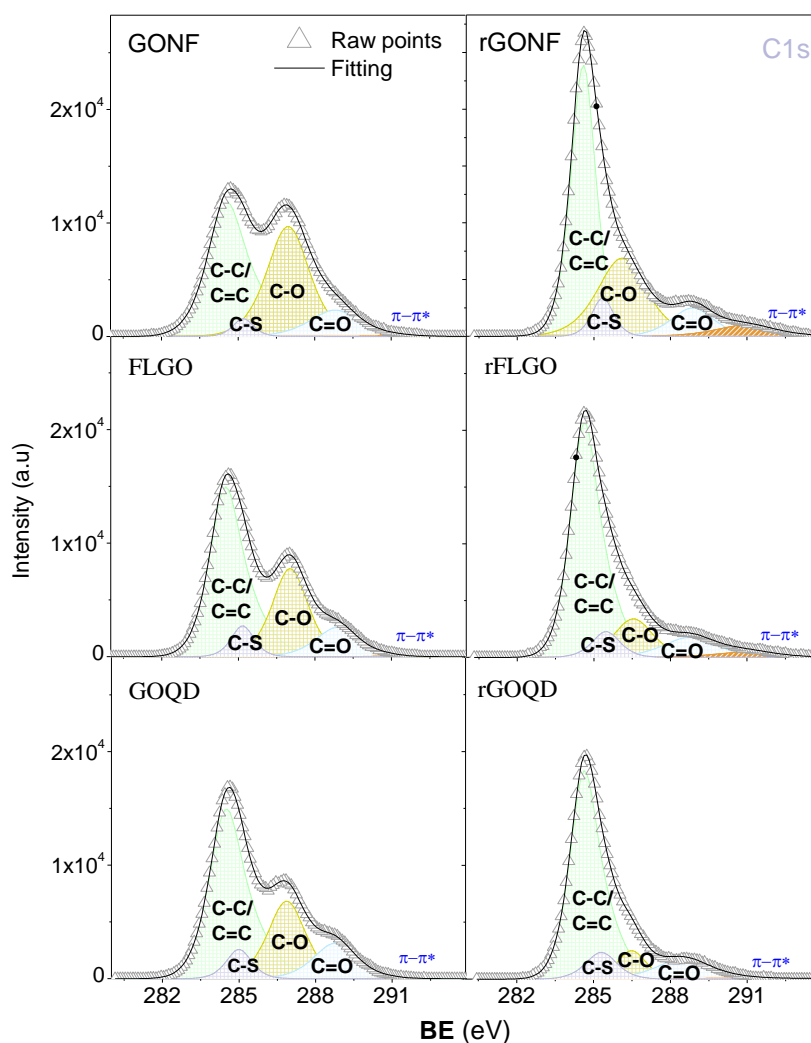
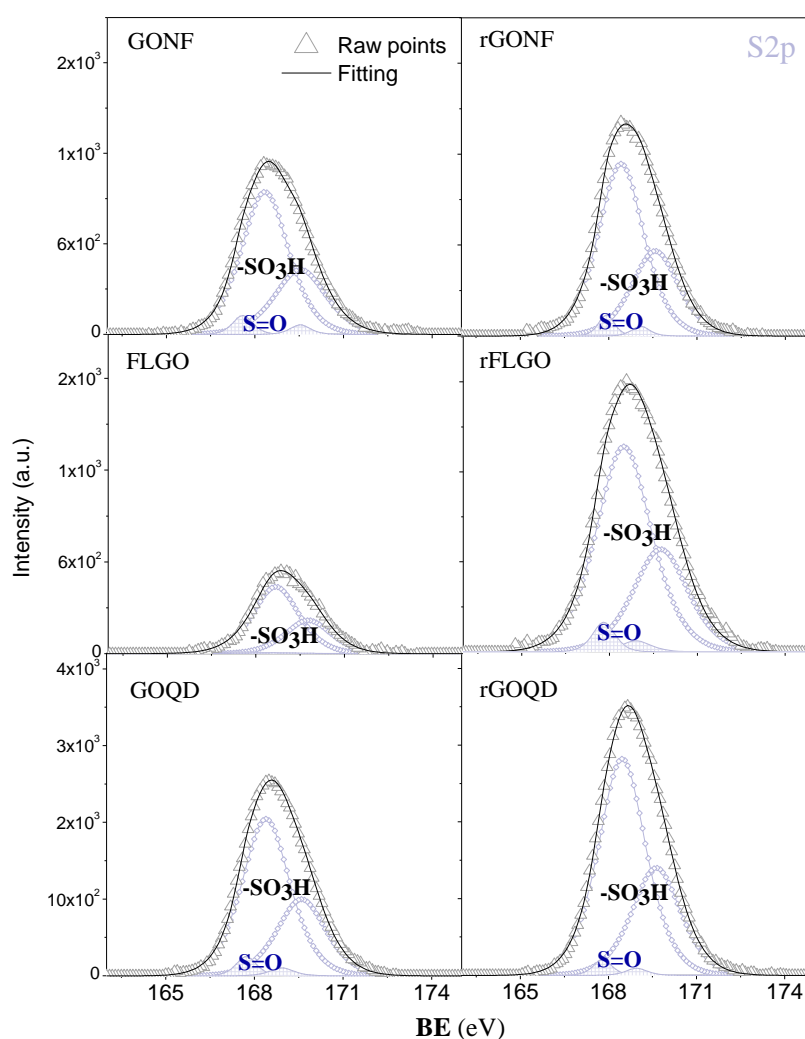


Figure 3.5 C1s XPS spectra before (left) and after (right) hydrothermal reduction.

Table 3.3 Chemical state of oxygen and sulphur species determined by XPS.

	C1s speciation					S2p speciation	
	C-C/C=C (284.6 eV)	C-O; (286.9 eV)	O-C=O (289.0eV)	π - π^* (291 eV)	C-S (285.2eV)	-SO ₃ H (268.4 eV)	C-SO ₂ -C (267.6 eV)
CNF _{600-ox} *	62.90	30.90	2.72	3.48	---	---	---
GONF	44.45	40.68	11.49	0.24	3.14	94.62	5.38
FLGO	51.29	29.80	11.93	0.18	6.60	96.80	3.19
GOQD	52.73	26.57	13.84	0.10	6.77	95.12	4.88
rGONF	51.72	27.52	9.79	5.44	5.53	95.90	4.10
rFLGO	64.52	14.71	10.48	3.29	7.01	94.47	5.53
rGOQD	67.26	9.14	12.28	1.96	9.36	97.22	2.79


Figure 3.6 S2p XPS spectra for the set of catalysts before (left) and after (right) hydrothermal reduction.

The oxidation degree of each fraction was closely related to their structural features, established by XRD (Figure 3.7). Given the multilayer graphitic nature of the starting precursor, CNF_{600-ox}

exhibited a sharp diffraction peak at $2\theta=26.36^\circ$ characteristic of the graphite (002) plane reflection, and a set of broader signals at $2\theta =43.2^\circ$, 45.2° , 53.8° and 78.5° indexed to their (100), (101), (004) and (110) faces, respectively. The (002) peak position and its width diffraction line defined an average nanosheet size (L_c) of 6.89 nm with a basal spacing (d) of 0.338 nm between layers ($n=21.4$). The stacked structure remained on GONF which doubled its interlayer distance ($d=0.813$ nm) to accommodate the multiple O- and S-functionalities within their sheets. The progressive oxidation further broke the carbon lattice into smaller sp^2 domains and separated the graphene sheets. The exfoliation extent was evidenced by a lower number of layers in the GO materials ($n=4.9$ and 3.1 for GONF and FLGO, respectively). Table 3.4 compiles the evolution of all these structural parameters while a simplified model of these morphologies is sketched in Figure 3.8. Overall, the (002) peak position shifted to (002)*, $2\theta=10.8-11.2^\circ$ as the interlayer spacing was expanded whereas their diffraction lines were vanished with decreasing on the crystal size, ranging from 3.19 or 1.67 nm for GONF and FLGO, respectively, to below the detection limit for GOQD. Remains of pristine graphite were simultaneously present over all GO samples, displaying a slight enlargement of their d -spacing from GONF to GOQD (Inset of Figure 3.7-a). Despite this bimodal character, the structural inheritance from the parent CNF did not exceed the 1.86 nm in size (shown by GONF). On the contrary, the (002) plane emerged on a series of partially reduced samples, pointing towards certain graphitic re-ordering (Figure 3.7-

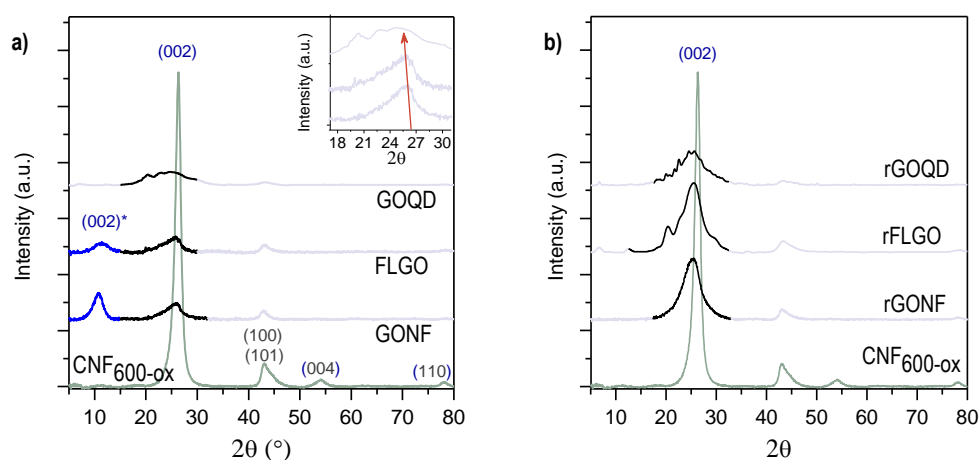


Figure 3.7 XRD diffraction patterns of the starting graphitic precursor (CNF_{600-ox}) and derived GO-based materials in the original form (a) and after hydrothermal reduction (b).

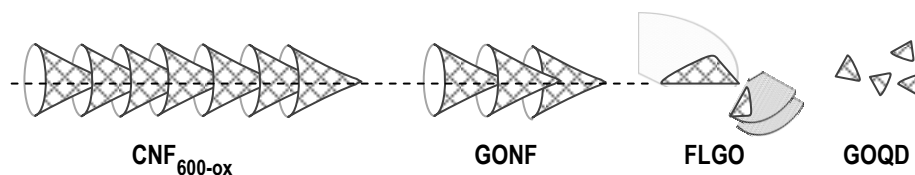


Figure 3.8 Graphical representation of different carbon nanostructures (Adapted from reference [109]).

Table 3.4 Structural parameters determined by XRD from (002) and (002)* peak position: interplanar spacing, d ; crystallite size, L_c and number of layers, n .

Catalyst	2θ ($^\circ$)		L_c (nm)		d (nm)		N	
	(002)	(002)*	(002)	(002)*	(002)	(002)*	(002)	(002)*
CNF _{600-ox}	26.36	---	6.89	---	0.338	---	21.4	---
GONF	25.93	10.87	1.86	3.19	0.343	0.813	6.4	4.9
FLGO	25.97	11.19	1.84	1.67	0.343	0.790	6.4	3.1
GOQD	24.38	---	0.52	n.d ^a	0.365	---	2.4	< 2 ^a
rGONF	25.24	---	1.81	---	0.352	---	6.1	---
rFLGO	25.51	---	1.54	---	0.349	---	5.4	---
rGOQD	25.22	---	1.10	---	0.353	---	4.1	---

^a Below the detection limit of the instrument.

The morphological appearance of GO and rGO sample series was inspected by TEM (Figure 3.9). GONF (a-b) and rGONF (g-h) maintained part of the filamentous structure of the starting CNF. Due to the oxidation/exfoliation process, these expanded nanofilaments had a lower aspect ratio than that of the CNF sample. FLGO (c-d) and rFLGO (i-j) were arranged into shorter graphene (or GO) domains of few layers. The layer stacking can be observed for both fractions. In turn, GOQD (e-f) and rGOQD (k-l) exhibited a membrane-like structure with wrinkled features, whose transparency suggests its thin thickness. According to a previous work, this “membrane” would be composed of small overlapped sp^2 carbon domains [199]. In general, micrographs of rGO samples resemble those original ones, with a certain level of aggregation and well-aligned orientation. Since GO fractions were separated in size by centrifugation, their reduced counterparts maintained the same trend in size and aspect ratio.

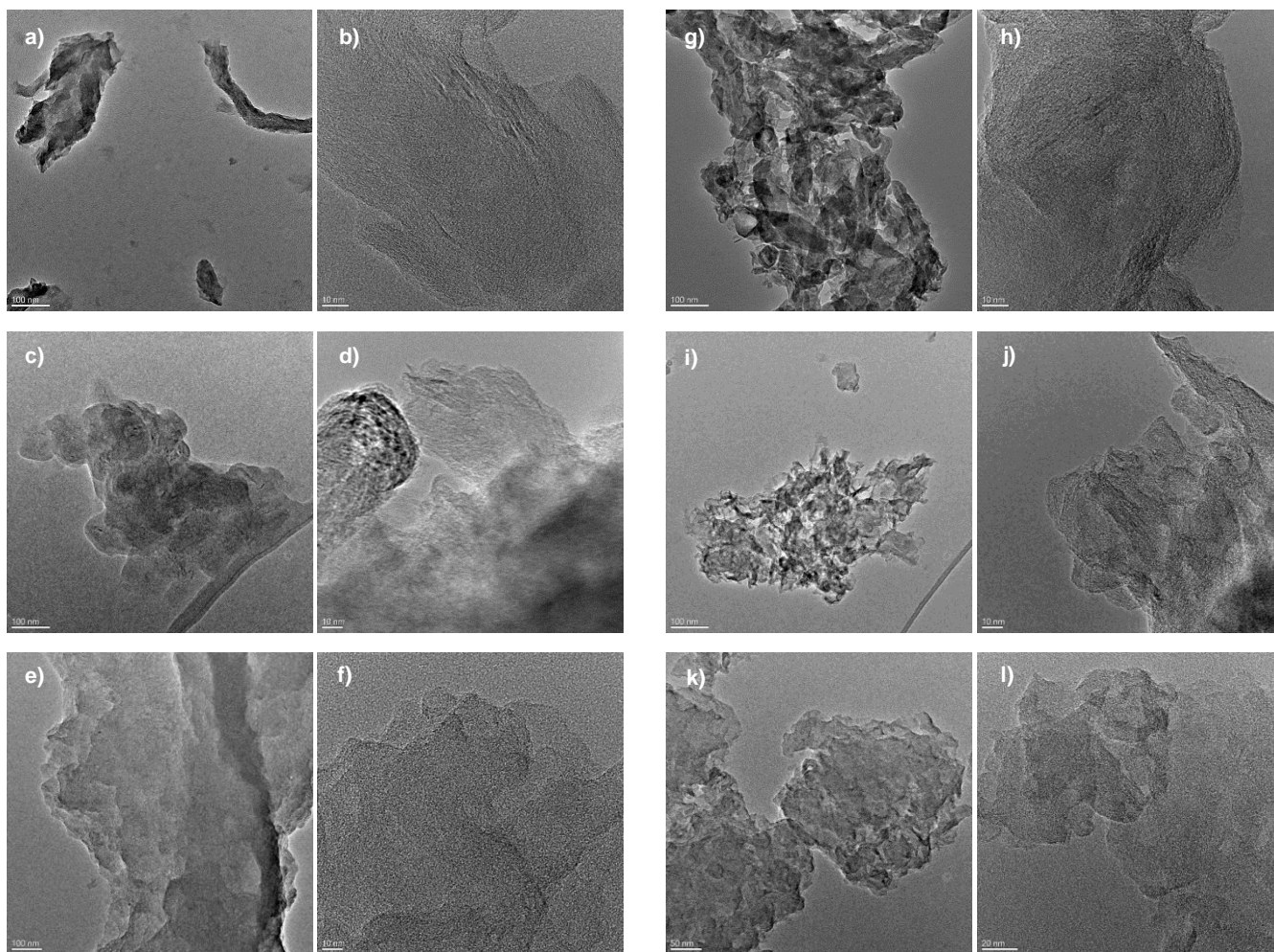


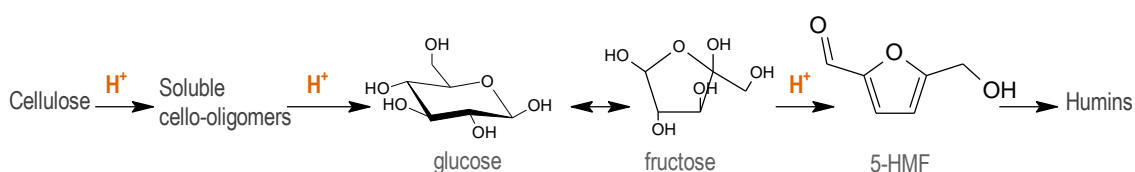
Figure 3.9 TEM images of GO and rGO materials: a-b) GONF, c-d) FLGO, e-f) GOQD, g-h) rGONF, i-j) rFLGO and k-l) rGOQD.

3.3.2 CATALYTIC ACTIVITY

3.3.2.1 Conventional heating

a) *Reaction conditions and surface chemistry*

A critical point in cellulose hydrolysis reaction lies on defining proper experimental conditions, aimed to control the delicate balance between the cellulose depolymerisation and the sugars degradation rates [200]. The succession of reactions in cascade is illustrated in Scheme 3.1.



Scheme 3.1 Reaction network for the conversion of cellulose into glucose and products degradation.

The hydrothermal stability of glucose in contact with a sulfonated activated carbon catalyst (AC-SO₃H) for 24 h was previously investigated by Onda *et al.* [187]. In that work, glucose yield increased with temperature in the range of 130-160 °C, while further elevation on temperature prompted several side reactions [187]. On this basis, runs of 24 h at 150 °C have long been considered as benchmark conditions for hydrolysis tests mediated by carbon-based materials, employing catalyst doses equal to the substrate [201, 202]. In order to ascertain this issue in this Thesis, the most favourable situation, i.e., using ball-milled cellulose (amorphous) and GOQD as the catalyst (showing a large content of O and S) was firstly addressed. However, only 16.6 % of the glucose was recovered from the reaction media under the above-mentioned conditions, whereas the extensive formation of dark-brown furan-compounds (humins) become apparent (42.9%) (data not shown). In this case, the caramelization of the sugars into insoluble by-products could be misleading the cellulose conversion measurement (66.5%) and it may be initiated by the acidity of the solution (pH~2.5) that arises from the dissociation of catalyst functionalities in the aqueous phase. Glucose susceptibility towards decomposition was limited by softening the reaction temperature down to 135 °C, albeit its profile was dependent on the

residence time (Figure 3.10). Specifically, the glucose concentration was linearly accumulating into the reaction medium as the reaction occurred and it reached a maximum of 61.4% after 24 h when 83.9 % of cellulose was converted. Longer reaction time decreased the glucose yield in favour of dehydration products (5-HMF) and poly-condensed compounds. Hence, 135 °C and 24 h were set as the reference conditions for subsequent runs. Table 3.5 summarizes the most relevant results on the hydrolysis study of amorphous cellulose.

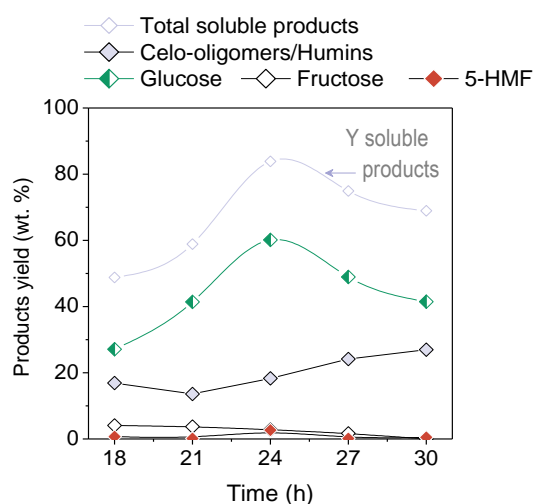


Figure 3.10 Time-resolved product profiles during amorphous cellulose hydrolysis over GOQD at 135°C.

Almost no cellulose conversion (2.1%) was noted in control experiments without catalyst (Entry 1), which appeared to be partially dissolved into cello-oligomers (1.9%). This result neglected any hydrolytic contribution from hydrothermal conditions or the cellulose ball-milling stage. Moreover, nor important catalytic activity was noted for the CNF_{ox} parent (6.94% of cellulose conversion and no glucose detected, Entry 2), which is consistent with its poor oxidation degree and the lack of strong acid groups ($-\text{HSO}_3$).

In comparison with other GO morphologies, GOQD exhibited the highest catalytic performance (Entries 3-5). In particular, the cellulose conversion increased in the sequence GONF (70.0%) < FLGO (73.6%) < GOQD (83.9%), although this order was not followed by the glucose yield: 50.7%, 33.9% and 60.1% (Entries 3-5).

Table 3.5 Catalytic results for the hydrolysis of amorphous cellulose (ball milled for 8h at 600 rpm) over different GO-based materials. Reaction conditions: 135 °C, 24h.

Entry	Catalyst	Conversion (%)	Product distribution (wt. %)			
			Glucose	Fructose	5-HMF	Others*
1	Blank	2.1	0.2	0.0	0.0	1.9
2	CNF _{600-ox}	6.9	0.2	0.0	0.0	6.7
3	GONF	70.0	50.7	3.6	1.0	14.7
4	FLGO	73.6	33.9	5.9	2.0	31.7
5	GOQD	83.9	60.1	2.8	2.7	18.3
6	rGONF	54.7	33.3	3.0	0.2	18.2
7	rFLGO	34.8	26.6	0.6	4.2	3.4
8	rGOQD	71.8	42.7	0.0	2.3	26.8
9	rGOQD ^[a]	71.0	43.9	0.0	0.7	26.4

*including cello-oligomers and humins.

^[a] reaction time was extended to 30 h

As stated above, thermal/acid boundary conditions render highly reactive glucose molecules, precluding any attempt to reach the integral hydrolysis of cellulose through an increase on the reaction time or temperature. Conceivably, a possible imbalance in the catalyst composition, that is, a higher density of strong acid sites such as -HSO_3 (pK_a of *ca.* -2.8) than the weakly-acidic ones like -OH and -COOH groups (pK_a of *ca.* 4.7 and 10, respectively), shall favour the hydrolytic kinetic over sugars degradation routes [149]. Such disproportion onto the functional groups can rightly be tuned by hydrothermal reduction. Nonetheless, a sharp decrease in their catalytic activities was noted for the entire set of reduced fractions (Table 3.5, Entries 6-8), highlighting the importance of the hydroxyl groups within the catalysts-to-substrate interaction. The instrumental role of -OH groups as cellulose binders was earlier emphasized in the literature [161]. For instance, Chen *et al.* blocked by silylation the -OH groups of a sulphonated graphene quantum dots, reducing the hydrophilicity index from 2.86 to 2.62. The catalytic activity dramatically decreased both in terms of conversion (91.8 % *vs.* 69.8 %) and 5-HMF yield (51.7 % *vs.* 29.1 %) [160]. In our research, despite disparities on cellulose conversion values (drops of 15.3, 38.8, 12.1 % for rGONF, rFLGO and rGOQD), the glucose yield followed the same sequence of reactivity than their original counterparts (yield of 33.3, 26.6 and

42.7 %, respectively). No further improvement in the glucose yield was attained over rGOQD upon prolonging the reaction time up to 30 h (merely 1.2 %, Entry 9).

With this knowledge in mind, the option to reinforce the catalyst acid strength through a hydrothermal treatment was discontinued, as it also incurs into a loss of the carbon affinity for the substrate. This last property seems to be equally important within a transformation characterized by diffusion and adsorption phenomena, rather than the acid reactivity of the catalyst on its own.

b) *Correlation between graphene oxide structure and catalytic activity*

At first glance, GOQD seems to have the size and surface chemistry ideally suited for the molecular interaction with cellulose. Their use as catalyst introduces, indeed, some interesting questions related to the solid-solid interface such as if the reaction takes place onto the cellulose surface or in the bulk matrix. Another mechanistic consideration that can be disclosed is whether the hydrolysis transformation is controlled by the cellulose structure or the catalyst morphology. To answer these points, a series of additional experiments was performed.

To verify the intercalation ability of GOQD inside the raw cellulosic matrix, the ball-milling duration was progressively shortened so as the index of crystallinity increased (CrI). In these trials, shown in Figure 3.11, the fact that catalytic results were influenced by the CrI suggests that GOQD were not fully interspersed within the cellulose structure. In other words, the exponential decline in catalytic activity with cellulose CrI reveals that even using type of morphology, the reaction is interfacial. As such, the mix-milling practice, aimed to promote the effective physical contact between both solid reactants, is expected to be of benefit.

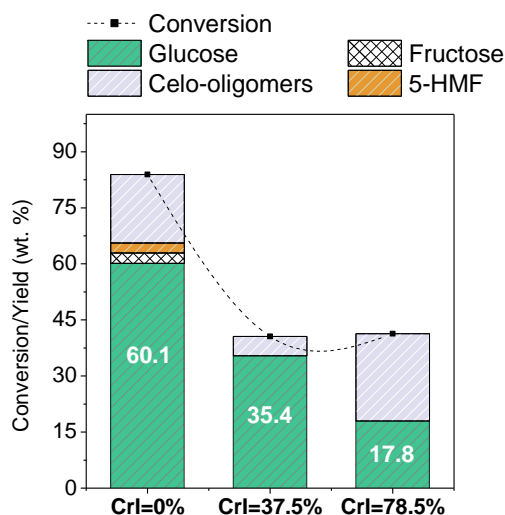


Figure 3.11 Catalytic activity of GOQD as a function of the cellulose crystallinity index (CrI).
Reaction conditions: 135 °C, 24h.

When the GOQD catalyst and cellulose were ball-milled together for 10 min at 600 rpm, the glucose yield rose to 83.5% (Figure 3.12-a), being the cellulose completely hydrolyzed. The fractions based on FLGO and GONF yielded 71.3% and 60.4% of glucose, respectively. Just under these circumstances, an obvious correlation between catalytic results and the oxidation/exfoliation degree of the GO was found. Numerical distances were shortened by extending the mix-milling time from 10 to 120 min, enabling to obtain up to 90.8, 97.9 and 86.1 % of glucose from GONF, FLGO and GOQD, respectively (see Figure 3.12-b). It is remarkable to note that 11.6 % of glucose underwent isomerisation to fructose over GOQD, more likely due to the electron vacancies of carbon network acting as Lewis acid centres [203]. In any case, the mechanical exfoliation of carbon materials after 2 h of ball-milling should not be ruled out. As it was corroborated by XRD (Figure 3.13), the structure of GONF suffered from significant delamination and fragmentation during mix-milling step. The impact of ball-milling on their morphological features is detailed in Table 3.6. Specifically, the crystalline domain size (L_c) decreased from 3.19 to 1.40 nm during the first 10 min of milling, dropping up to 0.67 nm upon 120 min. In the meantime, the number of layers was reduced from 4.9 to 2.6 and 1.7 and the d -distance expanded ($d=0.813$, 0.880 and 0.916, respectively). Likewise, it is believed that numerous reactive carbon species (radicals and ions) could be tentatively created onto the

carbon lattice of GOQD after 120 min of ball-milling through the mechanochemical cleavage of graphitic C-C bonds [204] and serve as Lewis active sites for the glucose-to-fructose interconversion [203].

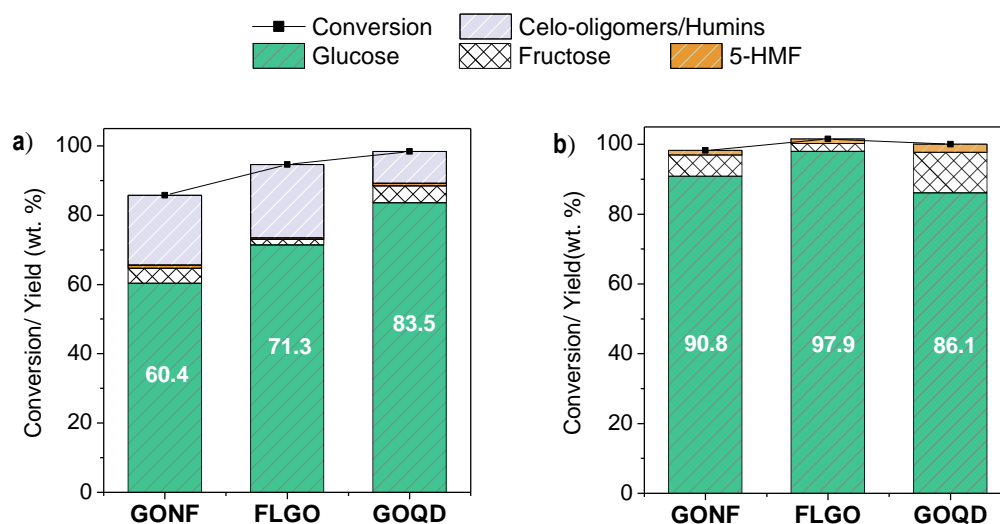


Figure 3.12 Catalytic activity of different graphene oxide mix-milled with cellulose for 10 min (a) and 120 min (b). Reaction conditions: 135 °C, 24h.

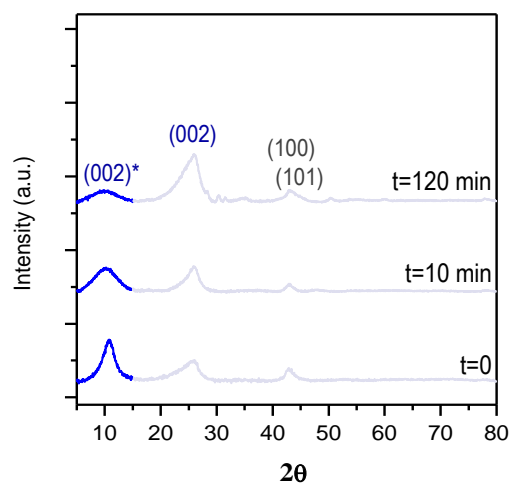


Figure 3.13 Structural evolution of GONF during ball-milling stage.

Table 3.6 Changes on structural parameters induced by ball-milling.

Catalyst	Ball-milling time (min)	2θ (°)		Lc (nm)		d (nm)		N	
		(002)	(002)*	(002)	(002)*	(002)	(002)*	(002)	(002)*
GONF	0	25.93	10.87	1.86	3.19	0.343	0.813	6.4	4.9
GONF	10	26.09	10.04	2.22	1.40	0.341	0.880	7.5	2.6
GONF	120	26.08	9.65	1.96	0.67	0.341	0.916	6.7	1.7

At any rate, the feasibility of using various GO-materials for the quantitative conversion of cellulose into glucose was demonstrated, positioning among the best sugar productivities ever reported for the hydrolysis of cellulose [48]. Yet, catalytic results were largely conditioned by the ball-milling operation, pointing to a catalytic transformation primarily governed by the molecular collision between reactants [89]. In addition, long residence times (24 h) and mild conditions (135 °C) had to be used, in order to manage the kinetic control the hydrolysis rate against sugar degradation reactions. In this context, microwave (MW) technology could bring significant rewards [161, 174, 205].

3.3.2.2 Microwave heating

a) *Delimiting the operational intervals under different heating sources*

MW dielectric heating obeys to heating patterns (direct molecular activation, faster and selective) that are difficult to emulate by conventional means but generally reduces the reaction timescales from hours down to minutes [206]. In the previous section, runs of 24 h were required for the hydrolysis of cellulose (aqueous solution of 0.25 wt. %) heated at 135 °C by conduction and convective currents. These conditions were the starting point for MW-heating tests but at shorter time-runs (no longer than 120 min). In such experiments, the hydrolysis proceeded at a relatively slow pace. As it is depicted in Figure 3.14-a, a cellulose conversion of 21.3% (0.4 % of glucose) was achieved after 60 min at 135 °C using GONF as the catalyst. This value was increased up to 31.4 % (5.55 % of glucose) upon doubling the irradiation time. In a similar manner, the glucose yield monotonically increased from 20 to 120 min at 150 °C and 165 °C. After 120 min, 44.0 % and 76.5 % of the initial cellulose was converted, rendering 23.7 % and 37.1 % of glucose, respectively. Conversely, an extension on the reaction time at 180 °C had a minimal effect on the glucose yield (37.4 and 33.4 % after 20 and 60 min, respectively). Detailed analysis of some other minor compounds was compiled in Table 3.7, including levulinic and formic acids (2.3 and 5.1 %, respectively), levoglucose (2.3 %) and fructose (0.7 %). Overall, the formation of these products timidly arised above 165 °C at prolonged contact

times (longer than 60 min), reaching a maximum value of 10.4 wt. % at the most severe conditions (i.e., 180 °C, 60 min).

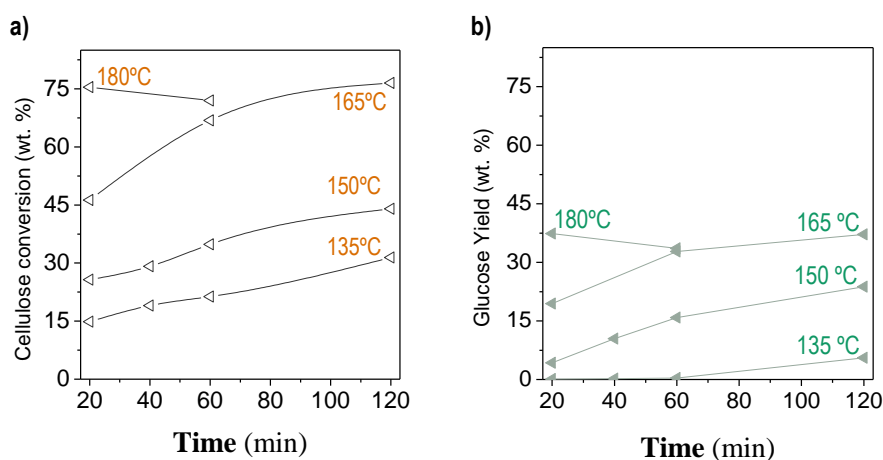


Figure 3.14 Kinetic profiles of hydrolysis from a starting suspension of 0.25 wt. % in cellulose and using GONF as the catalyst a) cellulose conversion and b) glucose yield.

Table 3.7 Cellulose conversion and products distribution for the MW-assisted hydrolysis, GONF as catalyst (starting solution of 0.25 wt.%).

Entry	Temp (°C)	Time (min)	Cellulose conversion	Y _{PRODUCTS} (wt. %)					
				Glucose	Fructose	Levoglucose	Levulinic acid	Formic acid	Others ^[a]
1	135	20	14.9	0.1	0.2	n.d	n.d	n.d	14.6
2		40	19.0	0.2	0.2	0.1	0.2	3.5	14.8
3		60	21.3	0.4	0.3	0.1	n.d	0.7	19.8
4		120	31.4	5.5	0.5	0.4	n.d	1.9	23.6
5	150	20	25.7	4.3	0.6	0.3	0.2	1.9	18.4
6		40	29.1	10.5	0.6	0.6	0.0	1.8	15.6
7		60	34.9	15.8	0.7	0.6	0.0	3.0	14.8
8		120	44.0	23.7	0.7	0.9	0.1	2.9	15.7
9	165	20	46.3	19.5	0.6	0.9	0.1	2.1	23.1
10		60	66.9	32.8	0.8	1.5	0.7	4.2	26.9
11		120	76.5	37.1	0.8	2.0	1.4	5.9	29.3
12	180	20	75.4	37.4	0.8	2.1	0.2	3.1	31.8
13		60	72.0	33.4	0.7	2.3	2.3	5.1	23.0

[a] including cello-oligomers and humins.

n.d: not detected

Hydrolysis activity was also boosted when GOQD was used as catalyst instead of GONF (Figure 3.15 and Table 3.8). In particular, similar evolutions with temperature and reaction time

were observed, i.e., increasing the temperature (from 150 to 165 °C) or prolonging the reaction time enhanced the glucose yield. However, the formation rate of sugars stayed higher over GOQD, regardless the reaction conditions. The rich surface chemistry of GOQD and its unique morphology, with no mass transfer limitations, surely accounted for its superior performance. The best result, 52.1 % of glucose, was attained after 60 min at 165 °C. Based on the characterization results, an intermediate situation between the hydrolysis ability of GONF and GOQD is expected for FLGO. For this reason, this morphology was omitted in this first screening of variables.

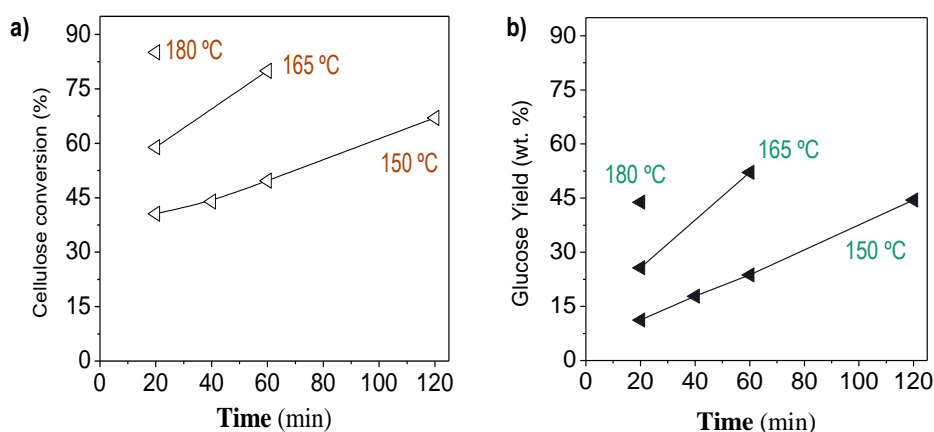


Figure 3.15 Kinetic profiles of cellulose hydrolysis over GOQD as catalyst from a starting suspension of 0.25 wt. % in cellulose.

Table 3.8 Cellulose conversion and products distribution for the MW-assisted hydrolysis, GOQD as catalyst (starting solution of 0.25 wt.%).

Entry	Temp (°C)	Time (min)	Cellulose conversion	Y _{PRODUCTS} (wt. %)					
				Glucose	Fructose	Levoglucose	Levulinic acid	Formic acid	Others ^[a]
1	150	20	40.6	10.8	0.3	0.5	n.d	2.9	26.1
2		40	44.0	17.9	0.7	0.7	n.d	2.2	22.5
3		60	49.7	23.7	0.7	0.9	n.d	3.0	21.4
4		120	67.0	44.5	2.6	0.9	1.0	1.9	16.1
5	165	20	58.9	25.7	0.8	1.1	n.d	3.2	28.1
6		60	80.0	52.2	2.9	2.5	2.6	2.3	17.5
7	180	20	85.1	43.9	0.9	2.3	1.0	4.0	33.0

[a] including cello-oligomers and humins

n.d: not detected

Another important parameter controlling the hydrolysis rate is the cellulose-to-water ratio. In dilute solutions, an excess of water may be absorbing the incident MW energy without important participation in the reaction. MW radiation would instead be channeled toward the actual reacting molecules (both catalyst and cellulose) upon increasing their loading in the system [165]. Experimental results provided additional support to this explanation. As Figure 3.16 displays, an increase in the cellulose-to-water ratio from 0.25 to 2 wt. % rose the yield of glucose 25-fold (from 0.4 to 10.2 %) after 60 min at 135 °C in contact with GONF. This tendency was somewhat repeated irrespectively of the catalyst morphology or the reaction temperature except for GOQD at 165 °C. At this point, a substantial amount of the glucose underwent successive degradation routes, driven by the acidic medium generated from the aqueous-deprotonation of catalyst functionalities. The use of higher doses of GOQD, owning the highest density of surface groups, probably upsurges this effect. Very differently, an increase on the cellulose-to-water ratio (2.0 wt. %) was detrimental in conventional heating, dropping the glucose yield from 50.7 % down to 31 % in favor of recombination reactions of sugars to furan-based compounds (data not shown). The comparison was performed using GONF as catalyst and keeping the rest of conditions equal otherwise (24 h, 135 °C).

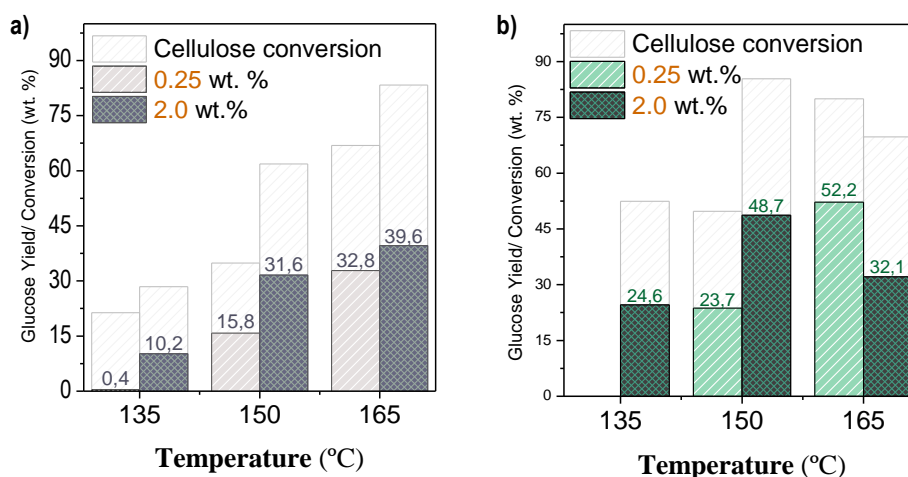


Figure 3.16 Catalytic results as a function of the concentration of the initial suspension over GONF (a) and GOQD (b) as the catalysts (Holding time of 60 min).

b) Influence of GO morphologies

In order to gain a more in-deep comparison between different GO morphologies, a parametric optimization of the reaction was addressed over an initial cellulose suspension of 2 wt. %. Figure 3.17 displays the conversion of cellulose as a function of time at threesome temperatures (135, 150, 165 °C) for each catalyst. As a general trend, the order of reactivity of the GO-nanostructures followed the order of their oxidation/exfoliation degree: GOQD > FLGO > GONF. However, the opposite behavior was observed at 165 °C from 40 min onwards due to the formation of insoluble by-products. Sugars degradation occurred to a greater extent over more acidic catalysts (GOQD), while it was much slower when less functionalized carbon materials (GONF) were used. For a given GO-fraction, the hydrolysis rate significantly increased by raising the temperature from 135 °C to 150 °C and 165 °C, as it was evidenced from the escalating conversion levels. Accordingly, the reaction time was shortened 60 min for each step rise of 15 °C (180, 120 and 60 min at 135, 150 and 165 °C, respectively). Nonetheless, the vast majority of the reaction progress seemed to occur during the early stages but gradually leveled off. Such profile could reflect an eventual catalytic deactivation over the course of reaction. Besides, MW alone were unable to hydrolyze the cellulose at the relatively mild processing conditions applied in this work, as it was corroborated from non-catalytic experiments. In the absence of a catalyst, cellulose conversion was meager (6.61 % after 120 min at 150 °C and 7.87 % after 60 min at 165 °C) with negligible glucose formation (merely 0.2 % at 165 °C).

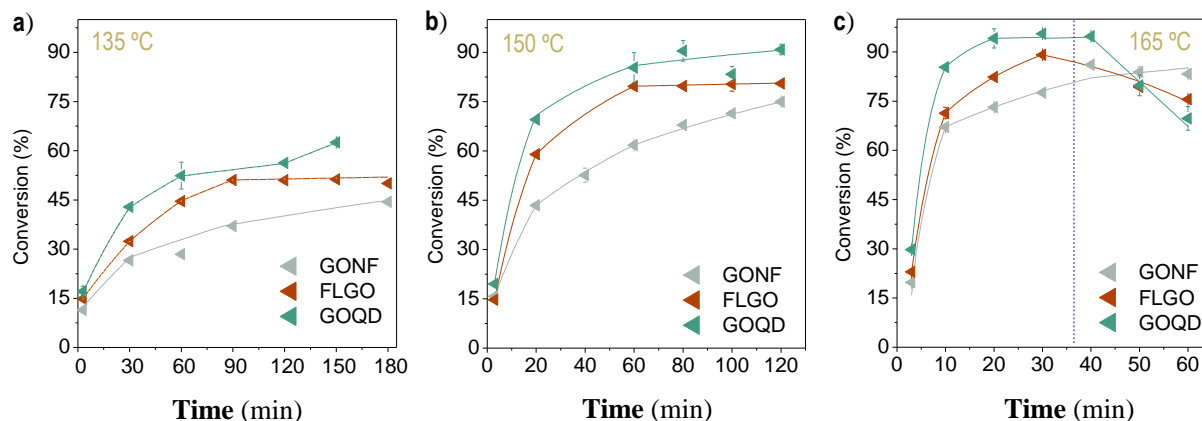


Figure 3.17 Time-course of cellulose conversion in hydrolysis reaction using different GO-derivatives at several temperatures a) 135 °C, b) 150 °C and c) 165 °C. (2.0 wt. % of cellulose in the initial solution).

The fate of dissolved cellulose was strongly time and temperature dependent. The formation of sugars can be traced in Figure 3.18, including glucose as the primary product (> 90 wt.%) and minor quantities of cellobiose, fructose and levoglucosan (a dehydration product of glucose). Tables 3.9-11 list the specific distribution of products. Overall, the amount of compounds quantified by HPLC did not entirely account for the mass of liquid-phase products due to the formation of water-soluble cello-oligomers. In an initial induction period, cellulose is randomly broken down into shortened polymeric chains (cello-oligomers of varying lengths) which gradually decrease on their polymerization degree and finally produce the monosaccharide of glucose [1]. Sugars releasing evolved smoothly at 135 °C with negligible degradation over time (Figure 3.17-a). The highest glucose yield (44.16 %; 48.6 % of sugars) was attained from GOQD after 150 min. Lower glucose yields were comparatively obtained after 150 min of reaction in contact with FLGO (36.6 %) or GONF (32.5 %), which did not upgrade when extending the reaction time to 180 min. As cellulose conversion did, sugars production rose at 150 °C and 165 °C. However, glucose was no longer stable in the reaction medium with increasing in severity of conditions (Figure 3.17 b-c). Specifically, three main regions can be distinguished. In the first interval, glucose formation grew very fast. Thereupon, the reaction time loosely enhances the glucose production, but rather impact on its degradation. At 150 °C, the glucose yield reached a maximum after 80 min of reaction (62.1 % with GOQD, 55.4 %

with FLGO and 48.9 % with GONF) followed by a small decline with increasing the hydrolysis duration. An increment in the temperature up 165 °C intensified this profile: glucose was rapidly produced, reaching a plateau at around 20 min (63.7% of glucose over GOQD). From 40 min onward, glucose was consumed by secondary side reactions. These diminishments are in line with the catalytic activity of the materials: GOQD > FLGO > GONF, suggesting that the carbon catalysts also exert a significant influence on secondary reactions, leading to glucose transformation into other species.

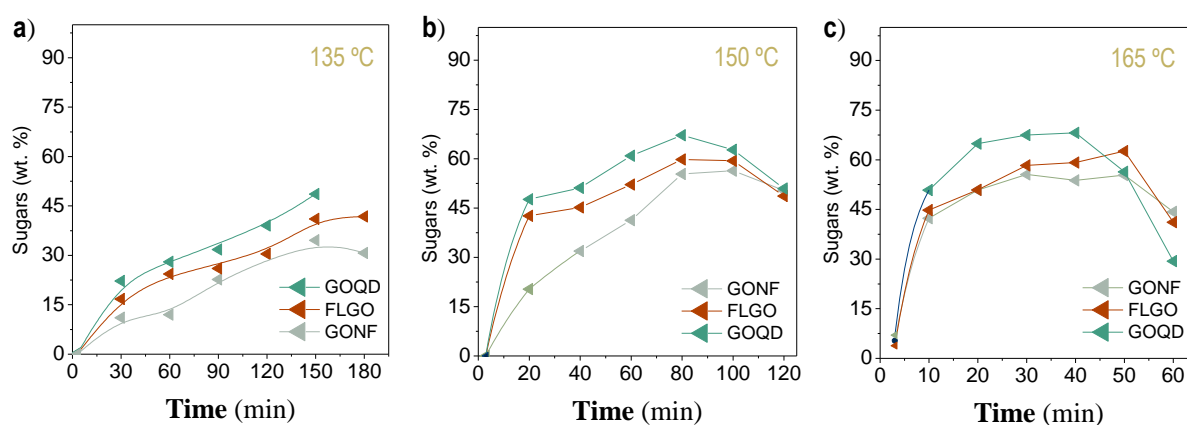


Figure 3.18 Kinetic curves of sugars production over different GO-morphologies at 135°C (a), 150°C (b) and 165 °C (c). (2.0 wt. % of cellulose in the initial solution)

Specifically, glucose depletion went on par to a steady increased on the levulinic acid yield (Figure 3.19). This compound, accounting up to 19.2 % over GOQD (13.6 % on FLGO and 9.1 % on GONF), is the result of a series of acid-catalyzed transformations, involving the glucose isomerization to fructose and its further dehydration into 5-hydroxymethylfurfural (5-HMF). The subsequent hydrolysis of 5-HMF in aqueous phase leads to the formation of levulinic and formic acids (Scheme 3.2). Most of these intermediates, as well as several other by-products from glucose decomposition (organic acids like formic and acetic and levoglucosan), were present in traces amounts in the liquid effluent. Afterward, poly-condensation reactions into humins were the major degradation pathways.

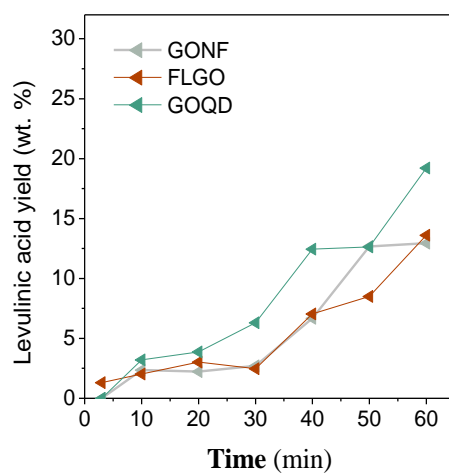
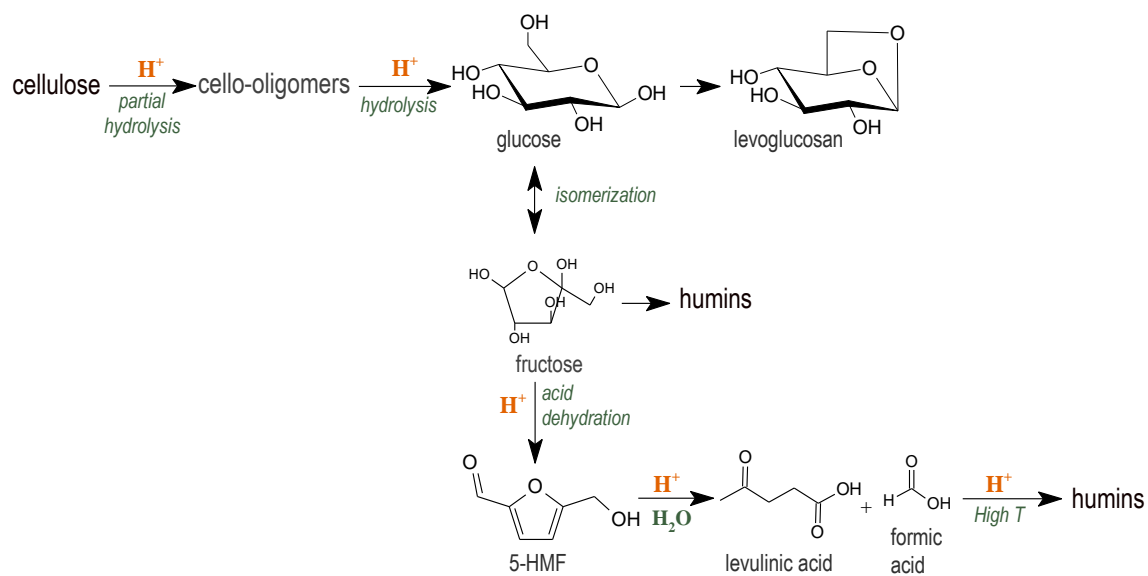


Figure 3.19 Temporal evolution of levulinic acid at 165 °C.



Scheme 3.2 Reactions network from cellulose to levulinic acid.

Table 3.9 Cellulose conversion and products distribution for the MW-assisted hydrolysis using GONF as catalyst and a starting solution of 2.0 wt. %.

Entry	Temperature (°C)	Time (min)	Cellulose conversion	Y _{PRODUCTS} (wt. %)								
				Cellulobiose	Glucose	Fructose	Levoglucose	5-HMF	Levulinic acid	Formic acid	Acetic acid	Others ^[a]
1	135	3	11.5	n.d	n.d	n.d	0.03	n.d	0.04	0.3	n.d	11.1
2		30	26.6	0.7	9.9	n.d	0.3	n.d	1.4	1.9	0.2	12.2
3		60	28.4	0.5	10.6	n.d	0.3	n.d	2.6		0.6	13.8
4		90	37.1	0.7	20.9	n.d	0.6	0.03	2.8	2.9	0.5	8.7
5		120	57.5	0.3	29.6	0.3	1.3	n.d	0.6		1.0	24.4
6		150	58.9	n.d	32.5	2.6	1.1	n.d	0.9		1.0	20.8
7		180	44.4	0.2	27.5	1.6	0.8	n.d	0.8		0.6	12.8
8	150	3	15.8	n.d	n.d	0.1	n.d	0.03	n.d	n.d	2.1	13.5
9		20	43.5	0.5	18.6	0.7	0.6	n.d	0.7	3.9	0.4	18.0
10		40	52.7	0.4	29.0	0.4	1.2	0.6	0.7	1.0	0.4	10.3
11		60	61.8	0.2	37.1	0.4	1.2	n.d	2.8		2.0	19.0
12		80	67.9	0.3	49.0	n.d	1.6	1.4	3.1	1.8	1.1	10.7
13		100	71.5	0.3	50.0	2.8	1.8	1.7	2.7	2.0	0.5	10.7
14		120	75.1	0.4	45.3	0.6	0.2	n.d	4.6	5.4	1.5	18.5
15	165	3	19.8	0.8	4.0	2.1	0.2	n.d	n.d	0.3	0.2	11.2
16		10	67.2	0.3	38.8	0.7	1.7	n.d	2.4	2.2	1.6	30.0
17		20	73.2	0.3	44.7	0.8	2.2	n.d	2.2	3.64	2.1	10.9
18		30	77.6	0.4	52.5	2.7	2.2	2.8	2.7	1.8	0.5	10.9
19		40	86.1	n.d	51.4	0.3	2.4	n.d	6.7		n.d	30.4
20		50	83.9	0.2	51.5	2.3	2.4	4.4	12.7	3.8	1.3	10.9
21		60	83.3	n.d	39.6	0.5	2.0	n.d	12.9	9.1	2.7	21.3

[a] including cello-oligomers and humins

Table 3.10 Cellulose conversion and products distribution for the MW-assisted hydrolysis, using FLGO as catalyst and a starting solution of 2.0 wt. %.

Entry	Temperature (°C)	Time (min)	Cellulose conversion	Y _{PRODUCTS} (wt. %)								
				Cellobiose	Glucose	Fructose	Levogluco	5-HMF	Levulinic acid	Formic acid	Acetic acid	Others ^[a]
1	135	3	14.9	n.d	n.d	n.d	0.05	n.d	0.01	0.4	0.1	14.4
2		30	32.4	0.7	15.2	0.1	0.5	0.05	2.5	0.6	0.3	12.5
3		60	44.7	0.4	22.5	0.6	0.6	0.03	2.4	0.9	0.2	15.0
4		90	51.1	0.3	23.8	0.3	0.7	n.d	0.8		0.9	26.2
5		120	51.0	0.3	24.6	1.4	0.7	n.d	0.7		3.4	19.9
6		150	51.3	0.3	36.6	3.3	1.1	0.7	2.7	2.7	2.5	1.6
7		180	50.0	0.3	38.2	1.08	1.2	0.6	2.7	1.5	1.5	4.0
8	150	3	14.7	n.d	0.03	0.04	n.d	n.d	n.d	0.3	0.2	14.1
9		20	59.0	0.4	40.0	2.9	1.5	0.8	2.3	1.2	1.0	9.6
10		40	62.4	0.3	42.6	2.6	1.5	0.9	2.2	2.0	0.9	10.2
11		60	79.7	0.3	50.2	0.7	1.7	n.d	1.5			25.7
12		80	79.8	0.3	55.4	2.5	2.1	2.1	5.2	2.5	1.2	10.5
13		100	80.4	0.4	55.0	2.6	2.1	2.0	5	2.8	1.3	10.9
14		120	80.6	0.3	44.4	0.8	1.7	n.d	4.2	6.3	2.3	15.3
15	165	3	23.0	0.6	3.0	0.5	0.2	n.d	1.3	0.4	0.1	16.9
16		10	71.4	0.2	39.0	0.8	2.2	n.d	2.0	4.3	3.4	20.2
17		20	82.3	n.d	42.4	0.8	1.8	n.d	3.0	6.8	n.d	27.0
18		30	89.1	0.4	55.2	2.7	2.1	2.1	2.5	1.7	0.6	18.7
19		40	85.8	0.4	52.6	0.7	2.6	1.7	7.0		3.6	13.3
20		50	79.3	0.3	58.2	3.6	2.5	3.6	8.5	3.1	1.5	n.d
21		60	75.6	n.d	36.3	0.4	2.0	n.d	13.6	13.8	2.8	11.7

[a] including cello-oligomers and humans

Table 3.11 Cellulose conversion and products distribution for the MW-assisted hydrolysis using GOQD as catalyst and a starting solution of 2.0 wt. %.

Entry	Temperature (°C)	Time (min)	Cellulose conversion	Y _{PRODUCTS} (wt. %)								
				Cellobiose	Glucose	Fructose	Levoglucose	5-HMF	Levulinic acid	Formic acid	Acetic acid	Others ^[a]
1	135	3	17.1	n.d	n.d	0.03	n.d	n.d	0.01	0.1	0.2	0.3
2		30	42.9	n.d	16.4	n.d	n.d	n.d	5.8	n.d	n.d	22.2
3		60	52.4	0.3	26.2	0.3	0.8	n.d	0.6	3.7	0.5	28.1
4		90	48.7	0.3	29.3	0.4	0.9	n.d	0.5	2.4	1.0	31.8
5		120	56.3	0.2	34.5	2.2	1.0	0.5	2.9	1.3	0.7	39.1
6		150	62.6	0.3	44.2	1.4	1.3	1.0	n.d	1.7	0.4	48.6
7	150	3	19.5	n.d	0.1	0.1	n.d	n.d	n.d	0.1	0.2	19.0
8		20	69.6	0.5	45.0	3.3	1.5	0.6	1.9	1.1	0.8	15.2
9		40	67.5	0.4	47.8	2.9	1.6	1.3	1.7	1.5	0.4	10.2
10		60	85.4	0.2	60.8	0.8	n.d	n.d	4.8			28.5
11		80	90.5	0.4	62.1	2.7	2.2	2.4	4.8	3.0	0.7	13.7
12		100	83.4	0.3	57.9	2.7	2.1	2.5	11.1	3.2	1.5	13.2
13		120	90.9	0.1	46.3	0.6	1.6	n.d	7.04	8.07	3.0	24.2
14	165	3	29.8	0.9	4.9	0.5	0.3	n.d	n.d	1.8	1.0	19.8
15		10	85.4	0.4	46.1	1.0	2.1	n.d	3.2	3.1	2.3	18.5
16		20	94.1	0.2	63.7	1.7	n.d	2.6	3.9	3.5	1.0	5.7
17		30	95.6	0.4	62.8	2.8	2.4	2.9	6.3	2.1	1.8	16.1
18		40	94.8	0.03	59.6	1.8	2.0	3.8	12.5	10.2	6.6	
19		50	79.8	0.2	52.9	2.1	2.3	3.6	12.6	4.3	0.9	5.4
20		60	69.7	n.d	26.7	0.2	n.d	n.d	19.2	16.7	2.7	11.1

[a] including cello-oligomers and humins

Zero-dimensional and highly oxygenated GOQD arise as a wisely designed structure for the hydrolysis of cellulose. In order to quantitatively compare their reaction rate over other arrays of GO, the concentration profiles of cellulose were used for determining the kinetic constant (k , min^{-1}) and activation energy (E_a , KJ/mol) for each catalyst. In a simplified approach, the hydrolysis reaction can be described by a pseudo-first-order kinetic model with respect to the reactant concentration [1, 66, 75, 207-209]. The analytical solution of this differential equation fits to a linear regression when the logarithm of the residual cellulose concentration is represented as a function of the reaction time, whose slope determines the value of k .

Table 3.12 compiles the resultant values determined from the linear region for each reaction condition. Based on the correlation coefficient (R^2), experimental data can be adjusted to a pseudo-first-order kinetic model at the beginning of the reaction. However, this reaction pattern is not maintained over time. There is a breakdown point upon which the reaction slows down and any catalytic activity is hardly discerned. Still, proximate but useful estimations can be depicted from these *ab initio* calculations. As it was expected, the kinetic constants gradually increased from GONF to FLGO and GOQD, although all values fall within the same order of magnitude. For a given GO morphology, the reaction rate increased with every $15\text{ }^\circ\text{C}$ rise in temperature. The interdependency of the reaction rate (k) with temperature follows the Arrhenius law. By plotting the logarithm of the k value ($\ln k$) against the reciprocal of the absolute temperature ($1/T$), a straight relationship is obtained, whose slope and intercept equal to $-E_a/R$ and the pre-exponential factor ($\ln A_0$), respectively [75, 208]. The Arrhenius parameters are summarized in Table 3.12. According to these estimations, it is possible to decrease the apparent activation energy from 172 KJ/mol to 149 KJ/mol and 135 KJ/mol as gradually downsizing on the catalyst morphology from GONF to FLGO and GOQD, which underscore the definite role of GOQD with respect to other GO nanostructures. The shortcoming around these values is that they are only valid for the initial stage of the reaction, as all profiles meet after a certain point, upon which actual kinetic constants remain rather lower than those predicted from data taken from the first interval. Taking as reference the catalytic activity of

FLGO at 150 °C, for example, the experimental data showed a gradual decay in the kinetic constant from 0.044 to 0.017 and 0.0008 min⁻¹. This observation is worthwhile to investigate in more detail in the future, as it could be a sign of the catalyst deactivation over time. This fact keeps the maximum glucose yield attained in our study (63.7 %) at the same level as previous studies on the MW-assisted hydrolysis using GO (61 % of glucose after 60 min at 180 °C), not least because some of the unique features of FLGO and GOQD such as their inherent monolayer structure and surface functionalities were likely affected under MW radiation, declining expectations to overcome these values through the GO-design.

Table 3.12 Kinetic parameters for MW-assisted hydrolysis reaction at the beginning of the reaction.

Catalyst	k_{135} (min ⁻¹)	R ²	k_{150} (min ⁻¹)	R ²	k_{165} (min ⁻¹)	R ²	lnA ₀ (KJ/mol)	E _a (KJ/mol)
GONF	0.004	0.91	0.027	0.97	0.114	0.99	49.11	171.6
FLGO	0.006	0.98	0.044	0.99	0.128	0.99	43.05	148.9
GOQD	0.010	0.95	0.059	0.99	0.147	0.96	39.44	135.2

As a final remark, it is interesting to note that the kinetic parameters developed for the first interval favourably compare with the E_a found in acid hydrolysis of microcrystalline cellulose in conventional systems (170 kJ/mol in H₂SO₄ [75, 208]). In addition, the use of graphene oxide morphologies in concert with MW energy showed the potential to achieve similar kinetic profiles than previously reported sulfonated carbons (110 kJ/mol) but using considerably less amount of catalyst (cellulose-to-catalyst ratio 12-fold lower) [75].

3.3.2.3 Comparison between conventional and microwave heating

To conclude this Chapter, Table 3.13 summarizes the most representative results using conventional electric heating and microwave energy in the catalytic hydrolysis of amorphous cellulose with GOQD and GONF as catalysts. As it can be seen, both processes achieved similar glucose yield once the operational conditions were specifically optimized for each system. The highest production of glucose was assessed in the range of 60.1-63.7 % using GOQD as the



catalysts. MW-technology, however, enables to process higher loadings of cellulose (2.0 instead of 0.25 wt. %) at shorter times (20 min *vs* 24 h). That means numerically that one batch of MW-assisted hydrolysis produces the same amount of glucose as 8 hydrolysis cycles conducted at a traditional electric heating reactor, which is a landmark achievement towards the process intensification.

Table 3.13 Summary chart of catalytic hydrolysis results under different heating sources.

Catalyst	Heating source	Temp. (°C)	Time (h)	Initial loading 0.25 wt. %		Initial loading 2.0 wt. %	
				Cellulose conversion	Glucose Yield	Cellulose conversion	Glucose Yield
GONF	Conventional	135	24	70.0	50.7	53.9	33.8
	MW	135	2	31.4	5.5	57.5	29.6
		165	0.3	46.3	19.5	73.2	44.7
GOQD	Conventional	135	24	83.9	60.1		
	MW	165	0.33	58.9	25.7	94.1	63.7

3.4 Conclusions

This Chapter aims to outline a fundamental understanding on how the structure and surface composition of CNF influence on their hydrolysis activity. To this end, a series of oxidative treatments were initially explored for surface modification. Among them, only the modified Hummers' method allowed for the extensive functionalization of CNF (acid density of 0.6 mmol $-\text{SO}_3\text{H}/\text{g}$). The same synthesis method incorporated at the same time an assortment of oxygen groups ($-\text{COOH}$, $-\text{OH}$, $-\text{COC}-$) on the carbon backbone, accounting to 45.6 wt. % of the bulk composition. This resulted in the surface overlay of multiple chemical groups with various pK_a , whose relative abundance can be subsequently adjusted by hydrothermal treatment (180 °C, 6 h). The nature of functional groups, distribution and density could be further tuned through the fine control of the layered structure, planar size and edges-to-basal planes ratio. Thus, an obvious increase on the oxidation degree was noted from their exfoliated and dimensionless counterparts: 47.2 wt. % of O for FLGO and 54.7% on GOQD. Sulphur percentage was also much higher on these morphologies (2.1 and 6.1 % over FLGO and GOQD, respectively).

Tailoring the graphene domain size at nanometric scale not only arises as a neoteric strategy for surface modification but also may help to suppress mass transfer limitations. From a holistic perspective, the hydrolyzing ability of three GO morphologies, differing structurally in morphology and size, was compared. Zero-dimensional GOQD, featuring with the smallest size and the highest content in surface functionalities showed the best catalytic activity. However, its behaviour was still dependent on the crystalline features of the starting cellulose and the substrate-to-catalyst interaction degree. Thus, only 17.8% of raw cellulose was depolymerized into sugars after 24 h at 135 °C, which rose to 60.1 % upon enhancing its reactivity by ball-milling (8h, 600 rpm). More importantly, a simple mix-milling of the cellulose with the catalyst for 10 min enabled an effective solid-solid contact, rendering complete conversion and 83.5% of glucose. In comparison, 71.3% and 60.4% of glucose was obtained from their sister counterparts: FLGO and GONF, respectively. Presumably, such short-run milling stage neither energetically penalizes the process nor damages the catalyst structural integrity.



Alternative heating sources such as microwave radiation emerge as a more time-effective route than conventional devices, enabling to work at shorter time length (20 min) while the glucose yield is maintained. Nevertheless, the comparison between both heating methods is not straightforward and the operational variables should be redefined for each particular system. Whereas conventional heating requires soft conditions (135 °C) and high dilution ratios (0.25 wt. % of cellulose); shorter time runs in MW-systems (20-120 min) become compatible with harsh conditions (150-165 °C) and higher cellulose loadings (2.0 wt. %), which is a significant contribution towards the process intensification. Under carefully controlled conditions, the maximum productivity of sugars (64.9%; with 63.7% of glucose) was obtained after 20 min at 165 °C over GOQD. The most highlighted influence of the GO morphology was noted during the first reaction interval, with an activation energy that ranked in the following decreasing order: 171.6 KJ/mol (GONF) > 148.9 KJ/mol (FLGO) > 135.2 KJ/mol (GOQD). However, all GO morphologies underwent a gradual decay on their hydrolysis performance over time, which likely prevented from a better glucose production.

Chapter 4.

Hydrolytic hydrogenation of cellulose
into sugar alcohols

Chapter 4.

Hydrolytic hydrogenation of cellulose into sugar alcohols

Abstract

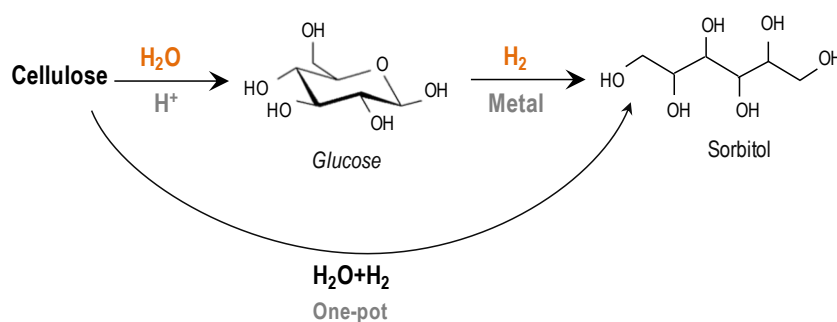
Direct transformation of cellulose into sugar alcohols (*one-pot* conversion) over Ni catalysts represents an attractive chemical route to control the sugars reactivity under hydrothermal conditions, enabling the use of subcritical water in the hydrolysis step. The overall selectivity, however, depends on the kinetic control of a complex reaction network, involving the hydrolysis of cellulose to monossacharides via cello-oligomers, glucose hydrogenation into sorbitol and hydrogenolysis side-reactions of sugars and sorbitol to low molecular weight polyols. Therein, subtle changes of the catalyst composition and process conditions might have a strong impact on the final product distribution.

In this Chapter, the influence of a broad number of variables on the reaction mechanism was quantitatively described. The hydrogenation rate was determined by the availability of H₂ species, metal surface area and the effective contact between the catalyst and the solid substrate (primarily defined by the structural features of cellulose). All these aspects were individually considered by starting from feedstocks with different polymerization degree. First, the metal function was optimised using the conversion of cellobiose as hydrogenation test (190 °C, 3 h, 4.0 MPa H₂). The screening of catalysts included mono-and bimetallic compositions within a wide range of sizes and weight metal fractions. Such conditions turned out to a low reaction extent when raw cellulose was used as substrate, and a further parametric optimization was required to sustain the high-yield production of hexitols. Special emphasis was drawn on two apparently antagonist effects of temperature, affording high diffusion conditions for cellulose decrystallization and dissolution but also promoting products degradation pathways. The

interplay between operational conditions (reaction time and temperature) and cellulose features (crystallinity degree) on catalytic results (conversion and selectivity) was studied following to the Design of Experiments methodology. The sorbitol yield derived from the optimized conditions was further improved by raising the H₂ pressure and applying an additional mix-milling of the catalyst and the cellulose for 30 min.

4.1 Introduction

The quest for effective strategies for cellulose processing has prompted the search of alternative reaction pathways to overcome mass transfer limitations and low chemical selectivity that often govern its heterogeneous transformation. A very promising route is the hydrolytic hydrogenation of cellulose into sugar alcohols (*one-pot* conversion). Herein, glucose molecules are *in situ* reduced into its metastable counterpart (sorbitol) once they are released (Scheme 4.1). This approach circumvents the easy acid/thermal sugar degradation under typical hydrolysis conditions, allowing to work at relatively high temperatures (180-250 °C) with high product selectivity [200, 210].



Scheme 4.1 Catalytic conversion of cellulose into hexitols
 (Adapted from reference [78])

The final product is a versatile platform molecule featured in the top 10 list of valuable bio-based chemicals by the U.S. Department of Energy (DoE) [44]. It finds direct application in cosmetic and pharmaceutical industry as sweetener and emulsifier [211]. Further upgrading routes enable its valorization to sorbitan and isosorbide through dehydration reactions or into other polyols via hydrogenolysis. Isosorbide is used for the synthesis of fuel additives, surfactants and bio-based plastics where it is regarded as a surrogate compound of bisphenol A [207, 212]. On the other hand, short-chain polyols are downstream products with promising prospects in the petrochemistry industry (Figure 4.1) [213, 214].

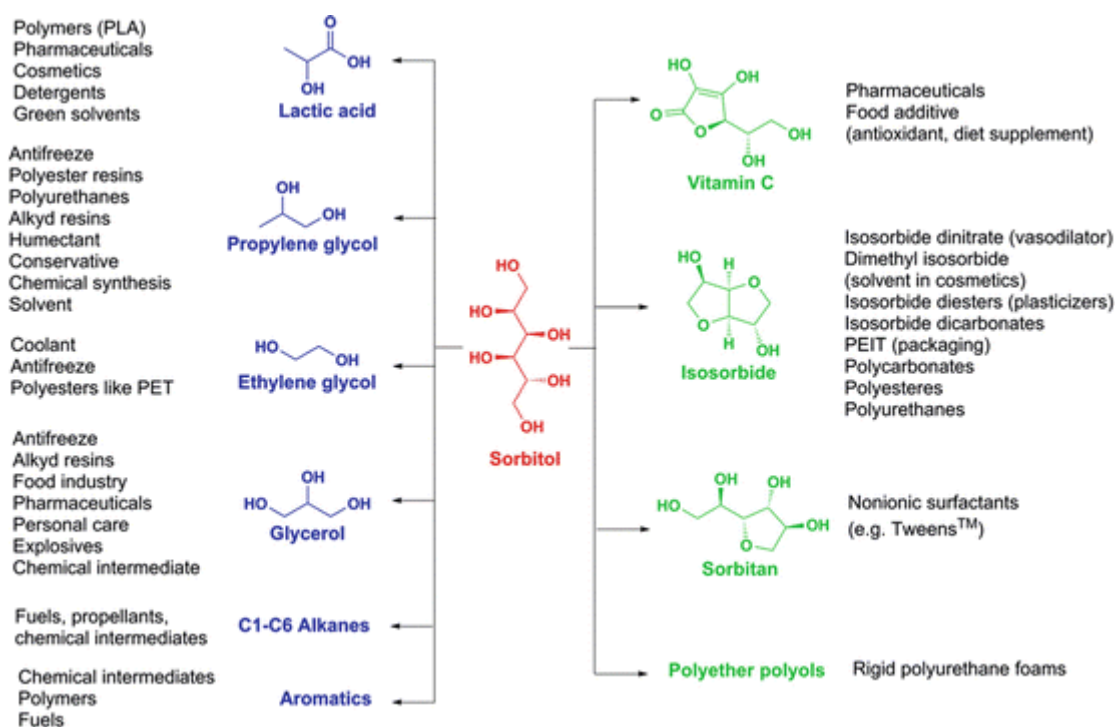


Figure 4.1 Sorbitol as platform molecule: currently manufactured products are coloured in *green* whereas those potentially obtainable at industrial scale are marked in *blue* (Source: [215]).

First investigations on the production of polyols from polysaccharides date back to an initial report by Balandin *et al.* in the late 1950s, combining mineral acids (H_2SO_4 , H_3PO_4 and HCl) with a supported metal catalyst (Ru/C) [216, 217]. In 2006, Fukuoka and Dhepe pioneered the conversion of cellulose into sugar alcohols in aqueous phase over a bifunctional catalyst ($\text{Pt}/\gamma\text{Al}_2\text{O}_3$), reporting 31 % of hexitols under optimized conditions (24 h at 190 °C and 5.0 MPa H_2). In that system, Pt not only promoted both the hydrogenation but also the hydrolysis step through the generation of protic sites by H_2 splitting onto the metal surface and subsequent spill over onto the support [65, 79]. The intrinsic acid function of the support ($\gamma\text{-Al}_2\text{O}_3$) may likely contribute to the cellulose hydrolysis, although its hydration into boehmite ($\text{AlO}(\text{OH})$) prevented from the catalyst recycling [83]. Similarly, Luo *et al.* applied elevated temperatures to reversibly generate *in situ* H^+ ions from hot water dissociation and ruthenium nanoclusters supported on carbon active (Ru/C) for hydrogenation. After 30 min at 245 °C and 6.0 MPa H_2 , a 39 % yield of C6 sugar alcohols could be attained at 85 % of conversion. In this case, the hydrolysis activity was entirely ascribed to acid sites created under hydrothermal conditions



since almost equal cellulose conversion (87.5 %) was measured from non-catalyzed control experiments. More convincingly, no raise on the initial rate of cellulose conversion was noted irrespective of the metal loading (38.1 and 37.9 % of conversion after 5 min of reaction for 1 and 8 wt. % of Ru/C, respectively) [80].

Since then, extensive research work has been devoted to enhance the process selectivity to target polyols, either through a better catalyst design and/or the careful selection of optimal reaction conditions [218]. Numerous materials have been tested as catalytic support, including acid zeolites [219, 220], metal oxides such as silica [221], alumina [222], ceria-based mixed oxide [223] or carbon materials [224-227]. The use of graphitic materials may bring some advantages over other options such as hydrothermal stability, high mechanical strength, tunable surface chemistry and large surface area [228]. Additional benefits in H₂ adsorption, spillover and electron transfer have been recognized for carbons in hydrogenation reactions [81].

Meanwhile, a variety of transition metals have also been explored as metal active sites for sugars hydrogenation. Among them, noble metals such as Pt and Ru are some of the most preferred options, although the major drawback lies on their high price [211, 219, 229, 230]. In an attempt to make the process more cost-competitive, alternative metal phases have also been scanned, ranging from non-noble metals such as Ni, Co, Fe or Cu [81] to bimetallic compositions [79, 82]. Special attention has recently been drawn to Ni, after showing quite interesting results. It is remarkable the high catalytic activity obtained from the as-produced carbon nanofibers containing Ni particles originally used for their growth, affording 56.5 % of hexitols after treating ball-milled cellulose at 190 °C and 4.0 MPa H₂ for 24 h [152]. This value was further improved to 75.6% after a proper balance between the acid/metal functions [153]. Unfortunately, these findings cannot be always transferred to the overall set of Ni catalysts, as a rather poorer catalytic activity was reported by many other authors [79, 225, 231-236]. For instance, the maximum yield to hexitols reported by Wang *et al.* over various supported Ni catalyst barely accounts to 12.5%, which was obtained from microcrystalline cellulose (95 % of conversion) after 2 h at 245 °C and 6.0 MPa H₂ on a 20 wt. % Ni/SiO₂ upon testing many

support materials (ZnO, Al₂O₃, ZrO₂, SiO₂, TiO₂, MgO, AC and kieselguhr) [232]. Similar productivity (11.6 % of hexitols) was attained by Zheng *et al.* after converting 71.9 % of microcrystalline cellulose on a 20 wt. % Ni/AC catalyst for 30 min at 245 °C [235]. In other cases, the catalytic systems on study show relative high yield of total polyols but low selectivity to hexitols. For instance, Zhang *et al.* immobilized Ni nanoparticles (12.5 wt. %) onto several carbons. Through a rigorous control on the number of meso- and /macroporous, the optimized Ni/MMC catalysts permit the effective conversion of microcrystalline cellulose into C3-C6 polyols (45 wt. %) at 240 °C, 4.0 MPa H₂ and 2.5 h. Out of them, only 20% corresponded to hexitols [234]. These discrepancies denote that many variables related to the catalyst preparation and process conditions may concur in determine the final product spectrum. A sound reason to explain such variations could be based on the Ni loading requirements [153, 237]. The effect of metal content (2.6-10.4 wt. %) was discussed by Sels's group on a series of Ni/CNF, showing a similar metal dispersion (D) and particle size distribution (D=1.7-2.1 wt. %, 16 nm). The hexitols yield increased with increasing the Ni loading up to 7.5 wt. % whereas an excessive amount of Ni promoted successive hydrogenolysis reactions. Up to 69.4 % of sorbitol was converted in contact with 10.4 wt. % Ni/CNF under *one-pot* reaction condition (24 h, 190 °C, 6 MPa H₂), with mannitol (11%) and C2-C5 molecules (37.5 %) as the major degradation products [153]. Taking as reference a catalyst with low hydrogenolysis ability, Liang *et al.* employed a zeolite supported Ni catalyst (Ni/ ZSM-5) to illustrate the importance of Ni microstructure (morphology, crystallinity and reducibility) on the hexitols selectivity. Yields of 24.7, 58.2 and 40 % were noted upon a gradual increase on the Ni content from 5 to 17 and 40 wt. %. Under identical reaction conditions (230 °C, 4.0 MPa H₂, 6 h), only a minor portion of hexitols (2.6-8.6 %) suffered from hydrogenolysis. The superior catalytic activity of 17% Ni/ZSM-5 was ascribed to a specific petaloid-like morphology with predominantly exposed Ni (111) crystal planes and stronger support interaction [238]. In a follow-up study, this catalyst was noble metal-modified with a nominal metal fraction of 1 wt. % (M=Pd, Pt, Ru, Rh and Ir) to enhance its hydrothermal stability. All bimetallic catalysts outperformed the Ni/ZSM-5 behaviour (52.7 % of hexitols) except for Ir-Ni. The highest hexitols yield (76.9 %) was



obtained from the Ni-Pt/ZSM-5 catalyst, after treating microcrystalline cellulose at 240 °C and 4.0 MPa H₂ for 4 h. The good dispersion of Pt-Ni nanoparticles (mean size of 8.4 nm vs 19 nm on monometallic Ni) together with the remarkable hydrogen spillover from the alloy surface was reasoned to explain this excellent hydrogenation outcome [239]. It remains unclear, however, if an increase on the metal surface area, induced at smaller particle size, could reduce the metal content needs. For example, Ribeiro and co-workers managed to produce 69.8 % of hexitols (61 % of sorbitol) after 5 h at 205 °C and 5.0 MPa H₂ on a Ru-Ni/CNT catalyst with a rather lower metal loading (Ni:Ru= 3:0.4 wt. %) [240].

The support nature also plays an essential role on the hexitols selectivity over Ni catalysts. In this regard, the use of carbon materials was demonstrated beneficial since the lack of acid-base pair sites could retard the hexitols dehydrogenation to unsaturated species, which is the preceding step to a series of concatenated transformations (retro-aldol condensation, hydrogenation and dehydration) that end-up forming short-chain polyols [241]. However, these reactions are also sensitive to temperature and can be equally promoted under the action of the H⁺/OH⁻ ions generated from hot water dissociation [241], an equilibrium which is often used to accelerate the depolymerization of microcrystalline cellulose [77, 80, 134]. Given this background, with temperature playing two antipathetic roles, a right control of the residence time could be key. Another option to explore is the pretreatment of cellulose which disrupts in advance the crystalline structure and permits its dissolution at milder conditions. For instance, the hydrothermal dissolution of microcrystalline cellulose was reported to occur at low extent at 190 °C (35 % upon 24 h) [65] whereas up to 71.0 % of ball-milled cellulose was solubilised after only 16 h at the same temperature [83].

In brief, the most relevant bibliographic reports suggest that multiple factors are prone to compromise the hexitols selectivity over supported Ni catalysts, whose combined understanding is still needed. In this Chapter, a series of controlled reactions were performed to experimentally investigate the role of a wide range of variables on target transformation, including catalysts design details (metal loading and crystal size), mechanistic considerations (Ni-catalyzed



reactions and the influence of experimental conditions-time and temperature) and mass transport effects (primarily determined by the crystallinity index of cellulose and H₂ gas pressure). The interrelation between temperature, time reaction and cellulose crystallinity on catalytic results (cellulose conversion rate and products distribution) was evaluated and interpreted according to the experimental design methodology.

4.2 Experimental

4.2.1 CATALYST PREPARATION

4.2.1.1 Support synthesis

Fishbone-type carbon nanofibers (CNF₆₅₀) were used as catalytic support in this Chapter. The experimental procedure of this synthesis was detailed in Chapter 2, Section 2.2.1.1. Raw CNF₆₅₀ were purified from metal remnants and oxidized through a step-wise procedure, first in HCl (60 °C, 4 h) and then reflux in HNO₃ (130 °C, 1h). For simplicity, the oxidized carbon nanofibers are hereafter denoted as CNF.

4.2.1.2 CNF-supported metal catalysts

a) *Monometallic Ni catalysts*

Three different impregnation techniques were used to prepare CNF-supported Ni catalysts with various particle sizes. The nominal metal content was modulated for each sample in order to compensate the available Ni surface:

- Homogeneous Deposition-Precipitation (DP)

Ni(OH)₂ nanoparticles were precipitated from an aqueous solution (150 mL, Milli-Q water, 0.055 μS/cm) of nickel nitrate (Ni(NO₃)₂·6H₂O, Alfa Aesar, 98 %) by means of pH changes, following the method elsewhere described [242]. In practice, the suspension was basified to pH=8.2 with ammonia (NH₄OH, Panreac, 30 vol. %), and maintained in contact with the support (CNF, 1.35 g) under mild stirring (200 rpm) for 30 min at 40 °C [243]. Solid sample was then separated by vacuum filtration, washed with distillate water to neutral pH and dried at 60 °C overnight. Fresh catalyst was stored until reduction. The amount of dissolved nickel nitrate varied in 0.83 and 1.27 g according to the desired metal loading (10-14 wt. %), and assuming a Ni deposition percentage of 90 % for the first approach.

- Dry impregnation (DI)

By this procedure, the salt precursor was dissolved in just the amount of liquid needed to fill the pore volume of the catalyst support (2.7 mL/g CNF, experimentally determined). In this case, an aqueous solution (9.45 mL) of nickel nitrate (1.9661 g, $\text{Ni}(\text{NO}_2)_2 \cdot 6\text{H}_2\text{O}$, 98%, Alfa Aesar) was drop-wised to the support (3.5 g CNF), which is then dispersed ultrasonically for 10 min and dried at 60 °C overnight.

- Grafting of pre-reduced Ni nanoparticles onto CNF (NPs Ni)

Uniform-sized Ni nanoparticles (monodispersed) were pre-formed by liquid-phase reduction, using borane triethylamine ($\text{Et}_3\text{N} \cdot \text{BH}_3$) as reducing agent and a mixture of oleylamine (OAm) and oleic acid (OA) as surfactants [244]. Broadly, the synthesis consists in the *ex-situ* reduction of metal colloids in the organic medium, followed by their self-assembly onto the carbon material. Then, the metal surface was cleaned from adventitious organic ligands by oxidation in air and reduced to regain the metallic state. A schematic illustration of the experimental set-up is depicted in Figure 4.2 and described more accurately in the next paragraphs:

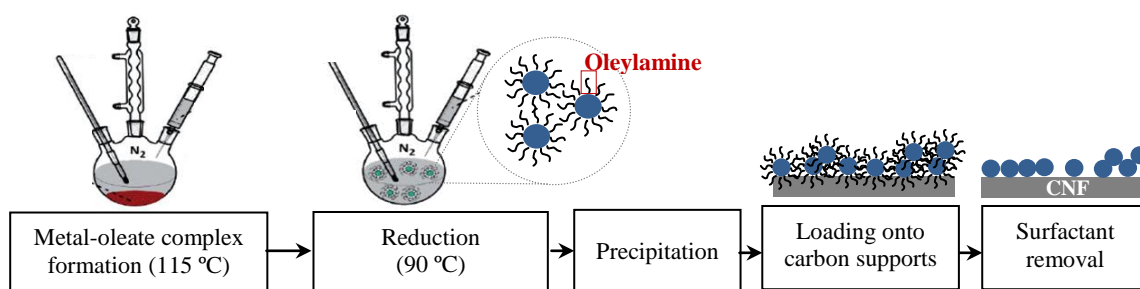


Figure 4.2 Typical steps for the synthesis of Ni catalysts following colloidal-deposition approaches.

In detail, Nickel II acetate (1,24 g, $\text{Ni}(\text{ac})_2 \cdot 4\text{H}_2\text{O}$, Sigma Aldrich, 99.8%) was dissolved in a mixture of OAm (75 mL, 70%, Aldrich) and OA (1.6 mL, 99.5%, Aldrich), inside a three-necked round-bottom flask (250 mL). The solution was degassed and dehydrated at 110 °C for 1 h under a gentle N_2 flow and vigorous stirring (950 rpm) while a green Ni-oleate

complex was formed. At this point, the solution was cooled down to 90 °C and then reduced by fast-injection of $\text{Et}_3\text{N}\cdot\text{BH}_3$ (2,5 mL, Fluka, 95%) and further aging for 1 h. Once at room temperature, the excess of oleylamine was extracted by dissolving it in a double volume of ethanol (150 mL, 96 %). Black Ni NPs are finally collected by centrifugation (8500 rpm, 8 min), re-dispersed in hexane (300 mL) and grafted onto CNF (4.5 g). To ensure the complete adherence onto the support, the colloidal mixture was mechanically stirred (450 rpm) for 3 days at room temperature. After then, the catalyst was dried by rotator evaporation under vacuum, and the metal surface was activated by thermal annealing at 185 °C for 5 h in air (40 mL/min) [245]. This cleaning stage, although necessary to remove organic ligands around the metal surface, modifies the Ni metal state and a second reduction stage with H_2 was required (Figure 4.3).

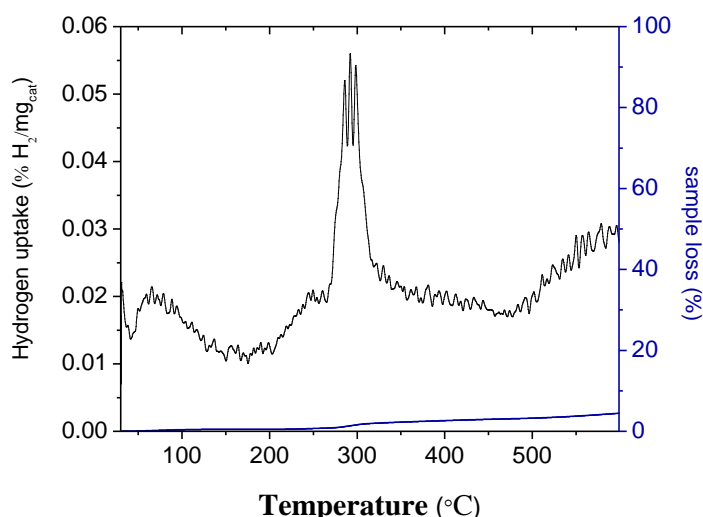


Figure 4.3 TG- H_2 profile for NPs $\text{Ni}/\text{CNF}_{\text{ox}}$ after removing the organic surfactants by air-oxidation (185 °C, 5 h).

Fresh catalysts were finally reduced in a tubular furnace (750×15 mm, Figure 4.4-a). For this purpose, the samples were thermally treated for 1h at 450 °C (heating rate of 10 °C/min) under inert atmosphere (75 mL/min N_2 , 99,9992 %, Air Liquid), and then reduced at the same temperature by a H_2 stream (100 mL/min, 99,9992 %, Air Liquid) during 2 h. After cooling down to room temperature, metal surface was passivated by an oxygen-limited stream (O_2/N_2 , 1% vol./vol.; 40 mL/min, Air Liquid) an overnight. This step creates a protective oxide layer

around Ni surface that prevents from an eventual bulk re-oxidation upon air exposure. A typical cycle of catalyst reduction is shown in Figure 4.4-b. Reduction temperature was defined on the basis of the TPR-pattern for Ni/CNF_{DI}, depicted in Figure 4.4-c. A similar reduction range was reported for the catalyst prepared by deposition-precipitation in the reference literature [243]. CNF-supported NPs Ni were simply treated by a H₂ stream at 300 °C for 1 h according to their TPR-profile (Figure 4.3) and then passivated.

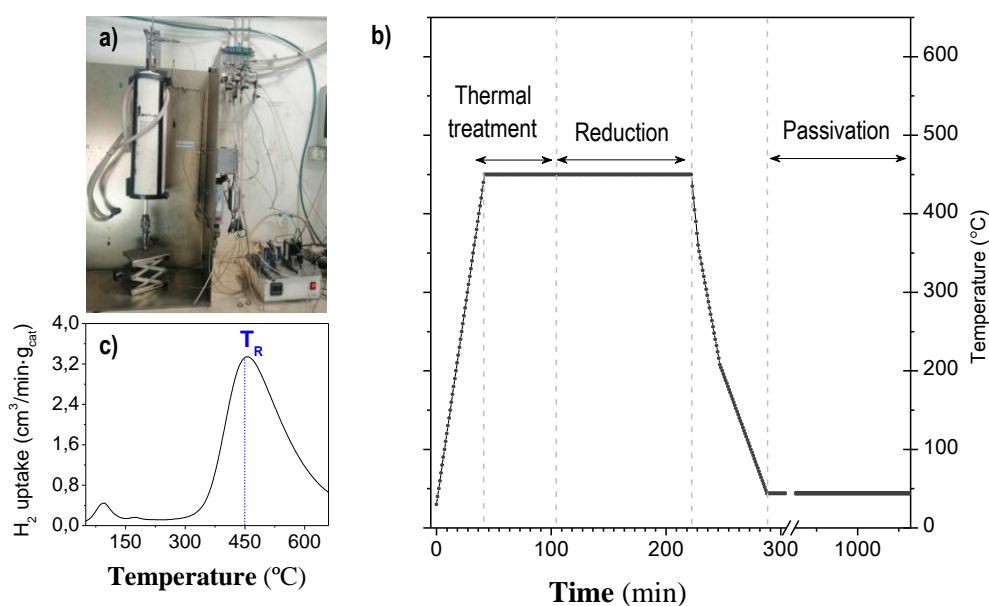


Figure 4.4 Details for catalyst reduction a) Reduction reactor, b) Typical temperature program used for metal catalyst preparation and c) TPR-H₂ profile for Ni/CNF prepared by dry impregnation (10 wt. %).

b) *Bimetallic Ni-noble metal (Pt, Pd, Ru) catalysts*

Bimetallic catalysts, with an intended Ni loading of 3.0 wt. % and 0.5 wt. % of noble metal (Ru, Pt and Pd), were prepared by a co-impregnation of both salts precursors, followed by thermal decomposition and reduction with H₂. Typically, the pore volume of the support material (2.7 mL/g CNF) was filled by a dissolution containing the precursor salt amount needed to adjust the metal loading. In this case, an aqueous solution (4.05 mL, deionized water) containing the elemental precursors was added drop-wise to the support (1.5 g CNF), and then dispersed ultrasonically for 10 min and dried at 60 °C overnight. Nickel (II) nitrate (Ni(NO₃)₂·6H₂O, 98 %, Alfa Aesar), hydrogen hexachloroplatinate (IV) solution (H₂PtCl₆·H₂O,

8 wt. % in H₂O, Sigma Aldrich), palladium (II) chloride (PdCl₂, 99.999 %, Acros Organics) and ruthenium (II) chloride (RuCl₂·H₂O, Reagent Plus[®], Sigma Aldrich) were chosen as Ni, Pt, Pd and Ru salt precursors, respectively. Pure alloy compounds were similarly prepared.

The thermal reduction of the impregnated catalysts was carried out in a tubular furnace according to TPR-H₂ conditions (*vide infra*). Briefly, 1.2 g of solid, placed in a quartz tube (750×15 mm), was first thermally treated under a N₂ flow (75 mL/min, 99,9992 %, Air Liquid) during 3 h (heating rate of 10 °C/min) and subsequently reduced with H₂ (100 mL/min, 99,9992 %, Air Liquid) at the same temperature for another 3 h. Finally, the catalyst was cooled down to room temperature under a N₂ flow (75 mL/min) and passivated by an oxygen-limited stream (O₂/N₂, 1:99 vol./vol.; 40 mL/min, Air Liquid) overnight. The materials were labeled as Ni/CNF, Pt/CNF, Ru/CNF, Pd/CNF, Ni-Pt/CNF, Ni-Pd/CNF and Ni-Ru/CNF, according to their metallic composition.

4.2.2 CATALYST CHARACTERIZATION

Supported metal catalysts were characterized by different instrumental techniques. These include temperature programmed reduction (TPR) and thermogravimetric analysis for reducibility studies, X-ray photoelectron spectroscopy (XPS) for surface chemistry analyses and metal valence state and actual metal loading by Inductively Coupled Plasma-Optical Emission Spectroscopy (ICP-OES). The morphology of nanoparticles and their crystalline features was studied by Transmission Electron Microscopy (TEM) and X-ray Diffraction (XRD) analyses, respectively. Experimental details of each characterization technique can be found in Chapter 2, Section 2.3. The specific surface area of Ni (S_{Ni}) was estimated from the Ni particle size distribution profiles measured by TEM following the expressions included in the last segment of the Section 2.3.2.2 (Chapter 2).

4.2.3 CATALYTIC ACTIVITY AND CELLULOSE PRE-TREATMENT

4.2.3.1 Cellulose pre-treatment

Prior to the reaction, the accessibility and reactivity of commercial cellulose (Avicel[®] PH-101, Fluka, 20-100 μm) were enhanced by ball-milling. The crystallinity index (CrI) of cellulose was tuned by varying the operation time from 2 to 8 h (including 10 min cool down cycles after every 50 min of rotation at 600 rpm) and it was estimated from the XRD pattern by the peak height method (See details in Chapter 2, Section 2.3.3) [62].

4.2.3.2 Catalytic tests

a) *Monometallic Ni catalysts*

For these tests, cellobiose (Sigma Aldrich, purity >98%), commercial cellulose microcrystalline (Avicel PH-101, Fluka, CrI=78.5 %) and pre-treated with various crystallinity degrees (CrI=37.5% and amorphous state) were used as substrates.

The hydrolytic hydrogenation reaction was studied in a batch high-pressure autoclave (Parker Autoclave Engineers, 100 mL) equipped with a PID controller and magnetic stirrer. In a typical run, 300 mg of substrate, 150 mg of catalyst and water (30 mL) were charged in the reactor. The apparatus was then sealed, purged and vented with N_2 and H_2 , in sequence. Afterwards, the autoclave was pressurized with H_2 and heated to the desired temperature under mild stirring (300 rpm). Zero time was considered when set-point temperature was reached and the stirring rate raised to 1000 rpm. At the end of the test, the reactor was quenched, depressurized and opened. The insoluble fraction, containing unreacted material and the spent catalysts, was separated by vacuum filtration (cellulose, 0.22 μm , Whatman[®]). After washing it with neat water to desorb possible retained products, it was dried overnight (60 $^\circ\text{C}$) and weighted. The solution pH was monitored using a pH electrode GLP 21⁺ (Crison). Substrate to catalyst weight ratio was kept at 2:1 in all the cases.

Hydrolytic hydrogenation of cellobiose was tested at 190 °C, 3 h and 4.0 MPa H₂ whereas the study for the cellulose conversion was planned according to a full factorial design, 2-level-3-factor Box Wilson Face Centered (CCF). Like that, the number of runs was defined by the expression 2^k , being k the number of factors or independent variables, namely, cellulose crystallinity (CrI: 0, 37.5, 78.5 %), reaction time (t : 3, 14.5, 26 h) and temperature (T : 190, 210, 230 °C). Six additional axial trials allowed for the assessment of non linear effects and possible interactions between variables. Besides, the experimental error was determined through four replicates at the center point. The analysis of variance (ANOVA) was used in the results interpretation using the software Design Expert (Stat Mode Easy, USA).

As an *addendum*, a series of experiments was finally performed to quantify the influence of hydrogen pressure, which was progressively increased to 6.0 and 8.0 MPa H₂ under optimized reaction conditions (190 °C, 26 h). In these experiments, both amorphous cellulose and amorphous cellulose with an additional mix-milling step of 30 min were used. Table 4.1 lists the specific operational conditions for each run and the effective pressure of the system.

Table 4.1 Experimental conditions for each run. (Inlet solution: 300 mg of substrate, 150 mg of catalyst (Ni/CNF_{DI}) and 30 mL of H₂O).

Run	Substrate (CrI)	H ₂ pressure (MPa)	Temp. (°C)	Effective pressure (MPa)	Time (min)
1	Microcrystalline (78 %)	4.0	190	6.5	3
2	Microcrystalline (78 %)	4.0	190	6.6	26
3	Amorphous (0 %)	4.0	190	6.5	3
4	Amorphous (0 %)	4.0	190	6.5	26
5	Amorphous (0 %)	4.0	230	7.7	3
6	Microcrystalline (78 %)	4.0	230	7.8	3
7	Amorphous (0 %)	4.0	230	7.8	26
8	Microcrystalline (78 %)	4.0	230	7.8	26
9-12	Semi-crystalline (37.5 %)	4.0	210	7.0	14.5
13	Amorphous (0 %)	4.0	210	6.9	14.5
14	Microcrystalline (78 %)	4.0	210	7.0	14.5
15	Semi-crystalline (37.5 %)	4.0	190	6.4	14.5
16	Semi-crystalline (37.5 %)	4.0	230	7.7	14.5

17	Semi-crystalline (37.5 %)	4.0	210	7.2	3
18	Semi-crystalline (37.5 %)	4.0	210	7.0	26
19	Amorphous (0%)	6.0	190	9.2	26
20	Amorphous (0%)	8.0	190	11.4	26
21	Amorphous (0 %) ^[a]	8.0	190	11.4	26
22	Amorphous (0 %) ^[a]	4.0	190	6.4	26

^[a] Mix-milled sample for 30 min at 600 rpm.

b) *Bimetallic catalysts*

The catalytic activity of different bimetallic catalysts was tested in batch mode in a high-pressure autoclave reactor (Parr Instruments Co., Series 5500, 300 mL) with temperature and stirring control (Mod. 4836) and using D-(+)-cellobiose (purity > 98 %, Sigma Aldrich[®]) as reactant. In a typical set-up, an aqueous dissolution of cellobiose (150 mL, 0.25 wt. %) and the catalyst (187.5 mg) was loaded into the Teflon-lined reactor. The equipment was then sealed and inertized by filling the chamber with ~4.0 MPa of N₂ gas and flushing it repeatedly. N₂ volume was then displaced to H₂ gas, applying an identical purge protocol. Next, the autoclave was pressurized to 4.0 MPa of H₂ (RT) and heated to the desired temperature (180 °C, 190 °C or 200 °C) under mild stirring (300 rpm). Zero time was considered when the set-pointed temperature is reached and then stirring rate rose to 1000 rpm. The reaction course was monitored every 30 min by periodical withdrawal of samples (~5 mL) for analysis. The pressure drop was restored after each sampling by a make-up of H₂ gas. At the end of the test (after 3 h), the catalyst was separated by vacuum filtration (cellulose, 0.22 μm, Whatman[®]) and possible changes on the solution pH were measured using a pH electrode GLP 21⁺ (Crison). Sampling representativeness was verified by comparisons between the sample taken at 3 h and the total final. Cellobiose to catalyst weight ratio was kept at 2:1 in all cases.



4.2.4 PRODUCT ANALYSIS

4.2.4.1 High Performance Liquid Chromatography (HPLC)

The analysis of water-soluble products was performed by high performance liquid chromatography (HPLC). The system, LC-2000 Plus Series by Jasco, is fitted with a refractive index detector (Jasco RID-2031), and a strong cation-exchange resin column (ReproGel Pb, 9 μm , 8 \times 300 mm, ReproGel[®], Maisch). The experimental setup and measurement conditions were fully described in Chapter 2, Section 2.3.5.1.

4.2.4.2 Gas chromatography

For the samples generated over bimetallic catalysts, a second analysis by Gas chromatography (GC, Perkin Elmer Instruments, Clarus[®]580) of their silylated analogues authenticated the separation by HPLC. Both quantification methods were reproducible within a mean deviation of 3.6 wt. %.

In cellulose conversion tests, a complementary analysis by gas-chromatography-mass spectroscopy (GC/MS) allowed the determination of various 1,2 alkanediols products in the mass balance.

For the entire set of experiments, gas phase was sampled and included in the mass balance using a Micro GC (Varian CP4900). Details of these procedures and instrument specifications were included in Chapter 2 (Section 2.3.5.2).

4.2.4.3 Conversion measurements and products yield

The conversion of cellobiose was estimated as the difference between the initial concentration and the one determined by HPLC at a given reaction time:

$$X_{\text{CELLOBIOSE}} (\%) = \left(1 - \frac{\text{mass of unreacted cellobiose}}{\text{mass of cellobiose fed}} \right) \cdot 100 \quad [4.1]$$



Cellulose conversion determinations were based on the weight difference of dried cellulose before and after the reaction (upon subtracting the solid catalyst mass):

$$X_{\text{CELLULOSE}} (\%) = \left(1 - \frac{\text{mass of unreacted cellulose}}{\text{mass of cellulose}}\right) \cdot 100 \quad [4.2]$$

The moisture content of the substrate, around 3 wt. % in cellobiose and 4.8 % in cellulose, was taken into account in the mass balance. The products yield (Y) was expressed in wt. % and calculated as the ratio between their mass and the initial mass of the substrate (cellobiose or cellulose):

$$Y (\%) = \left(\frac{\text{product mass}}{\text{mass of substrate}}\right) \cdot 100 \quad [4.3]$$

4.3 Results and discussion

4.3.1 HYDROLYTIC HYDROGENATION OF CELLOBIOSE: SCREENING OF CATALYSTS FOR SUGARS HYDROGENATION

The thermolabile nature of glucose at typical *one-pot* conditions (180-230 °C) needs metal catalysts with high hydrogenation ability, whose rate outpaces other sugar competing reactions [214]. In this section, all those items related to the hydrogenation effectiveness and catalyst preparation are discussed using a model compound reaction, the hydrolytic hydrogenation of cellobiose. This represents a simplified pathway by which hydrogenation variables can be more easily discriminated due to the fact that it is started from a soluble substrate with negligible diffusion resistances [246, 247].

4.3.1.1 Monometallic Ni catalysts

4.3.1.1.1 *Catalyst characterization*

a) *Support characterization*

CNF used as catalytic support exhibit an entangled morphology, forming porous bundles in the micrometer range (Figure 4.5-a). Before purification, raw CNF hold at their tip the metal catalyst used for their growth, arranged as elongated pear-shaped clusters of NiCo/Al₂O₃ whose size coincides with the filament diameter (Figure 4.5-b). On the whole, the catalyst content was 9.3 wt. % (3.1 wt. % of Ni, 3.2 % of Co and 1.6 % of Al in the form of Al₂O₃, measured by ICP-OES).

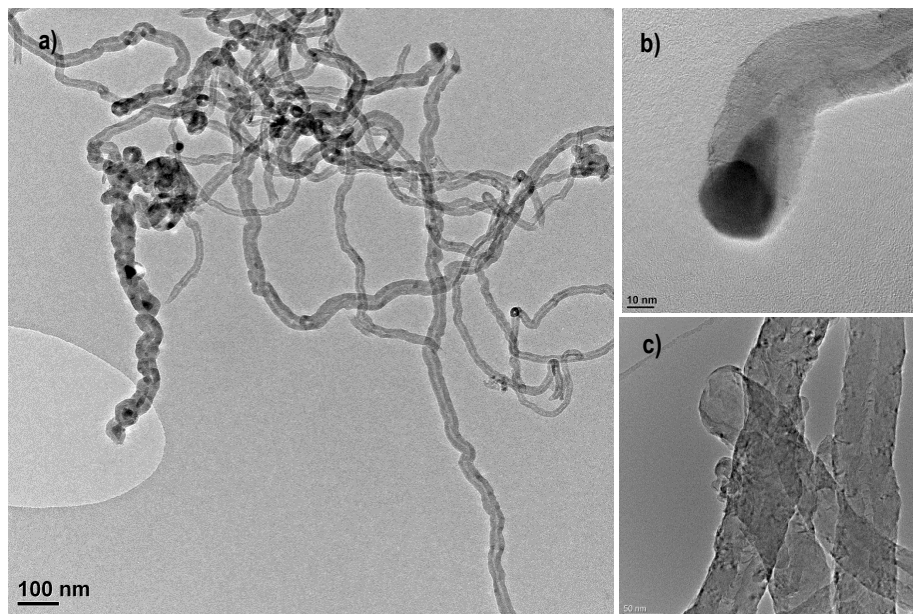


Figure 4.5 TEM images of CNF before and after purification.

Originally, XRD pattern of CNF exhibits characteristic reflections of graphite-like structure along with metal signals of NiCo catalysts (Figure 4.5). Metal signals vanished after the subsequent treatment in acid whereas carbon diffractions lines remained unchanged, as shown in the inset of Figure 4.5. These results confirm that the two-step purification successfully eliminate most part of metal fraction without altering the structural integrity of CNF. Only minute amounts of metal residues (0.54 wt. % of Ni, 0.41 % of Co and 0.67 % of Al) remained still embedded onto the acid-treated CNF, as measured by ICP-OES.

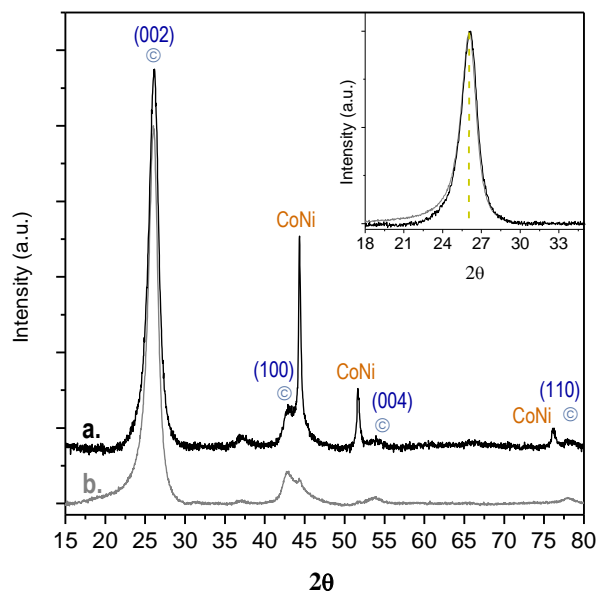


Figure 4.6 XRD pattern of raw CNF (a) and oxidized CNF (b).

The activation of CNF by an oxidative treatment also creates various oxygen-containing surface groups onto the CNF backbone, useful as anchoring points for metal precursors during the impregnation process [94, 118]. Surface chemistry analysis by XPS revealed that most part of the oxygen atoms involve C-O-C species (286.5 eV) such as hydroxyl/epoxides groups among other carbonyl/carboxylic groups (O-C=O, 288.5 eV) that appeared in minor proportions (Figure 4.7).

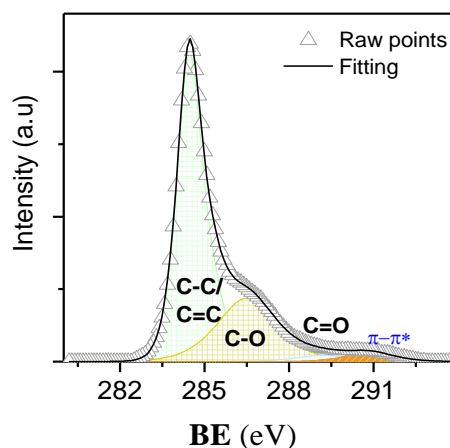


Figure 4.7 C1s XPS spectra for oxidized CNF.

b) Ni-based catalysts

The three impregnation methods (precipitation in basic media, incipient wetness impregnation and the self-assembly of *ex-situ* pre-synthesized nanoparticles) rendered Ni catalysts with

different crystal sizes measured by TEM (Figure 4.8) and metal loadings by ICP (Table 4.2). Nearly monodispersed nanoparticles of small dimensions (5.8 ± 1.7 nm) were prepared from the surfactant-mediated synthesis (NPs Ni), achieving a final Ni loading of 5 wt. %. On the other hand, a broad size distribution and large mean diameter was shown for the Ni/CNF_{DP} (14.4 ± 7.8 nm) with a Ni loading of 7.3 wt. %. Middle size particles were obtained from the Ni/CNF_{DI} catalyst (11.3 ± 6.7 nm, 10.7 wt. % Ni).

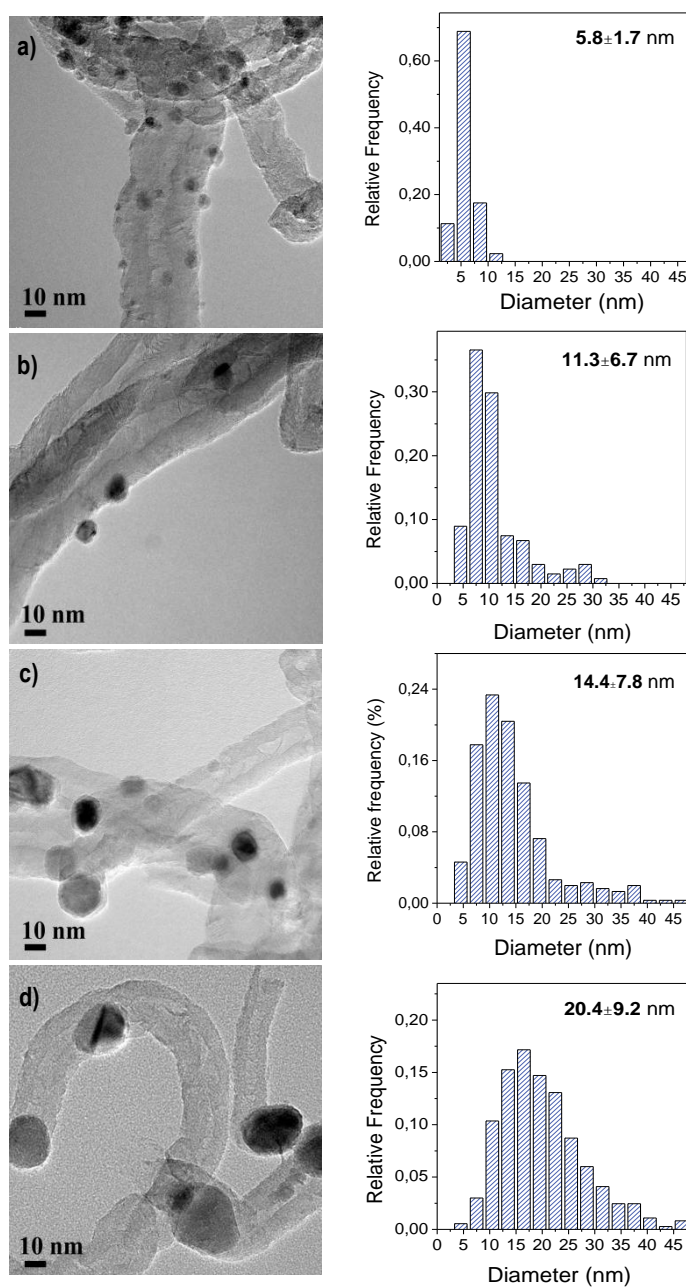


Figure 4.8 HRTEM images and derived particle size histograms a) NPs Ni/CNF, b) Ni/CNF_{DI}, c) 7.3 % Ni/CNF_{DP} and 14 % Ni/CNF_{DP}.

The analysis of particle size gives indication of their geometrical area, which is an indirect measurement of the total surface area available for catalysis. Approximate but useful calculations can be performed from TEM measurements using the surface-area weighted diameter (\bar{d}_s) and the metal density ($\rho_{Ni}=8.9 \text{ g/cm}^3$) on the assumption of an hemispherical form. As shown in Table 4.2, the surface exposure of Ni per unit mass (m^2/g_{Ni}) decreased with increasing the mean size of particles as follows: 99.1 ($\bar{d}_s=6.8 \text{ nm}$) < 38.3 ($\bar{d}_s=17.6 \text{ nm}$) < 30.7 ($\bar{d}_s=22.0 \text{ nm}$) for NPs Ni/CNF, Ni/CNF_{DI} and Ni/CNF_{DP}, respectively. In catalysis, the shrink in the surface to volume ratio derived from the use of larger particles must be compensated with higher bulk metal concentrations in order to ensure a minimum number of catalytic sites. Therefore, these values served as reference to further adjust the metal Ni loading in the DP catalyst (which only showed a Ni specific surface area per mass unit of $2.13 \text{ m}^2/\text{g}_{cat}$ at 7.3% of Ni loading) until a comparable Ni surface area as those obtained for NPs Ni/CNF and Ni/CNF_{DI} (4.42 and $3.89 \text{ m}^2/\text{g}$, respectively) was achieved. Thus, a second 14 wt. % Ni catalyst was prepared by the deposition-precipitation method. The increase on the metal content from 7.3 to 14.0 wt. % led to rather large particles (14.4 vs. 20.4 nm, determined by TEM) and an increase of ca. 60% in the Ni specific surface area ($3.46 \text{ m}^2/\text{g}$). As a result, three catalysts with $3.92 (\pm 0.47) \text{ m}^2$ of Ni per gram of catalyst were prepared when using a bulk metal fraction of 5, 10.7 and 14 wt. % for NPs Ni/CNF, Ni/CNF_{DI} and Ni/CNF_{DP} catalysts, respectively.

Table 4.2 Physicochemical properties of various CNF-supported Ni catalysts: Ni loading by ICP, particle diameter, (\bar{d}_s) from XRD and TEM characterization, surface-area weighted diameter (d_s), Ni surface area per metal gram (m^2/g_{Ni}) and catalyst mass unit ($\text{m}^2/\text{g}_{cat}$) and oxidation state ratio by XPS.

Sample	Ni loading ^[a] (wt. %)	d_p (nm) XRD	d_p (nm) TEM	\bar{d}_s (nm)	S_{Ni} (m^2/g_{Ni})	S_{Ni} ($\text{m}^2/\text{g}_{cat}$)	$\text{Ni}^{0+}/(\text{Ni}^{II}+\text{Ni}^0)$
NPs Ni/CNF	5.0	---	5.8 ± 1.7	6.8	99.1	4.42	5.4 %
Ni/CNF _{DI}	10.7	12.5	11.3 ± 6.7	17.6	38.3	3.89	9.2 %
Ni/CNF _{DP}	7.3	20.3	14.4 ± 7.8	22.0	30.7	2.13	12.6 %
Ni/CNF _{DP}	14.0	24.1	20.4 ± 9.2	26.2	25.7	3.46	22.4 %

[a] including 0.54 wt. % of Ni from CNF support. This value was excluded from the characterization results.

The crystalline nature of the metal phase was examined by XRD (Figure 4.9). Clear diffraction lines, centered at $2\theta=44.5$, 51.8 and 76.3° , were noticed for Ni/CNF_{DI} and Ni/CNF_{DP} samples, which were indexed to (111), (200), (220) crystallographic facets of Face-Centered Cubic (FCC) nickel, respectively. The shape and size of the Ni (111) peak defined a mean crystallite size at around 12.5, 20.3 and 24.1 nm (Table 4.2), based on the Debye-Scherrer's formula. These values lie within the size range quoted from TEM analysis. No Ni reflections were shown by NPs Ni/CNF catalyst, which is consistent with a smaller particles and a lower metal content. Nor characteristic diffraction lines of oxidized phase were observed, revealing the absence of metal oxide crystallites (i.e., smaller than 5 nm) in any case. The broad signal at $2\theta=26.09^\circ$, signature of the (002) graphitic plane, as well as other characteristic minor peaks of the support at $2\theta=42.5$ (100), 44.3 (101), 53.9 (004) and 78° (110) could be distinguished over the whole set of samples.

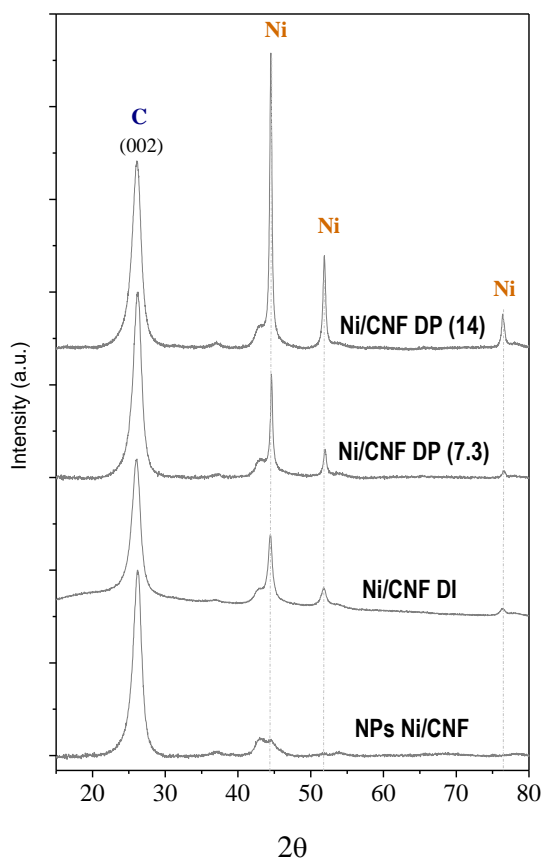
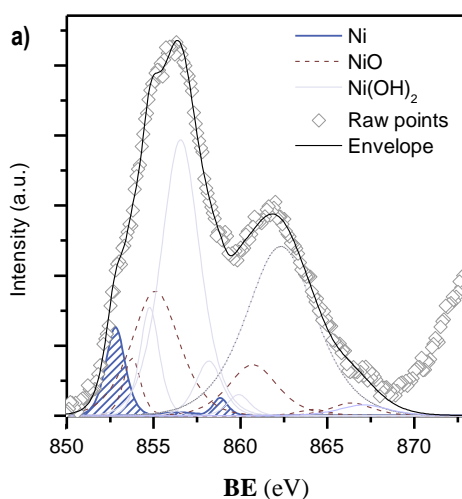


Figure 4.9 X-ray diffraction pattern for the set of Ni/CNF catalysts

To gain further information about the oxidation state of Ni species at near surface, X-ray spectroscopy (XPS) measurements were performed (Figure 4.10). Ni 2p curve fitting was resolved with a multiplet splitting, shake-up and plasmon loss structures, whose empirical fitting parameters, (i.e. peak positions and spacing, FWHM and area percentages) were taken from literature [248]. A spin-orbit splitting distance of 17.3 eV is large enough to only consider the more intense component (2p 3/2) of the line-shape envelope. The width of this region is broad and includes contributions from both metallic and oxidized species in all cases. Three main peaks can be used to isolate the reduced form from such complex spectral profile, including the major signal (79.6 %) at a BE of 852.6 eV and twinned satellites, positioned at 856.3 and 858.7 eV, with a relative area contribution of 5.6 and 14.8 %, respectively. Accordingly, the proportion of surface Ni atoms corresponding to the active phase ($\text{Ni}^0/(\text{Ni}^{\text{II}}+\text{Ni}^0)$) rose from 5.4 to 9.2 and 12.6-22.4 % for NPs Ni/CNF, Ni/CNF_{DI} and Ni/CNF_{DP} catalysts, respectively (Table 4.2). The rest of Ni fraction belongs to an almost overlapped distribution of various oxidized states (i.e., NiO, Ni(OH)₂).



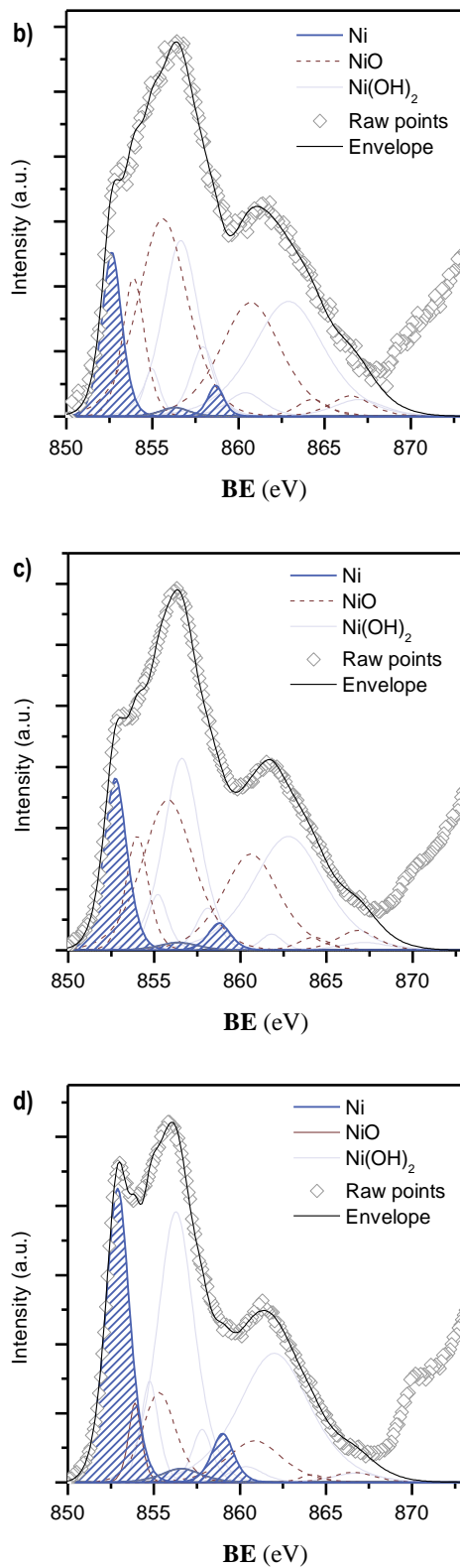


Figure 4.10 Ni 2p 3/2 core level spectra a) NPs Ni/CNF, b) Ni/CNF_{DI} and c) 7.3 % Ni/CNF_{DP} and d) 14 % Ni/CNF_{DP}. Metallic Ni state contributions are marked in blue.

4.3.1.1.2 Catalytic activity

The hydrogenation ability of the full set of CNF-supported Ni-based catalysts was assessed for the conversion of cellobiose at 190 °C under 4.0 MPa H₂. Figure 4.11 displays the main catalytic results obtained after 3 h of reaction while the specific products distribution was itemized in Table 4.3.

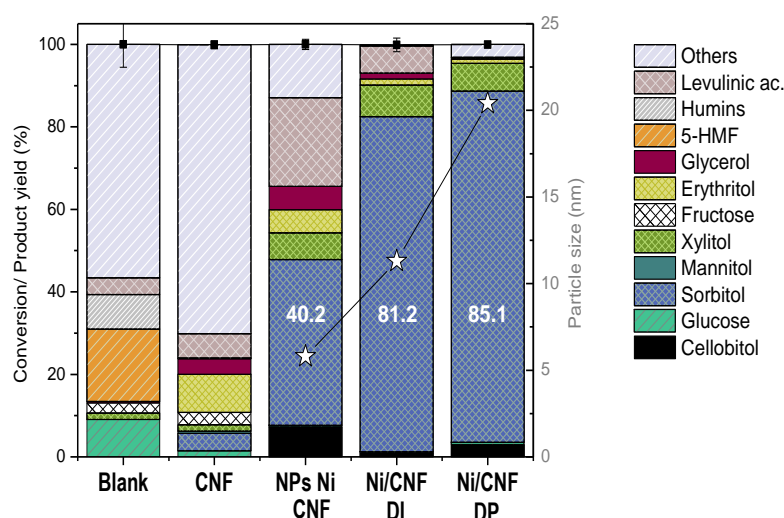


Figure 4.11 Catalytic results for hydrolytic hydrogenation of cellobiose (Reaction conditions: 190°C, 3 h, 4 MPa H₂ (RT)). Error bars indicate \pm standard deviation (n=2).

Table 4.3 Cellobiose conversion and products distribution using Ni-based catalysts.

Catalyst	X (%)	Y _{PRODUCTS} (mass %)							Others ^[c]
		Sugars ^[a]	Levulinic acid	Sugar alcohols ^[b]					
				C12	C6	C5	C4	C3	
Blank	100	11.5	4.0	n.d	n.d	1.5	n.d	0.3	82.7
CNF	99.9	4.5	5.9	n.d	4.8	1.6	9.3	3.8	70.0
NPs Ni/CNF	100	0.4	21.5	7.3	40.2	6.5	5.5	5.7	12.9
Ni/CNF _{DI}	99.9	0.3	6.6	1.0	81.2	7.7	1.5	1.5	0.1
Ni/CNF _{DP} (14 wt. %)	99.9	0.5	n.d	1.8	85.2	6.7	1.0	0.2	4.5
Ni/CNF _{DP} (7.3 wt. %)	99.9	0.3	17.5	2.9	49.8	6.7	5.1	4.3	13.3

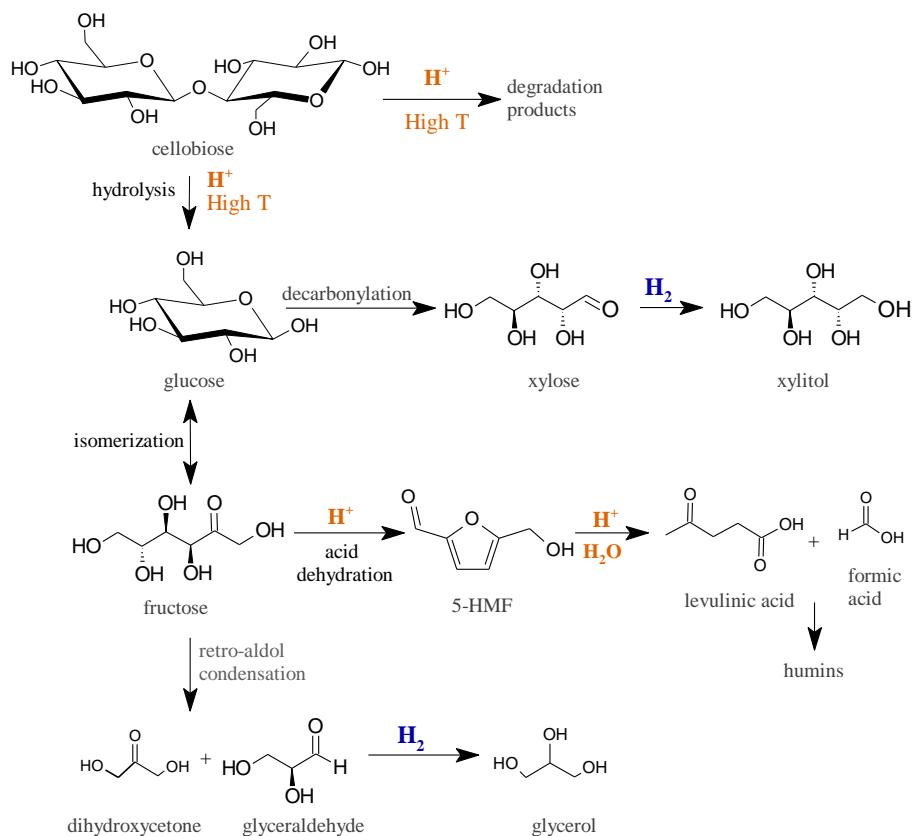
[a] sum of glucose and fructose

[b] C12=cellobitol, C6=sum of sorbitol and mannitol, C5=xylitol, C4= erythritol, C3=glycerol

[c] Including 5-HMF, Humins and undefined products.

n.d=not detected

As it can be seen, nearly complete conversion of cellobiose (>99.9 %) was attained upon a non-catalyzed hydrothermal treatment (blank test). At these conditions, the acidity of the system generated from the auto-hydrolysis of water at high temperature was enough to entirely hydrolyze the β -1,4-glycosidic bonds. Nonetheless, only a minor percentage of glucose units was recovered from the liquid solution (9.1 %), being mostly of it thermally decomposed (90.9 %). Scheme 4.2 depicts the major pathways for glucose degradation under hydrothermal conditions. In particular, a small fraction of sugars (2.5 %) isomerised to fructose, which further underwent dehydration reactions to 5-hydroxymethyl furfural (5-HMF, 17.6 %). This compound was either not stable into the aqueous media, being readily hydrolysed into levulinic (4.0 %) and formic acids and finally condensed to furan-based insoluble substances (humins, 8.4 %). Almost no hydrogenation products were detected in the blank test, excluding small quantities of xylitol (1.5 %) and glycerol (0.3 %) which presumably come from sugars retro-aldol reactions and subsequent hydrogenation. The rest of the degradation products (56.6 %) remained without identification not least because they were not detected by chromatography (Figure 4.12 shows the resultant chromatogram). The extensive formation of by-products under non-catalytic conditions is commonly reported for this reaction and ascribed to the presence of chemically unstable aldehyde group [249]. It must be appointed that a certain fraction of humin-based compounds may be soluble and account on this percentage.



Scheme 4.2 Reaction network involved in the cellobiose hydrolysis (adapted from [250] and [251]).

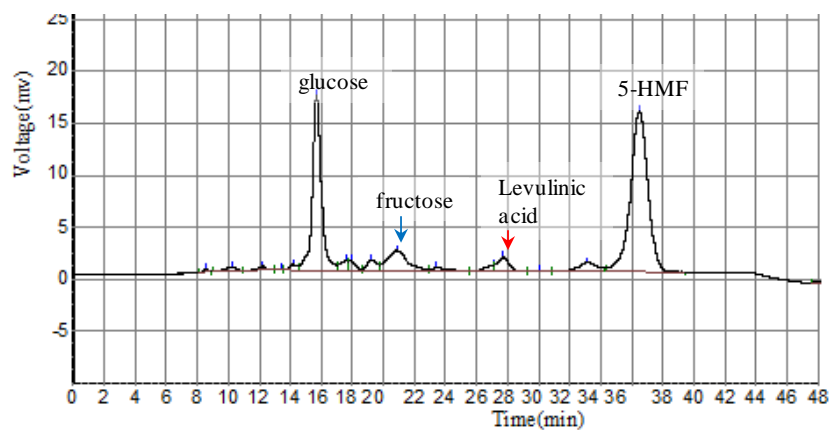


Figure 4.12 HPLC chromatogram resulting from blank test (Reaction conditions: 190°C, 3 h, 4 MPa H₂ (RT)).

The catalytic activity of the Ni-Co/Al₂O₃ particles before the CNF purification stage, was also checked (CNF, Entry 2). Despite their distinguished morphological features (i.e particles are reshaped during the catalytic decomposition of biogas reaction and utterly dispersed) [252], no

important hydrogenation activity was attained (4.8 % of hexitols; 4.25 % of sorbitol). Small molecular polyols were also detected in little quantities such as xylitol (1.6 %), erythritol (9.2 %) and glycerol (3.8 %). This result departs from those previous studies, reporting 56.5 % of hexitols from ball-milled cellulose on a similar 3 wt. % Ni/CNF catalyst, probably because in the case of CNF used in this Thesis, Ni particles are embedded between graphene layers and so, inaccessible for the reaction [152]. This fact was visually verifiable by electron microscopy of individual particles (Figure 4.13).

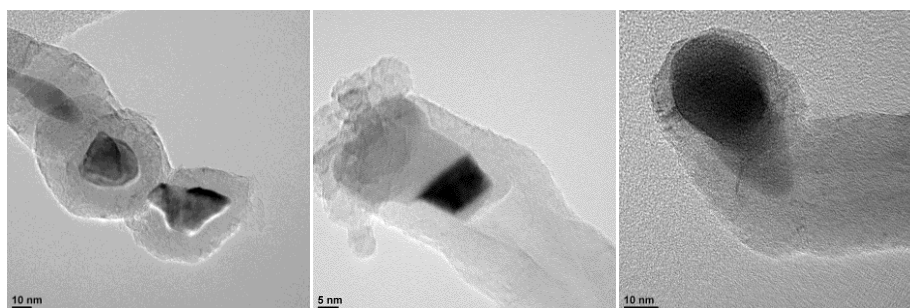


Figure 4.13 Representatives TEM micrographs of raw CNF with occluded metal nanoparticles.

Another argument to explain such catalytic disparities could be based on metal phase composition differences, including an additional fraction of Co in equimolar proportions (Ni-Co alloy, 50:50, 6.3 wt. %). However, a high-yield production of sorbitol (86 %) was also reported for a HZSM-5 zeolite supported NiCo alloy (Ni:Co = 10:5 wt. %) at complete conversion of cellobiose (180 °C, 5.0 MPa H₂, 5 h) [253].

The use of catalyst bearing similar Ni surface area ($\sim 3.92 \text{ m}^2/\text{g}_{\text{cat}}$, $\epsilon=12.2 \%$) resulted in a remarkable stabilization of sugars, affording overall mass recoveries higher than 87.1 % and a product distribution mainly composed of sorbitol. Together, some other by-products were detected in the reaction media, including smaller molecular polyols such as xylitol, erythritol and glycerol *inter alia*. The sum of C5-C3 polyols ranged between 7.9-17.7 %, increasing for catalysts with lower hydrogenation activity. Likewise, glucose degradation in levulinic acid occurred as the hydrogenation rate decayed, accounting up to 21.5 wt. % for NPs Ni/CNF and in less extent (6.6 %) on Ni/CNF_{DT}.

Despite the relatively close Ni surface area values for the three catalysts tested, significant differences were found in the catalytic results (Figure 4.11), pointing to a plausible correlation between the proportion of sorbitol and the crystal size. Thus, sorbitol yield rose from 40.2 to 81.2 wt. % the average Ni size (defined by TEM) increased from 6 to 11 nm. Further enlargement on the crystal size to 20 nm, resulted in a little sorbitol yield gain (from 81.2 to 85.1 wt. %). Herein, the catalytic activity seemed not to be solely controlled by the availability of surface atoms but rather suggests a different reactivity of the surface atoms at various crystal sizes. The reason behind this may be tentatively linked to the oxidation state of the metal phase due to the fact that small Ni particles are more susceptible to surface oxidation upon air contact [249]. This interpretation is consistent with the metal speciation proposed from XPS results, where the smallest particles (the less active) retained a lower proportion of metallic Ni atoms at the outermost surface layer, whereas samples with larger particle sizes (more active) were mostly reduced. These observations suggest the need of using larger Ni particles (> 11 nm) as a way to preserve its metallic character, which is the active phase in the hydrogenation reaction. Similar conclusions were drawn by Fukuoka *et al.* in the range of 2.7-16 nm (by XRD) on higher Ni loadings (10-70 wt. %) [249]. A fair compromise between the Ni surface area ($3.89 \text{ m}_{\text{Ni}}^2/\text{g}_{\text{cat}}$) and its resistance against oxidation (9.53 at. % Ni^0) can be found for intermediate crystallite size ($\sim 11.3 \text{ nm}$) loaded at 10.7 wt. %.

It must be remarked, however, that the positive effect on catalytic activity derived from the use of larger particles is by no means counterpointed by a lower Ni content. To illustrate this point, it was compared the catalytic performance of two catalysts at different metal loadings (10.7 and 7.3 wt. %), both exhibiting a Ni crystal size and atomic Ni^0 above the aforementioned critical values (Table 4.2). In this case, a reduction on the Ni bulk loading from 10.7 to 7.3 % dropped the metallic interfacial area from 3.89 to $2.13 \text{ m}_{\text{Ni}}^2/\text{g}_{\text{cat}}$ and the ulterior sorbitol formation (81.2 % down to 49.8 %), depicting a clear correlation between the Ni surface area and the catalytic performance (Figure 4.14). A decrease on the hydrogenation rate prompted the formation of other by-products from secondary off-path routes. The two most well-known examples included

shorter polyols (6.7 % of xylitol, 5.1 % of erythritol and 4.3 % of glycols) via retro-aldol reactions and levulinic acid (17.5 %) from sugars degradation pathways.

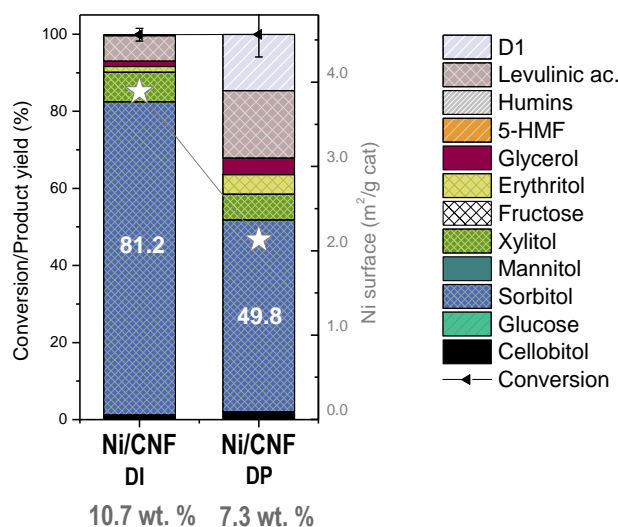


Figure 4.14 Effect of Ni loading on hydrogenation performance over Ni/CNF. Error bars indicate \pm standard deviation (Reaction conditions: 190°C, 3 h, 4 MPa H₂ (RT)).

The Ni leaching into the aqueous phase after runs of 3 hours was checked by ICP-OES. In all cases, a small percentage of the original Ni was dissolved into the reaction solution (5.26, 2.33 and 2.11 % for NPs Ni/CNF, Ni/CNF_{DI} and Ni/CNF_{DP} (14wt. % Ni), respectively. Hence, a subsidiary advantage of using larger Ni particle sizes could be related with their poorer tendency to metal leaching, although the role of the catalyst preparation method cannot be discarded.

As a summary statement, higher Ni loading (10-14 wt. %) and larger crystal particle sizes (11-20 nm) have been identified as key design parameter to ensure the availability and reactivity of Ni atoms in the catalyst surface.

4.3.1.2 Bimetallic Ni catalysts

In the first part of this Chapter, expectations to reduce the metal bulk loading throughout the use of smaller Ni crystallites were hold back by their inherent tendency to deactivation by surface re-oxidation (at least under the work conditions applied in this study). An attractive direction to reinforced the Ni oxidation resistance on highly dispersed samples with minimal metal content

consists in doping it with small quantities of noble metals [254]. On this premise, a series of Ni-based bimetallic compositions (Ni-Ru, Ni-Pt, Ni-Pd) supported on CNF were synthesized (nominal content Ni:Noble metal = 3:0.5 wt. %) and tested in the hydrolytic hydrogenation of cellobiose (180 °C, 3 h, 4.0 MPa H₂). To more clearly depict this function, reaction tests were performed at slightly milder reaction temperature (180 °C) while monitoring the reaction every 30 min, aimed to have the kinetic profiles at intermediate conversion values. The catalytic behavior was compared with their monometallic counterparts and it was rationalized according to the characterization results. The influence of reaction temperature was finally assessed in the range of 190-200 °C using the most promising metal alloy.

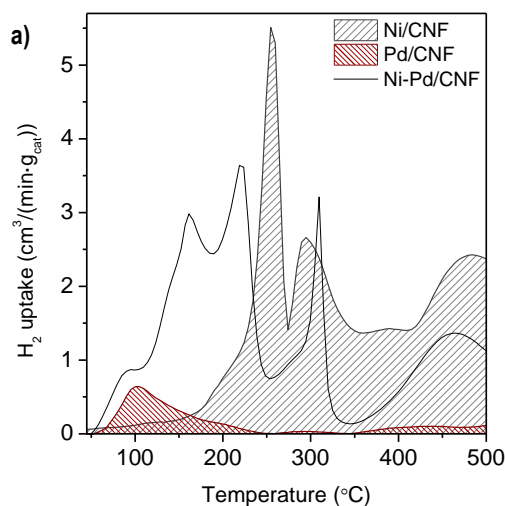
4.3.1.2.1 Catalyst characterization

In order to ensure the complete reduction of metal precursors while minimizing thermal sintering effects on final nanoparticles, reduction temperature (T_R) was singly defined from the TPR-H₂ profiles of the fresh catalysts (Figure 4.15). A higher H₂ consumption in Ni/CNF stood out from the series of monometallic catalysts, since the metal content is also higher (Table 4.4). This profile presented three reduction regions centered, around 255, 300 and 450 °C and assigned to the reduction of NiO species with different support interactions [255, 256]. A slight H₂ consumption is also related to carbon support gasification, which already happens on bare CNF but it is catalyzed by most of the metals tested [257].

Aside from the catalytic methanation of the support at high temperature, the TPR-profiles for Ru/CNF, Pt/CNF and Pd/CNF were described by a main peak of H₂ consumption located at temperatures below 250 °C and attributed to the reduction of their respective chlorides to metallic state (Pt⁰, Pd⁰ and Ru⁰). Therefore, this temperature was chosen as T_R , except for monometallic Pt catalyst, whose reduction was already completed at 200 °C. In the case of bimetallic catalysts, reduction regions appeared displaced with respect to their pure compounds. More specifically, the noble metals were first reduced and the Ni reduction peaks shifted to

lower temperatures (promoter effect) [254]. The reason behind the enhancement of Ni reducibility may stem from its exposure to a H₂-enricher environment (migration of chemisorbed hydrogen molecules on Pt, Pd or Ru particles to Ni vicinity) [258]. A more efficient reduction of Ni atoms was supported by an overall decrease in the H₂ uptake (set as the area delimited by the TPR-profile). Nevertheless, the reduction of bimetallic catalysts, just like the Ni/CNF, was performed at 450 °C in order to cover the reduction of those minor metal species with stronger support interaction.

On the other hand, the characteristic peak of the Ni reduction at 300 °C could be used as a preliminary indicator of the alloy miscibility degree [239, 258]. Accordingly, a higher segregation between Ni and Pd phases is anticipated on the Ni-Pd/CNF catalyst, since the Ni peak partially holds its identity in the TPR profile. Likewise, a more developed alloy between both precursors and the formation of a homogeneous system can be predicted for Ni-Pt/CNF (indiscernible Ni shoulder). An intermediate situation is expected on Ni-Ru/CNF.



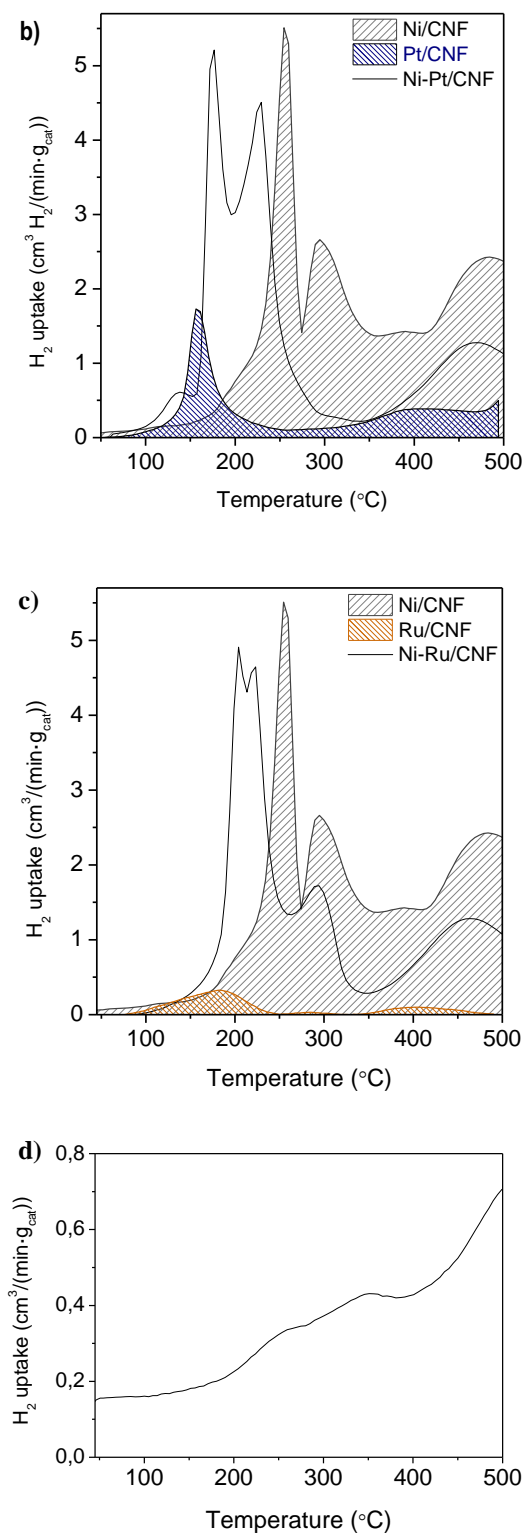


Figure 4.15 Comparison between TPR-H₂ profiles of mono- and bimetallic catalysts a) Pd, Ni and Ni-Pd, b) Pt, Ni and Ni-Pt and c) Ru, Ni and Ni-Ru. The signal correspondent to the CNF gasification (d) was subtracted in all cases.

The support tolerance to the methanation reaction during the reduction stage may explain the small differences between the metal loading measured by ICP-OES and the nominal one (Table 4.4) due to the loss of carbon material. An additional Ni percentage (up to 0.54 wt. %) is also ascribed to residual Ni-Co/Al₂O₃ particles occluded between graphitic layers. Only Ru remained slightly below its theoretical value (0.36 and 0.30 wt. % for Ru/CNF and Ni-Ru/CNF, respectively).

Table 4.4 Metal content and average crystallite size determined by ICP-OES, XRD and TEM, respectively.

Sample	Loading (wt. %)		Ni and Ni-NM crystal size (nm)		Ni and Ni-NM lattice parameter
	Ni *	Noble metal	XRD	TEM	a (Å)
Ni/CNF	3.40	---	6.9	11.4±7.2	3.520
Pd/CNF	---	0.60	---	2.5±1.1	---
Pt/CNF	---	0.70	---	1.5±0.6	---
Ru/CNF	---	0.36	---	1.2±0.4	---
Ni-Pd/CNF	3.60	0.50	13.7	8.7±2.1	3.525
Ni-Pt/CNF	3.50	0.69	6.1	3.3±2.1	3.533
Ni-Ru/CNF	3.70	0.30	7.6	2.1±1.2	3.524

*0.54 wt. % Ni, 0.67 % Al and 0.41 % Co are contained on the CNF (ICP-OES analysis).

Such metal content was unevenly covering the catalyst surface depending on the sample, as revealed TEM observations (Figure 4.16). In general terms, single phase nanoparticles based on noble metals were finely coating the carbon filaments within a narrow size distribution (1.2±0.4 nm for Ru/CNF and 1.5±0.6 nm for Pt/CNF) even though the Pd/CNF catalyst pointed to a bit larger particles (2.5±1.1 nm). Rather large crystals with a wider size distribution (11.4±7.2 nm) were found for Ni particles in the Ni/CNF catalyst, which shifted to smaller and well-dispersed ones upon alloying with Ru (2.1±1.2 nm) or Pt (3.3±2.1 nm) in Ni-Ru/CNF and Ni-Pt/CNF, respectively. This effect was less pronounced for Ni-Pd/CNF (8.7±7.1 nm).

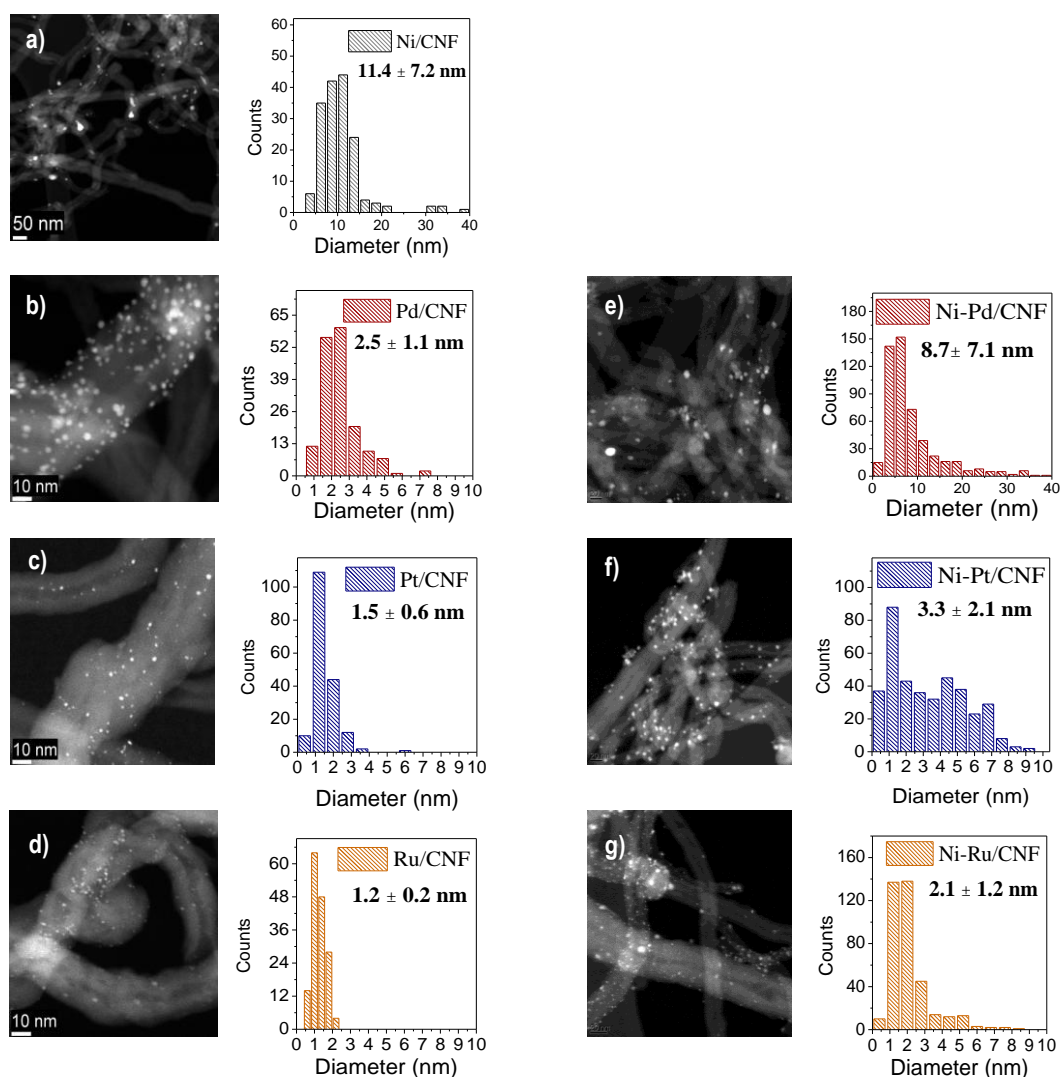


Figure 4.16 HRTEM images and derived histograms of the metal particle size of a) Ni/CNF, b) Pd/CNF, c) Pt/CNF, d) Ru/CNF, e) Ni-Pd/CNF, f) Ni-Pt/CNF and g) Ni-Ru/CNF.

Chemical analysis by EDX evidenced the bimetallic character of most individual nanoparticles inspected, since both metals coexisted in the same particle, although in non-uniform molar proportions (EDX spectra can be found in Figure 4.17). Two main populations could be distinguished in the Ni-Pd/CNF catalyst: large particles comprising the two metals (Figure 4.17-a) and smaller ones, primarily composed by Ni (Figure 4.17-b). As it was anticipated from the TPR-H₂ results, the Pd concentration in clusters indicates a rather weak interaction between the Ni and the Pd and so, separated aggregates tend to be formed. A more homogeneous distribution between the metal regions was observed in turn for the Ni-Pt/CNF and the Ni-Ru/CNF catalysts (Figure 4.17 c-d), showing a high alloying degree.

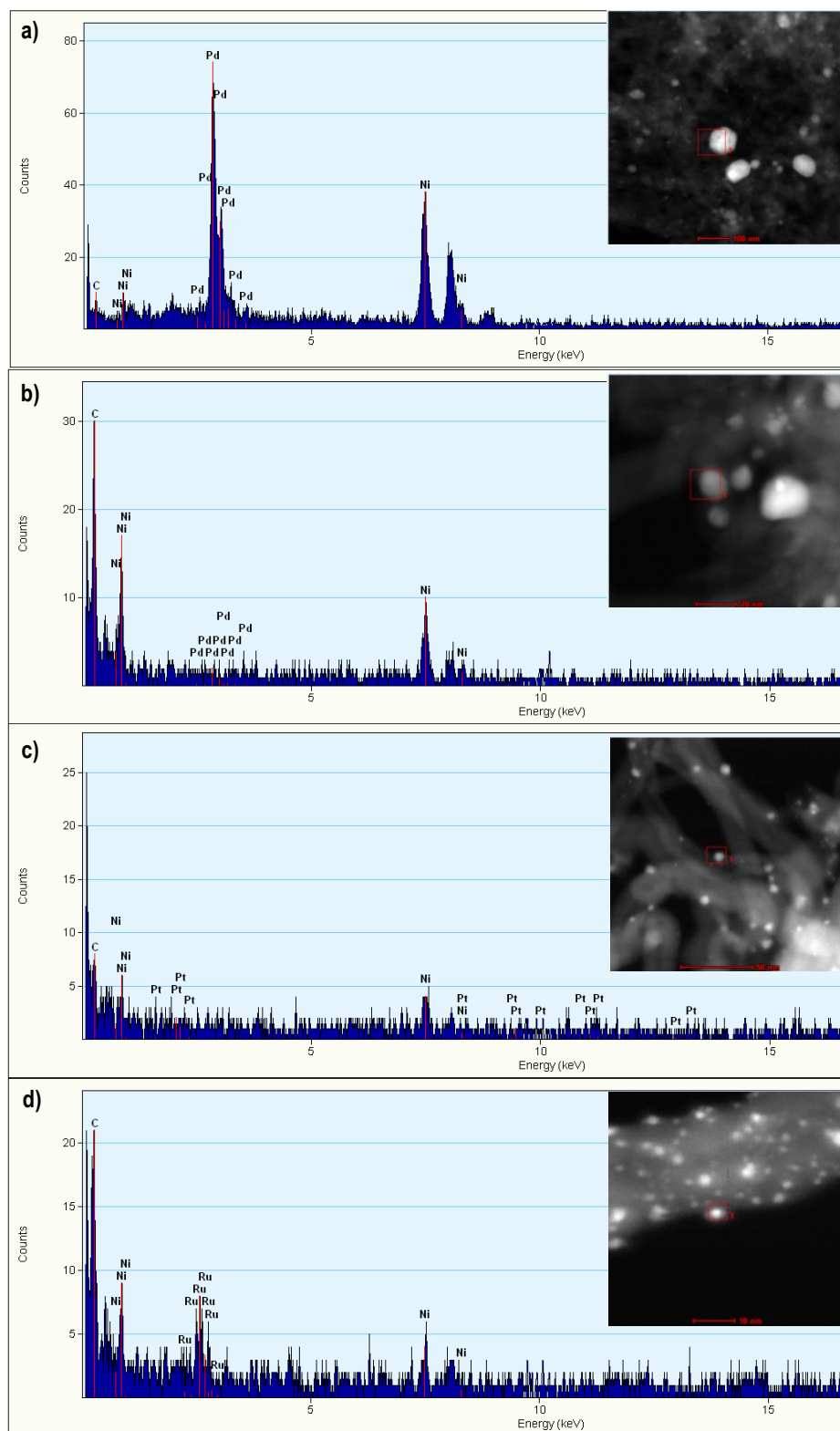
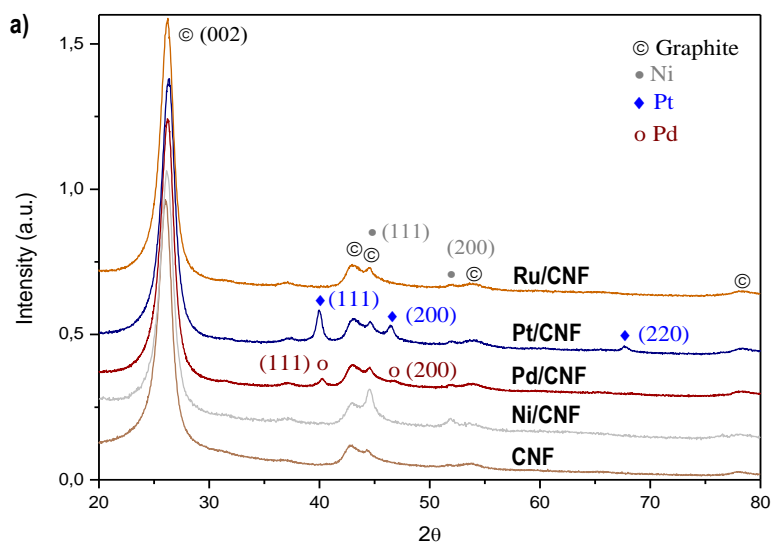


Figure 4.17 Chemical composition of arbitrary bimetallic nanoparticles determined by EDX analysis: a-b) Ni-Pd/CNF, c) Ni-Pt/CNF and d) Ni-Ru/CNF

By means of XRD technique, it is possible to obtain information on crystal phases structure (lattice parameters, crystallite domain size, composition and atomic arrangement) [259].

However, the small particle dimensions (mostly smaller than 3 nm by HRTEM), together with their low metal fraction (0.5-3.0 wt. %), resulted in diffraction lines close to the detection threshold (Figure 4.18). This fact was aggravated by the interference from the graphitic signals at $2\theta = 42.5^\circ$ (100) and 44.3° (101), which overlap the metallic reflections (depicted as inset of Figure 4.19-b). As a result, only those largest particles (namely, Ni, Pd and Pt single-phases) displayed their characteristic diffraction planes ($2\theta = 39.7^\circ$ (111), 46.2° (200) and 67.4° (220) for Pt; 40.1° (111) and 46.3° (200) for Pd and $2\theta = 44.5^\circ$ and 51.7° , corresponding to (111) and (200) crystallographic planes of Ni). The wide peak positioned at $2\theta = 26.09^\circ$ (002) and the weak signals at $2\theta = 53.9^\circ$ (004) and 78° (110) belong to the support too. The disappearance of the Pt and Pd signals in the bimetallic catalysts, along with a slight enlargement in the Ni lattice parameter (Table 4.4) could be indicative of the alloy formation [259]. The shift in the lattice parameter is known as Vegard's law and can be related to the compression or expansion of Ni-Ni bond length upon the insertion of secondary atoms by metal alloying [259, 260].



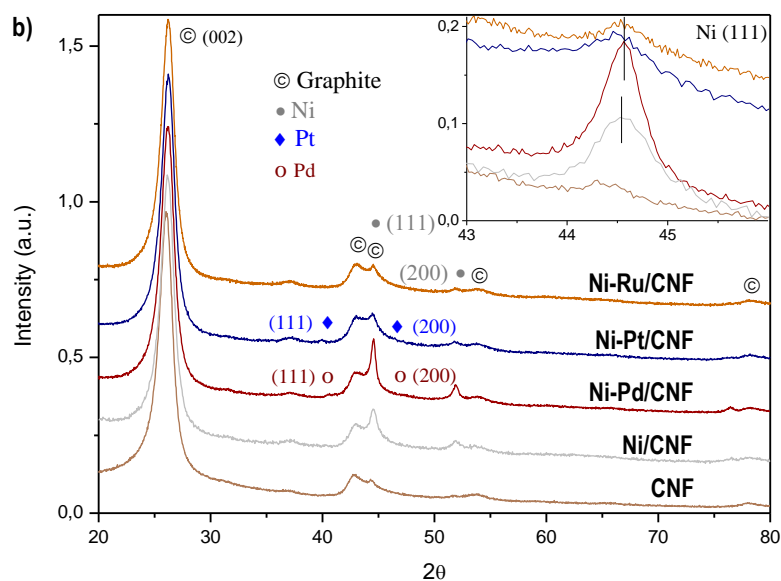


Figure 4.18 X-ray diffraction patterns of supported catalysts a) pure and b) alloy metals.

4.3.1.2.2 Catalyst performance

a) Support catalytic activity

As a first test, the catalytic activity of CNF was assessed using the experimental conditions set for this study (180 °C, 4 MPa H₂, 3 h). As shown in Figure 4.19, the conversion of cellobiose increased as reaction proceeded and it reached 84.2 % after 3 h. The concentration of glucose, expected as the main hydrolysis product, rose in the first interval until a constant value at around 27.2 % from 1.5 h onwards. A small fraction of glucose was consumed by consecutive side-reactions such as isomerization to fructose or by acid dehydration into 5-hydroxymethylfurfural (5-HMF) and further decomposition to levulinic and formic acids (Scheme 4.3) [261]. Such secondary reactions became more important over time and they contributed up to 12.5 % in the final mass balance (Table 4.5). Overall, the sum of sugars and related degradation products did not exceed 46.5 % in selectivity. No formation of polycondensed organic compounds was detected, while only small amounts (0.8 %) of gaseous products (CO₂ and CH₄) were quantified. In the absence of metal particles, hydrogenated products were not identified, excluding any background hydrogenation from metal remnants attached on CNF.

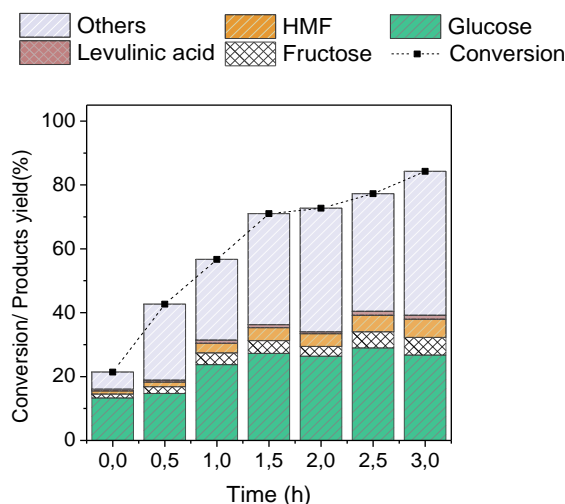


Figure 4.19 Performance of the support (CNF) in the hydrolytic hydrogenation of cellobiose. (Reaction conditions: 180 °C, 0-3 h, 4.0 MPa H₂ (RT)).

Table 4.5 Cellobiose conversion and products yields during the hydrolytic hydrogenation tests on CNF.

Time (h)	Cellobiose conversion	Y _{PRODUCTS} (mass %)				
		Glucose	Fructose	HMF	Levulinic acid	Others ^[a]
0	21.40	13.25	1.26	1.00	0.50	5.39
0.5	42.66	14.67	2.11	1.46	0.64	23.77
1	56.68	23.69	3.72	3.00	0.98	25.28
1.5	71.02	27.24	3.96	4.12	0.91	34.79
2	72.73	26.35	3.04	3.99	0.60	38.75
2.5	77.24	28.92	5.09	5.18	1.22	36.84
3	84.24	26.70	5.56	5.71	1.23	45.05

[a] Determined as the difference between the cellobiose conversion and the sum of quantified products.

In order to explain the gap between reacted cellobiose and the total quantified products, a possible adsorption of cellobiose on the catalysts surface was also considered. The adsorption of the reactants on the catalyst surface is a pre-requisite to any heterogeneous transformation. In fact, the easy adsorption of the substrate and the rapid products desorption is proposed as an essential catalyst requirement during its design. In this regard, the surface functional groups of CNF surely take part in such interaction between molecules, bridging H bonds between the carbon surface and the hydroxyl groups (-OH) of cellobiose [143]. Since a cellobiose molecule doubles in number of -OH groups to glucose unit, its stronger retention ability onto the support can be immediately inferred [82, 208]. However, this could distort the cellobiose concentration

in the liquid phase and overestimates the conversion measurements, particularly in determinations by sampling. Such possibility was neglected upon an analysis of the water collected after a thorough rinse of the catalyst ($t=3$ h), where no adsorbed cellobiose was detected. Therefore, it can be concluded that nearly a half of cellobiose degradation (53.5 %) occurs through the aldose group, presumably towards the formation of acids type compounds which lowered the media pH from 6.09 to 3.92. These compounds were lumped in the unidentified products fraction named as “others”. The other half (46.5 %) can be attributed to the hydrolysis reaction, under the combined action of the oxygen functional groups included in the acid-treated CNF and the protons generated from hot water dissociation [262]. Both contributions resulted in a moderate reaction rate. Nevertheless, these results cannot rigorously be transferred to CNF-supported metal catalysts, as part of the oxygen surface groups will be thermally removed during the reduction treatment [263].

b) Monometallic components

As expected, a Ni content of 3 wt. %, merely providing $0.78 \text{ m}^2 \text{ Ni/g}_{\text{cat}}$ (10.0 at. % Ni⁰ by XPS), was not enough to entirely hydrogenate the glucose units (Figure 4.20). Therefore, the hexitols formed after 3 h of reaction (15.0 %) were accompanied by intermediate sugars (14.0 %) and ulterior degradation products (10.2 %).

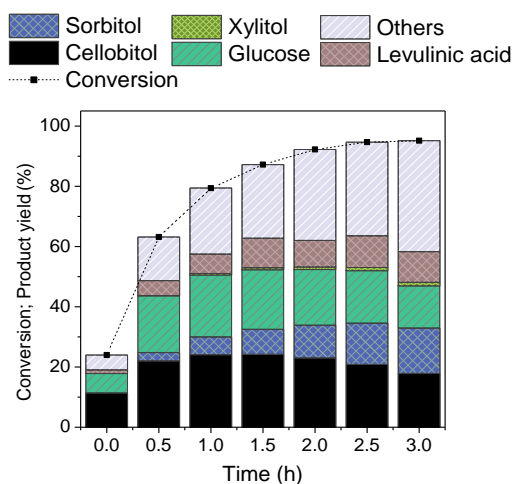
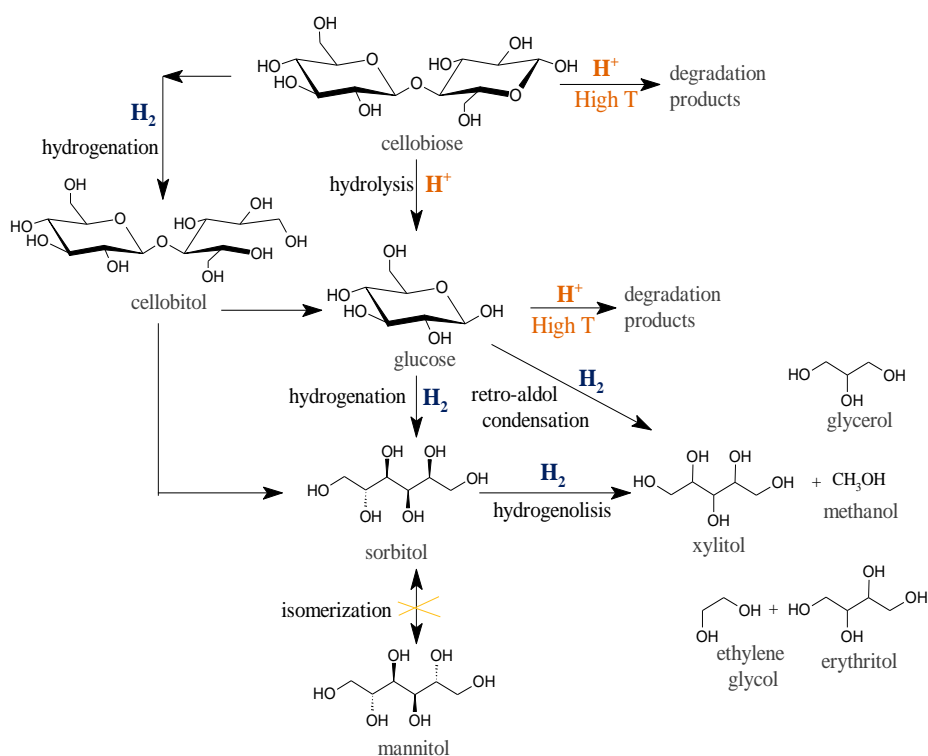


Figure 4.20 Evolution of the cellobiose conversion and products distribution using Ni/CNF as catalyst. (Reaction conditions: 180 °C, 0-3 h, 4.0 MPa H₂ (RT)).

Similar to the support test, an important fraction of the cellobiose (36.8 %) was degraded under reaction conditions through aldose group (others) while another portion (up to 17.9 %) was stabilized via cellobitol formation (3- β -D-glucopyranosyl-D-glucitol). This compound results from the hydrogenation of the C-O bond on one of the glucose rings within the cellobiose molecule (Scheme 4.3). The isolation of cellobitol from cellobiose was previously documented using catalytic systems with slow hydrolysis rate [247, 262, 264]. The subsequent cleavage of the 3- β -(1,4)-glycosidic bond splits the cellobitol molecule into sorbitol and a glucose unit, which means that at least a 50 % of the quantified cellobitol will end up into the sorbitol form. Sequential retro-aldol and hydrogenation reactions of sugars or sorbitol isomerization into mannitol were not noticed.



Scheme 4.3 Reaction network involved in the hydrogenation step (adapted from [214], [250], [261]).

Catalytic results obtained from the noble metal-based monometallic catalysts turned out to be strongly dependent on the noble metal nature (Figure 4.22 a-c). Ru/CNF catalyst showed high hydrogenation activity, even when owning the lowest metal loading (Figure 2.21-a). It is interesting to note that most part of the cellobiose (84.9 %) was already transformed into

cellobitol during warm-up stage and it reached complete conversion 30 minutes later. Determined by the hydrolysis rate, the cellobitol was then quantitatively converted into sorbitol. After 3 h of reaction, 45.9 % of sorbitol yield was attained while a 46.5 % of cellobitol remained as a hydrogenated but unhydrolyzed intermediate compound. Small quantities of xylitol (3.9 %) and glucose (3.6 %) closed the products balance.

Neither Pd/CNF nor Pt/CNF were active in the reaction (Figure 4.21 b-c). Only a marginal hydrogenation was noted for the Pt/CNF catalyst (maximum yield of hydrogenated products of 26.0 %, including cellobitol and sorbitol at a 91.0 % of conversion). In both cases, catalytic results are characterized by high conversion rates (~ 90.0 %), poor hexitols yield (3.3 % for Pd/CNF and 13.3 % for Pt/CNF) and glucose accumulation (in the same order as the support test with CNF). Table 4.6 summarizes the most relevant catalytic results from monometallic components.

Table 4.6 Cellobiose conversion and products distribution over monometallic catalysts.

Catalyst	Time (h)	X (%)	Y _{PRODUCTS} (mass %)							
			Glucose	Levul. Acid	Sugar alcohols ^[a]					Others
					C12	C6	C5	C4	C3	
Ni/CNF	0	23.9	6.5	1.2	11.3	n.d	n.d.	n.d	n.d	4.9
	3	95.1	14.0	10.2	17.9	15.0	1.2	n.d	n.d	36.8
Ru/CNF	0	89.8	2.7	n.d	84.9	2.1	n.d	n.d	n.d	0.1
	3	100	3.6	n.d	46.5	45.9	3.9	n.d	n.d	0.1
Pd/CNF	0	9.8	6.4	3.2	n.d	0.2	n.d	n.d	n.d	n.d
	3	91.6	20.9	21.8	n.d	0.4	3.6	2.3	2.1	40.5
Pt/CNF	0	20.2	8.7	0.2	11.2	n.d	n.d	n.d	n.d	0.1
	3	91.0	24.4	9.8	12.7	13.3	n.d	2.7	1.4	26.7

[a] C12=cellobitol, C6=sum of sorbitol and mannitol, C5=xylitol, C4= erythritol, C3=glycerol

c) Bimetallic catalysts

All bimetallic catalysts enhanced the catalytic performance with respect to the single phase Ni catalyst (Figure 4.21, d-f). Again, cellobitol was quantified as the main reaction product, delivering sorbitol as the C-O-C bond was broken and the hydrogenation of the second

carboxylic groups occurred. At the end of the tests, yields of 37.5, 28.5 and 44.4 % in sorbitol were obtained from Ni-Ru/CNF, Ni-Pd/CNF and Ni-Pt/CNF catalysts, respectively.

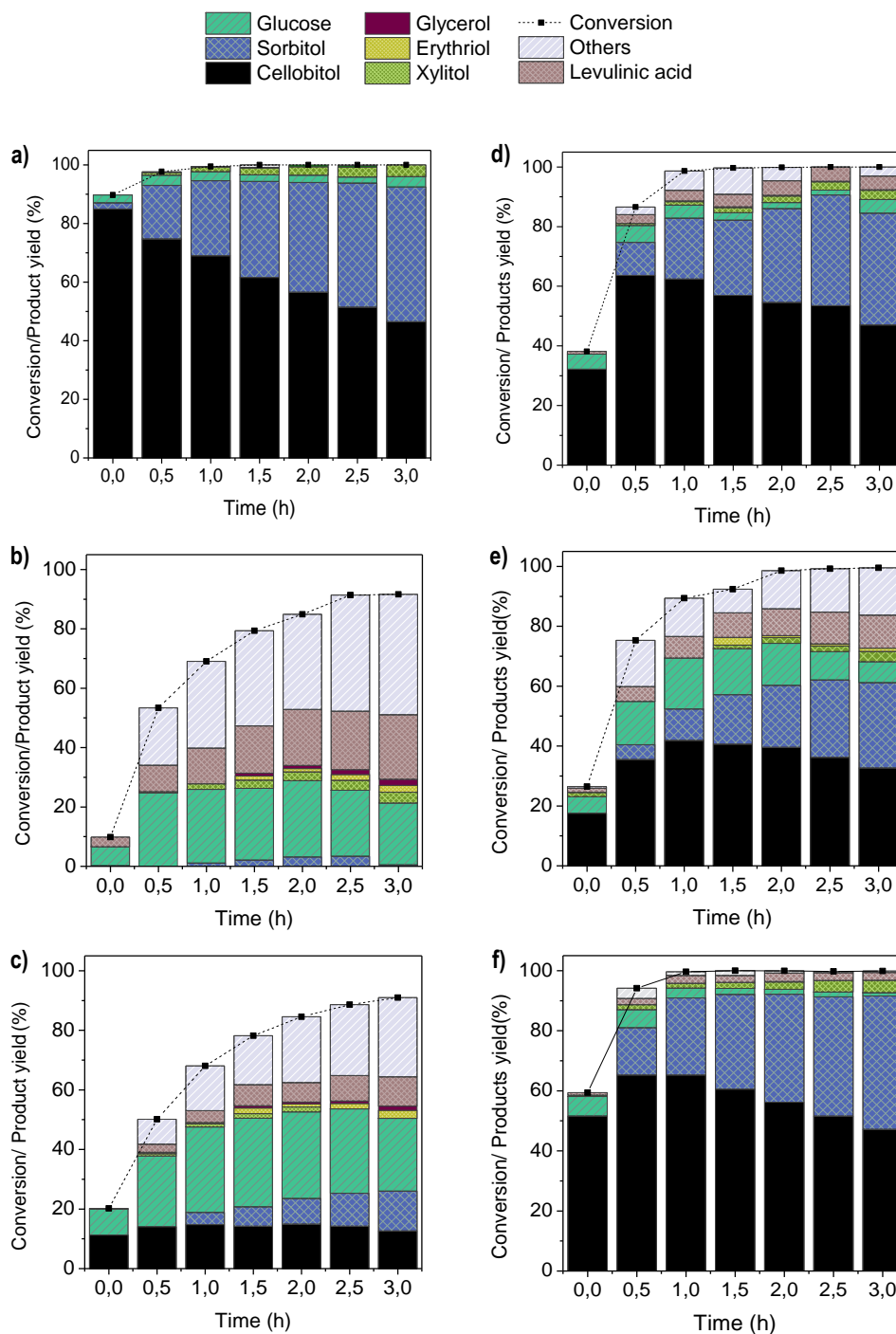


Figure 4.21 Evolution of cellobiose conversion and products distribution for noble metal-based monometallic catalysts and bimetallic compositions: a) Ru/CNF, b) Pd/CNF and c) Pt/CNF, d) Ni-Ru/CNF, e) Ni-Pd/CNF and f) Ni-Pt/CNF. (Reaction conditions: 180 °C, 0-3h, 4.0 MPa H₂)

Being the first hydrogenation compound, the cellobitol formation rate at the earliest stage, that is, at zero time, could be considered as a second guideline for the comparison between different

catalyst systems, particularly useful under environments where target hexitols are prone to undergo consecutive reactions. At this point, the cellobitol yield determined for Ni-Ru/CNF, Ni-Pd/CNF and Ni-Pt/CNF was 32.1, 17.6 and 51.6%, respectively.

For ease of comparison, the specific distribution of products at the initial and end reaction was compiled in Table 4.7. Either criterion met into the following order of reactivity: Ni-Pt/CNF > Ni-Ru/CNF > Ni-Pd/CNF. The best catalytic results were provided by the Ni-Pt/CNF system, where only 1.0 % of glucose remained without hydrogenation after a contact time of 3 h. Small amounts of xylitol were also detected within the products spectrum, showing a gradual increase from 1.6 to 4.2 % and probably coming from successive hydrogenolysis reactions of sorbitol [80, 232]. This metal alloy was chosen for subsequent research studies.

Table 4.7 Cellobiose conversion and products distribution over bimetallic catalysts.

Catalyst	Time (h)	X (%)	Y _{PRODUCTS} (mass %)							
			Glucose	Levul. Acid	Sugar alcohols ^[a]					Others
					C12	C6	C5	C4	C3	
Ni-Ru/CNF	0	38.1	5.1	0.9	32.1	n.d	n.d	n.d	n.d	n.d
	3	100	4.6	4.6	47.0	37.5	3.1	0.2	n.d	3.0
Ni-Pd/CNF	0	26.4	5.5	1.3	17.6	n.d	1.4	n.d	n.d	0.6
	3	99.5	7.0	11.0	32.7	28.5	3.4	1.1	n.d	15.8
Ni-Pt/CNF	0	59.4	6.5	0.8	51.6	n.d	n.d	0.5	n.d	n.d
	3	99.9	1.1	2.6	47.2	44.4	4.2	n.d	n.d	0.4

[a] C12=cellobitol, C6=sum of sorbitol and mannitol, C5=xylitol, C4= erythritol, C3=glycerol

The inferior catalytic behavior of Ni-Pd/CNF can be tentatively explained from a worse metal dispersion and a non-homogeneous formation of the alloyed system (as previously commented) whereas in the case of Ni-Ru/CNF, it could be ascribed to a lower noble metal content (0.3 wt. % of Ru instead of 0.6 wt. % for Pt according to the ICP-OES results). However, the addition of an extra Ni quantity on Ru/CNF catalyst would not be justified in the composition Ni-Ru, as a 0.3 wt. % of this noble metal was enough to entirely hydrogenate the sugars. In fact, the initial cellobitol formation over Ni-Ru/CNF catalyst (32.2 %) was not as fast as the Ru/CNF (84.9 %).

A lower hydrogenation rate could prompt the incipient degradation of the cellobiose (3.1 % of undefined products) as well as the glucose units to levulinic acid (4.6 %).

Overall, it is considered that an improved hydrogen transfer (by spillover effect of molecular hydrogen onto the noble metal particles) as well as the increase in the Ni catalytic surface (induced at smaller particle size) could be the origin of a better catalytic activity of bimetallic catalysts. The addition of noble metals could also retard the Ni lost by leakage since less amount of this metal was determined into the outlet effluent by ICP-OES (1.87, 2.27 and 1.55 ppm for Ni-Ru/CNF, Ni-Pd/CNF and Ni-Pt/CNF catalysts, which represents a 4.0, 5.9 and 3.5 wt. % of the original Ni content). At least an 8.2 wt. % of Ni was instead leached out using pure Ni/CNF (3.5 ppm) whereas no noble metal was found in the reaction solution by this technique (< 100 ppb). Nor important morphological changes were observed by XRD on the spent catalysts, revealing the absence of severe metal sintering. Figure 4.22 shows an illustrative example for Ni-Pt/CNF and their single components. Slightly sharper diffraction lines of bimetallic compositions did not echoed in an enlargement on the particle size distribution determined by TEM, as it was supported by the analysis of the spent Ni-Pt/CNF catalyst (Figure 4.23).

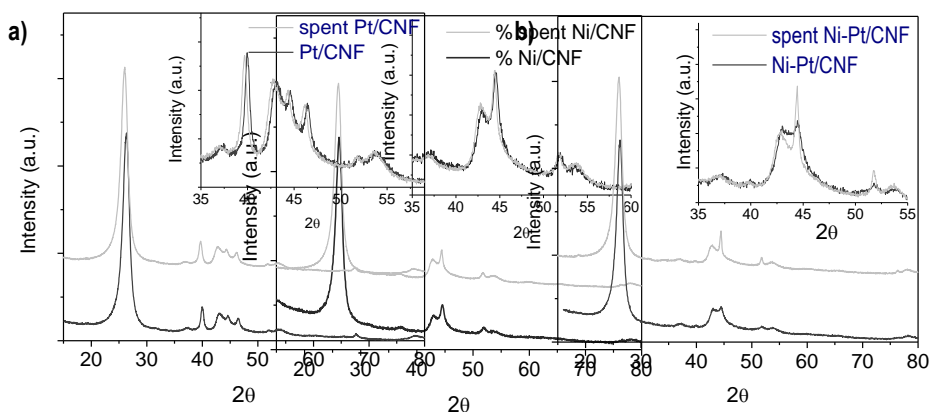


Figure 4.22 Comparison between XRD signal of fresh and spent Ni-Pt/CNF catalysts before and after the reaction

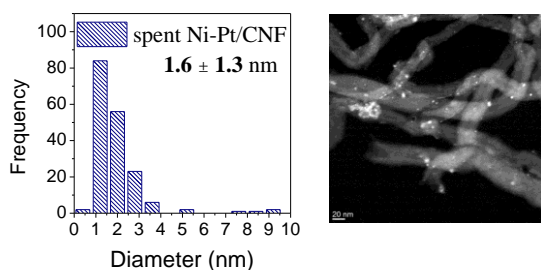
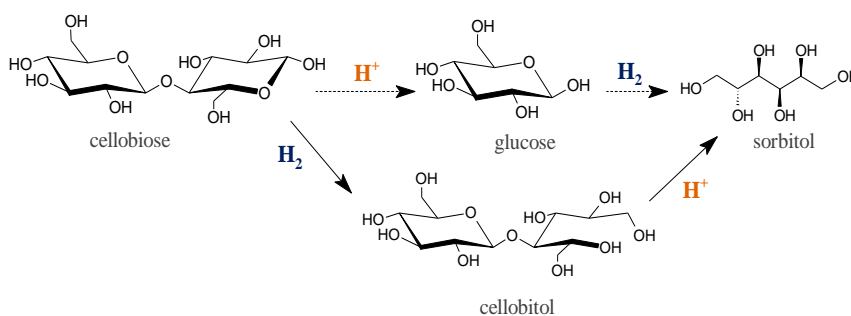


Figure 4.23 HRTEM micrographs and derived histogram for spent Ni-Pt/CNF catalyst.

d) Reaction pathway

The most widely accepted scheme to describe the one-pot conversion of cellulose (cellobiose) involves an initial hydrolysis stage to glucose and the subsequent hydrogenation to sorbitol (Scheme 4.4) [141]. This reaction sequence was inverted under current experimental conditions and the cellobitol becomes the main intermediate compound as a result of a modest hydrolysis rate. In kinetic modeling and mechanistic studies published by Palkovits *et al.*, it is stated that both reaction pathways compete to each other before sorbitol delivering, whose relative importance can be controlled through changes on the reaction temperature, catalyst loading or acid strength. Accordingly, catalytic conversion of cellobiose over supported metal particles (Ru/AC) and silico-tungstic acids preferentially occurred via cellobitol formation at 120 °C while an increase on the reaction temperature to 170 °C favored the direct hydrolysis of cellobiose [246]. Likewise, a possible exchange in the reaction order by thermal effect was assessed using Ni-Pt/CNF as the catalyst.



Scheme 4.4 Alternative reaction pathways in the cellobiose conversion into sorbitol (adapted from [246] and [262]).

As it is displayed in Figure 4.24, an increment in the reaction temperature from 180 to 200 °C accelerated the formation rate of sorbitol from cellobitol. In this case, the speedy breakage of α -glycosidic bonds is highly likely related to a larger amount of hydronium species, sourced from the shift on the water autohydrolysis equilibrium with temperature [77]. Yields of sorbitol of

44.4, 60.6 and 65.4 % were reached at the end of the test at 180, 190 and 200 °C, respectively (Table 4.8). The maximum productivity in this compound (73.7 %) was attained at 200 °C after 1.5 h, which undergoes consecutive degradation reactions to smaller polyols (xylitol, erythritol and glycerol) at prolonged contact times. Side-reactions of glucose were simultaneously promoted at higher temperatures and products such as levulinic acid were more readily formed (8.4 %). In any case, the transformation mechanism via cellobitol stands as the dominant reaction pathway.

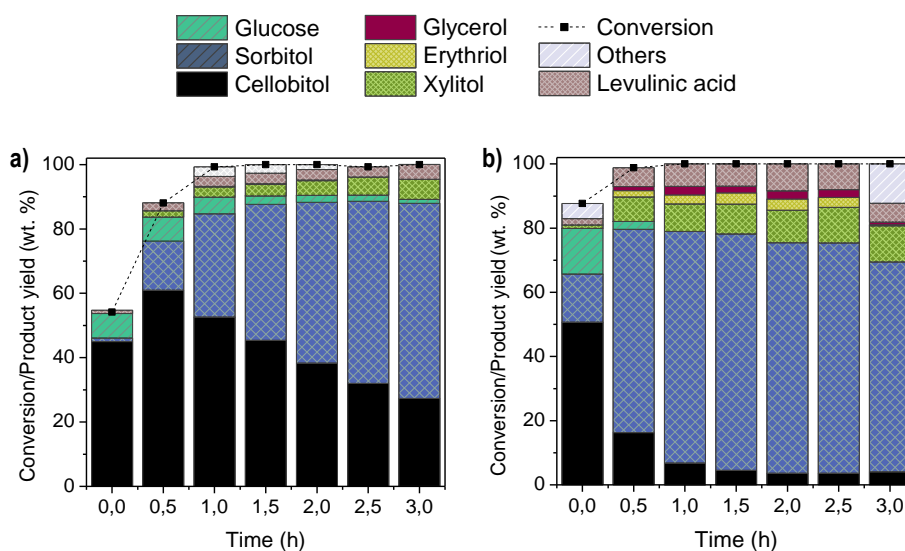


Figure 4.24 Temperature effect on product distribution using Ni-Pt/CNF: a) 190 °C and b) 200 °C.

Table 4.8 Cellobiose conversion and products distribution over Ni-Pt/CNF catalyst after 3 h of reaction at various temperatures.

Temp. (°C)	X (%)	Y _{PRODUCTS} (mass %)							
		Glucose	Levul. Acid	Sugar alcohols ^[a]					Others
				C12	C6	C5	C4	C3	
180	99.9	1.1	2.6	47.2	44.4	4.2	n.d	n.d	0.4
190	100	1.2	4.6	27.3	60.6	6.2	n.d	n.d	0.1
200	100	n.d	5.8	4.1	65.4	11.2	0.3	0.8	12.4

[a] C12=cellobitol, C6=sum of sorbitol and mannitol, C5=xylitol, C4= erythritol, C3=glycerol

4.3.2 HYDROLYTIC HYDROGENATION OF CELLULOSE

So far, the work described in this Chapter has been focused on the optimal metal function of the catalyst that ensures its hydrogenation ability. The remainder of this section highlights several aspects controlling the hexitols selectivity when cellulose is used as substrate, from crystalline nature to its reactivity under various operating conditions. The full set of experimental conditions studied is listed in Table 4.1 and briefly recalled in Table 4.9. To address this issue, the former Ni/CNF_{DI} was selected, a catalyst in the middle ground between the metal surface availability (11.3 nm, 10.7 wt. % Ni) with relative high resistance against surface oxidation (9.53 at. % Ni⁰). A back-to-back comparison with Ni/CNF_{DP} (14 wt. %) suggests that a Ni overload of 3.3 wt. % is perhaps not supported by a net gain in sorbitol of 3.9 %. On the other hand, the use of catalyst based on Ni-Pt/CNF alloy rendered sorbitol percentage always below than that obtained from Ni/CNF_{DI}.

4.3.2.1 Effect of pre-treatment, time and temperature reaction on cellulose conversion and products distribution

The influence of reaction time, temperature and cellulose crystallinity was disclosed at a fixed H₂ pressure of 4.0 MPa (RT), according to the experimental design defined in Table 4.1. The three variables showed a strong impact on cellulose conversion, product range and selectivity as later is discussed. A detailed account of the product distribution for each condition is included in Table 4.9.

**Table 4.9** Catalytic conversion of cellulose over Ni/CNF_{DI} under 4.0 MPa H₂.

	1	2	3	4	5	6	7	8	9	10	11	12	13	14	15	16	17	18
Conditions:																		
Cellulose (CrI)	78	78	0	0	0	78	0	78	37.5	37.5	37.5	37.5	0	78	37.5	37.5	37.5	37.5
Temp. (°C)	190	190	190	190	230	230	230	230	210	210	210	210	210	210	190	230	210	210
Time (h)	3	26	3	26	3	3	26	26	14.5	14.5	14.5	14.5	14.5	14.5	14.5	14.5	3	26
Conversion (wt. %)	11.7	47.5	37.9	88.7	97.1	85.0	100	100	94.4	95.6	95.5	96.3	98.9	82.6	63.7	99.7	66.3	99.4
Product yield (wt. %)																		
Cello-oligomers	3.6	8.6	19.5	15.1	0.8	10.1	0.7	0.4	2.3	4.8	5.7	0.8	1.8	20.9	10.0	0.3	11.2	6.5
Glucose	0.6	1.1	3.5	<1.d	1.1	0.9	1.8	1.0	1.1	1.3	1.6	1.1	1.9	0.8	2.1	2.3	1.3	2.0
Sorbitol	1.5	7.3	9.5	35.5	15.5	15.7	7.8	7.2	10.1	22.5	20.0	10.5	24.8	12.8	22.5	12.9	26.6	18.5
Mannitol	0.9	1.5	0.9	2.1	3.2	1.3	0.2	<1.d	0.1	1.9	2.3	3.0	2.5	1.8	1.6	1.8	1.7	<1.d
Xylitol	0.7	2.6	2.1	8.6	10.1	6.9	6.1	4.3	7.3	7.8	8.7	7.2	8.9	6.4	5.7	7.3	7.3	7.4
Erythritol	<1.d	<1.d.	<1.d	2.3	8.4	5.8	10.7	9.6	6.5	6.9	5.5	7.3	6.5	4.3	0.8	9.5	2.1	7.4
1,2 PG/Glycerol	<1.d	0.3	0.2	0.7	2.4	1.7	0.1	5.0	2.6	2.9	2.0	3.6	1.6	1.5	0.4	5.0	0.5	2.3
EG	0.9	<1.d	<1.d	1.4	3.8	2.8	<1.d.	7.1	3.8	4.1	3.2	5.7	2.2	2.8	<1.d.	6.6	<1.d.	2.8
1,2 alkanediols*	0.1	0.3	0.2	2.1	5.5	4.6	1.0	10.9	7.1	7.4	5.0	10.7	3.3	4.5	0.3	10.4	0.7	4.6
CO ₂	0.2	0.4	0.2	0.5	1.7	1.2	1.9	1.7	0.4	1.3	1.0	2.0	0.6	0.7	1.3	3.0	0.5	0.6
Others	3.2	25.4	1.8	20.4	44.6	34.0	69.7	52.8	53.1	34.7	40.5	44.4	44.8	26.1	19.0	40.6	14.4	53.8

*including 1,2 hexandiol, 1,2 pentanediol and 1,5 pentanediol, 1,4 butandiol and 1,2 butanedio

As evidenced in Figure 4.25-a, the polymeric and crystalline structure of cellulose makes it much more resistant towards hydrolysis than cellobiose. As a matter of fact, only a modest 11.7 % of conversion was obtained from raw cellulose after 3 h at 190 °C (Run 1), which started to be partially depolymerised into soluble cello-oligomers with shorter chain length (3.6 %). The conversion of microcrystalline cellulose remained rather low (47.5 %) even upon extending the reaction time to 26 h (Run 2), yielding cello-oligomers (8.6 %) and small percentage of sugar alcohols (11.8 %; including 8.8 % of sorbitol and 2.6 % of xilitol) as main products.

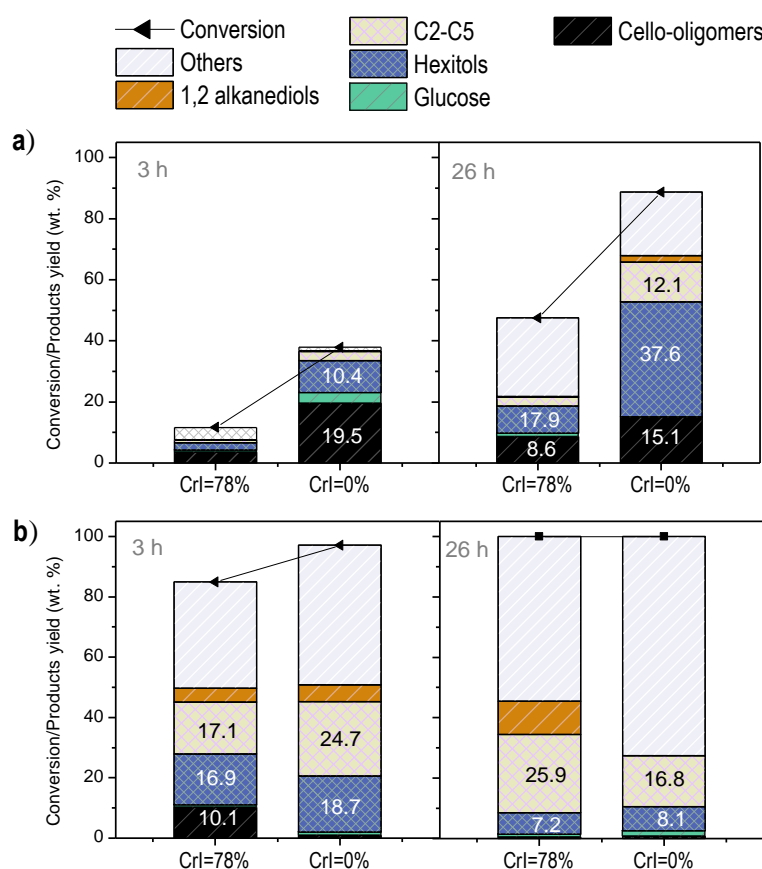


Figure 4.25 Catalytic results as a function of reaction temperature, time and cellulose crystallinity a) 190 °C and b) 230 °C.

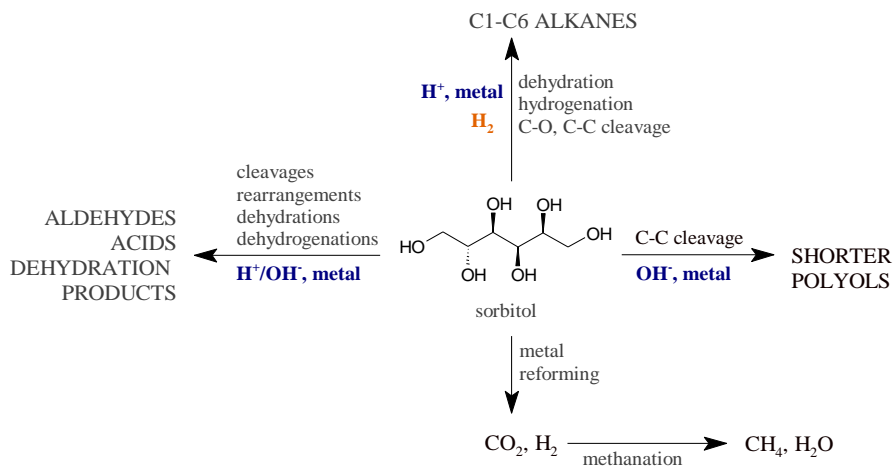
The aforesaid data evidence how mild hydrothermal environment hardly influences the transformation of highly crystalline cellulose. It is indeed at these conditions when the dissolution-conversion of cellulose may benefit from the use of ball-milling. As already introduced in Chapters 1 and 3, the ball-milling enhances the accessibility and reactivity of cellulose through the disruption of its crystalline structure, giving rise to an overall increase on



the reaction rate. Catalytic results before and after ball-milling (8 h, 600 rpm) were compared in the Figure 4.25. As it can be seen, conversion of ball-milled cellulose (amorphous) proceeds faster than microcrystalline (37.9 and 88.7 % after 3 and 26 h of reaction, respectively). In addition, the formation of sugar alcohols becomes apparent from the earliest stages of the reaction (12.7 % after 3 h) to reach around 50.7 % at the end of 26 h (Run 3, 4). This term encloses 37.6 % of C6-sugar alcohols and a variety of polyhydric alcohols such as xylitol (2.3 %), erythriol (8.6 %) and low carbon glycols (2.2 %, sum of 1,2-propylenglycol and ethylenglycol) that come from two parallel pathways, involving the rupture of glucose backbone followed by hydrogenation and/or via hydrogenolysis reactions of sorbitol (*vide infra*).

To accelerate the reaction rate, heating at higher temperatures is usually effective [64, 265]. The positive kinetic effect can be explained from a down shift on the ionic product of water with temperature, yielding a pool of H_3O^+ ions that readily diffuse into the cellulose molecule and facilitate the activation of the glucosidic linkages [77, 266, 267]. By these means, most part of microcrystalline cellulose was already converted within 3 h at 230 °C (Figure 4.25-b). Also, there are no major differences on cellulose conversion between the crystalline form (85.0 %) and the amorphous state (97.1 %), likely due to a weakening on the hydrogen bond network at elevated temperature (Run 5, 6). However, the contribution of subcritical water to enhance the hydrolysis of cellulose cannot be considered a selective route for sorbitol production, at least at the residence time here studied, as it severely increases the number of secondary side-reactions, limiting the yield to 16.9 -18.7 % after 3 h of reaction but not being stable for a long period of time. After 26 h of reaction, only 7.2-8.1 wt. % of hexitols was recovered in favor to a large spectrum of degradation products, including small quantities of shorter polyols. The sum of C2-C5 products ranged between 17.1-24.7 wt. % in the 3 h-run and remained fairly constant after 26 h. Table 4.9 lists the specific distribution of such products (Run 5-8). Apart from sugar alcohols, a family of 1,2 alkanediols (deoxy polyols) was quantified, involving 1,2 hexanediol, 1,2-pentanediol and 1,2-butanediol whose amount did not exceed the 5.5-4.6 % at the initial stages and slightly rose to 10.9 % at the end of the reaction from non-treated cellulose. Overall,

the mass balance closed at around 19.4-31.1 % upon 26 h, which evidenced that a rather low carbon utilization of the starting cellulose can be achieved. Scheme 4.5 gives an overview of plausible routes of sorbitol degradation at high temperature.



Scheme 4.5 Sorbitol degradation pathways at high temperature and in the presence of metal catalysts (Source: [64]).

The above experimental analysis recognize the convenience of working at milder conditions (190 °C) and longer residence times (26 h) for the selective transformation of cellulose to hexitols. That required the use of a prior pre-treatment of cellulose to reach reasonable reaction rates. At this point, a series of additional experiments was performed to evaluate combinatorial possibilities at intermediate reaction conditions.

The influence of pre-treatment duration was disclosed over cellulose samples with different crystallinities at 210 °C for 14.5 h (Figure 4.26, Run 9-12, 13, 14). A progressive decrease on the crystalline index (CrI) from 78 to 37.5 and 0% led to better results on both conversion and yield. In terms of conversion, the most significant difference was noted for non-treated cellulose with a 84.6 % conversion (lower than ball-milled cellulose) and rendering a products spectrum primarily composed by large oligomers (30.1 %). Intriguingly, no important changes were discerned between the amorphous material and the partially crystalline one (CrI=37.5 %), showing similar conversion rates (98.9 and 95.5 %) and oligosaccharides percentages (13.0 and 10.1 %). However, the yield in hexitols remained higher from amorphous cellulose (27.3 %

compared to 19.9 % for cellulose CrI=37.5 %). These results underline once more the importance of diffusional aspects on cellulose catalytic transformation under heterogeneous conditions. Thus, a high accessibility of cellulose becomes essential for the effective contact with metal catalyst, allowing for the rapid hydrogenation of glucose units which otherwise will be thermally degraded.

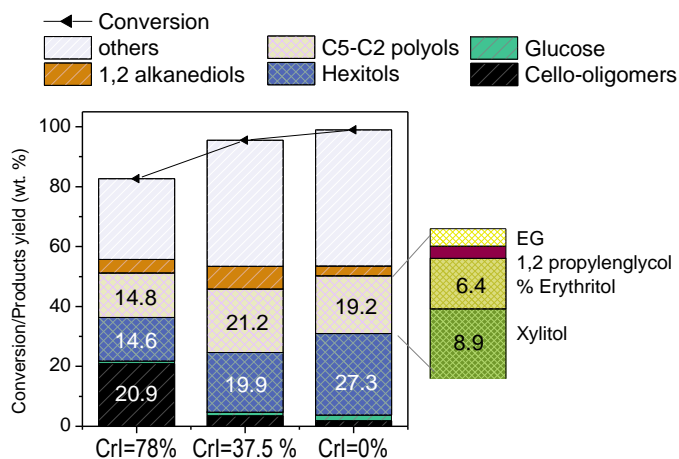
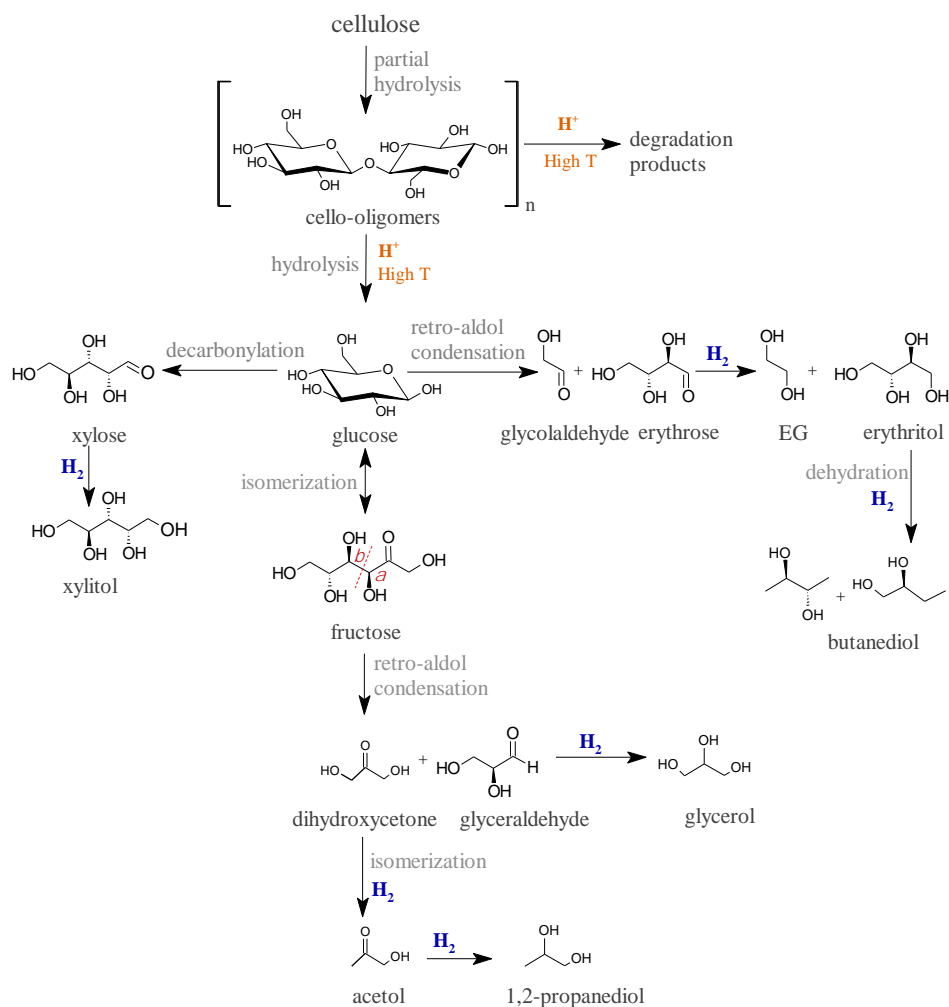


Figure 4.26 Influence of cellulose crystalline degree on catalytic conversion at 210 °C and 14.5 h.

The main reactions occurring under these circumstances are based on the retro-aldol condensation of sugars to aldehydes and ketones through β -C-C bond scissoring [268]. The retro-aldol reaction of glucose generates glycolaldehyde (C2) and erythrose (C4), which are then hydrogenated into ethylenglycol and erythriol. If glucose is first isomerized to fructose, then 1,2 propanediol and glycerol are formed with dihydroxyacetone (C3) as intermediate compound (Scheme 4.6). These compounds may subsequently undergo dehydration or hydrogenation routes to yield a mixture of deoxygenated compounds as it was attested by small percentages of 1,2 alkanediols (7.5 and 3.3 % from cellulose with CrI=37.5 and 0%, respectively).



Scheme 4.6 Reaction routes for glucose degradation in presence of hydrogen and metal catalysts (Adapted from [269]).

Trends arising from products distribution with temperature were investigated for cellulose with 37.5 % of crystallinity and at a residence time of 14.5 h (Figure 4.27, Run 9-12, 15, 16). Rather predictable, the use of high temperature facilitated the hydrolysis step which is reflected by a gradual increase on the cellulose conversion from 63.7 to 95.5 and 99.7 % when working at 190, 210 and 230 °C, in that order. The fraction of cello-oligomers simultaneously decreased from 10.0 % at 190 °C to negligible amounts of 3.4 and 0.3 % at 210 and 230 °C, respectively. Nonetheless, an increase on the operating temperature had a detrimental effect on the hexitols selectivity, likely due to a worse solubility of hydrogen gas in the aqueous phase (clearly adverse in hydrogenation reactions) and the product instability at relatively harsh conditions. As a consequence, the hexitols yield declined from 24.1 down to 19.9 and 14.7 % whereas low

carbon polyols are proportionally accumulated. The percentage of these compounds, barely accounting to 6.9 % at 190 °C, rose to 21.2 % at 210 °C and up to 28.4 % at 230 °C. A representative distribution of different polyol for 230 °C is shown in the Figure 4.27, comprising xylitol, erythritol, glycerol and ethylenglycol in almost equal proportions by mass (7.3, 9.5, 5.0 and 6.6 %, respectively).

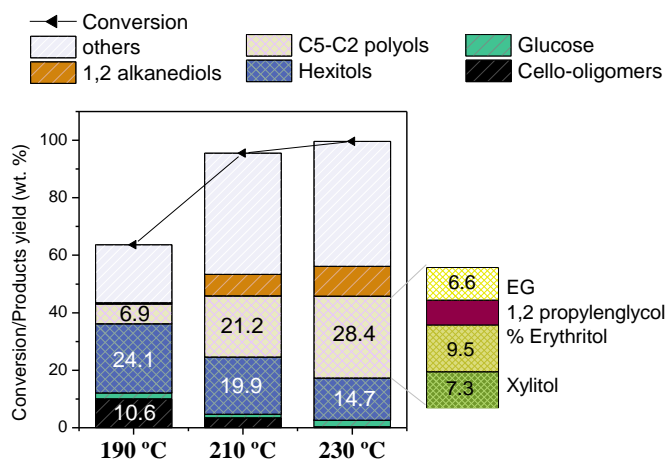


Figure 4.27 Influence of reaction temperature on the catalytic conversion of cellulose (CrI=37.5 %) after 14.5 h.

The instability of the hexitols at 210 °C could be confirmed from their temporal evolution profile (Figure 4.28, Run 9-12, 16, 18), pointing to catalytic cracking of hexitols into smaller alcohols as one of the primary routes for products degradation above 190 °C.

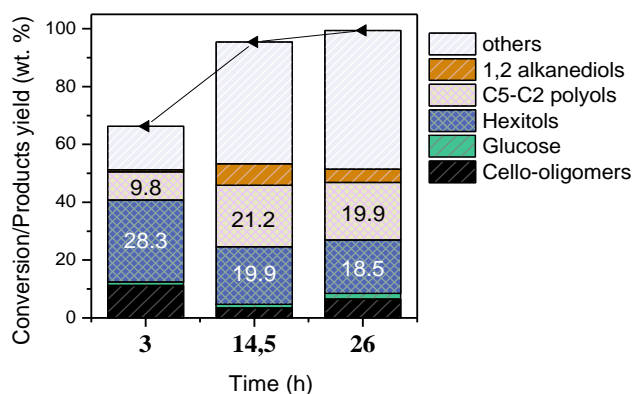
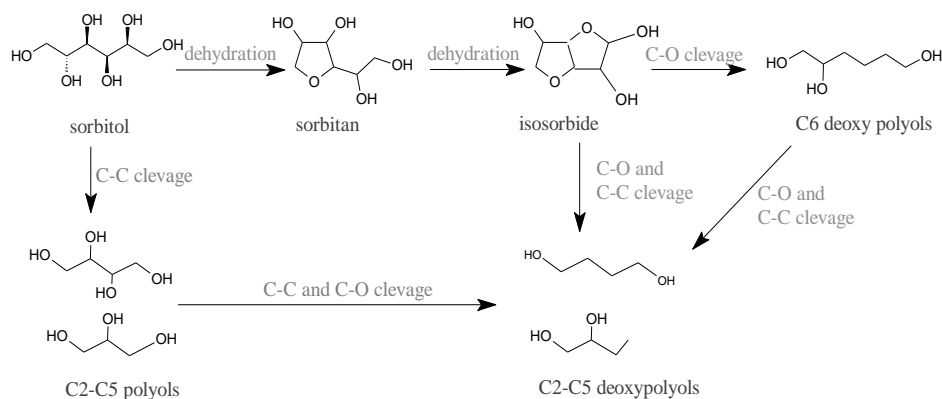


Figure 4.28 Conversion profile of cellulose (CrI=37.5 %) at 210 °C

Mechanistically, these reactions take place through various steps, whereby sorbitol is first dehydrated to sorbitan and isosorbide and successively converted into various C1 and C5

compounds through hydrogenolysis/dehydroxylation reactions. The C-O cleavage occurs by dehydration routes whereas C-C cleavage reaction goes throughout retro-aldol condensation of the unsaturated intermediate [214]. The most common products resulting from hydrogenolysis of sorbitol are illustrated in Scheme 4.7 [6].



Scheme 4.7 Major reaction pathways of sorbitol hydrogenolysis (Source: [6]).

4.3.2.2 Statistical analysis and model fitting

From dataset results, an empirical model was developed to make predictions of catalytic activity within the range of operational conditions used on this work. The latter was made following the response surface methodology (ANOVA). This tool of statistical analysis relates the process variables, namely, cellulose crystallinity (Cr), temperature (T) and reaction time (t) with a given response variable, taking into consideration their individual influence (linear and quadratic effects) and all possible interactions between them. The polynomial expression that describes the model can be generalized as the equation [4.4]:

$$y = \beta_0 + \sum_{i=1}^k \beta_i x_i + \sum_{i=1}^k \beta_{ii} x_i^2 + \sum_{i < j} \beta_{ij} x_i x_j \quad [4.4]$$

In this expression, y is the desired response variable, β_0 and β_i stand for the independent term and the regression coefficients whereas x_i refer to the independent variables (e.g. Cr, T, t). In order to estimate the effect of process variables in equal terms, their lower and upper limits were normalized from -1 to +1. The coded equation not only can be useful to make predictions about



the response but also is informative about the relative impact of the variables by comparison of their coefficients.

The three variables chosen as response were cellulose conversion, yield of hexitols and short-chain polyols (C2-C5). For each response variable, a model fitting and the analysis of significance within 95 % confidence (p-value=0.05) was performed. The values of the coefficients determined for the regression model as well as some of the statistical parameters are tabulated in Table 4.10. The analysis of variance (ANOVA) for the response surface model indicated that all model terms are statistically significant, showing p-value below than 0.05. The goodness of fit was additionally validated by a regression coefficient (R^2) close to unit in all the cases ($R^2=0.999$, 0.960 and 0.989 for cellulose conversion, yield of hexitols and C2-C5 polyols) and no significant lack of fit (p-value residual > 0.05). The p-value of lack of fit was 0.1124, 0.3320 and 0.222 for cellulose conversion, yield of hexitols and C2-C5 polyols, respectively. It can be inferred, therefore, that the regression model truly represents the relationship between the responses and the independent variables within the conditions range of this research. The visualization of response surfaces can be found in Figure 4.29-31.

Table 4.10 Analysis of variance for response surface model

Response	R ²	Indep. Term	A T	B T	C Cr	A ²	B ²	C ²	AB	AC	BC	ABC	A ² B	AB ²	A ² B ²
Conversion ± 1.26 (%)	0.9993	95.45	17.95 (10.64)	16.55 (25.91)	-9.50 (16.09)	-13.80 (7.92)	-12.60 (3.57)	-4.70 (2.42)	-8.69 (9.94)	6.81 (7.06)	n.s.	3.46 (3.42)	-3.39 (0.37)	6.66 (9.13)	6.56 (3.54)
Hexitols yield ± 2.76 (wt. %)	0.9597	23.21	-1.77 (12.71)	-4.90 (2.05)	-5.20 (13.94)	-5.30 (7.86)	n.s.	-3.75 (6.44)	-6.76 (1.83)	4.26 (11.00)	-2.49 (23.83)	2.69 (10.08)	6.56 (10.25)	n.s.	n.s.
C5-C2 polyols yield ± 1.59 (wt. %)	0.9891	21.25	10.75 (11.33)	5.05 (26.81)	-1.37 (11.28)	-3.60 (1.45)	-6.40 (6.37)	-4.25 (4.85)	-1.39 (8.82)	1.54 (1.12)	n.s.	3.29 (5.69)	-3.44 (0.80)	-2.69 (21.17)	6.06 (0.32)

Numbers in brackets represent the relative influence of each variable (%) according to Pareto chart.

$$Response = \beta_0 + \beta_1A + \beta_2B + \beta_3C + \beta_4A^2 + \beta_5B^2 + \beta_6C^2 + \beta_7A \cdot B + \beta_8A \cdot C + \beta_9B \cdot C + \beta_{10}A \cdot B \cdot C + \beta_{11}A^2 \cdot B + \beta_{12}A \cdot B^2 + \beta_{13}A^2 \cdot B^2$$

A= temperature; B=time and C=crystallinity; n.s:no significative with an interval of confidence of 95%.

As seen from Figure 4.29, cellulose conversion gradually increases with reaction time and temperature even when reaction rate slow down at higher degrees of crystallinity. The former means that more severe conditions are required for the entire transformation of untreated samples. For instance, the whole conversion of amorphous cellulose is reached in 15.8 h at 206.8 °C whereas 24.4 h and 227.1 °C will be necessary to degrade crystalline cellulose completely (99.0 %). The impact of independent variables on cellulose conversion, based on the Pareto charts, ranked in the following extent: residence time (25.9 %), crystallinity degree (16.1 %) and reaction temperature (10.6 %). Afterwards, the linear and quadratic interaction of reaction time with temperature was equally important (9.94 and 9.13 % in $T-t$ and $T-t^2$, respectively).

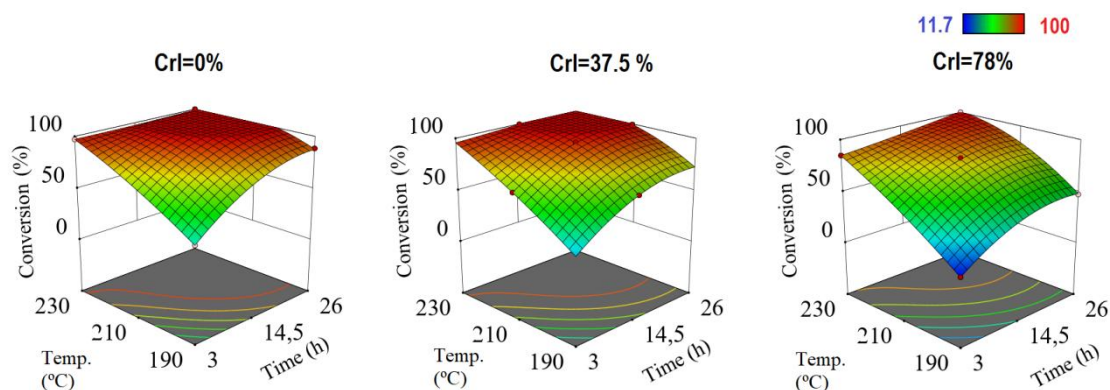


Figure 4.29 Response surface for cellulose conversion from samples with different crystallinities.

Variations of hexitols yield at different conditions were graphically illustrated in Figure 4.30. As shown, the model predicts a stepped decline as the degree of cellulose crystallinity increases. Irrespective of the starting material, the response surface plot depicts the same turning point at 210 °C for short-time runs (3 h). So, the proportion of hexitols at low contact times increases with increasing process temperature from 190 to 210 °C whereas a further elevation on these conditions causes a drastic yield decrease in favour of shorter polyols (C2-C5). The effect of reaction time was strongly dependent on reaction temperature. At mild conditions (190 °C), the hexitols yield linearly increase on time. The magnitude of these variations is more marked on amorphous than untreated cellulose (remaining likely unchanged). An opposite tendency was

observed at temperatures above 200 °C, indicating degradation pathways of hexitols. The detailed impact of these variables and the most meaningful interactions on hexitols production are summarized in Table 4.10. Almost similar contributions were determined for cellulose crystallinity and reaction temperature (13.94 and 12,71 %, respectively) whereas the reaction time seems to have lower impact on the model (2.05 %). Nevertheless, the most significant influence on the general equation was exerted by the linear interaction between cellulose crystallinity and time (variable t-Cr, 23.83 %) and to a lesser extent the combined factors T-Cr (11.00 %), T^2 -t (10.25 %) and T-t-Cr (10.08 %).

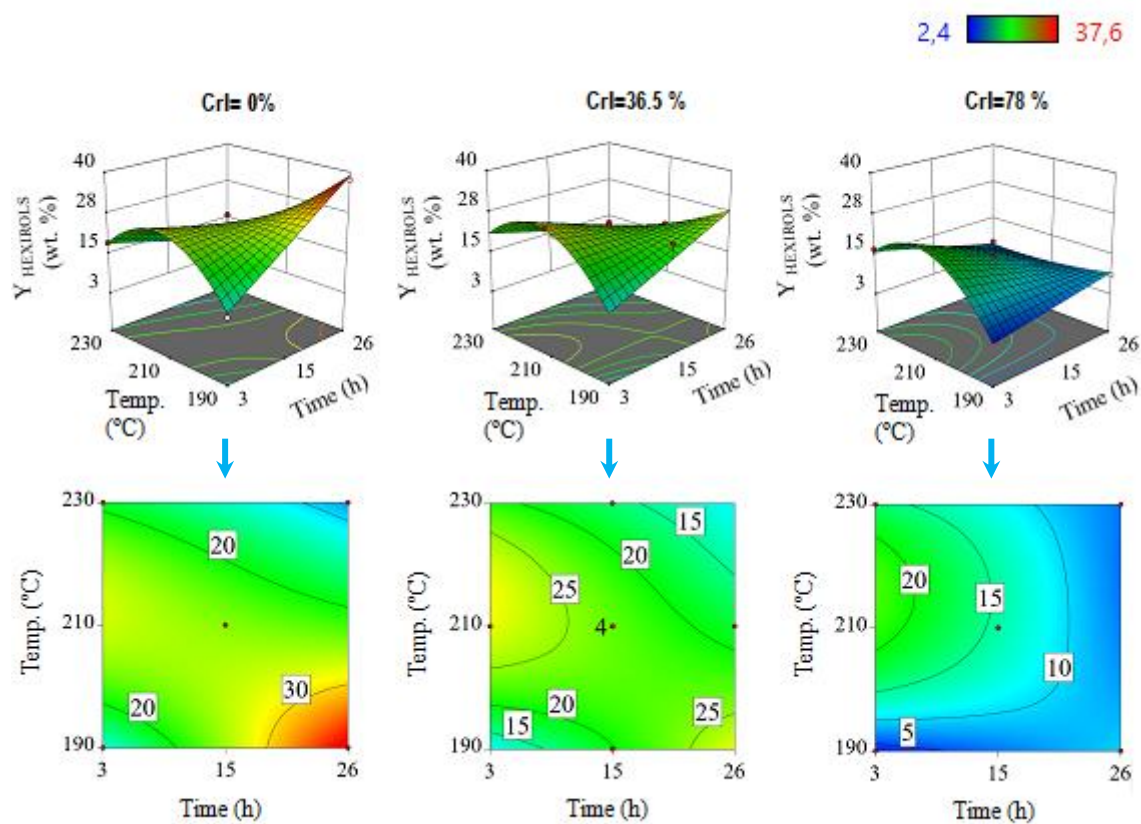


Figure 4.30 Response surface and contour plot of hexitols yield obtained from cellulose with different crystallinities.

In quantitative terms, the hexitols yield ranged from 3.48 to 39.0 wt. % with a deviation standard of 2.76. The best value was attained from amorphous cellulose at the lowest temperature (190 °C) and longest residence time (26 h) of the experimental plan. Based on statistical calculations, such operational conditions should coincide with optimal scenario to produce the maximum theoretical yield of hexitols (38.99 % at 87.92 % of cellulose



conversion), working under unlimited conditions of ball-milling duration or reaction time. However, a closer look on the contour plots reveals that some other runs can be conducted at a considerable shorter timeframe, either by reducing the duration of reaction or the previous pre-treatment, without strongly sacrifice on yield. One of the most conservative possibilities relies on the amorphous cellulose treatment at 190 °C during a shorter time length (19.6 h) at the expense of a small decrease on the hexitols fraction (31.4 %). A more pragmatic solution but comparatively less ambitious is the synthesis of 26 % of hexitols from amorphous cellulose after only 3 h at 205.6 °C. Alternatively, a combined optimum that maximizes the production of hexitols (23.3 %) at minimal duration of ball-milling pre-treatment (2.54 h) could be achieved when processing cellulose with 31.75 % of crystallinity at 213,4 °C for 14.9 h. Fairly close results (20.54 % of hexitols) are expected from a crystalline index of 44.46 % (milling time of 1.52 h) upon 13 h at 222.3 °C.

As extensively outlined above, shorter polyhydric alcohols (C2-C5) arise from two main degradation pathways, namely, retro-aldol reactions of intermediate sugars and hydrogenolysis of hexitols fostered from 210 °C onwards. Both contributions converge at a maximum value of 28.4 % obtained from semi-crystalline cellulose after 14.6 h at 230 °C (Figure 4.31). At this point, the total of sugar alcohols (including hexitols) reaches 43.2 % at a level conversion of 99.6 %. According to the Pareto estimations, the most influential independent variable was the residence time, with a relative contribution (26.81 %) more twice than cellulose crystallinity (11.28 %) and reaction temperature (11.33 %). Afterwards, the interaction $T-t^2$ was particularly noteworthy (21.17 %).

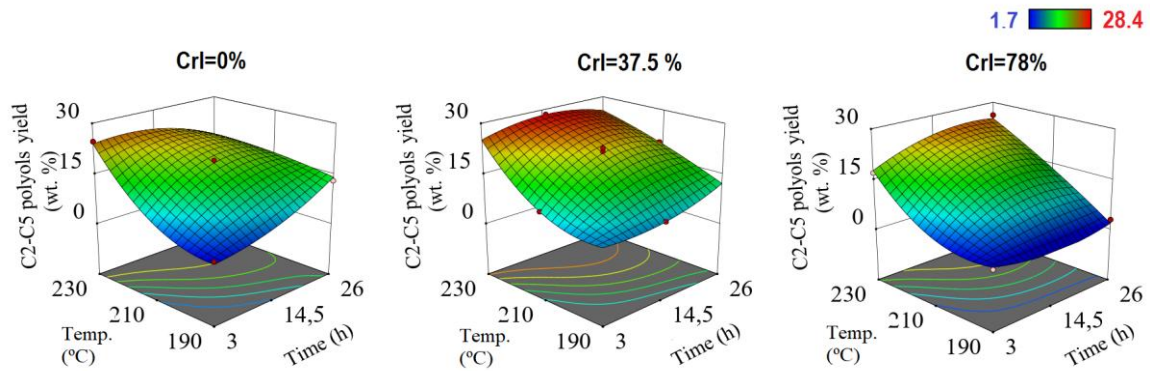


Figure 4.31 Response surface for the production of C2-C5 polyols obtained from cellulose samples with different crystallinities.

To sum it up, Table 4.11 compiles four main scenarios built for the theoretical reaction optimization, targets and the optimal solution that satisfies the criteria.

Table 4.11 Theoretical optimization: objectives, relative importance (from 1 to 5) and the optimal solution predicted by the model (operational conditions and response variables).

	Cellulose crystallinity ^[a] (%)	Temp. (°C)	Time (h)	Cellulose conversion (°C)	Y _{HEXITOLS} (wt. %)	Y _{C2-C5 POLYOLS} (wt. %)
Scenario 1						
Target	None	None	None	Max.	Max.	Min.
Importance				2	5	2
Solution	0	190	26	87.9	39.0	14.2
Scenario 2						
Target	Max.	None	None	Max.	Max.	Min.
Importance	5			2	5	2
Solution	78	216.4	3	63.5	22.5	7.3
Scenario 3						
Target	None	None	None	Max.	None	Max.
Importance				2		5
Solution	38.5	230	14.6	99.6	16.1	28.4
Scenario 4						
Target	None	None	None	Max.	Máx.	Max.
Importance				2	5	5
Solution	27.9	220.1	12.4	100	22.6	24.9

^[a] Inversely correlated with the ball-milling duration



4.3.2.3 Effect of H₂ pressure

As already discussed, the successful conversion of cellulose into sorbitol is largely conditioned by the initial rate of hydrogenation. This is because unsaturated acid aldehyde must be immediately hydrogenated or else degradation reactions occur. However, even starting from a substrate highly accessible (amorphous) and using a catalyst with proved hydrogenation ability; the maximum yield of hexitols from cellulose was still modest (37.6 %). Besides, the formation of by-products was significant (20.6 %). In this context, a final set of experiments was performed to determine whether H₂ pressure may alter the product distribution by working under suboptimal conditions. From a theoretical viewpoint, catalytic hydrogenation of sugars involves a three-phase catalytic system, in which H₂ gas is first solubilized in aqueous phase and then diffuses to the liquid-solid interface of the metal catalyst. Activated H species finally interact with the hemiacetal group of sugars on the external surface of the support [213, 270]. On this layout, hydrolytic hydrogenation of cellobiose does not ensure the absence of diffusional effects but only neglects the lack of gas-liquid mass transport limitations. The extrapolation of the reaction to bulk cellulose might witness certain liquid-solid mass transfer limitations of H₂ when large-size molecules are processed. This may be partially resolved with a large excess of molecular species (H^{*}) in the vicinity of the catalyst and the substrate, which is achieved by working at higher gas external pressure. In order to ascertain this issue, the initial H₂ pressure was gradually increased in the range of 4.0-8.0 MPa (Figure 4.32-a). An additional inlet of H₂ pressure markedly improved the yield in hexitols from 37.6 % (4.0 MPa) to 40.4 (6.0 MPa) and 54.3 % (8.0 MPa), revealing that hydrogenation of macromolecules like cellulose faces to severe H₂-diffusion internal resistances. Table 4.14 details the specific product distribution, with xylitol as the second major product (8.2-8.6 %) followed by erythritol (2.1-2.7 %).

In order to mitigate the internal mass-transfer limitations, an additional mix-milling of the catalyst and substrate for 30 min was carried out (Figure 2.32-b). In analogy to what occurred in Chapter 3 for the hydrolysis reaction, the practise of mix-milling eases concerns of H₂ gas

transfer in two ways. First, it promotes the production of water-soluble oligomers, which are more rapidly hydrolyzed. Secondly, a better contact between the cellulose and the solid catalyst allows the close proximity between different reacting species (i.e., catalyst, cellulose and the hydrogen species dissociated onto the metal surface) for the rapid hydrogenation of sugars. In effect, an additional mix-milling for 30 min enhanced the sorbitol production from 37.6 % to 52.9 % at 4.0 MPa H₂. Only after a supplemental mix-milling for 30 min at 8.0 MPa H₂, the sorbitol production reached yields as high as 61.5 % at 8.0 MPa H₂ (77.0 % of total sugar alcohols and 15.5 % of by-products).

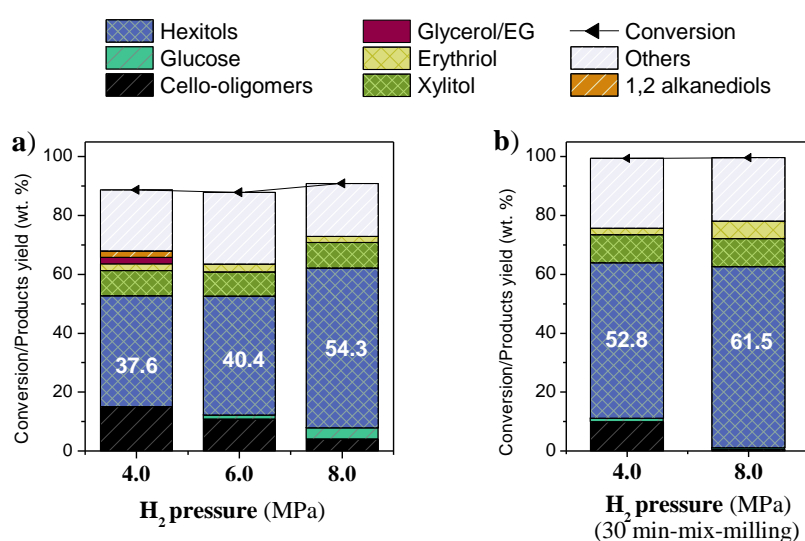


Figure 4.32 Effect of H₂ pressure on catalytic results (Reaction conditions: 190 °C, 26 h, amorphous cellulose).

Table 4.12 Influence of H₂ pressure on cellulose conversion and products distribution after 26 h at 190 °C.

H ₂ pressure (MPa)	X (%)	Y _{PRODUCTS} (mass %)							
		Cello-oligomers	Glucose	Sugar alcohols ^[a]					Others
				C6	C5	C4	C3	C2	
4.0	88.7	15.1	< l.d.	37.6	8.6	2.3	2.2	1.4	20.8
6.0	87.9	10.7	1.5	40.4	8.2	2.7	n.d	n.d	24.4
8.0	90.9	3.9	3.9	54.3	8.6	2.1	n.d	n.d	18.05
4.0 ^[b]	99.4	9.9	1.2	52.9	9.5	2.2	n.d	n.d	23.7
8.0 ^[b]	99.6	0.5	0.6	61.5	9.5	5.9	n.d	n.d	21.5

[a] C6= sum of sorbitol and mannitol, C5=xylitol, C4= erythritol, C3=1,2propanediol, glycerol, C2=ethyleneglycol

[b] after a supplemental mix-milling of 30 min



The best catalytic results of this Thesis were achieved from a mix-milled amorphous cellulose after 26 h at 190 °C and 8.0 MPa H₂, affording 61.5 % of sorbitol and 77.0 % of total sugar alcohols. This productivity compares with the highest data reported in the literature.



4.4 Conclusions

Hydrolytic hydrogenation mediated by CNF-supported Ni catalysts arises as a feasible route for cellulose valorisation, applying preparation procedures relatively easy and earth abundant metals. The rational control of products distribution, however, requires for a detailed understanding behind the operating conditions, catalyst composition and mass transport limitations. All these aspects can be individually studied by starting from feedstock with different polymerization degree and crystallinity.

Correlations between Ni metal loading (3-14 wt. %) and particle size (2.1-20.4 nm) were established using the *one-pot* conversion of cellobiose as hydrogenation test (190 °C, 3h). An optimum yield of sorbitol (81.2 %) was found from catalyst prepared by dry impregnation (10.7 wt. % of Ni, mean diameter of 11.3 nm). The ease oxidation of Ni at smaller particles sizes impedes the use of low-loaded catalysts with high metal dispersion. This tendency could be somewhat reverted when it was doped with small quantities of noble metals (Ni:noble metal=3:0.5 wt. %). Noble metals (Pd, Pt and Ru) induced changes on the size and dispersion of the Ni phase and favored the reductive conditions (H₂ spillover from noble metal to Ni), which was translated into an enhancement on their catalytic performance (higher number of exposed Ni sites for catalysis, suppression to deactivation by surface oxidation and a greater availability of active atomic hydrogen surrounding the metal particles to take part in the hydrogenation). Consequently, all bimetallic combinations (Ni-Pt, Ni-Pd and Ni-Ru) enhanced the Ni selectivity to hydrogenation products (91.6 %, 61.2 % and 84.5 wt. % of cellobitol and sorbitol), compare with a 32.9 % for Ni/CNF. Unlike to the Ni-Pt and Ni-Pd catalysts, which produced more sorbitol than either single metal constituents, the addition of Ni would not be justified in the case of Ni-Ru (3.0:0.5; wt. %), as a 0.3 wt. % of Ru is enough to completely hydrogenate the sugars by itself (92.4 %).

To further extent the conversion to cellulose feedstock, it was mandatory to adjust the experimental conditions to achieve reasonable conversion rates. High conversion degree (88.7

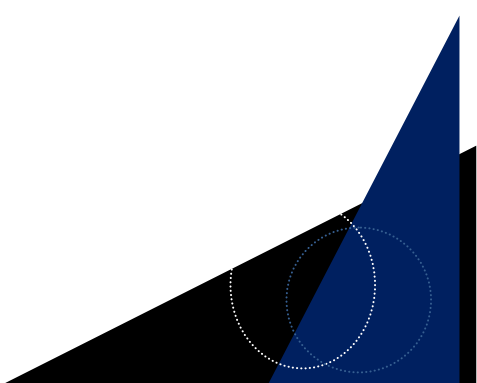


%) with low impact of secondary routes was attained from mild temperature (190 °C) and long residence time (26 h). The highest productivity of polyols (62.8 %; 37.6 % of hexitols) could be obtained from amorphous cellulose pre-treated by ball-milling. The pre-treatment of cellulose not only promote the dissolution and hydrolysis step but also enhance the contact with metal catalysts for its effective hydrogenation. This point becomes essential for preventing the cleavage reaction of (C-C and C-O) bonds from sugar intermediates. Further increase on the hydrogen pressure from 4.0 to 8.0 MPa of H₂ (RT) enabled to conquer plausible gas internal diffusional resistances, giving rise to an improvement on the sorbitol yield to 52.1 % (2.1 % of mannitol). After a supplemental mix-milling of only 30 min, a hexitols yield of 61.5 % was attained. Altogether, results present in this Chapter provide a unified picture of the chemistry involved in the hydrolytic hydrogenation of cellulose using Ni catalyst.



Chapter 5.

Catalytic valorization of the effluents generated during nanocellulose extraction from almond hulls: a biorefinery approach



Chapter 5.

Catalytic valorization of the effluents generated during nanocellulose extraction from almond hulls: a biorefinery approach

Abstract

Selective scissoring of cellulose into highly crystalline domains of nanometric scale from natural resources is gaining keen interest in the field of materials science. Besides, the implementation of catalytic technologies for further upgrading of all intermediate side streams would not only resolve the major waste disposal issues but also contribute to a better utilization of the starting feedstock.

In this Chapter, an example of a comprehensive use of biomass is depicted using almond hulls as raw material for the simultaneous recovery of a chemical-rich organic phase and sugar alcohols (mainly sorbitol and xylitol) in addition to cellulose nanofibrils as the prime product. In this scheme, several catalytic hydrotreatment technologies (hydrogenation and hydrodeoxygenation) were interconnected with proper separation and refining stages and annexed to the main production line. The new value chain demonstrates the feasibility of a biorefinery concept based on nanocellulose extraction from a real feedstock using already known chemical transformations for downstream processing. For this purpose, a supported ruthenium catalyst (Ru/CNF, 0.38 wt. %), previously validated in Chapter 4 for the hydrolytic hydrogenation of carbohydrates, was applied.

5.1 Introduction

To the stoics, the answer is turn something negative into an opportunity. This old adage can be quoted to describe the third strategy for cellulose utilization that closures this Thesis. Thus, the crystalline arrangement of cellulose, whereas it constitutes one of the major obstacles for its catalytic conversion, also endows it with outstanding mechanical properties. The modulus of elasticity for a perfect crystal of native cellulose has been estimated between 130 and 250 GPa, which is similar to Kevlar (100-124 GPa) and even stronger than steel (200-220 GPa), while the tensile strength was assessed in the range of 0.8-1.0 GPa [271, 272]. The stiffness and strength, combined with other genetic characteristics such as biodegradability, lightweight and low thermal expansion coefficient, have set the stage of novel applications of cellulose when it is isolated from the amorphous fraction and reduced to nanometric scale [273-275]. This kind of nano-sized cellulose is nowadays being regarded as a smart green material in many applications like papermaking, biomedical (drug delivery), environmental remediation, food packaging or materials science, either as a standalone material or as a reinforcement in composites [276, 277]. In addition, the high surface area and abundant hydroxyl groups open access to a unique platform for chemical modification, leading to an endless number of nanocellulose derivatives [51].

The hierarchical structure of cellulose enables its breakdown into different nanodimensional structures with various shapes and forms such as microfibrils, nanofibrils or nanocrystals (Figure 5.1). Following the TAPPI W13021 standard nomenclature, cellulose nanocrystals are described as rod-shaped particles with high crystallinity whereas cellulose nanofibers are longer segments that contain both amorphous and crystalline regions [278].

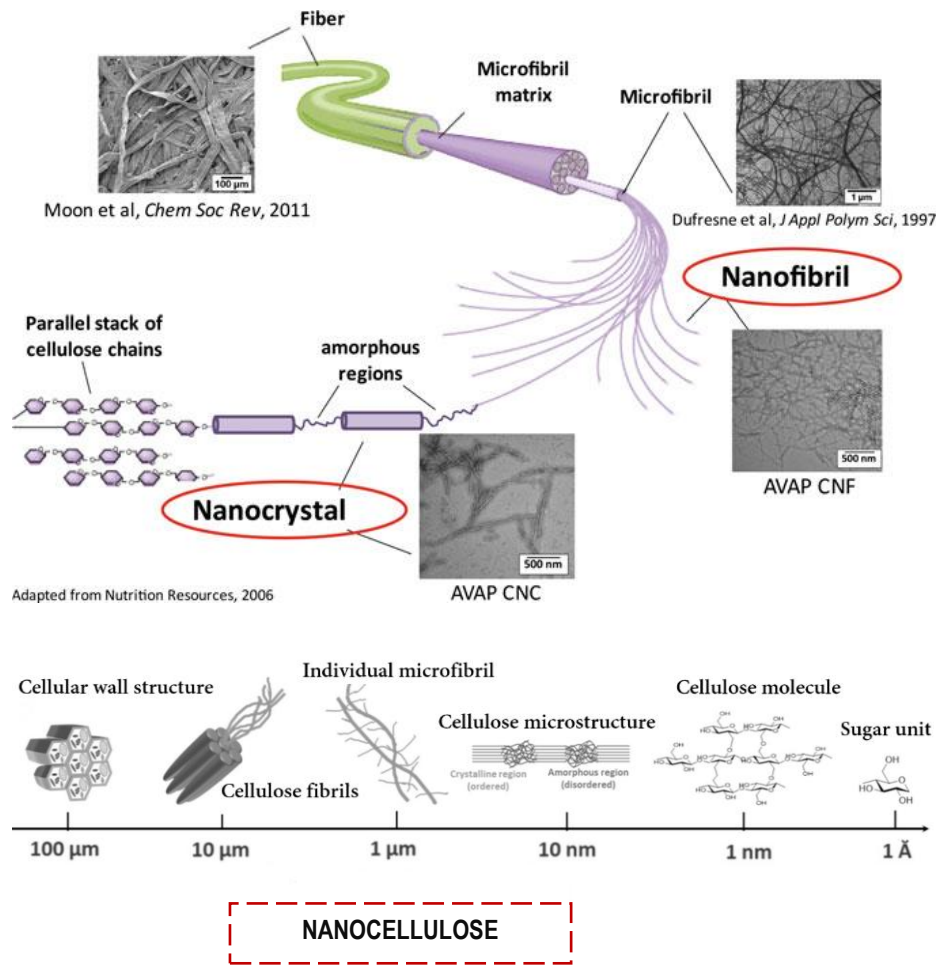


Figure 5.1 Hierarchical structure of cellulose fibers (Source: [279]).

Typically, the isolation of elementary fibrils is achieved by shear forces whereas acid treatment yield cellulose nanocrystals or whiskers [280]. Common mechanical techniques are high-pressure homogenization, micro-fluidization, micro-grinding, milling, cryo-crushing, electrospinning, centrifugal spinning and pressurized gyration. Besides, several chemical and enzymatic stages may be applied before defibrillation process to reduce the energy consumption and facilitate the release of more or less individualized fibrils. Some of these procedures include pulping and bleaching, hydrolysis (alkaline, acid and enzymatic), steam explosion or the introduction of charged groups through carboxymethylation or (TEMPO)-mediated oxidation [280, 281]. However, the use of these pretreatments is often time-consuming and the utilization of chemical reagents generates wastewater treatment issues and overall high expenses [282]. Another drawback of such methods is the degradation of the C6 fraction of hemicellulose, which is often disposed as a waste and reduces the carbon efficiency. Therefore, further

improvements on the extraction processes in terms of low cost, time-efficiency or reduced environmental footprint are worth being sought. A promising green alternative in this field relies on the selective hydrolysis of amorphous and semi-crystalline regions of cellulose in subcritical water. The exclusive use of water as hydrolyzing agent allows to work under high diffusion conditions within a process environmentally benign in nature (i.e., free additives, low corrosion, cleaner effluents and so on) [283]. Following this method, Novo *et al.* managed to degrade cellulose substrates into nanocrystals in the yield of 21.9 % after 60 min at 120 °C and 20.3 MPa [284]. Later, de Melo *et al.* reported a microwave-assisted hydrothermal method to produce simultaneously mesoporous nanocellulose fibrils and crystals from orange peel residues at relatively low temperatures (120-220 °C) and a shorter time frame (15 min) [285]. Shortly afterwards, the activation of biomass lignocelluloses by MW-radiation for nanocellulose extraction was extended to many other sources such as bamboo [282], citrus [286], ginger [287], pea haulm [288], banana stems [289] or peel and bract [290], to name a few. In these processes, the nature of the feedstock, MW processing conditions and pre-treatment exert a significant influence on the yield and properties of the resulting material. One of the key parameters is the yield, which is determined by the chemical composition of the starting material (cellulose portion) and the severity of hydrolysis conditions: too short treatment may lead to a poor reaction impact whereas long residence times or extremely high temperature prompt the cellulose structure destruction (polymorph conversion). Likewise, many other attributes such as morphology, crystallinity, thermal stability and mechanical behaviour are ruled by the extraction procedure and the cellulose source [291]. This fact makes mandatory a specific process assessment for obtaining cellulose nanomaterials with target properties from different raw materials.

Recently, much attention has been paid on the exploitation of different wastes derived from crop production and food industry as cellulose source, a sector that generates at around 1.3 billion tonnes of waste per year [292-294]. In one of such examples, Sulaeman *et al.* evaluated the production of microfibrilated (MFC) cellulose through a microwave-assisted hydrothermal



treatment from two alternative feedstocks, namely, cassava peel and almond hulls [295]. In that work, the influence of the pretreatment, using polar and non-polar solvents, and the microwave processing temperature (120-220 °C) on the yields and properties of MFC was well-established. Their study provides a facile method for the rapid and controlled production of advanced cellulose nanomaterials from non-edible resources. In the long term, however, the success of this process also depends on the integration of energetically efficient proposals together with optimal recovery of the other biomass fractions. To do so, searching for new valorization processes of side-streams becomes essential. The production of nanocellulose within a biorefinery scheme may contribute to reduce residues, add product flexibility and provide additional revenues.

Several biorefinery concepts may be referred to illustrate plausible fuels and chemicals co-product opportunities derived from a baseline process scheme [296]. A typical scenario is the pulp manufacturing industry (e.g, Kraft process). Kraft operation is perhaps the dominant pulp technology for hardwood feedstocks [297]. It entails the chemical digestion of wood chips by a mixture of NaOH and Na₂S to delignify and separate the cellulose matter. Pulping reagents are commonly recovered for reuse whereas the spent cooking liquours are mostly burnt to generate electricity and steam and become in part source of additional chemicals [298]. For instance, many kraft pulp mills collect certain extractives like turpentine and tall-oil as a way to achieve an extra value of these streams [299]. Turpentine is rich in α -pinene, comphene and limonene, with applications in fragrances, polymer additives and solvents whereas tall-oil can be converted into a phletora of functional products of industrial relevance (food additives such as sitosterol and sitostanol, soap and lubricants, to name a few). Potential uses of tall oil as a viable resource for biodiesel have also been highlighted in the literature [299]. Several other options that could be beneficially integrated with a kraft pulp operation include the extraction of lignin from the black liquor and the gasification of black liquor to synthesis gas. A recent interest is the pre-extraction of hemicellulose from wood before cooking for separate valorization, taking

into consideration the chemically dissimilar structures of lignocelluloses components. Besides, high-purity tannins could be recovered from incidental wastes such as bark [297].

In a similar manner, many other schemes could be run to extent the range of products and maximize economic returns in modern-day biorefinery approaches [300]. To have an estimate on the impact that different biorefinery configurations may have on profits margin, Zhang *et al.* employed for discussion the production of ethanol from corn stover. The economic analysis based on the product incomes showed that the simple utilization of sugars to produce ethanol and biobased products together with the lignin fraction as burning fuels, could reach potential revenues of \$145 per ton of biomass. Instead, that co-utilization of lignocelluloses components (by means of glucose conversion to ethanol, xylose and minor sugars into added value compounds, the use of lignin as polymeric materials and acetic acid as commodity) would increase the net margin up to 6.2 fold (\$641/ton) [2].

These results are a strong incentive to explore innovative high-efficient biorefinery schemes based on nanocellulose production, through a meaningful combination of various conversion and extraction technologies for new stream applications. To progress in this direction, this follow-up study describes a conceptual process design for the valorization of intermediates and side streams generated during the nanocellulose production from almond hulls, with simultaneous co-production of sugar alcohols (sorbitol and xylitol), bioactive extractable compounds (3-hydroxypyridines) and stable fuel intermediates. Sorbitol and xylitol may serve as precursors for production of fuels such as alkanes, aromatics or hydrogen [207] whereas biomass-derived organic oil can be subsequently deoxygenated for fuel production or used as precursor for the synthesis of fine chemicals. The work was conducted in collaboration with York University in the context of a research stay at Green Chemistry Centre of Excellence (GCCE).



5.2 Experimental

The present Chapter builds on an earlier work from GCCE, at the University of York, in which the experimental conditions for the extraction of nanocellulose from almond hulls were optimized [295]. The best suited reaction conditions were set at 220 °C (MW reaction, 30 min), including an organosolv pre-treatment in ethanol. Under the umbrella of this process, a biorefinery approach for the full valorisation of almond hulls was designed, in which all intermediates and side streams were integrated within the overall strategy of valorisation to furnish different categories of products, namely, sugar alcohols (sorbitol and xylitol), 3-hydroxypyridines and a stabilized organic phase that can be potentially used as fuel precursors. The flow-sheet of the process, including various conversion alternatives, is schematically represented in Figure 5.2 and further described in the next subsections.

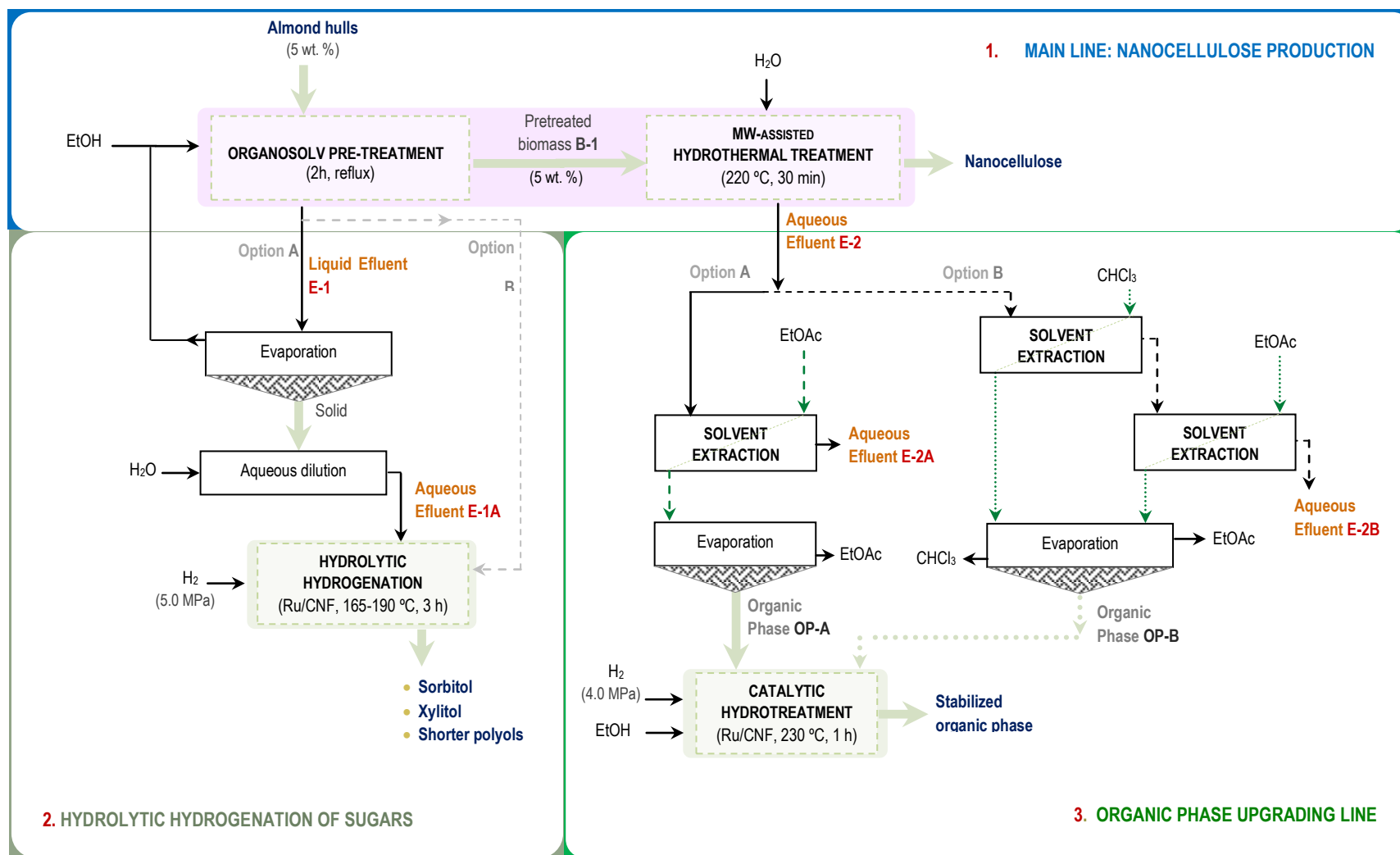


Figure 5.2 Process flowchart of the nanocellulose biorefinery concept from almond hulls

5.2.1 RAW MATERIAL

Almond hulls are a by-product of almond farming. It is the outer green shell that covers the stony almond seed (Figure 5.3). Depending on the specie, almond hulls may account for about 40-70 % of the total fruit weight whereas the shell and kernel (skin included) represent an average percentage of 33 and 15 wt. %, respectively [301, 302]. These numbers are only a reflection of the amount of wastes that are discarded from hulling operation and thus, widely available for high-value chemicals production [303]. In particular, the high content of carbohydrates (12.6 % of cellulose, 19.4 % of hemicellulose) and relatively low lignin fraction (25.1 %) make it a convenient raw material for the synthesis of cellulose nanomaterials. Other physicochemical characteristics of the starting feedstock were compiled in Chapter 2 (Table 2.1).



Figure 5.3 Parts of almond fruit [301].

5.2.2 SAMPLE PREPARATION

As the starting point, biomass was conditioned in terms of size reduction and chemically treated to prevent mold growth. For this purpose, samples were sprayed in ethanol once they were received, dried in air, grounded and sieved with a 50-mesh. More experimental details of this stage can be found in the Section 2.1.3.3 (Chapter 2).

5.2.3 PROCESS SCHEME

5.2.3.1 Nanocellulose production

The isolation of nanocellulose from almond hulls comprises a two-step procedure, whereby biomass was first submitted to an organosolv treatment in ethanol to dissolve the non-cellulosic polar matter followed by a MW-assisted hydrothermal microfibrillation.

a) Organosolv pre-treatment

In this stage, 20 g of biomass was soaked in 100 mL of ethanol (96 %, Panreac) using a round-bottom flask (250 mL) and heated at boiling conditions for 2 h under magnetic stirring. Afterwards, the mixture was filtered under vacuum, recovering a solid fraction (biomass pre-treated, B-1) and a sugar-rich liquor (E-1). Unless otherwise stated, the filtrate was concentrated by evaporation, weighted and further diluted in water (194 mL). The volume of water was defined to maintain the solid content of this stream, coded as E-1A, in same range as the effluent E-2. In principle, the ethanol separated might be recovered and reused.

b) MW-assisted hydrolysis

The hydrothermal treatment was conducted in a CEM Mars 6 microwave reactor (CEM Corporation, North Caroline, US), described in Chapter 2 (section 2.2.3.2). Typically, 2.0 g of pre-treated biomass (B-1) and 40 mL of deionized water (5 % w/v) were loaded in closed vessels (EasyPrep Plus[®], Teflon, 100 mL) and placed on the rotor tray. Samples were heated to 220 °C with a set ramp time of 30 min and a maximum power inlet of 600 W. Next, the suspension was cooled down to room temperature and filtered through a Whatman filter paper. This operation separated an aqueous hydrolysate effluent (E-2) from an insoluble residue, which was thoughtfully rinsed with water, hot ethanol and acetone and finally air-dried until mass constant. The resulting solid was quantified by gravimetric analysis and denoted as cellulose microfibrils (MFC) owing its high cellulose fiber content. The yield of this product (Y) was



calculated as the mass percentage of the solid residue to the original mass almond hulls ratio (Equation 5.1):

$$Y \text{ (MFC)} = \frac{\text{mass of MFC}}{\text{mass of dried biomass}} \cdot 100 \quad [5.1]$$

The aqueous solution E-2 was stored at 4 °C until further analysis and experimentation.

5.2.3.2 Downstream catalytic conversion technologies

The effluents E-1 and E-2 were used as inlet streams for subsequent valorization processes, namely, hydrolytic hydrogenation into sugar alcohols and catalytic hydrotreatment for chemical stabilization, in either case. For such experiments, a ruthenium supported catalyst (Ru/CNF) was selected. The choice of this catalyst was based on the good hydrogenation activity observed in Chapter 4. Details about synthesis and catalyst characterization can be found in titled Chapter. Just as a reminder, it was prepared by incipient wetness impregnation with a nominal metal content of 0.5 wt. % (actual loading of 0.38 ± 0.03 wt. % determined by ICP-OES) and a mean Ru particle size of 1.2 ± 0.2 nm (measured by TEM). Reactions were performed in a 45-mL stainless steel reactor (Berghof Products, BR-40 series) fitted with a temperature controller (BTC-3000) and a magnetic stirring. The technical specifications of this unit were included in Chapter 2 (Section 2.2.3.1.1).

a) *Hydrolytic hydrogenation of sugars*

Hydrolytic hydrogenation of E1 or E1-A (depending on the solvent) were studied using 3 h-runs under various operational conditions. In a typical essay, 20 mL of effluent was loaded in the reaction vessel and put in contact with an appropriate quantity of metal catalyst (Ru/CNF, 1.4 g cat/g C). Considering the carbon weight of the feed by elemental analysis, the amount of catalyst corresponds to a mass ratio of catalyst to solids equal to 0.5. The autoclave was then sealed and fluxed with N₂ and H₂ gas and finally pressurized to 5.0 MPa of H₂ (RT). Next, the

system was heated to the desired temperature (165 or 190 °C) and maintained for 180 min under magnetic stirring (1400 rpm). At the end of the test, the solution was quenched in a tap water bath. Catalyst and solids were recovered by filtration, rinsed with deionized water, dried and weighed. Table 5.1 lists the full set of reaction conditions used for these tests, including the effective pressure data of the system (i.e., measured at work conditions).

Table 5.1 Details of reaction conditions for each run

Run	Solvent	Catalyst	H ₂ pressure (MPa) RT ^[a]	Effective pressure (MPa)	Temperature (°C)	Time (h)
1	H ₂ O	---	5.0	8.0	165	3
2	H ₂ O	Ru/CNF	5.0	8.0	165	3
3	H ₂ O	Ru/CNF	5.0	9.0	190	3
4	EtOH	Ru/CNF	---	4.0	165	3

^[a]RT stands for room temperature conditions

b) *MW-hydrolysate upgrading line: organic phase extraction and mild hydrotreatment*

The extraction by solvents was explored as a valorisation path of E-2, recovering a biomass-derived organic oil (bio-oil) with potential as energy and chemicals source. The extract quality was enhanced through a consecutive catalytic hydrotreatment. The effectiveness of this process was discussed in parallel to a bio-oil sample obtained from thermochemical routes (MW-assisted pyrolysis).

• **Extraction process**

The organic phase was separated from the aqueous phase (E-2) by means of a series of liquid-liquid extractions. Experimental conditions used for the extraction were investigated using ethyl acetate (EtOAc) as single solvent or either through a sequential procedure with chloroform (CHCl₃) followed by ethyl acetate. The volumetric ratio of solvent to E-2 effluent was kept at (2:1) for EtOAc and (1:1) for CHCl₃. The organic product derived from the single solvent extraction was termed as OP-A whereas OP-B stands for that extracted by dual solvents.

In practice, the extraction was achieved by adding the solvent to a fixed volume of E-2 (30 mL) in a separating funnel (100 mL, Figure 5.4). The mixture was then vigorously shaken and decanted several times (usually thrice). Then, the organic phase were collected and replaced by an equal volume of fresh solvent. For each solvent, three consecutive extractions were made. The liquids collected in each stage were mixed together, getting one bio-oil sample for experiment. Next, the extract was concentrated by evaporation (40 °C, vacuum), dried and weighted.

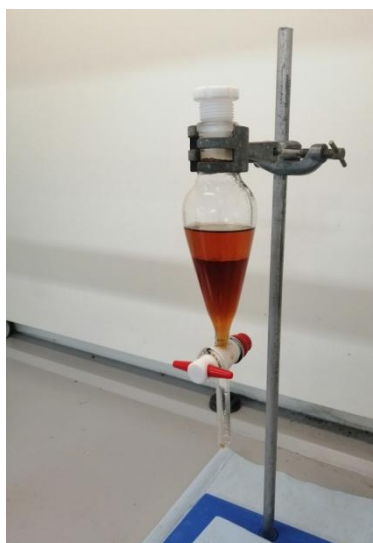


Figure 5.4 Experimental set-up for bio-oil extraction

The organic products yield was defined as the mass percentage (wt. %) of compounds extracted from aqueous phase to the organic solvent while the extraction efficiency was determined taking into consideration the carbon content of both fractions. In order to validate the measurement reproducibility and obtain enough amount of product, the extraction was conducted at least by quadruplicate. Results correspond to an average value expressed as mean \pm standard deviation.

- **Pyrolysis of almond hulls**

For comparative purposes, almond hulls were pyrolyzed in a CEM Discovery laboratory microwave reactor according to the reaction conditions previously established by the GCCE research group (unpublished data). In detail, 1.0 g of dry biomass was transferred to a MW vial



(Pyrex®, 35 mL) and sealed with a MW tube lid. The sample was then irradiated at 260 °C for 3 min. Experiments were performed in dynamic mode with a maximum power inlet of 75 W. The resulting material was then divided into three categories of products: non-condensable gases, liquid phase (bio-oil) and a solid char. The gas yield was determined by carefully monitoring the mass lost before and after MW treatment over an opened vessel. Subsequently, the bio-oil fraction was stripped with ethyl acetate (10 mL×3). Bio-char yield was determined by weighting the dried solid remained once the bio-oil was removed. The yield of bio-oil was finally calculated by subtraction. On average, the product fraction ratio of bio-oil and char varied in the range of 17.5 % (± 2.5) and 41.6 % (± 0.7) whereas the gas yield accounted to 40.9 % (± 3.0) of the initial mass.

- **Catalytic hydrotreatment for bio-oil stabilization**

The set of organic oils (OP-A, OP-B and pyrolysis-oil) was partially deoxygenated in ethanol under an initial pressure of 4.0 MPa H₂. Typically, 300 mg of bio-oil was dissolved in 20 mL of ethanol (96%, Panreac) and put in contact with the metal catalyst (Ru/CNF, 1.4 g cat/g C). The amount of catalyst was adjusted to maintain the mass ratio of catalyst to carbon equals to 1.4, according to the elemental analysis of each bio-oil. This criterion is more accurate than a pre-fixed mass catalyst by considering possible fluctuations on the oxygen content on various feedstocks. Next, the autoclave was purged and vented several times first with N₂ and then with H₂ and finally pressurized to 4.0 MPa H₂. The reaction was conducted at 230 °C for 60 min under magnetic stirring (1400 rpm), working at an effective pressure of 10.2 MPa. After that, the system was quenched in water. Gas products were collected for analysis and the liquid phase separated from solid products by vacuum filtration. During this procedure, the solid retained onto the filter was rinsed with ethanol until become colourless. Afterwards, ethanol soluble fraction was evaporated to remove the solvent. At last, the oil residue was dried with a N₂ line until mass constant and weighted to calculate the yield. Coke formation was estimated after



discounting the initial weight of catalyst from the total solid weight, assuming no loss of catalyst.

5.2.4 PRODUCT ANALYSIS

5.2.4.1 Effluents composition

Liquid-phase products were quantitatively characterized by High Performance Liquid Chromatography (HPLC), using the instruments and analytical conditions described in Chapter 2 (section 2.3.5.1). The former analysis was complemented to gas chromatography coupled to mass spectrometry (GC/MS, see details in 2.3.5.2). The yield of products was expressed on carbon mass basis, according to the carbon content of the starting effluent determined by elemental analysis.

5.2.4.2 Gas products

Gas phase was sampled and analysed by a Micro GC (Varian CP4900), tracing the volume % composition for the following gas species: CH₄, CO₂, CO, H₂.

5.2.4.3 Bio-oil and organic phases characterization

The characterization of bio-oil included elemental and chemical composition and higher heating value (HHV). The elemental composition (CNSH) was determined using a Thermo Flash 1112 Analyzer, calculating the oxygen content by difference. The HHV was determined from the CHN/O data using the empirical formula developed by Channiwala [112]. All details of this characterization were given in 2.3.4.1 part (Chapter 2). The degree of deoxygenation (DOD) was estimated according to the following expression:

$$\text{DOD (\%)} = \left(1 - \frac{\text{weight of oxygen in product}}{\text{weight of oxygen in feed}} \right) \cdot 100 \quad [5.2]$$



The chemical composition was analyzed by gas chromatography (GC/MS) using an Agilent 7890 instrument equipped with a capillary column coated with HP-FFAP (Agilent, 30 m×0.25 mm i.d., 0.25 μ m film thickness). Each compound was identified by matching their mass spectrum with that of the spectral library (NIST 05 database). A semi-quantitative analysis was performed using the peak area ratio of an individual compound with total cumulative peak area of all compounds.

5.3 Results and discussion

Nanocellulose extraction can be prospectively performed within a biorefinery approach using an integrated processing scheme for effluents valorization. Therein, the dissolved substances from the spent effluents are recovered and used as the basis for additional source of energy and valuable co-products through the implementation of downstream catalytic technologies. On this premise, this work suggests a feasible waste treatment cycle for simultaneous recovery of sorbitol, xylitol and energy precursors using side-streams originated from nanocellulose extraction line. The flowsheet of this proposal can be organised around three main sections, namely, nanocellulose production, hydrolytic hydrogenation of sugars from hemicellulose fractionation and MW-hydrolysate upgrading line.

5.3.1 MAIN LINE: NANOCELLULOSE PRODUCTION AND PRODUCT PROPERTIES

Following the previous study, the isolation of cellulose nanostructures from almond hulls involves two main stages. First, the biomass is pre-soaked in ethanol (solvothermal process) to remove polar extractives. During this treatment, sugars, dimers and waxes are preferentially dissolved and separated from the biomass. The foremost goal of this step is alter the biomass structure, creating access to the cellulose matter through a material with higher porosity and inner surface [304]. Moreover, these compounds readily undergo unwanted degradation reactions at high temperature, forming humins that hamper the product purification.

The second stage is dedicated to the production of cellulose microfibrils. The former applies a MW-assisted hydrothermal treatment to separate the cellulosic portion from the polymeric matrix (remains of hemicellulose, pectin and lignin). It also expels the amorphous regions from the cellulose structure, giving rise to a cellulose-rich solid of high crystallinity. The unique role of MW energy to enhance the solubilisation of non-cellulose components in this process was hypothesized by Hue *et al.* [305]. According to the authors, the MW radiation enables the rapid internal heating of species with high polarity (carbohydrates) whereas the apolar compounds (lignin) remain unheated. Such selective heating provokes an uneven distribution of



temperatures within the biomass material, including localized zones where temperature is much higher than the bulk (hot spots). The high-frequency rotation of polar parts, trying to align with electric field, combined with the inhomogeneity of temperatures among different constituents was proposed to facilitate the separation and eventually disrupt their inter-twined structure [305-307]. At optimal reaction conditions (220 °C, 30 min, MW-HT), bundles of needle-shaped cellulose microfibrils with dimensions of 4.0-4.3 nm in width and a few μm in length were isolated from almond hulls in 33.4 % yield (on pretreated biomass weight basis, B1). Taking into consideration that pre-treatment step densifies the biomass upon removal of C5-C6 sugars; this yield corresponds to a 27.8 % of raw material. Strictly, the cellulosic material obtained from this process should be denoted as (ligno)cellulose microfibrils, in reference to a product primarily composed by cellulose but still containing some dangling lignin. The presence of residual lignin was previously confirmed by Attenuated Total Internal Reflectance Infrared Spectroscopy (ATR-IR) and ^{13}C CPMAS NMR analysis and it is also consistent with the mass yield of product, above the theoretical value expected from the almond hulls composition (12.6 wt. % of cellulose), showing needs of bleaching treatments to increase the product purity depending on the final application. The material obtained at these conditions showed the highest crystalline degree (61.5 %), superior thermal stability (364 °C) and film forming properties as thoughtfully discussed in the preceding study to this work [295].

5.3.2 HYDROLYTIC HYDROGENATION OF SUGARS

The ethanosolv process before MW-hydrothermal reaction not only enhances nanocellulose properties but also results in the fractionation of hemicellulose, allowing opportunities for its valorisation into other compounds that otherwise would be lost. Hemicellulose portion was recovered from this stage as soluble sugars in the stream designated as E-1. On mass basis, the overall yield of E-1 corresponded to 16.8 % of the initial biomass. The analysis by HPLC determined a xylose and glucose content of 24.6 and 18.4 % of the total carbon together with small amounts of lactic acid (2.3 %) and cellobiose (1.9 %). A symbolic amount of 1.5 % of

sorbitol was also detected, likely forming part of the natural composition of the plant [308]. The sum of these compounds accounted for *ca.* 40.9 % of the hemicellulose content of the raw biomass (i.e., 19.4 wt. %). Owing the chemical richness in sugars of this stream, it was proposed for the straightforward synthesis of sugar alcohols via hydrolytic hydrogenation. To this end, various operational conditions were mapped (see details in Table 5.1). The specific products distribution for each run is outlined in Figure 5.5.

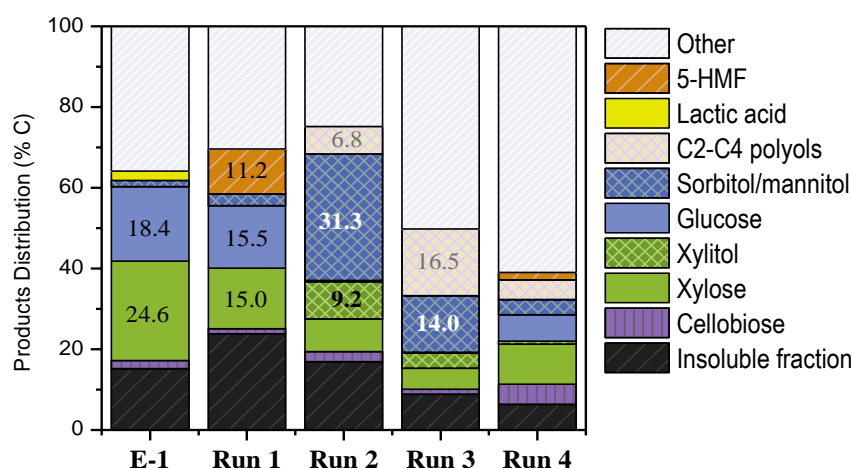
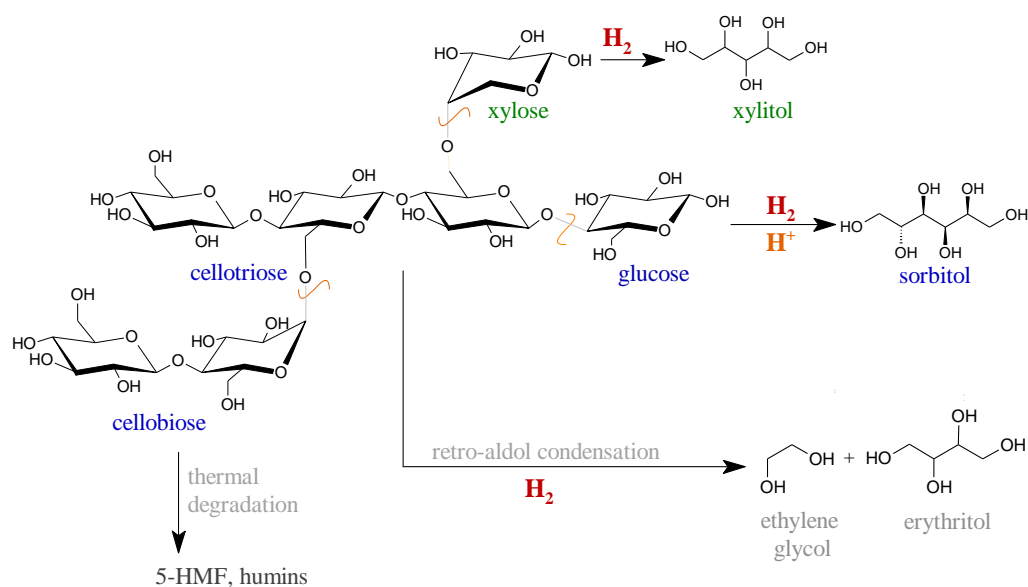


Figure 5.5 Product distribution for E-1 downstream valorization by hydrolytic hydrogenation under different reaction conditions.

As a first case study, hydrolytic hydrogenation of E-1 was studied in aqueous phase conditions. So, E-1 was vaporized to recycle ethanol and the solid residue was then diluted with deionized water to form E1-A effluent. At this point, the high volatility of ethanol comes as a clear advantage for the ease recovery of the solvent by simply distillation [304]. After that, a water-insoluble fraction, amounting to 15.2 % of C, was generated and separated by filtration. The aqueous soluble fraction was then subjected to hydrolytic hydrogenation under 5.0 MPa of H₂ (RT) at 165 °C for 3 h. Almost no sugar alcohols (merely 1.3 %) were formed in a control experiment without catalyst (blank test, Run 1). Instead, degradation routes of sugars became notorious, losing around 39.1 % of the initial xylose and 16.0 % of glucose. The consumption of sugars went on par to a growth of 5-HMF and poly-condensed products or humins (11.2 and 8.6 % of the total C). In turn, the hydrolytic hydrogenation of E-1 was very efficient under



analogous catalytic conditions, affording 31.3 % of sorbitol at the end of the test (Run 2). This number exceeded in 7.4 % the value expected from the complete conversion of glucose and cellobiose, showing contributions from larger polysaccharides. Besides, at around one-third of the pentose fraction was transformed into xylitol (9.2 %) with another 8.1 % remaining unconverted. The rest of xylose (7.3 %) was probably transformed through secondary degradation pathways, either into shorter polyols from xylitol hydrogenolysis or by thermal effect. The formation of low molecular weight polyols could be observed in certain extent (6.8 %), being erythritol and ethylenglycol the most representative species. [76, 309]. Scheme 5.1 summarizes the primary reaction routes involved in the transformation. Under these mild conditions, the amount of solid residue formed from condensation/re-polymerization routes was very low (merely 1.7 %). Such percentage was added to the original insoluble fraction of 15.2 % in the product distribution graph. On the whole, 75.5 % of the carbon content in E-1 was quantified as different products out of which 47.4 % were sugar alcohols. The above results not only confirm the true catalytic activity of ruthenium catalyst but also illustrate the intrinsically different reactivity between xylose and glucose.



Scheme 5.1 Main reaction routes involved in the catalytic hydrogenation of E1-A.

A second issue in this subset of experiments concerns the reaction temperature. As learnt from the previous Chapters, the hydrolysis reaction occurs at a very low extent below 190 °C. This



fact may lead to underestimate the true potential of utilization of E-1A into sugar alcohols when working at 165 °C if longer carbohydrates chains remain unhydrolyzed. In order to ascertain this point, a third run was performed at 190 °C including the insoluble fraction in the feed effluent. Under the new conditions, an additional fraction of this solid was solubilised, recovering only a 6.3 %. However, this variation did not incur into any enhancement on the product yield, which shifted from C6-C5 compounds to shorter chain polyols (16.5 %) as a result of C-C and C-O bond cracking. The strong impact of hydrogenolysis reactions after 3 h at 190 °C may be likely explained by the presence of certain basic promoters like N-containing proteins and other biomass-derived impurities (matrix effect). Globally, the carbon balance closed in lower level at higher temperature (49.8 %) with only 14.0 % of sorbitol and 3.7 % of xylitol.

From a broader perspective, hydrogen for this reaction route can either be supplied by molecular hydrogen gas or generated from hydrogen donating species through the catalytic transfer hydrogenation mechanism. This mechanism can be depicted as the fusion of two catalytic reactions, involving the initial activation of the organic hydrogen donor species and the subsequent reduction of sugars. Because alcohols are frequently used as hydrogen donors and E-1 is originally dissolved in ethanol, its direct use as feed could potentially obviate the need of an external hydrogen source [310, 311]. To explore this option, a final test was performed using raw E-1 effluent, under autogenous pressure and inert atmosphere (Run 4). In this experiment, however, no evidence of reduction was found upon 3 h in contact with Ru catalyst (Ru/CNF) at 165 °C. Only trace levels of sorbitol (3.7 %), xylitol (0.7 %) and other shorter molecular polyols (4.9 % of C2- C4 compounds) were detected whereas most part of the sugars were thermally degraded. Based on the above experience, it can be deduced that many other factors related to the catalyst and process conditions could be relevant to complete the catalytic cycle. Thus, the catalyst redox properties, the presence of water as co-solvent or even the synergetic effects between the metal and acid-base sites of the support have been claimed to facilitate the activation of the alcohols on metallic surface in previous reports [222, 312].



Considering the entire set of experiments, the best suited conditions for treating E-1 by hydrolytic hydrogenation reaction were set at mild temperature (165 °C) using hydrogen gas (4.0 MPa) in aqueous solution for 3 h. That results in a carbon recovery as high as 75.5 % with 47.4 % to sugar alcohols, which is an attractive and feasible option to reinforce the profitability of the stream. Merely on economic grounds, the market prize of sugar alcohols is often considerably higher than that of the mother liquor. The wholesale price for a syrup rich in xylose and glucose ranges between US \$480-600/ton, depending on the reducing sugars content, whereas a typical commercial value for sorbitol is US \$650/ton and up to \$3900/ton for xylitol [313, 314].

5.3.3 ORGANIC PHASE UPGRADING LINE

Theoretically, the liquid fraction derived from hydrothermal liquefaction (E-2) may contain decomposition products of lignin, hemicelluloses and amorphous cellulose that leach during this treatment. Lignin dissolution tends to yield oligomers and phenolic compounds while carbohydrates principally lead to C5 and C6 saccharides. Some of the hydroxyl groups in sugars may be acetylated (galacturonic acid, lactic acid...). However, most part of the sugars evolved at the relatively harsh conditions applied for nanocellulose extraction (220 °C) towards dehydration compounds like furfural (0.8 %), 5-hydroxymethylfurfural (5-HMF, 1.0 %) and other by-products such as formic and levulinic acids (2.4 and 4.3 %, respectively). This effluent is actually a complex liquid mixture, characterized by a relative high organic content in a wide range of chemical compounds and compositions of which only a 43.6 % of C could be identified (Table 5.2). It mainly consisted of acetic acid (9.1 %), xylose (8.2 %), organic acids, lactic acid (3.1 %), hydroxyacetone (2.9 %) and even ketones (7.0 %).

Table 5.2 Compositional analysis of E-2 by GC/MS and HPLC.

Compound	Molecular Formula	[% C]
Cellobiose	C ₁₂ H ₂₂ O ₁₁	0.17
Galacturonic Acid	C ₆ H ₁₀ O ₇	0.71
Arabinose/Rhamnose	C ₅ H ₁₀ O ₅	1.03
Levogluconan	C ₆ H ₁₀ O ₅	1.38
5-HMF	C ₆ H ₆ O ₃	0.97
Levulinic acid	C ₅ H ₈ O ₃	4.30
Formic acid	CH ₂ O ₂	2.38
Furfural	C ₅ H ₄ O ₂	0.84
Lactic acid	C ₃ H ₆ O ₃	3.12
Xylose	C ₅ H ₁₀ O ₅	8.25
Acetic acid	CH ₃ COOH	9.09
Hydroxyacetone	C ₃ H ₆ O ₂	2.92
Propanoic acid	C ₃ H ₆ O ₂	0.13
2-Cyclopenten-1-one, 2-hydroxy-3,4 dimethyl	C ₇ H ₁₀ O ₂	1.59
2-Cyclopenten-1-one, 2-hydroxy-3-methyl	C ₆ H ₈ O ₂	4.00
2-Cyclopenten-1-one, 3-ethyl-2-hydroxy	C ₇ H ₁₀ O ₂	1.43
3-hydroxy pyridine	C ₅ H ₅ NO	1.29
Total		43.63

Such heterogenous composition, along with the small concentration of each component limits its selective conversion to single products, seemingly not apt for valorization by hydrolytic hydrogenation. This hypothesis was experimentally confirmed after a treatment at 165 °C and 5.0 MPa H₂ for 3 h, in which only minor amounts of xylitol and sorbitol were detected by HPLC (0.4 and 2.5 % in terms of carbon yield). Again, at around one-third of the xylose was recovered without reacting (2.9 %) whereas up to 71.4 % of the carbon remained unidentified (Figure 5.6).

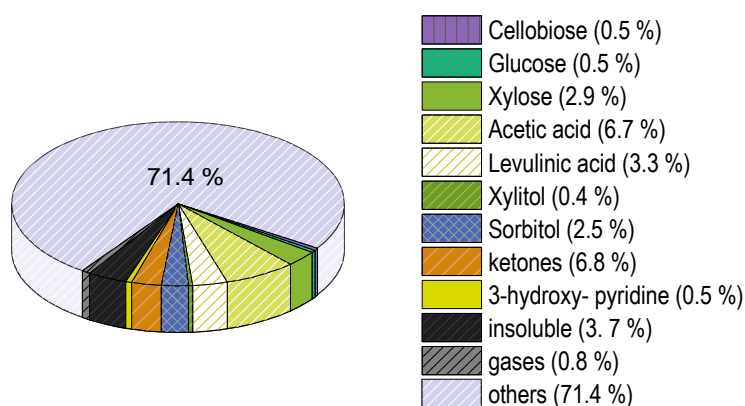


Figure 5.6 Hydrolytic hydrogenation of E-2 stream
(Reaction conditions: 5.0 MPa H₂, 165 °C, 3 h)

However, the relative high organic content of this effluent (0.96 % C from elemental analysis) make it an attractive feedstock for additional co-products. To recover and use the water-soluble chemicals, a multi-step liquid extraction method with various extracting agents was evaluated and the main results are summarized in Table 5.3.

The extraction was initially assessed using ethyl acetate as solvent. After three extractions, ethyl acetate retained an 18.7 % of the carbon of the aqueous phase, rendering an organic fraction (OP-A) in a mass yield of 8.5 ± 1.1 wt. % (Entry 1). To increase the extraction efficiency, E-2 effluent was sequentially extracted with chloroform and ethyl acetate following the methodology proposed by Ren *et al.* [315]. Notwithstanding, almost no increase on the carbon recovery (19.8 %) was noted through the newly developed extraction train and the organic phase yield remained at 9.7 % (± 1.4) on mass basis (Table 5.3, Entry 2). For practical purposes, the sole use of ethyl acetate could be enough for the extraction of this phase.

Table 5.3 Chemical extraction of E-2.

Organic phase	Organic Solvent	Volumetric ratio (effluent: organic solvent)	Yield (wt. %)	Extraction efficiency (% C)
OP-A	Ethyl acetate	(2:1)	8.5 ± 1.1	18.7
OP-B	Choroform- Ethyl Acetate	(1:1) (2:1)	9.7 ± 1.4	19.8



The compositional analysis of the extract by GC-MS revealed that most part of the volatile fraction was described by one major peak area based on N-heterocyclic structures derived from pyridine and collectively known as 3-hydroxypyridines. The relative distribution of these species are itemised in Figure 5.7. It includes 3-hydroxypyridine as the predominant one (49.0 %) and minor percentages of 3-hydroxy-2-methylpyridine (0.9 %) and 3-hydroxy-6-methylpyridine (2.2 %), which were likely originated from reactions between sugars degradation products (i.e., furfurals from dehydration pathways) and ammonia (issued from deamination of hydrolyzed proteins) as previous works suggested [316]. Overall, the area ratio of these species accounted up to 52.0 % of the total area ratio of identified compounds in OP-A by gas chromatography (Table 5.4). In addition, smaller percentages of acetic acid (10.5 %), phenolics (6.0 %) and 2-cyclopenten-1-one, 3-methyl (6.4 %) were detected from this fraction. OP-B is essentially akin to OP-A but showing a higher proportion in 3-hydroxypyridine (61.3 %). Interestingly, such unexpected selectivity towards specific extractable compounds, could find utility in certain niche applications. In particular, 3-hydroxypyridine may serve as synthesis precursor of numerous compounds with pharmacological activity and uses in medicine (vitamin B₆, pterocellin A, furopyridines, pirtuberol) or as pesticides (trifloxysulfuron) among other daily products [317-320].

Table 5.4 Chemical composition of organic extracts.

Chemical composition	Peak area (%)	
	OP-A	OP-B
Phenolic compounds	6.0	4.2
3-hydroxy pyridines	52.0	61.3
2-Cyclopenten-1-one, 3-methyl-	6.4	5.6
5-hydroxymethylfurfural	5.8	5.9
Acetic acid	10.5	9.8
2-Propanone, 1-hydroxy-	2.4	n.d
Butanoic acid derivatives	1.1	1.6
Pentanoic acid derivatives	0.7	1.3

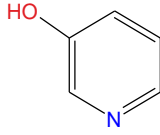
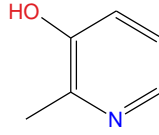
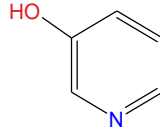
			
	3-hydroxy-pyridine	3-hydroxy-2-methylpyridine	3-hydroxy-6-methylpyridine
OP-A	49.0 %	0.9 %	2.2 %
OP-B	59.9 %	n.d	0.9 %

Figure 5.7 Chemical structure and relative distribution of various 3-hydroxypyridine-derived compounds.

It should be stressed, however, that this value does not entirely represent the overall mass sample due to the presence of high-molecular weight and polar compounds that are not detected by gas chromatography [57, 321]. Preliminary estimations indicate that 3-hydroxypyridines may account up to 17.9-18.2 wt. % of the OP-A and OP-B on the elemental composition basis.

The rest of this fraction, based on the oligomeric fraction, could be used as valuable starting material for energy and bio-fuels production.

As a benchmark reference, the organic extract was compared to a bio-oil obtained from the MW-pyrolysis of almond hulls, a dark brown liquid with a high heating value (HHV) of 28.7 MJ/kg. Table 5.5 compiles the elemental analysis data for the entire set of samples. As it can be seen, the energy density of OP-A (22.7 MJ/kg) is a few points lower than the bio-oil produced from pyrolysis, which is ascribed to a higher percentage of oxygen moieties (35.5 % vs. 24.2 %). The oxygen-rich condition of OP-B (38.7 %) further decreases the HHV to a slightly lower value (21.6 MJ/kg). In all the cases, the energy content remains greater than the raw biomass (15.7 MJ/kg).

Together with the calorific value, the analysis of elemental composition gives indirect information on the predominant chemical nature of this fraction throughout the parameter of effective H/C molar ratio (H/C_{eff}). This number, calculated from the molar H/C ratio after discounting the oxygen content in the form of water, is around zero in sugars, close to unit in

aromatics and equal to 2 in alkanes [322]. On this basis, sugar-like structures are presumed for OP samples while the pyrolysis-oil will be closer to aromatics.

Table 5.5 Elemental analysis and derived bio-oil properties.

Property	Bio-oil (pyrolysis)	OP-A	OP-B
Elemental analysis (wt. %)			
Carbon	64.7 ± 3.3	55.9 ± 0.6	52.1 ± 4.1
Hydrogen	7.3 ± 0.5	5.86 ± 0.1	6.31 ± 0.1
Nitrogen	3.7 ± 0.4	2.76 ± 0.2	2.8 ± 0.1
Sulphur	±0.1	n.d	n.d
Oxygen ^[a]	24.2 ± 4.3	35.5 ± 0.6	38.7 ± 3.9
Molar H/C	1.36 ± 0.02	1.26 ± 0.02	1.46 ± 0.14
Molar O/C	0.28 ± 0.06	0.48 ± 0.01	0.56 ± 0.10
H/C _{eff} ^[b]	0.8	0.3	0.34
HHV (MJ/kg)	28.7 ± 2.2	22.7 ± 0.4	21.6 ± 1.7

n.d.= not detected

[a] calculated by difference; [b] $H/C_{\text{eff}} = H/C - 2O/C$ on molar basis [322]

Nevertheless, the organic phases derived from the above stages are inappropriate for its direct use as transportation fuels, mainly due to a series of detrimental features inherited from the oxygenated groups such as low energy density and miscibility, corrosiveness, high viscosity, instability, poor ignition and aging properties [323, 324]. In order to meet the bio-oil quality to the industry standards, crude bio-oils are commonly upgraded by subsequent catalytic techniques. One route that it is often explored is the catalytic hydrodeoxygenation (HDO). The HDO process, usually carried out at high temperature (300-600 °C) in contact with metal catalysts and hydrogen pressure, permits the removal of oxygenates as H₂O, CO and CO₂ through several reaction pathways like hydrogenation, hydrogenolysis, dehydration, decarboxylation, decarbonylation, hydrocracking and repolymerization [321]. To control the excessive polymerization at the temperature levels required for HDO, a previous stabilization stage at low-severity conditions is recommended, whereby the most reactive compounds are converted to more stable ones. Typically, carbonyl and carboxyl functional groups are reduced to alcohols while C=C bonds are saturated [321, 325-328]. Following this two-step approach, earliest proposed by Gagnon and Kaliaguine and presently adopted in the most routine



operations for HDO to minimize coke formation and clogging issues, the oil is first stabilized at mild conditions ($T^a < 280$ °C) and then submitted to a deep deoxygenation to hydrocarbons at higher temperature (350-600 °C) [325, 329-331]. Common catalysts for the low-temperature pre-treatment are Pt, Ru and Pd whereas Ru, Ni or sulfided CoMo catalysts are typically applied for the severe hydrotreatment step [329]. At this point, it was speculated that such first stabilization step could be performed over the same Ru/CNF catalyst employed for hydrolytic hydrogenation but at elevated conditions (230 °C). The usefulness of ruthenium catalysts in this application is well-documented in the literature [321, 323, 328, 332-335]. For convenience, these runs were carried out in ethanol as reaction media. The use of ethanol as solvent avoids the need of subsequent extraction stages whereas its low dielectric constant facilitates the dissolution of high molecular weight products. Also, hydrogen solubility in ethanol is better than water [322, 336-340]. Tables 5.6-7 show the properties of hydro-treated samples and product yield under such reaction conditions for 60 min and 4.0 MPa H_2 . Only a minimal formation of coke (1.1-2.4 wt. %) and CO_2 gas (0.98-1.1 wt. %) was observed, revealing the absence of important decarboxylation, decarbonilation or repolymerization reactions at such low-severity conditions that reduce the oil yield to gaseous or solid products.

Changes on chemical composition after the hydrotreatment of OP-A and OP-B are summarized in Table 5.6. Again, the 3-hydroxypyridines dominate the analysis of volatile products by GC/MS (51.1 and 67.6 % of the area ratio). Since they were already present in the initial samples, the experimental evidence proved the tolerance of these species towards the catalytic hydrotreatment at low temperature. Therefore, their separation from the main effluent could be optionally performed before or after the mild stabilization stage without significant loss of yield. Another important observation that can be made regarding the relative distribution of these species, remaining about constant as the original feed, is that most of oligomeric structures were unable to crack, which otherwise will be denoted from a large alteration between volatile species distribution.

Table 5.6 Chemical composition of hydro-treated samples based on the analysis of volatile compounds.

Chemical composition	Hydro-treated	Hydro-treated
	OP-A	OP-B
Peak area (%)		
Phenolic compounds	6.9	n.d.
3-hydroxy pyridines	51.1	67.6
Butanoic acid derivatives	21.7	29.7
Pentanoic acid derivatives	5.1	2.7

Besides 3-hydroxypyridines, the hydro-treated OP samples contained relative large amounts of organic acids, including butanoic acid and their derivatives, which made up to 21.7- 29.7 %, and less proportions of pentanoic acids (5.1-2.7 %). In principle, the boiling point distances between 3-hydroxypyridines (~ 280 °C) and butanoic acids (~ 164 °C) are conducive for an eventual separation of both species by simple distillation. Two primary compounds have been identified on the second group, namely, diethyl ester of butanedioic acid (11.1-12.4 %), also known as diethyl succinic acid (DES), and 2-hydroxy diethyl ester of butanedioic acid (10.6-17.3 %). DES is an important platform chemical in many industries. It is used as food additive, flavouring agent and pigment solvent. In addition, its physical and chemical properties have been suitable as oxygenated additive for diesel fuels to reduce particulate emissions or as fuel blending agent when it is combined with a cetane number improver [341].

Overall, the loss of certain oxygenated species like acetic acid and 2-propanone, 1-hydroxy-, along with the oxygen reduction on the elemental composition, confirms the effectiveness of the mild hydrotreatment as a stabilization method. The former was unambiguously certified on the MW-pyrolysis oil, whose volatile fraction was almost completely converted into phenolics compounds. In particular, the initial bio-crude was mainly composed of phenolic-like compounds (67.9 %), together with some aromatics hydrocarbons (naphthalenes, 13.4 %) and ketones (2-cyclopenten-1-one, 3-methyl, 3.5 %). Among many phenolic compounds, it was found phenol (8.8 %) and phenolics substituted at various positions: phenol-2 methyl (6.8 %), phenol-4 methyl (5.8 %), phenol-3 ethyl (5.3 %) and phenol-2,4 dimethyl (6.1 %). The



stabilization process dramatically increased the content in phenolic groups, providing up to 89.8 % area ratio. More than twenty phenolic compounds were identified in this sample, including phenol (10.8 %), phenol 3- methyl (9.2 %), phenol 4-methyl (6.8 %), phenol 3-ethyl (8.3) and phenol, 2,4-dimethyl (8.9 %) as the most representatives. The relative proportion of naphthalenes groups slightly decreased after upgrading from 13.4 to 6.5 %. No obvious changes on the molecular weight distributions before and after catalytic hydrotreatment were noted (122.7 ± 0.2 on raw bio-oil and 120.4 ± 2.9 for the hydro-treated bio-oil, based on the analysis of volatile fraction), suggesting that severe chain cracking does not occur during this stage. On the contrary, a marked decreased on the average molecular weight will be apparent. The lack of cracking of oligomeric chains is consistent with the results obtained for OP-(A, B) samples, while it is expected to gain in importance on the second part of the HDO process, working at more severe conditions. This stage is outside the scope of this work.

In terms of oxygen removal, the degree of deoxygenation (DOD) for MW-pyrolysis oil was estimated in 16.9 %, which means a reduction of the oxygen content of 4.1 wt. % points lower than the feed (20.1 vs. 24.2 wt. %). As a result, HHV increased from 28.7 MJ/kg to 30.5 MJ/kg. Similar deoxygenation levels were noted for the organic phases OP-A,B (14.6-14.1 %), although their compositions differ considerable from the pyrolysis oil and also contain higher oxygen percentages (30.3 and 33.2 % for OP-A and OP-B, respectively, Table 5.7). As compared to the original samples, the oxygen content decreased an average value of 5.3 wt. % (± 0.2) with a concurrent improvement in their HHV around 1.9 MJ/kg (± 0.4). Both fractions own rather close heating values and oxygen levels even when the degree of oxygenation of OP-B is slightly higher. The highest heating value (24.9 MJ/kg) and minimum ratio of O/C (0.37) was shown by the OP-A followed by OP-B (23.3 MJ/kg, O/C=0.43).

Drawing analogies with the MW-pyrolysis oil, a rather low content in phenolic species on OP samples may be explained from two aspects: a) the use of less dramatic conditions during the hydrothermal treatment (220 °C instead of 260 °C used in the MW-pyrolysis) that prevents from the extensive chain cracking and b) the loss of the lignin attached on the cellulose fibres and

discarded during washing. This fact, combined with the absence of severe cracking during mild catalytic hydrotreatment, makes the true potential of the oligomeric fraction of OP as fuel precursor difficult to appoint. Some inferences can be made based on indirect information from bio-oil sample derived from MW-pyrolysis, especially regarding the effectiveness of the hydrotreatment towards chemical stabilization of their constituent compounds. On this basis, more research efforts should be devoted on the assessment of the potential application of the organic phase as fuel precursor, by enhancing the recovery of the lignin fragments and further cracking of the oligomeric molecules.

The elemental composition of the hydrotreated samples, and particularly in comparison with the initial sample, lends further insights into the changes occurring in the organic phase chemistry during the stabilization. In this case, the catalytic hydrotreatment in subcritical ethanol rendered a product with reduced O/C ratio and also lower H/C values irrespective of the sample under evaluation, pointing towards dehydration pathways as the most likely reaction routes [35, 322].

Table 5.7 Chemical characterization of hydro-treated samples.

Property	Hydro-treated OP-A	Hydro-treated OP-B
Elemental analysis (wt. %)		
Carbon	60.8 ± 0.1	58.2 ± 0.5
Hydrogen	5.8 ± 0.1	5.5 ± 0.1
Nitrogen	3.1 ± 0.1	3.0 ± 0.1
Sulphur	n.d	n.d
Oxygen ^[a]	30.3 ± 0.3	33.2 ± 0.5
Degree of deoxygenation (%)	14.6	14.1
H/C	1.15 ± 0.02	1.13 ± 0.04
O/C	0.37 ± 0.01	0.43 ± 0.01
H/C _{eff}	0.41	0.27
HHV (MJ/kg)	24.9 ± 0.2	23.3 ± 0.1

^[a] calculated by difference



In summary, a family of bioactive compounds based on 3-hydroxypyridines could be extracted from the organic phase previously discarded MW-hydrolysate stream and separated by distillation. The subsequent catalytic hydrotreatment of the organic extract permit the additional synthesis of the fuel additives such as diethyl succinic acid (DES) and partially deoxygenated fuel intermediates.

5.3.4 OVERALL MASS BALANCES

From a commercial viewpoint, the nanocellulose production as part of a fully integrated biorefinery concept seems a more realistic solution than a single product-based production scheme. In this Chapter, an exploratory assessment for effluents management was addressed, drawing additional co-products to support the nanocellulose extraction. The Sankey diagram of this process is outlined in Figure 5.8, where the arrow width is proportional to the flow rate.

By this approach, it was possible to recover 7.9 wt. % of the whole biomass as sugar alcohols, which approximately represents 40.7 % of the total hemicellulose (19.4 %). Assuming that cellulose portion (12.6 %) was almost entirely recovered as cellulose nanofibrils, it can be roughly estimated that around 64.1 wt. % of the structural carbohydrate composition of almond hulls (i.e., the sum of cellulose and hemicelluloses) was successfully converted to speciality chemicals. At the same time, the implementation of extraction methodologies enabled the valorisation of an additional 19.8 % of the C contained in the EF-2 as a chemicals-rich oil. Despite the apparently low levels of bio-oil extraction (9.2 % of the mass yield), this fraction may represent a relatively large weight of the initial mass biomass (8.1 wt. %) when the flow mass of this stream (83.2 %) is considered. The extracted phase was then catalytically hydrotreated into stable intermediates and fuel additives (diethyl ester of succinic acid), including an inter-stage separation of bioactive compounds (3-hydroxypyridine, 1.5 wt. %). On the whole, up to 37.8 % of the initial mass could be recovered as valuable chemicals, which



introduces an enhancement on the recovery efficiency of 42.3 % when it is compared with the earlier scheme for nanocellulose production.

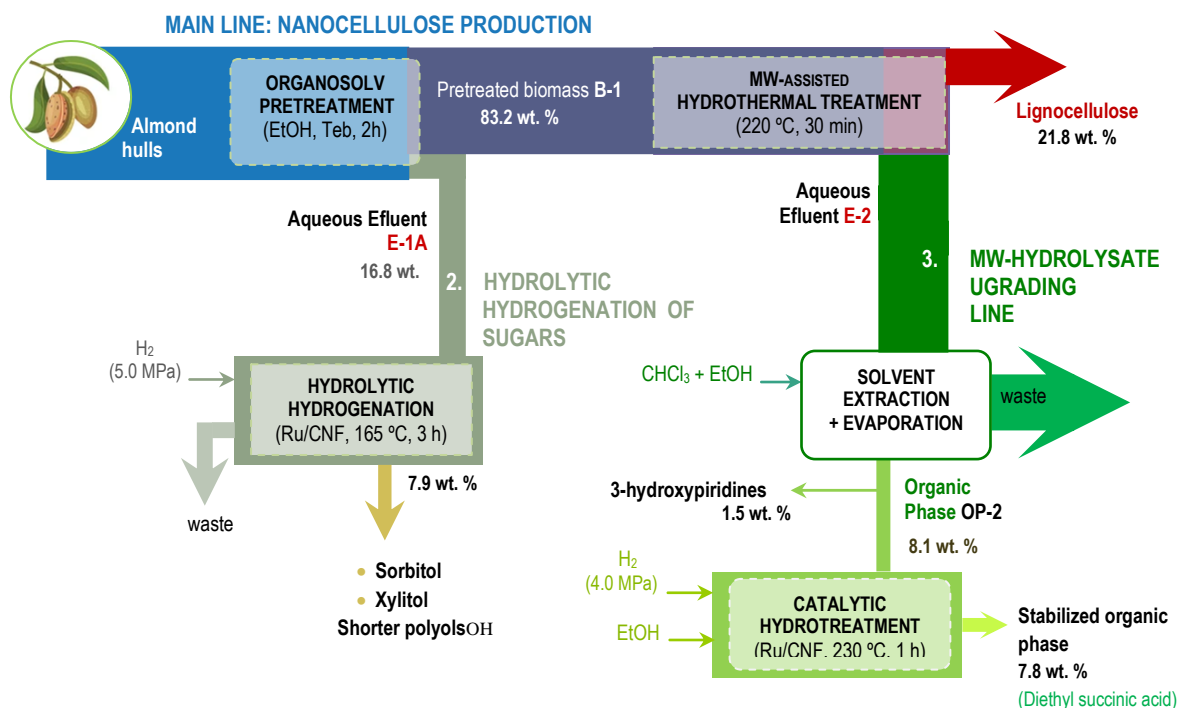


Figure 5.8 Sankey diagram for nanocellulose biorefinery concept from almond hulls.

5.4 Conclusions

Production of nanocellulose from almond hulls opens new business opportunities from a by-product currently under-utilized and cumulated in huge amounts from the agro industry. To ensure the economic and sustainability profile of this process, however, all side-streams should be integrated within the overall processing strategy, taking advantage of feedstock fractioning and plausible product synergies.

In this case, the biomass pre-treatment in ethanol generates a sugar-rich liquor readily amenable to be converted into sugar alcohols by hydrolytic hydrogenation. Soft reaction conditions (i.e., 165 °C, 3 h) and 5.0 MPa of H₂ pressure guarantee the high selectivity toward sorbitol and xylitol (40.5 % of total C) when using a ruthenium supported catalysts (Ru/CNF). Harsher conditions (i.e., 190 °C), however, lead to the rupture of the carbon chain and the formation of a wider spectrum of polyols: 14.0 % of C6-hexitol, 3.7 % of C5-pentitol and 16.5 % of C2-C4 polyols.

Soluble products from the spent effluent derived from the MW-liquefaction step can be further recovered and concentrated by extraction using ethyl acetate and chloroform as solvents, affording an organic fraction with a maximum mass yield of 9.7 %. It is especially noteworthy that some chemicals present on this fraction can offer complementary valorization opportunities. For instance, 3-hydroxypyridines released from the biomass proteins and sugars degradation reactions were selectively extracted in relatively high yields, accounting up to 18.2 wt. % of the organic phase. These are N-heterocyclics structures useful for the synthesis medical drugs and agricultural chemicals.

The modular design of this process enhances the product flexibility and illustrates how the hydrolytic hydrogenation reaction can be integrated within a real process. Moreover, the same reaction concept can be further generalized to other applications such as the catalytic hydrotreatment of organic phases to stabilize and partially deoxygenate bio-oils that are apt for



subsequent upgrading to hydrocarbons. Some of the compounds present in this phase could optionally be isolated and served as fuel additives (diethyl succinic acid).

Clearly, the approach presented in this work depicts a competitive landscape for nanocellulose production, recovering sugar alcohols (sorbitol and xilitols), 3-hydroxypyridines and fuel precursors and/or additives (diethyl succinic acid) as value added co-products.

Main conclusions



Main conclusions

Selective conversion of cellulose, as the mayor component of biomass, is one of the main issues in the successful development of the upcoming biorefinery concept. The uniform and polyfunctional nature of this biopolymer, composed exclusively by glucose units, make it an ideal precursor for the synthesis of valuable products with minimal alteration on the parent molecule. However, such chemical simplicity at a molecular level belies a complex crystalline assembly, conferring it with high stability. As a corollary, the intermediates products are often more reactive than cellulose itself, undergoing a series of parallel and consecutive pathways that complicates the initial reaction network. This fact makes difficult to draw individual target products in high throughput, whose net yield is the result of a subtle interplay between the cellulose reactivity and process conditions by one hand, and the catalyst activity on the other.

With this backdrop, this Thesis outlined various chemocatalytic strategies based on carbon nanostructures for two processes of cellulose conversion: i) the hydrolysis of cellulose into glucose using low dimensional carbons; and ii) the hydrolytic hydrogenation to sugar alcohols (mainly sorbitol) on metal supported carbons.

The blueprints of catalytic hydrolysis were essentially controlled by the limited interaction between solid cellulose and the active sites of the granular carbon. Two main tools were used to stretch the contact between both solids: favouring the accessibility of the substrate through ball-milling pre-treatment and the morphological modulation of the catalyst. In addition, the presence of weakly acid oxygenated functionalities onto the catalyst surface became indispensable as cellulose binders. An effective molecular interaction was achieved by means of a soft mix-milling stage (600 rpm, 10 min) and using a catalyst with high amount of functional groups (54.7% O and 6.1% S) and sterically accesibles as dimensionless structures based on GOQD offer. In this manner, complete conversion of cellulose and glucose yields as high as 83.5% was attained within 24 h at 135 °C. Lower conversion levels (89.5% and 98.2%) and glucose percentages (60.4 and 71.3%) were obtained from FLGO and GONF, respectively. Yet,



long residence times and mild conditions had to be used to balance the hydrolysis rate against sugar degradation reactions. Harnessing the good dielectric properties of carbon materials, the use of microwave energy as alternative heating source was later assessed to reduce the hydrolysis time. The maximum glucose production (63.7 %), was reached using GOQD as catalyst after only 20 min under MW-radiation at 165 °C but treating solutions with a rather higher concentration ratios (2.0 wt. % instead of 0.25 wt. %), which is a significant contribution towards the process intensification.

Direct synthesis of sorbitol from cellulose (*one-pot* conversion) is another promising valorisation route. The signature feature of this approach relies on the use of water acidity released from subcritical conditions on the hydrolysis step coupled with hydrogenation of sugars on supported metal catalysts under a H₂ source. The effectiveness of the process based on some key elements, such as designing catalysts with high hydrogenation ability (determined by metal composition, weight loading and particle size), delimiting the operational conditions of the system (reaction time and temperature) in addition to mass-transfer effects (H₂ pressure and cellulose crystallinity). In this contribution, the correlation between each parameter and the product spectrum was discussed on the basis of the reaction mechanism using various Ni-based catalysts supported on carbon nanofibers. The highest sugar alcohols yield (77.0 % of total polyols; 61.5 % of sorbitol) was obtained from amorphous cellulose after 26 h at 190 °C and 8.0 MPa H₂, including an additional mix-milling stage of 30 min. For these experiments, a Ni/CNF catalyst prepared by conventional dry impregnation (10.7 wt. % of Ni, mean diameter of 11.3 nm) was used. An important advance in this field was the substitution of noble metals to earth-abundant metals like Ni, bringing down the catalyst costs.

An outlier strategy for cellulose valorization is the separation of crystalline fibrils bundles, useful as standalone product in the field of materials science. This option might be of the higher efficiency since it avoids the need of pre-treatments to decrystallize the macromolecular structure. Following a previous work, cellulose microfibrils can be isolated from natural resources like almond hulls through a MW-assisted hydrothermal process (200 °C, 30 min)



preceded by an ethanol-solv stage. A value gap exists, however, when the spent liquors are discarded, as they may be source of additional co-products. Through a biorefinery approach that combines catalytic hydrogenation and extraction stages, the work included in this Thesis demonstrated that there is still significant chance to upgrade these effluents. For instance, sugars from hemicellulose appear as an intermediate stream of the nanocellulose production chain, which were catalytically hydrogenated (Ru/CNF, 165 °C, 3h, 5.0 MPa H₂) to value-added sugar alcohols (sorbitol and xylitol) with relatively high yield (47.4 %). Besides, a family of bioactive molecules based on 3-hydroxypyridines along with stabilized organic oil was extracted from the previous discarded MW-hydrolysate stream, with the latter including diethyl succinic acid in their volatile fraction. This approach, not only allows the recovery of an additional pool of marketable products to support the profitability of the nanocellulose trade but also marks a promising convergence for simultaneous valorisation of cellulose and hemicellulose fractions, often characterized by different reactivities.



Conclusiones principales

La conversión selectiva de celulosa, como componente principal de la biomasa, es uno de los principales desafíos en el desarrollo del concepto de biorrefinería. Por su estructura química uniforme y polifuncional, formada exclusivamente por unidades de glucosa, la celulosa podría ser un precursor ideal para la síntesis de productos de alto valor añadido con mínimas alteraciones en la molécula de partida. Sin embargo, esta simplicidad a nivel molecular contrasta con la complejidad de su empaquetamiento cristalino, haciéndola insoluble en el medio acuoso y resistente a las transformaciones químicas. Este hecho dificulta la obtención de rendimientos elevados de productos individuales, a menudo más reactivos que la celulosa de partida, desencadenando una serie de reacciones paralelas y/o consecutivas que complican el esquema de reacción inicial y cuyo rendimiento final es el resultado neto de un balance entre la reactividad de la celulosa y las condiciones del proceso por un lado, y la actividad catalítica por otro.

Con este telón de fondo, esta Tesis ha abordado varias estrategias catalíticas heterogéneas basadas en el uso de nanoestructuras de carbono en dos procesos de conversión de celulosa: i) despolimerización ácida en sus azúcares constituyentes mediante materiales de carbono de tipo grafénico (0D y 2D); y ii) la hidrogenación hidrolítica de celulosa en azúcares polialcohólicos (principalmente sorbitol) a través de catalizadores metálicos soportados sobre nanofibras de carbono.

La reacción de hidrólisis catalítica está esencialmente marcada por la baja interacción entre la celulosa cristalina y los sitios activos del catalizador granular carbonoso. Para mejorar este contacto se utilizaron dos herramientas principales: i) promover la accesibilidad de la celulosa inicial con técnicas de pre-tratamiento mecánico (molienda); y ii) la modulación morfológica del catalizador. Además, la presencia de grupos funcionales oxigenados de carácter débilmente ácido fue fundamental para el mejor contacto entre la celulosa y la superficie del catalizador. Se consiguió una interacción molecular efectiva entre ambos sólidos tras la molienda conjunta de



catalizador y celulosa durante 10 min (mix-milling, 600 rpm). Los mejores resultados se obtuvieron usando estructuras adimensionales basadas en GOQD como catalizador, decoradas con numerosos grupos funcionales (54.7% O y 6.1% S) estéricamente accesibles, alcanzando la conversión completa de celulosa (83.5% en glucosa) tras 24 h a 135 °C. Las fracciones basadas en FLGO and GONF mostraron comparativamente actividades catalíticas inferiores, tanto en términos de conversión (89.5% y 98.2%) como de rendimiento a glucosa (60.4 y 71.3%), respectivamente. No obstante, la aplicación de sistemas de calentamiento convencional para la activación de la reacción exigió trabajar en condiciones de temperatura suaves y largos tiempos de residencia, necesarios para lograr el control cinético del frágil equilibrio que separa la hidrólisis de celulosa de la degradación de los azúcares. En este contexto, la eficiencia del proceso se mejoró mediante el uso de fuentes de calentamiento alternativas basadas en energía microondas, aprovechando las propiedades dieléctricas de los materiales de carbono. La máxima producción de glucosa (63,7%) se alcanzó tras irradiar isotérmicamente (165 °C) una solución de celulosa amorfa (2.0 wt. %) durante 20 min en presencia de GOQD como catalizador. La reducción de la escala de tiempo de días a minutos, así como el empleo de ratios de dilución mayores (2.0 % en peso en lugar de 0.25 % en calentamiento convencional) representan una contribución significativa hacia la intensificación del proceso.

La transformación directa de celulosa en sorbitol (conversión *one-pot*) constituye una alternativa de valorización muy prometedora. La principal característica de esta vía se basa en el uso de la acidez del agua en condiciones subcríticas para facilitar la etapa de hidrólisis, seguida de la hidrogenación de los azúcares en presencia de partículas metálicas y atmosfera reductora. La eficacia del proceso se basa en algunos elementos clave, tales como el diseño de catalizadores con alta capacidad de hidrogenación (determinada por la composición de la fase metálica, su fracción en peso y el tamaño de partícula) y la correcta definición de los límites operacionales del sistema (tiempo y temperatura) además de los aspectos difusionales (presión de H₂ y cristalinidad de la celulosa inicial). En esta Tesis, el efecto de cada parámetro sobre la distribución de productos se discutió a partir del mecanismo de reacción utilizando varios



catalizadores de Ni soportados sobre nanofibras de carbono. El mayor rendimiento de azúcares polihídricos (77.0 % de polioles totales; 61.5 % de sorbitol) se alcanzó tras el procesamiento de celulosa amorfa a 190 °C y 8.0 MPa H₂ durante 26 h, incluyendo una etapa adicional de 30 min de mix-milling. En este caso, se utilizó un catalizador Ni/CNF preparado por impregnación húmeda incipiente (10.7 % en peso de Ni, diámetro medio de 11.3 nm). Un avance importante de esta propuesta fue la sustitución de metales nobles por el Ni, reduciendo significativamente los costes del catalizador.

Una estrategia diferente para la utilización de celulosa es la separación en sus fibras cristalinas elementales, de interés en el área de ciencia de materiales. Esta opción puede ser más eficiente, al eludir la necesidad de técnicas de pre-tratamiento que rompen su estructura macromolecular. Las microfibrillas de celulosa pueden ser extraídas de distintos tipos de biomásas naturales como los pericarpios de almendra a través de un tratamiento hidrotermal asistido por microondas (200 °C, 30 min) precedido de un proceso organosolv en etanol, tal y como se demostró en un trabajo anterior. Los efluentes generados durante este proceso pueden ser fuente de productos químicos de interés industrial. A través de una propuesta de biorefinería que combina tecnologías de hidrogenación catalítica y extracción, el trabajo incluido en esta Tesis demostró el potencial de valorización de estas corrientes. Por ejemplo, los azúcares de hemicelulosa que aparecen como una corriente intermedia de la cadena de producción de nanocelulosa se pueden hidrogenar hidrolíticamente a sorbitol y xilitol en porcentajes relativamente altos (47.4 %) en presencia de un catalizador de Ru/CNF tras 3 h de reacción a 165 °C y 5.0 MPa H₂. Además, del efluente hidrolizado procedente del tratamiento hidrotermal por microondas es posible extraer una familia de moléculas bioactivas basadas en las 3-hidroxipiridinas, junto con una fase orgánica estabilizada que incluye en su fracción volátil compuestos como el ácido dietil succínico. Este esquema de biorefinería, no sólo permite la recuperación adicional de un conjunto de productos para reforzar la rentabilidad comercial de la producción de nanocelulosa, sino que también representan una oportunidad para la valorización simultánea de las fracciones de celulosa y hemicelulosa, caracterizadas por una reactividad intrínsecamente diferente.

References

References

- [1] G.W. Huber, S. Iborra, A. Corma, Synthesis of Transportation Fuels from Biomass: Chemistry, Catalysts, and Engineering, *Chemical Reviews* 106(9) (2006) 4044-4098.
- [2] Y.H.P. Zhang, Reviving the carbohydrate economy via multi-product lignocellulose biorefineries, *Journal of Industrial Microbiology & Biotechnology* 35(5) (2008) 367-375.
- [3] D.C. Department Of Energy Washington, Roadmap for Biomass Technologies in the United States, 2002. <http://www.dtic.mil/docs/citations/ADA436527>.
- [4] P. National Research Council Committee on Biobased Industrial, Biobased Industrial Products: Priorities for Research and Commercialization, National Academies Press (US), Washington (DC), 2000.
- [5] L. Janeiro, L. Gutierrez, G. Prakash, D. Saygin, IRENA REmap EU 2018 - Renewable energy prospects for the European Union, REmap analysis to 2030, (2018).
- [6] A.M. Ruppert, K. Weinberg, R. Palkovits, Hydrogenolysis goes bio: from carbohydrates and sugar alcohols to platform chemicals, *Angewandte Chemie International Edition* 51(11) (2012) 2564-601.
- [7] A. Corma, S. Iborra, A. Velty, Chemical Routes for the Transformation of Biomass into Chemicals, *Chemical Reviews* 107(6) (2007) 2411-2502.
- [8] O.R. Inderwildi, D.A. King, Quo vadis biofuels?, *Energy & Environmental Science* 2(4) (2009) 343-346.
- [9] P. Yang, H. Kobayashi, A. Fukuoka, Recent Developments in the Catalytic Conversion of Cellulose into Valuable Chemicals, *Chinese Journal of Catalysis* 32(5) (2011) 716-722.
- [10] P. Lanzafame, G. Centi, S. Perathoner, Catalysis for biomass and CO₂ use through solar energy: opening new scenarios for a sustainable and low-carbon chemical production, *Chemical Society Reviews* 43(22) (2014) 7562-7580.
- [11] J.-P. Lange, Lignocellulose conversion: an introduction to chemistry, process and economics, *Biofuels, Bioproducts and Biorefining* 1(1) (2007) 39-48.
- [12] G. Berndes, B. Abt, A. Antti, A. Cowie, V. Dale, E. Gustaf, M. Lindner, L. Marelli, D. Paré, K. Pingoud, S. Yeh, Forest biomass, carbon neutrality and climate change mitigation. *From Science to Policy* 3 (2016).
- [13] R. Palkovits, I. Delidovich, Efficient utilization of renewable feedstocks: The role of catalysis and process design, *Philosophical Transactions of The Royal Society A Mathematical Physical and Engineering Sciences* 376 (2018) 20170064.
- [14] R. Rinaldi, F. Schuth, Design of solid catalysts for the conversion of biomass, *Energy & Environmental Science* 2 (2009) 610.
- [15] Y. Liao, B.O. de Beeck, K. Thielemans, T. Ennaert, J. Snelders, M. Dusselier, C.M. Courtin, B.F. Sels, The role of pretreatment in the catalytic valorization of cellulose, *Molecular Catalysis* 487 (2020) 110883.

- [16] M.E. Himmel, S.Y. Ding, D.K. Johnson, W.S. Adney, M.R. Nimlos, J.W. Brady, T.D. Foust, Biomass recalcitrance: engineering plants and enzymes for biofuels production, *Science (New York, N.Y.)* 315(5813) (2007) 804-7.
- [17] A. Barakat, H. de Vries, X. Rouau, Dry fractionation process as an important step in current and future lignocellulose biorefineries: A review, *Bioresource Technology* 134 (2013) 362-373.
- [18] D. Klemm, B. Heublein, H.-P. Fink, A. Bohn, Cellulose: Fascinating Biopolymer and Sustainable Raw Material, *Angewandte Chemie International Edition* 44(22) (2005) 3358-3393.
- [19] T. Heinze, Cellulose: Structure and Properties, In: Rojas O. (eds) *Cellulose Chemistry and Properties: Fibers, Nanocelluloses and Advances Materials. Advances in Polymer Science*, Springer Cham (Switzerland), 271 (2015) 1-52.
- [20] F.M. Gírio, C. Fonseca, F. Carvalheiro, L.C. Duarte, S. Marques, R. Bogel-Lukasik, Hemicelluloses for fuel ethanol: A review, *Bioresource Technology* 101(13) (2010) 4775-4800.
- [21] Y. Pu, D. Zhang, P.M. Singh, A.J. Ragauskas, The new forestry biofuels sector, *Biofuels, Bioproducts and Biorefining* 2(1) (2008) 58-73.
- [22] L. Negahdar, I. Delidovich, R. Palkovits, Aqueous-phase hydrolysis of cellulose and hemicelluloses over molecular acidic catalysts: Insights into the kinetics and reaction mechanism, *Applied Catalysis B: Environmental* 184 (2016) 285-298.
- [23] J. Zakzeski, P.C.A. Bruijninx, A.L. Jongerius, B.M. Weckhuysen, The Catalytic Valorization of Lignin for the Production of Renewable Chemicals, *Chemical Reviews* 110(6) (2010) 3552-3599.
- [24] S. Kang, X. Li, J. Fan, J. Chang, Hydrothermal conversion of lignin: A review, *Renewable and Sustainable Energy Reviews* 27 (2013) 546-558.
- [25] P.Y. Dapsens, C. Mondelli, J. Pérez-Ramírez, Biobased Chemicals from Conception toward Industrial Reality: Lessons Learned and To Be Learned, *ACS Catalysis* 2(7) (2012) 1487-1499.
- [26] A. Kumar, D.D. Jones, M.A. Hanna, Thermochemical Biomass Gasification: A Review of the Current Status of the Technology, *Energies* 2(3) (2009) 556-581.
- [27] T.L. Duong, P. Prasertcharoensuk, A. Phan, Biofuel Production from Lignocellulosic Feedstock via Thermochemical Routes, in: *Liquid Biofuel Production* (eds L.K. Singh and G. Chaudhary), Wiley, USA, (2019), 89-166.
- [28] M.F. Demirbas, M. Balat, Recent advances on the production and utilization trends of bio-fuels: A global perspective, *Energy Conversion and Management* 47(15) (2006) 2371-2381.
- [29] D. Esposito, M. Antonietti, Redefining biorefinery: the search for unconventional building blocks for materials, *Chemical Society Reviews* 44(16) (2015) 5821-5835.
- [30] P.N.R. Vennestrøm, C.M. Osmundsen, C.H. Christensen, E. Taarning, Beyond Petrochemicals: The Renewable Chemicals Industry, *Angewandte Chemie International Edition* 50(45) (2011) 10502-10509.
- [31] P. Gallezot, Conversion of biomass to selected chemical products, *Chemical Society Reviews* 41(4) (2012) 1538-1558.
- [32] P. Gallezot, Catalytic Conversion of Biomass: Challenges and Issues, *ChemSusChem* 1 (2008) 734-7.

- [33] P. Gallezot, Process options for converting renewable feedstocks to bioproducts, *Green Chemistry* 9(4) (2007) 295-302.
- [34] M. Dusselier, M. Mascal, B.F. Sels, Top Chemical Opportunities from Carbohydrate Biomass: A Chemist's View of the Biorefinery, in: K.M. Nicholas (Ed.), *Selective Catalysis for Renewable Feedstocks and Chemicals*, Springer International Publishing, Cham, 2014, pp. 1-40.
- [35] A.R. Ardiyanti, R. Venderbosch, W. Yin, H.J. Heeres, Catalytic hydrotreatment of fast pyrolysis oils using supported metal catalysts, *RSC Energy and Environment Series 2015* (2015) 151-173.
- [36] W. Schutyser, T. Renders, S. Van den Bosch, S.F. Koelewijn, G.T. Beckham, B.F. Sels, Chemicals from lignin: an interplay of lignocellulose fractionation, depolymerisation, and upgrading, *Chemical Society Reviews* 47(3) (2018) 852-908.
- [37] F. Carneiro, L. Duarte, F. Gírio, Hemicellulose biorefineries: A review on biomass pretreatments, *Journal of scientific and industrial research* 67 (2008) 849-864.
- [38] F. Carneiro, L.C. Duarte, F. Gírio, P. Moniz, Chapter 14 - Hydrothermal/Liquid Hot Water Pretreatment (Autohydrolysis): A Multipurpose Process for Biomass Upgrading, in: S.I. Mussatto (Ed.), *Biomass Fractionation Technologies for a Lignocellulosic Feedstock Based Biorefinery*, Elsevier, Amsterdam, (2016), 315-347.
- [39] B. Yang, C.E. Wyman, Effect of xylan and lignin removal by batch and flowthrough pretreatment on the enzymatic digestibility of corn stover cellulose, *Biotechnology and bioengineering* 86(1) (2004) 88-95.
- [40] S. Bhagia, H. Li, X. Gao, R. Kumar, C.E. Wyman, Flowthrough pretreatment with very dilute acid provides insights into high lignin contribution to biomass recalcitrance, *Biotechnology for Biofuels* 9(1) (2016) 245.
- [41] L. Shuai, M.T. Amiri, Y.M. Questell-Santiago, F. Héroguel, Y. Li, H. Kim, R. Meilan, C. Chapple, J. Ralph, J.S. Luterbacher, Formaldehyde stabilization facilitates lignin monomer production during biomass depolymerization, *Science* 354(6310) (2016) 329-333.
- [42] S. Qiu, M. Wang, Y. Fang, T. Tan, Reductive catalytic fractionation of lignocellulose: when should the catalyst meet depolymerized lignin fragments?, *Sustainable Energy & Fuels* 4(11) (2020) 5588-5594.
- [43] I. Delidovich, K. Leonhard, R. Palkovits, Cellulose and hemicellulose valorisation: an integrated challenge of catalysis and reaction engineering, *Energy & Environmental Science* 7(9) (2014) 2803-2830.
- [44] T. Werpy, J. Holladay, J. White, *Top Value Added Chemicals From Biomass: I. Results of Screening for Potential Candidates from Sugars and Synthesis Gas*, (2004).
- [45] J. Bozell, G. Petersen, Technology development for the production of biobased products from biorefinery carbohydrates—the US Department of Energy's "Top 10" revisited, *Green Chemistry* 12 (2010) 539-554.
- [46] P. Bhaumik, P. Dhepe, Conversion of Biomass into Sugars, in: *Biomass Sugars for Non-Fuel Applications*, RSC Green Chemistry No.44, Cambridge, UK (2015), 1-53.



- [47] R. Rinaldi, F. Schueth, Acid Hydrolysis of Cellulose as the Entry Point into Biorefinery Schemes, *ChemSusChem* 2 (2009) 1096-1107.
- [48] L. Hu, L. Lin, Z. Wu, S. Zhou, S. Liu, Chemocatalytic hydrolysis of cellulose into glucose over solid acid catalysts, *Applied Catalysis B: Environmental* 174-175 (2015) 225-243.
- [49] J.A. Geboers, S. Van de Vyver, R. Ooms, B. Op de Beeck, P.A. Jacobs, B.F. Sels, Chemocatalytic conversion of cellulose: opportunities, advances and pitfalls, *Catalysis Science & Technology* 1(5) (2011) 714-726.
- [50] C.-H. Zhou, X. Xia, C.-X. Lin, D.-S. Tong, J. Beltramini, Catalytic conversion of lignocellulosic biomass to fine chemicals and fuels, *Chemical Society Reviews* 40(11) (2011) 5588-5617.
- [51] A. Sheikhi, Chapter 9 - Emerging Cellulose-Based Nanomaterials and Nanocomposites, in: N. Karak (Ed.), *Nanomaterials and Polymer Nanocomposites*, Elsevier (2019), 307-351.
- [52] Y.-B. Huang, Y. Fu, Hydrolysis of cellulose to glucose by solid acid catalysts, *Green Chemistry* 15(5) (2013) 1095-1111.
- [53] R. Palkovits, K. Tajvidi, J. Procelewska, R. Rinaldi, A. Ruppert, Hydrogenolysis of cellulose combining mineral acids and hydrogenation catalysts, *Green Chemistry* 12 (2010) 972-978.
- [54] M. Rose, R. Palkovits, Cellulose-Based Sustainable Polymers: State of the Art and Future Trends, *Macromolecular rapid communications* 32 (2011), 1299-1311.
- [55] A. Shrotri, H. Kobayashi, A. Fukuoka, Recent Developments in the Use of Porous Carbon Materials for Cellulose Conversion, in: *Nanoporous Catalysts for Biomass Conversion*, Wiley, United States, US (2017), 79-98.
- [56] H. Staudinger, Über Polymerisation, *Berichte der deutschen chemischen Gesellschaft (A and B Series)* 53(6) (1920) 1073-1085.
- [57] D. Mohan, C.U. Pittman, P.H. Steele, Pyrolysis of Wood/Biomass for Bio-oil: A Critical Review, *Energy & Fuels* 20(3) (2006) 848-889.
- [58] M. Winger, M. Christen, W.F. van Gunsteren, On the Conformational Properties of Amylose and Cellulose Oligomers in Solution, *International Journal of Carbohydrate Chemistry* 2009 (2009) 307695.
- [59] M. Poletto, V. Pistor, A. Zattera, Structural Characteristics and Thermal Properties of Native Cellulose, in: *Cellulose-Fundamental Aspects*, Ed. Theo van de Ven; Louis Godbout, InTech, Croatia (2013), 45-68.
- [60] M. Jarvis, Chemistry - Cellulose stacks up, *Nature* 426 (2004) 611-2.
- [61] Y. Nishiyama, P. Langan, H. Chanzy, Crystal Structure and Hydrogen-Bonding System in Cellulose I β from Synchrotron X-ray and Neutron Fiber Diffraction, *Journal of the American Chemical Society* 124(31) (2002) 9074-9082.
- [62] T. Ennaert, B. Op de Beeck, J. Vanneste, A.T. Smit, W.J.J. Huijgen, A. Vanhulsel, P.A. Jacobs, B.F. Sels, The importance of pretreatment and feedstock purity in the reductive splitting of (ligno)cellulose by metal supported USY zeolite, *Green Chemistry* 18(7) (2016) 2095-2105.



- [63] S. Coseri, Cellulose: To depolymerize... or not to?, *Biotechnology Advances* 35(2) (2017) 251-266.
- [64] J. Verendel, T. Church, P. Andersson, Catalytic One-Pot Production of Small Organics from Polysaccharides, *Synthesis* 2011 (2011) 1649-1677.
- [65] V. Jollet, F. Chambon, F. Rataboul, A. Cabiac, C. Pinel, E. Guillon, N. Essayem, Non-catalyzed and Pt/ γ -Al₂O₃-catalyzed hydrothermal cellulose dissolution–conversion: influence of the reaction parameters and analysis of the unreacted cellulose, *Green Chemistry* 11(12) (2009) 2052-2060.
- [66] J.F. Saeman, Kinetics of Wood Saccharification - Hydrolysis of Cellulose and Decomposition of Sugars in Dilute Acid at High Temperature, *Industrial & Engineering Chemistry* 37(1) (1945) 43-52.
- [67] E.E. Harris, E. Beglinger, Madison Wood Sugar Process, *Industrial & Engineering Chemistry* 38(9) (1946) 890-895.
- [68] M.C. Hawley, S.M. Selke, D.T.A. Lamport, Comparison of hydrogen fluoride saccharification of lignocellulosic materials with other saccharification technologies, *Energy in Agriculture* 2 (1983) 219-244.
- [69] D.R. Thompson, H.E. Grethlein, Design and Evaluation of a Plug Flow Reactor for Acid Hydrolysis of Cellulose, *Industrial & Engineering Chemistry Product Research and Development* 18(3) (1979) 166-169.
- [70] F. Bergius, Conversion of Wood To Carbohydrates, *Industrial & Engineering Chemistry* 29(3) (1937) 247-253.
- [71] J. Harris, A. Baker, A.H. Conner, T. Jeffries, J. Minor, Two-stage, dilute sulfuric acid hydrolysis of wood: an investigation of fundamentals. Forest Service general technical report (Final), 1985.
- [72] K. Vigier, F. Jérôme, Heterogeneously-Catalyzed Conversion of Carbohydrates, *Topics in current chemistry* 295 (2010) 63-92.
- [73] G. Centi, S. Perathoner, D. Su, Nanocarbons: Opening New Possibilities for Nano-engineered Novel Catalysts and Catalytic Electrodes, *Catalysis Surveys from Asia* 18 (2014) 149-163.
- [74] A. Shrotri, H. Kobayashi, A. Fukuoka, Recent Developments in the Use of Porous Carbon Materials for Cellulose Conversion, *Nanoporous Catalysts for Biomass Conversion* 2017, pp. 79-98.
- [75] S. Suganuma, K. Nakajima, M. Kitano, D. Yamaguchi, H. Kato, S. Hayashi, M. Hara, Hydrolysis of cellulose by amorphous carbon bearing SO₃H, COOH, and OH groups, *Journal of the American Chemical Society* 130(38) (2008) 12787-93.
- [76] Y. Delgado Arcaño, O.D. Valmaña García, D. Mandelli, W.A. Carvalho, L.A. Magalhães Pontes, Xylitol: A review on the progress and challenges of its production by chemical route, *Catalysis Today* 344 (2020) 2-14.
- [77] N. Akiya, P.E. Savage, Roles of Water for Chemical Reactions in High-Temperature Water, *Chemical Reviews* 102(8) (2002) 2725-2750.
- [78] L. Ribeiro, J.J.M. Órfão, M. Pereira, Comparative study of different catalysts on the direct conversion of cellulose to sorbitol, *Green Processing and Synthesis* 4(2015), 71-78.

- [79] A. Fukuoka, P.L. Dhepe, Catalytic Conversion of Cellulose into Sugar Alcohols, *Angewandte Chemie International Edition* 45(31) (2006) 5161-5163.
- [80] C. Luo, S. Wang, H. Liu, Cellulose Conversion into Polyols Catalyzed by Reversibly Formed Acids and Supported Ruthenium Clusters in Hot Water, *Angewandte Chemie International Edition* 46(40) (2007) 7636-7639.
- [81] W. Deng, X. Tan, W. Fang, Q. Zhang, Y. Wang, Conversion of Cellulose into Sorbitol over Carbon Nanotube-Supported Ruthenium Catalyst, *Catalysis Letters* 133(1) (2009) 167-174.
- [82] J. Pang, A. Wang, M. Zheng, Y. Zhang, Y. Huang, X. Chen, T. Zhang, Catalytic conversion of cellulose to hexitols with mesoporous carbon supported Ni-based bimetallic catalysts, *Green Chemistry* 14(3) (2012) 614-617.
- [83] H. Kobayashi, Y. Ito, T. Komanoya, Y. Hosaka, P.L. Dhepe, K. Kasai, K. Hara, A. Fukuoka, Synthesis of sugar alcohols by hydrolytic hydrogenation of cellulose over supported metal catalysts, *Green Chemistry* 13(2) (2011) 326-333.
- [84] I.C. Gerber, P. Serp, A Theory/Experience Description of Support Effects in Carbon-Supported Catalysts, *Chemical Reviews* 120(2) (2020) 1250-1349.
- [85] L.S. Ribeiro, J.J. Delgado, J.J. de Melo Órfão, M.F.R. Pereira, Direct conversion of cellulose to sorbitol over ruthenium catalysts: Influence of the support, *Catalysis Today* 279 (2017) 244-251.
- [86] L. S. Ribeiro, J.J.M. Órfão, M.F. R. Pereira, Enhanced direct production of sorbitol by cellulose ball-milling, *Green Chemistry* 17(5) (2015) 2973-2980.
- [87] M. Benoit, A. Rodrigues, Q. Zhang, E. Fourré, K. De Oliveira Vigier, J.-M. Tatibouët, F. Jérôme, Depolymerization of Cellulose Assisted by a Nonthermal Atmospheric Plasma, *Angewandte Chemie International Edition* 50(38) (2011) 8964-8967.
- [88] H. Kobayashi, M. Yabushita, T. Komanoya, K. Hara, I. Fujita, A. Fukuoka, High-Yielding One-Pot Synthesis of Glucose from Cellulose Using Simple Activated Carbons and Trace Hydrochloric Acid, *ACS Catalysis* 3(4) (2013) 581-587.
- [89] M. Yabushita, H. Kobayashi, K. Hara, A. Fukuoka, Quantitative evaluation of ball-milling effects on the hydrolysis of cellulose catalysed by activated carbon, *Catalysis Science & Technology* 4(8) (2014) 2312-2317.
- [90] Y. Liao, Q. Liu, T. Wang, J. Long, Q. Zhang, L. Ma, Y. Liu, Y. Li, Promoting Hydrolytic Hydrogenation of Cellulose to Sugar Alcohols by Mixed Ball Milling of Cellulose and Solid Acid Catalyst, *Energy & Fuels* 28(9) (2014) 5778-5784.
- [91] E. Lam, J.H.T. Luong, Carbon Materials as Catalyst Supports and Catalysts in the Transformation of Biomass to Fuels and Chemicals, *ACS Catalysis* 4(10) (2014) 3393-3410.
- [92] H. Kobayashi, M. Yabushita, A. Fukuoka, Depolymerization of Cellulosic Biomass Catalyzed by Activated Carbons, in: M. Schlaf, Z.C. Zhang (Eds.), *Reaction Pathways and Mechanisms in Thermocatalytic Biomass Conversion I: Cellulose Structure, Depolymerization and Conversion by Heterogeneous Catalysts*, Springer Singapore, Singapore, (2016), 15-26.
- [93] S. Navalon, A. Dhakshinamoorthy, M. Alvaro, H. Garcia, Metal nanoparticles supported on two-dimensional graphenes as heterogeneous catalysts, *Coordination Chemistry Reviews* 312 (2016) 99-148.



- [94] P. Serp, M. Corrias, P. Kalck, Carbon nanotubes and nanofibers in catalysis, *Applied Catalysis A: General* 253(2) (2003) 337-358.
- [95] P. Serp, B. Machado, CHAPTER 1 Carbon (Nano)materials for Catalysis, *Nanostructured Carbon Materials for Catalysis*, The Royal Society of Chemistry, United Kingdom (2015), 1-45.
- [96] I.U. Din, M.S. Shaharun, A. Naeem, M.A. Alotaibi, A.I. Alharthi, M.A. Bakht, Q. Nasir, Carbon nanofibers as potential materials for catalysts support, a mini-review on recent advances and future perspective, *Ceramics International* 46(11, Part B) (2020) 18446-18452.
- [97] J. Zhu, A. Holmen, D. Chen, Carbon Nanomaterials in Catalysis: Proton Affinity, Chemical and Electronic Properties, and their Catalytic Consequences, *ChemCatChem* 5(2) (2013) 378-401.
- [98] F. Jérôme, S. Valange, Rational Design of Nanostructured Carbon Materials: Contribution to Cellulose Processing, *Nanotechnology in Catalysis* (2017), 627-654.
- [99] K. De Jong, J.W. Geus, Carbon Nanofibers: Catalytic Synthesis and Applications, *Catalysis Reviews* 42 (2000), 481-510.
- [100] V. Jiménez, P. Panagiotopoulou, P. Sánchez, J.L. Valverde, A. Romero, Synthesis and characterization of ruthenium supported on carbon nanofibers with different graphitic plane arrangements, *Chemical Engineering Journal* 168(2) (2011) 947-954.
- [101] G. Centi, S. Perathoner, Carbon Nanotubes for Sustainable Energy Applications, *ChemSusChem* 4 (2011) 913-925.
- [102] M. Fedel, Hemocompatibility of Carbon Nanostructures, *Journal of Carbon Research* 6(12) (2020).
- [103] J. Figueiredo, M. Pereira, The role of surface chemistry in catalysis with carbons, *Catalysis Today* 150 (10) 2-7.
- [104] P. Serp, B. Machado, *Nanostructured Carbon Materials for Catalysis*, Royal Society of Chemistry, Cambridge, UK, (2015).
- [105] C. Su, K.P. Loh, Carbocatalysts: Graphene Oxide and Its Derivatives, *Accounts of Chemical Research* 46(10) (2013) 2275-2285.
- [106] P.A. Russo, M.M. Antunes, P. Neves, P.V. Wiper, E. Fazio, F. Neri, F. Barreca, L. Mafra, M. Pillinger, N. Pinna, A.A. Valente, Solid acids with SO₃H groups and tunable surface properties: versatile catalysts for biomass conversion, *Journal of Materials Chemistry A* 2(30) (2014) 11813-11824.
- [107] L.J. Konwar, P. Mäki-Arvela, J.-P. Mikkola, SO₃H-Containing Functional Carbon Materials: Synthesis, Structure, and Acid Catalysis, *Chemical Reviews* 119(22) (2019) 11576-11630.
- [108] B. Garg, T. Bisht, Y. Ling, Graphene-Based Nanomaterials as Heterogeneous Acid Catalysts: A Comprehensive Perspective, *Molecules* 19 (2014) 14582-14614.
- [109] D.T. Gamarra, Nanofilamentos de carbono obtenidos mediante descomposición catalítica de corrientes ricas en metano como precursores de materiales gráficos, Universidad de Zaragoza, Instituto de Carboquímica, CSIC (2016).

- [110] E.O. Bernad, Desoxigenación de biomasa lignocelulósica y oleaginosa mediante catalizadores basados en nanomateriales de carbono, Universidad de Zaragoza, Instituto de Carboquímica, CSIC (2020).
- [111] L. Hu, Y. Luo, B. Cai, J. Li, D. Tong, C. Hu, The degradation of the lignin in *Phyllostachys heterocyclus cv. pubescens* in an ethanol solvothermal system, *Green Chemistry* 16(6) (2014) 3107-3116.
- [112] S.A. Channiwala, P.P. Parikh, A unified correlation for estimating HHV of solid, liquid and gaseous fuels, *Fuel* 81(8) (2002) 1051-1063.
- [113] J.L. Pinilla, S. de Llobet, R. Moliner, I. Suelves, Ni-Co bimetallic catalysts for the simultaneous production of carbon nanofibres and syngas through biogas decomposition, *Applied Catalysis B: Environmental* 200 (2017) 255-264.
- [114] S. de Llobet, J.L. Pinilla, M.J. Lázaro, R. Moliner, I. Suelves, Catalytic decomposition of biogas to produce H₂-rich fuel gas and carbon nanofibers. Parametric study and characterization, *International Journal of Hydrogen Energy* 37(8) (2012) 7067-7076.
- [115] J.L. Pinilla, D. Torres, M.J. Lázaro, I. Suelves, R. Moliner, I. Cañadas, J. Rodríguez, A. Vidal, D. Martínez, Metallic and carbonaceous -based catalysts performance in the solar catalytic decomposition of methane for hydrogen and carbon production, *International Journal of Hydrogen Energy* 37(12) (2012) 9645-9655.
- [116] I. Suelves, M.J. Lázaro, R. Moliner, Y. Echegoyen, J.M. Palacios, Characterization of NiAl and NiCuAl catalysts prepared by different methods for hydrogen production by thermo catalytic decomposition of methane, *Catalysis Today* 116(3) (2006) 271-280.
- [117] S. de Llobet, J.L. Pinilla, R. Moliner, I. Suelves, J. Arroyo, F. Moreno, M. Muñoz, C. Monné, I. Cameán, A. Ramos, N. Cuesta, A.B. Garcia, Catalytic decomposition of biogas to produce hydrogen rich fuels for SI engines and valuable nanocarbons, *International Journal of Hydrogen Energy* 38(35) (2013) 15084-15091.
- [118] M.L. Toebes, F.F. Prinsloo, J.H. Bitter, A.J. van Dillen, K.P. de Jong, Influence of oxygen-containing surface groups on the activity and selectivity of carbon nanofiber-supported ruthenium catalysts in the hydrogenation of cinnamaldehyde, *Journal of Catalysis* 214(1) (2003) 78-87.
- [119] Z. Ma, F. Zaera, Characterization of Heterogeneous Catalysts, in: *Surface and Nanomolecular Catalysis*, Tylor & Francis Group (CRC Press) US, (2006), 1-37.
- [120] F. Barroso-Bujans, J.L.G. Fierro, S. Rojas, S. Sánchez-Cortes, M. Arroyo, M.A. López-Manchado, Degree of functionalization of carbon nanofibers with benzenesulfonic groups in an acid medium, *Carbon* 45(8) (2007) 1669-1678.
- [121] C. Amorim, M.A. Keane, Palladium supported on structured and nonstructured carbon: A consideration of Pd particle size and the nature of reactive hydrogen, *Journal of colloid and interface science* 322(1) (2008) 196-208.
- [122] A. Romero, A. Nieto-Márquez, E. Alonso, Bimetallic Ru:Ni/MCM-48 catalysts for the effective hydrogenation of d-glucose into sorbitol, *Applied Catalysis A: General* 529 (2017) 49-59.
- [123] A. Nieto-Márquez, D. Toledano, P. Sánchez, A. Romero, J.L. Valverde, Impact of nitrogen doping of carbon nanospheres on the nickel-catalyzed hydrogenation of butyronitrile, *Journal of Catalysis* 269(1) (2010) 242-251.



- [124] A.A. Bunaciu, E.G. Udriștioiu, H.Y. Aboul-Enein, X-ray diffraction: instrumentation and applications, *Critical reviews in analytical chemistry* 45(4) (2015) 289-99.
- [125] A.L. Patterson, The Scherrer Formula for X-Ray Particle Size Determination, *Physical Review* 56(10) (1939) 978-982.
- [126] G.A. Dorofeev, A.N. Streletskii, I.V. Povstugar, A.V. Protasov, E.P. Elsukov, Determination of nanoparticle sizes by X-ray diffraction, *Colloid Journal* 74(6) (2012) 675-685.
- [127] L. Segal, C.M. Conrad, J.J. Creely, A.E. Martin, An Empirical Method for Estimating the Degree of Crystallinity of Native Cellulose Using the X-Ray Diffractometer, *Textile Research Journal* 29(10) (1959) 786-794.
- [128] S. Park, J.O. Baker, M.E. Himmel, P.A. Parilla, D.K. Johnson, Cellulose crystallinity index: measurement techniques and their impact on interpreting cellulase performance, *Biotechnology for Biofuels* 3(1) (2010) 1-10.
- [129] J. Song, H. Fan, J. Ma, B. Han, Conversion of glucose and cellulose into value-added products in water and ionic liquids, *Green Chemistry* 15(10) (2013) 2619-2635.
- [130] L. Hu, L. Lin, Z. Wu, S. Zhou, S. Liu, Chemocatalytic Hydrolysis of Cellulose into Glucose over Solid Acid Catalysts, *Applied Catalysis B: Environmental* 174 (2015) 225-243.
- [131] M.J. Climent, A. Corma, S. Iborra, Converting carbohydrates to bulk chemicals and fine chemicals over heterogeneous catalysts, *Green Chemistry* 13(3) (2011) 520-540.
- [132] G. Li, W. Liu, C. Ye, X. Li, C.-L. Si, Chemocatalytic Conversion of Cellulose into Key Platform Chemicals, *International Journal of Polymer Science* 2018 (2018) 1-21.
- [133] F.Z. Azar, M.A. Lillo-Ródenas, M.C. Román-Martínez, Cellulose hydrolysis catalysed by mesoporous activated carbons functionalized under mild conditions, *SN Applied Sciences* 1(12) 1739 (2019) 1-11.
- [134] F. Guo, Z. Fang, C.C. Xu, R.L. Smith, Solid acid mediated hydrolysis of biomass for producing biofuels, *Progress in Energy and Combustion Science* 38(5) (2012) 672-690.
- [135] Y.-B. Huang, Y. Fu, Hydrolysis of Cellulose to Glucose by Solid Acid Catalysts, *Green Chemistry* 15 (2013) 1095-1111.
- [136] S. De, S. Dutta, B. Saha, Critical design of heterogeneous catalysts for biomass valorization: current thrust and emerging prospects, *Catalysis Science & Technology* 6(20) (2016) 7364-7385.
- [137] P.L. Dhepe, A. Fukuoka, Cellulose Conversion under Heterogeneous Catalysis, *ChemSusChem* 1(12) (2008) 969-975.
- [138] Q. Zhang, M. Benoit, K. De Oliveira Vigier, J. Barrault, G. Jégou, M. Philippe, F. Jérôme, Pretreatment of microcrystalline cellulose by ultrasounds: effect of particle size in the heterogeneously-catalyzed hydrolysis of cellulose to glucose, *Green Chemistry* 15(4) (2013) 963-969.
- [139] P. Kumar, D.M. Barrett, M.J. Delwiche, P. Stroeve, Methods for Pretreatment of Lignocellulosic Biomass for Efficient Hydrolysis and Biofuel Production, *Industrial & Engineering Chemistry Research* 48(8) (2009) 3713-3729.



- [140] V.B. Agbor, N. Cicek, R. Sparling, A. Berlin, D.B. Levin, Biomass pretreatment: Fundamentals toward application, *Biotechnology Advances* 29(6) (2011) 675-685.
- [141] A. Shrotri, H. Kobayashi, A. Fukuoka, Cellulose Depolymerization over Heterogeneous Catalysts, *Accounts of Chemical Research* 51(3) (2018) 761-768.
- [142] L. Shuai, X. Pan, Hydrolysis of cellulose by cellulase-mimetic solid catalyst, *Energy & Environmental Science* 5(5) (2012) 6889-6894.
- [143] A. Shrotri, H. Kobayashi, A. Fukuoka, Air Oxidation of Activated Carbon to Synthesize a Biomimetic Catalyst for Hydrolysis of Cellulose, *ChemSusChem* 9(11) (2016) 1299-1303.
- [144] D. Verma, R. Tiwari, A.K. Sinha, Depolymerization of cellulosic feedstocks using magnetically separable functionalized graphene oxide, *RSC Advances* 3(32) (2013) 13265-13272.
- [145] Q. Yang, X. Pan, Bifunctional Porous Polymers Bearing Boronic and Sulfonic Acids for Hydrolysis of Cellulose, *ACS Sustainable Chemistry & Engineering* 4(9) (2016) 4824-4830.
- [146] X. Zhao, J. Wang, C. Chen, Y. Huang, A. Wang, T. Zhang, Graphene oxide for cellulose hydrolysis: how it works as a highly active catalyst?, *Chemical Communications* 50(26) (2014) 3439-3442.
- [147] J. Pang, A. Wang, M. Zheng, T. Zhang, Hydrolysis of cellulose into glucose over carbons sulfonated at elevated temperatures, *Chemical Communications* 46(37) (2010) 6935-6937.
- [148] X. Zhao, J. Xu, A. Wang, T. Zhang, Porous carbon in catalytic transformation of cellulose, *Chinese Journal of Catalysis* 36 (2015) 1419-1427.
- [149] K.-i. Shimizu, A. Satsuma, Toward a rational control of solid acid catalysis for green synthesis and biomass conversion, *Energy & Environmental Science* 4(9) (2011) 3140-3153.
- [150] H. Kobayashi, T. Komanoya, K. Hara, A. Fukuoka, Water-Tolerant Mesoporous-Carbon-Supported Ruthenium Catalysts for the Hydrolysis of Cellulose to Glucose, *ChemSusChem* 3(4) (2010) 440-443.
- [151] J.K. Chinthaginjala, K. Seshan, L. Lefferts, Preparation and Application of Carbon-Nanofiber Based Microstructured Materials as Catalyst Supports, *Industrial & Engineering Chemistry Research* 46(12) (2007) 3968-3978.
- [152] S. Van de Vyver, J. Geboers, M. Dusselier, H. Schepers, T. Vosch, L. Zhang, G. Van Tendeloo, P.A. Jacobs, B.F. Sels, Selective Bifunctional Catalytic Conversion of Cellulose over Reshaped Ni Particles at the Tip of Carbon Nanofibers, *ChemSusChem* 3(6) (2010) 698-701.
- [153] S. Van de Vyver, J. Geboers, W. Schutyser, M. Dusselier, P. Eloy, E. Dornez, J.W. Seo, C.M. Courtin, E.M. Gaigneaux, P.A. Jacobs, B.F. Sels, Tuning the Acid/Metal Balance of Carbon Nanofiber-Supported Nickel Catalysts for Hydrolytic Hydrogenation of Cellulose, *ChemSusChem* 5(8) (2012) 1549-1558.
- [154] L. Huang, H. Ye, S. Wang, Y. Li, Y. Zhang, W. Ma, W. Yu, Z. Zhou, Enhanced Hydrolysis of Cellulose by Highly Dispersed Sulfonated Graphene Oxide, *BioResources* 13(4) (2018) 8853-8870.
- [155] S. Stankovich, D.A. Dikin, G.H.B. Dommett, K.M. Kohlhaas, E.J. Zimney, E.A. Stach, R.D. Piner, S.T. Nguyen, R.S. Ruoff, Graphene-based composite materials, *Nature* 442(7100) (2006) 282-286.



- [156] S. Navalon, A. Dhakshinamoorthy, M. Alvaro, H. Garcia, Carbocatalysis by Graphene-Based Materials, *Chemical Reviews* 114(12) (2014) 6179-6212.
- [157] Z. Wei, Y. Yang, Y. Hou, Y. Liu, X. He, S. Deng, A New Approach Towards Acid Catalysts with High Reactivity Based on Graphene Nanosheets, *ChemCatChem* 6(8) (2014) 2354-2363.
- [158] A. Bianco, H.-M. Cheng, T. Enoki, Y. Gogotsi, R.H. Hurt, N. Koratkar, T. Kyotani, M. Monthieux, C.R. Park, J.M.D. Tascon, J. Zhang, All in the graphene family – A recommended nomenclature for two-dimensional carbon materials, *Carbon* 65 (2013) 1-6.
- [159] Y. Yan, J. Gong, J. Chen, Z. Zeng, W. Huang, K. Pu, J. Liu, P. Chen, Recent Advances on Graphene Quantum Dots: From Chemistry and Physics to Applications, *Advanced Materials* 31(21) (2019) 1808283.
- [160] K. Li, J. Chen, Y. Yan, Y. Min, H. Li, F. Xi, J. Liu, P. Chen, Quasi-homogeneous carbocatalysis for one-pot selective conversion of carbohydrates to 5-hydroxymethylfurfural using sulfonated graphene quantum dots, *Carbon* 136 (2018) 224-233.
- [161] Y. Wu, Z. Fu, D. Yin, Q. Xu, F. Liu, C. Lu, L. Mao, Microwave-assisted hydrolysis of crystalline cellulose catalyzed by biomass char sulfonic acids, *Green Chemistry* 12(4) (2010) 696-700.
- [162] E.B. Sangib, B.T. Meshesha, B.A. Demessie, F. Medina, Study on cellulose (96% crystalline) hydrolysis performance of sulfonated carbon catalyst in microwave-heated reactor at elevated temperatures, *Biomass Conversion and Biorefinery* 10(4) (2020) 901-913.
- [163] S. Horikoshi, T. Minagawa, S. Tsubaki, A. Onda, N. Serpone, Is Selective Heating of the Sulfonic Acid Catalyst AC-SO₃H by Microwave Radiation Crucial in the Acid Hydrolysis of Cellulose to Glucose in Aqueous Media?, *Catalysts* 7 (2017) 231.
- [164] E.G. Mission, A.T. Quitain, Y. Hirano, M. Sasaki, M.J. Cocero, T. Kida, Integrating reduced graphene oxide with microwave-subcritical water for cellulose depolymerization, *Catalysis Science & Technology* 8(21) (2018) 5434-5444.
- [165] E.G. Mission, A.T. Quitain, M. Sasaki, T. Kida, Synergizing graphene oxide with microwave irradiation for efficient cellulose depolymerization into glucose, *Green Chemistry* 19(16) (2017) 3831-3843.
- [166] X. Wang, X. Wu, K. Guo, J. Ren, Q. Lin, H. Li, S. Liu, Efficient Microwave-Assisted Hydrolysis of Microcrystalline Cellulose into Glucose Using New Carbon-Based Solid Catalysts, *Catalysis Letters* 150 (2020) 138-149.
- [167] A. Richel, P. Laurent, B. Wathélet, J.-P. Wathélet, M. Paquot, Current perspectives on microwave-enhanced reactions of monosaccharides promoted by heterogeneous catalysts, *Catalysis Today* 167(1) (2011) 141-147.
- [168] A. de la Hoz, Á. Díaz-Ortiz, A. Moreno, Microwaves in organic synthesis. Thermal and non-thermal microwave effects, *Chemical Society Reviews* 34(2) (2005) 164-178.
- [169] M. Takahashi, H. Takenaka, DC Electrical Conductivity of Cellulose, *Polymer Journal* 15(9) (1983) 625-629.



- [170] J. Fan, M. De bruyn, V.L. Budarin, M.J. Gronnow, P.S. Shuttleworth, S. Breeden, D.J. Macquarrie, J.H. Clark, Direct Microwave-Assisted Hydrothermal Depolymerization of Cellulose, *Journal of the American Chemical Society* 135(32) (2013) 11728-11731.
- [171] V.L. Budarin, J.H. Clark, B.A. Lanigan, P. Shuttleworth, D.J. Macquarrie, Microwave assisted decomposition of cellulose: A new thermochemical route for biomass exploitation, *Bioresource Technology* 101(10) (2010) 3776-3779.
- [172] J. Wang, J. Xi, Y. Wang, Recent advances in the catalytic production of glucose from lignocellulosic biomass, *Green Chemistry* 17(2) (2015) 737-751.
- [173] M.R. Rosana, Y. Tao, A.E. Stiegman, G.B. Dudley, On the rational design of microwave-actuated organic reactions, *Chemical Science* 3(4) (2012) 1240-1244.
- [174] A. Aguilar-Reynosa, A. Román, R. Ma. Rodríguez-Jasso, C.N. Aguilar, G. Garrote, H.A. Ruiz, Microwave heating processing as alternative of pretreatment in second-generation biorefinery: An overview, *Energy Conversion and Management* 136 (2017) 50-65.
- [175] D. Cantero, M. Bermejo, M. Cocero, Pressure Effect on Cellulose Hydrolysis in Pressurized Water, *Chemical Engineering Journal* 276 (2015) 145-154.
- [176] I.K.M. Yu, X. Xiong, D.C.W. Tsang, Y.H. Ng, J.H. Clark, J. Fan, S. Zhang, C. Hu, Y.S. Ok, Graphite oxide- and graphene oxide-supported catalysts for microwave-assisted glucose isomerisation in water, *Green Chemistry* 21(16) (2019) 4341-4353.
- [177] M. Möller, F. Harnisch, U. Schröder, Microwave-assisted hydrothermal degradation of fructose and glucose in subcritical water, *Biomass and Bioenergy* 39 (2012) 389-398.
- [178] M. Möller, P. Nilges, F. Harnisch, U. Schröder, Subcritical Water as Reaction Environment: Fundamentals of Hydrothermal Biomass Transformation, *ChemSusChem* 4(5) (2011) 566-579.
- [179] A. Laporterie, J. Marquié, J. Dubac, Microwave-Assisted Reactions on Graphite, in: *Microwaves in Organic Synthesis*, Wiley, Canada (2008), 416-455.
- [180] T. Besson, C.O. Kappe, Microwave Susceptors, in: *Microwaves in Organic Synthesis*, Wiley (2012) 297-346.
- [181] E.G. Mission, J.K.C.N. Agutaya, A.T. Quitain, M. Sasaki, T. Kida, Carbocatalysed hydrolytic cleaving of the glycosidic bond in fucoidan under microwave irradiation, *RSC Advances* 9(52) (2019) 30325-30334.
- [182] K.L. Klein, A.V. Melechko, T.E. McKnight, S.T. Retterer, P.D. Rack, J.D. Fowlkes, D.C. Joy, M.L. Simpson, Surface characterization and functionalization of carbon nanofibers, *Journal of Applied Physics* 103(6) (2008) 61301.
- [183] A.B. Dongil, B. Bachiller-Baeza, A. Guerrero-Ruiz, I. Rodríguez-Ramos, A. Martínez-Alonso, J.M. Tascón, Surface chemical modifications induced on high surface area graphite and carbon nanofibers using different oxidation and functionalization treatments, *Journal of colloid and interface science* 355(1) (2011) 179-89.
- [184] M.L. Toebes, J.M.P. van Heeswijk, J.H. Bitter, A. Jos van Dillen, K.P. de Jong, The influence of oxidation on the texture and the number of oxygen-containing surface groups of carbon nanofibers, *Carbon* 42(2) (2004) 307-315.



- [185] O.L. Li, L. Qin, N. Takeuchi, K. Kim, T. Ishizaki, Effect of hydrophilic/hydrophobic properties of carbon materials on plasma-sulfonation process and their catalytic activities in cellulose conversion, *Catalysis Today* 337 (2019) 155-161.
- [186] M. Hara, T. Yoshida, A. Takagaki, T. Takata, J.N. Kondo, S. Hayashi, K. Domen, A Carbon Material as a Strong Protonic Acid, *Angewandte Chemie International Edition* 43(22) (2004) 2955-2958.
- [187] A. Onda, T. Ochi, K. Yanagisawa, Hydrolysis of Cellulose Selectively into Glucose Over Sulfonated Activated-Carbon Catalyst Under Hydrothermal Conditions, *Topics in Catalysis* 52(6) (2009) 801-807.
- [188] J. Drelich, E. Chibowski, D.D. Meng, K. Terpilowski, Hydrophilic and superhydrophilic surfaces and materials, *Soft Matter* 7(21) (2011) 9804-9828.
- [189] M. Okamura, A. Takagaki, M. Toda, J.N. Kondo, K. Domen, T. Tatsumi, M. Hara, S. Hayashi, Acid-Catalyzed Reactions on Flexible Polycyclic Aromatic Carbon in Amorphous Carbon, *Chemistry of Materials* 18(13) (2006) 3039-3045.
- [190] O.L. Li, R. Ikura, T. Ishizaki, Hydrolysis of cellulose to glucose over carbon catalysts sulfonated via a plasma process in dilute acids, *Green Chemistry* 19(20) (2017) 4774-4777.
- [191] A. Rasheed, J.Y. Howe, M.D. Dadmun, P.F. Britt, The efficiency of the oxidation of carbon nanofibers with various oxidizing agents, *Carbon* 45(5) (2007) 1072-1080.
- [192] H. Jeong, H.-J. Noh, J.Y. Kim, M. Jin, C. Park, Y.H. Lee, X-ray absorption spectroscopy of graphite oxide, *EPL (Europhysics Letters)* 82 (2008) 67004.
- [193] L. Huang, H. Ye, S. Wang, Y. Li, Y. Zhang, W. Ma, W. Yu, Z. Zhou, Enhanced Hydrolysis of Cellulose by Highly Dispersed Sulfonated Graphene Oxide, *BioResources* 13(4) (2018) 8853-8870.
- [194] D.R. Dreyer, A.D. Todd, C.W. Bielawski, Harnessing the chemistry of graphene oxide, *Chemical Society Reviews* 43(15) (2014) 5288-5301.
- [195] S. Zhu, J. Wang, W. Fan, Graphene-based catalysis for biomass conversion, *Catalysis Science & Technology* 5(8) (2015) 3845-3858.
- [196] A. Lerf, H. He, M. Forster, J. Klinowski, Structure of Graphite Oxide Revisited, *The Journal of Physical Chemistry B* 102(23) (1998) 4477-4482.
- [197] High Resolution XPS of Organic Polymers: The Scienta ESCA300 Database (Beamson, G.; Briggs, D.), *Journal of Chemical Education* 70(1) (1993) A25.
- [198] M.M. Nasef, H. Saidi, Surface studies of radiation grafted sulfonic acid membranes: XPS and SEM analysis, *Applied Surface Science* 252(8) (2006) 3073-3084.
- [199] D. Torres, J.L. Pinilla, E.M. Gálvez, I. Suelves, Graphene quantum dots from fishbone carbon nanofibers, *RSC Advances* 6(54) (2016) 48504-48514.
- [200] A. Cabiac, E. Guillon, F. Chambon, C. Pinel, F. Rataboul, N. Essayem, Cellulose reactivity and glycosidic bond cleavage in aqueous phase by catalytic and non catalytic transformations, *Applied Catalysis A: General* 402(1) (2011) 1-10.
- [201] A. Onda, T. Ochi, K. Yanagisawa, Selective hydrolysis of cellulose into glucose over solid acid catalysts, *Green Chemistry* 10(10) (2008) 1033-1037.



- [202] S. Van de Vyver, L. Peng, J. Geboers, H. Schepers, F. Clippel, C. Gommaes, B. Goderis, J. Pierre, B. Sels, Sulfonated silica/carbon nanocomposites as novel catalysts for hydrolysis of cellulose to glucose, *Green Chemistry* 12(9) (2010) 1560-1563.
- [203] H. Wang, T. Deng, Y. Wang, X. Cui, Y. Qi, X. Mu, X. Hou, Y. Zhu, Graphene oxide as a facile acid catalyst for the one-pot conversion of carbohydrates into 5-ethoxymethylfurfural, *Green Chemistry* 15(9) (2013) 2379-2383.
- [204] I.-Y. Jeon, Y.-R. Shin, G.-J. Sohn, H.-J. Choi, S.-Y. Bae, J. Mahmood, S.-M. Jung, J.-M. Seo, M.-J. Kim, D. Wook Chang, L. Dai, J.-B. Baek, Edge-carboxylated graphene nanosheets via ball milling, *Proceedings of the National Academy of Sciences* 109(15) (2012) 5588-5593.
- [205] G. Chatel, R. Varma, Ultrasound and microwave irradiation: contributions of alternate physicochemical activation methods to Green Chemistry, *Green Chemistry* 21 (2019) 6043-6050.
- [206] Z. Zhang, Z. Zhao, Solid acid and microwave-assisted hydrolysis of cellulose in ionic liquid, *Carbohydrate research* 344 (2009) 2069-72.
- [207] J.S. Luterbacher, D. Martin Alonso, J.A. Dumesic, Targeted chemical upgrading of lignocellulosic biomass to platform molecules, *Green Chemistry* 16(12) (2014) 4816-4838.
- [208] L. Shuai, X. Pan, Hydrolysis of cellulose by cellulase-mimetic solid catalyst, *Energy & Environmental Science* 5(5) (2012) 6889-6894.
- [209] H.-X. Li, X. Zhang, Q. Wang, D. Yang, Q. Cao, L.e. Jin, Study on the hydrolysis of cellulose with the regenerable and recyclable multifunctional solid acid as a catalyst and its catalytic hydrolytic kinetics, *Cellulose* 27 (2020) 285-300.
- [210] P.L. Dhepe, A. Fukuoka, Cellulose conversion under heterogeneous catalysis, *ChemSusChem* 1(12) (2008) 969-75.
- [211] H. Kobayashi, A. Fukuoka, Synthesis and utilisation of sugar compounds derived from lignocellulosic biomass, *Green Chemistry* 15(7) (2013) 1740-1763.
- [212] F. Liguori, C. Moreno-Marrodan, P. Barbaro, Biomass-derived chemical substitutes for bisphenol A: recent advancements in catalytic synthesis, *Chemical Society Reviews* 49(17) (2020) 6329-6363.
- [213] J. Zhang, J.-b. Li, S.-B. Wu, Y. Liu, Advances in the Catalytic Production and Utilization of Sorbitol, *Industrial & Engineering Chemistry Research* 52(34) (2013) 11799-11815.
- [214] X. Liu, X. Wang, S. Yao, Y. Jiang, J. Guan, X. Mu, Recent advances in the production of polyols from lignocellulosic biomass and biomass-derived compounds, *RSC Advances* 4(90) (2014) 49501-49520.
- [215] J.R. Ochoa-Gómez, T. Roncal, Production of Sorbitol from Biomass, in: Z. Fang, J.R.L. Smith, X. Qi (Eds.), *Production of Platform Chemicals from Sustainable Resources*, Springer, Singapore, (2017), 265-309.
- [216] N.A. Vasyunina, A.A. Balandin, S.V. Chepigo, G.S. Barysheva, Catalytic hydrogenation of wood and other vegetable materials, *Bulletin of the Academy of Sciences of the USSR, Division of chemical science* 9(8) (1960) 1419-1419.

- [217] A. Balandin, N. Vasunina, S. Chepigo, G. Barysheva, Hydrolytic hydrogenation of cellulose, *Doklady Akademii Nauk SSSR* 128(5) (1959) 941-944.
- [218] J. Matthiesen, T. Hoff, C. Liu, C. Poeschel, R. Rao, J.-P. Tessonnier, Functional carbons and carbon nanohybrids for the catalytic conversion of biomass to renewable chemicals in the condensed phase, *Chinese Journal of Catalysis* 35(6) (2014) 842-855.
- [219] A. Negoii, K. Triantafyllidis, V.I. Parvulescu, S.M. Coman, The hydrolytic hydrogenation of cellulose to sorbitol over M (Ru, Ir, Pd, Rh)-BEA-zeolite catalysts, *Catalysis Today* 223 (2014) 122-128.
- [220] J. Geboers, S. Van de Vyver, K. Carpentier, P. Jacobs, B. Sels, Efficient hydrolytic hydrogenation of cellulose in the presence of Ru-loaded zeolites and trace amounts of mineral acid, *Chemical Communications* 47(19) (2011) 5590-5592.
- [221] D. Reyes-Luyanda, J. Flores-Cruz, P.J. Morales-Pérez, L.G. Encarnación-Gómez, F. Shi, P.M. Voyles, N. Cardona-Martínez, Bifunctional Materials for the Catalytic Conversion of Cellulose into Soluble Renewable Biorefinery Feedstocks, *Topics in Catalysis* 55(3) (2012) 148-161.
- [222] H. Kobayashi, H. Matsushashi, T. Komanoya, K. Hara, A. Fukuoka, Transfer hydrogenation of cellulose to sugar alcohols over supported ruthenium catalysts, *Chemical communications* 47 (2011) 2366-8.
- [223] B. Dar, S. Khalid, T. Wani, M. Mir, M. Farooqui, Ceria-Based Mixed Oxide Supported CuO: An Efficient Heterogeneous Catalyst for Conversion of Cellulose to Sorbitol, *Green and Sustainable Chemistry* 5 (2015) 15-24.
- [224] X. Zhao, J. Xu, A. Wang, T. Zhang, Porous carbon in catalytic transformation of cellulose, *Chinese Journal of Catalysis* 36(9) (2015) 1419-1427.
- [225] J.W. Han, H. Lee, Direct conversion of cellulose into sorbitol using dual-functionalized catalysts in neutral aqueous solution, *Catalysis Communications* 19 (2012) 115-118.
- [226] D.S. Park, D. Yun, T.Y. Kim, J. Baek, Y.S. Yun, J. Yi, A mesoporous carbon-supported Pt nanocatalyst for the conversion of lignocellulose to sugar alcohols, *ChemSusChem* 6(12) (2013) 2281-2289.
- [227] H. Wang, L. Zhu, S. Peng, F. Peng, H. Yu, J. Yang, High efficient conversion of cellulose to polyols with Ru/CNTs as catalyst, *Renewable Energy* 37(1) (2012) 192-196.
- [228] L.S. Ribeiro, J.J. de Melo Órfão, M.F. Ribeiro Pereira, An overview of the hydrolytic hydrogenation of lignocellulosic biomass using carbon-supported metal catalysts, *Materials Today Sustainability* (2020) 100058.
- [229] P.A. Lazaridis, S. Karakoulia, A. Delimitis, S.M. Coman, V.I. Parvulescu, K.S. Triantafyllidis, d-Glucose hydrogenation/hydrogenolysis reactions on noble metal (Ru, Pt)/activated carbon supported catalysts, *Catalysis Today* 257 (2015) 281-290.
- [230] D. Wang, W. Niu, M. Tan, M. Wu, X. Zheng, Y. Li, N. Tsubaki, Pt Nanocatalysts Supported on Reduced Graphene Oxide for Selective Conversion of Cellulose or Cellobiose to Sorbitol, *ChemSusChem* 7(5) (2014) 1398-1406.
- [231] A. Shrotri, A. Tanksale, J.N. Beltramini, H. Gurav, S.V. Chilukuri, Conversion of cellulose to polyols over promoted nickel catalysts, *Catalysis Science & Technology* 2(9) (2012) 1852-1858.



- [232] X. Wang, L. Meng, F. Wu, Y. Jiang, L. Wang, X. Mu, Efficient conversion of microcrystalline cellulose to 1,2-alkanediols over supported Ni catalysts, *Green Chemistry* 14(3) (2012) 758-765.
- [233] B. Kusserow, S. Schimpf, P. Claus, Hydrogenation of Glucose to Sorbitol over Nickel and Ruthenium Catalysts, *Advanced Synthesis & Catalysis* 345(1-2) (2003) 289-299.
- [234] B. Zhang, B. Chen, M. Douthwaite, Q. Liu, C. Zhang, Q. Wu, R. Shi, P. Wu, F. Zhao, G. Hutchings, Macroporous–mesoporous carbon supported Ni catalysts for the conversion of cellulose to polyols, *Green Chemistry* 20(15) (2018) 3634-3642.
- [235] M.-Y. Zheng, A.-Q. Wang, N. Ji, J.-F. Pang, X.-D. Wang, T. Zhang, Transition Metal–Tungsten Bimetallic Catalysts for the Conversion of Cellulose into Ethylene Glycol, *ChemSusChem* 3(1) (2010) 63-66.
- [236] P. Yang, H. Kobayashi, K. Hara, A. Fukuoka, Phase change of nickel phosphide catalysts in the conversion of cellulose into sorbitol, *ChemSusChem* 5(5) (2012) 920-6.
- [237] Y.-l. Cao, J.-w. Wang, Q.-f. Li, N. Yin, Z.-m. Liu, M.-q. Kang, Y.-l. Zhu, Hydrolytic hydrogenation of cellulose over Ni-WO₃/SBA-15 catalysts, *Journal of Fuel Chemistry and Technology* 41(8) (2013) 943-949.
- [238] G. Liang, H. Cheng, W. Li, L. He, Y. Yu, F. Zhao, Selective conversion of microcrystalline cellulose into hexitols on nickel particles encapsulated within ZSM-5 zeolite, *Green Chemistry* 14(8) (2012) 2146-2149.
- [239] G. Liang, L. He, M. Arai, F. Zhao, The Pt-Enriched PtNi Alloy Surface and its Excellent Catalytic Performance in Hydrolytic Hydrogenation of Cellulose, *ChemSusChem* 7(5) (2014) 1415-1421.
- [240] L.S. Ribeiro, J.J. Delgado, J.J.M. Órfão, M.F.R. Pereira, Carbon supported Ru-Ni bimetallic catalysts for the enhanced one-pot conversion of cellulose to sorbitol, *Applied Catalysis B: Environmental* 217 (2017) 265-274.
- [241] G. Liang, L. He, H. Cheng, W. Li, X. Li, C. Zhang, Y. Yu, F. Zhao, The hydrogenation/dehydrogenation activity of supported Ni catalysts and their effect on hexitols selectivity in hydrolytic hydrogenation of cellulose, *Journal of Catalysis* 309 (2014) 468-476.
- [242] I.E. Wachs, L.E. Fitzpatrick, *Characterization of Catalytic Materials*, Butterworth-Heinemann 1992.
- [243] J. Remón, J. Arauzo, L. García, P. Arcelus-Arrillaga, M. Millan, I. Suelves, J.L. Pinilla, Bio-oil upgrading in supercritical water using Ni-Co catalysts supported on carbon nanofibres, *Fuel Processing Technology* 154 (2016) 178-187.
- [244] Ö. Metin, V. Mazumder, S. Özkar, S. Sun, Monodisperse Nickel Nanoparticles and Their Catalysis in Hydrolytic Dehydrogenation of Ammonia Borane, *Journal of the American Chemical Society* 132(5) (2010) 1468-1469.
- [245] D. Li, C. Wang, D. Tripkovic, S. Sun, N.M. Markovic, V.R. Stamenkovic, Surfactant Removal for Colloidal Nanoparticles from Solution Synthesis: The Effect on Catalytic Performance, *ACS Catalysis* 2(7) (2012) 1358-1362.
- [246] L. Negahdar, J.U. Oltmanns, S. Palkovits, R. Palkovits, Kinetic investigation of the catalytic conversion of cellobiose to sorbitol, *Applied Catalysis B: Environmental* 147 (2014) 677-683.



- [247] J. Li, H.S.M.P. Soares, J.A. Moulijn, M. Makkee, Simultaneous hydrolysis and hydrogenation of cellobiose to sorbitol in molten salt hydrate media, *Catalysis Science & Technology* 3(6) (2013) 1565-1572.
- [248] M.C. Biesinger, B.P. Payne, L.W.M. Lau, A. Gerson, R.S.C. Smart, X-ray photoelectron spectroscopic chemical state quantification of mixed nickel metal, oxide and hydroxide systems, *Surface and Interface Analysis* 41(4) (2009) 324-332.
- [249] H. Kobayashi, Y. Hosaka, K. Hara, B. Feng, Y. Hirosaki, A. Fukuoka, Control of selectivity, activity and durability of simple supported nickel catalysts for hydrolytic hydrogenation of cellulose, *Green Chemistry* 16(2) (2014) 637-644.
- [250] P.A. Lazaridis, S.A. Karakoulia, C. Teodorescu, N. Apostol, D. Macovei, A. Panteli, A. Delimitis, S.M. Coman, V.I. Parvulescu, K.S. Triantafyllidis, High hexitols selectivity in cellulose hydrolytic hydrogenation over platinum (Pt) vs. ruthenium (Ru) catalysts supported on micro/mesoporous carbon, *Applied Catalysis B: Environmental* 214 (2017) 1-14.
- [251] P.J.C. Hausoul, J.U. Oltmanns, R. Palkovits, Chapter 5 Hydrogenolysis of Cellulose and Sugars, *Catalytic Hydrogenation for Biomass Valorization*, The Royal Society of Chemistry (2015), 99-124.
- [252] X. Duan, J. Ji, G. Qian, X. Zhou, D. Chen, Recent advances in synthesis of reshaped Fe and Ni particles at the tips of carbon nanofibers and their catalytic applications, *Catalysis Today* 249 (2015) 2-11.
- [253] B. Zada, L. Yan, Y. Fu, Effective conversion of cellobiose and glucose to sorbitol using non-noble bimetallic NiCo/HZSM-5 catalyst, *Science China Chemistry* 61(9) (2018) 1167-1174.
- [254] D. Li, Y. Nakagawa, K. Tomishige, Methane reforming to synthesis gas over Ni catalysts modified with noble metals, *Applied Catalysis A: General* 408(1) (2011) 1-24.
- [255] A.B. Dongil, I.T. Ghampson, R. García, J.L.G. Fierro, N. Escalona, Hydrodeoxygenation of guaiacol over Ni/carbon catalysts: effect of the support and Ni loading, *RSC Advances* 6(4) (2016) 2611-2623.
- [256] B. Mile, D. Stirling, M.A. Zammit, A. Lovell, M. Webb, The location of nickel oxide and nickel in silica-supported catalysts: Two forms of “NiO” and the assignment of temperature-programmed reduction profiles, *Journal of Catalysis* 114(2) (1988) 217-229.
- [257] A. Tomita, N. Sato, Y. Tamai, Hydrogenation of carbons catalyzed by nickel, platinum and rhodium, *Carbon* 12(2) (1974) 143-149.
- [258] A. Tanksale, J.N. Beltramini, J.A. Dumesic, G.Q. Lu, Effect of Pt and Pd promoter on Ni supported catalysts—A TPR/TPO/TPD and microcalorimetry study, *Journal of Catalysis* 258(2) (2008) 366-377.
- [259] F. Liao, T.W.B. Lo, S.C.E. Tsang, Recent Developments in Palladium-Based Bimetallic Catalysts, *ChemCatChem* 7(14) (2015) 1998-2014.
- [260] N. Moitra, K. Kanamori, Y.H. Ikuhara, X. Gao, Y. Zhu, G. Hasegawa, K. Takeda, T. Shimada, K. Nakanishi, Reduction on reactive pore surfaces as a versatile approach to synthesize monolith-supported metal alloy nanoparticles and their catalytic applications, *Journal of Materials Chemistry A* 2(31) (2014) 12535-12544.



- [261] J. Verendel, T. Church, P. Andersson, Catalytic One-Pot Production of Small Organics from Polysaccharides, *Synthesis* 11 (2011) 1649-1677.
- [262] W. Deng, M. Liu, X. Tan, Q. Zhang, Y. Wang, Conversion of cellobiose into sorbitol in neutral water medium over carbon nanotube-supported ruthenium catalysts, *Journal of Catalysis* 271(1) (2010) 22-32.
- [263] L.S. Ribeiro, J.J. Delgado, J.J. de Melo Órfão, M.F. Ribeiro Pereira, Influence of the Surface Chemistry of Multiwalled Carbon Nanotubes on the Selective Conversion of Cellulose into Sorbitol, *ChemCatChem* 9(5) (2017) 888-896.
- [264] L. Negahdar, Kinetic investigation of the hydrolytic hydrogenation of oligosaccharides to sorbitol, 2015.
- [265] T. Gagić, A. Perva Uzunalic, Ž. Knez, M. Škerget, Hydrothermal degradation of cellulose at temperature from 200 °C to 300 °C, *Industrial & Engineering Chemistry Research* 57 (2018) 6576-6584.
- [266] S. Hunter, P. Savage, Recent advances in acid- and base-catalyzed organic synthesis in high-temperature liquid water, *Chemical Engineering Science* 59 (2004) 4903-4909.
- [267] S.S. Toor, L. Rosendahl, A. Rudolf, Hydrothermal liquefaction of biomass: A review of subcritical water technologies, *Energy* 36(5) (2011) 2328-2342.
- [268] A. Bayu, A. Abudula, G. Guan, Reaction pathways and selectivity in chemo-catalytic conversion of biomass-derived carbohydrates to high-value chemicals: A review, *Fuel Processing Technology* 196 (2019) 106162.
- [269] O.V. Manaenkov, O.V. Kislitsa, V.G. Matveeva, E.M. Sulman, M.G. Sulman, L.M. Bronstein, Cellulose Conversion Into Hexitols and Glycols in Water: Recent Advances in Catalyst Development, *Frontiers in Chemistry* 7(834) (2019).
- [270] E. Crezee, B.W. Hoffer, R.J. Berger, M. Makkee, F. Kapteijn, J.A. Moulijn, Three-phase hydrogenation of d-glucose over a carbon supported ruthenium catalyst—mass transfer and kinetics, *Applied Catalysis A: General* 251(1) (2003) 1-17.
- [271] T. Zimmermann, E. Pöhler, T. Geiger, Cellulose Fibrils for Polymer Reinforcement, *Advanced Engineering Materials* 6(9) (2004) 754-761.
- [272] C. Yadav, A. Saini, W. Zhang, X. You, I. Chauhan, P. Mohanty, X. Li, Plant-based nanocellulose: A review of routine and recent preparation methods with current progress in its applications as rheology modifier and 3D bioprinting, *International Journal of Biological Macromolecules* 166 (2021) 1586-1616.
- [273] A. Dufresne, Nanocellulose: a new ageless bionanomaterial, *Materials Today* 16(6) (2013) 220-227.
- [274] R.J. Moon, A. Martini, J. Nairn, J. Simonsen, J. Youngblood, Cellulose nanomaterials review: structure, properties and nanocomposites, *Chemical Society Reviews* 40(7) (2011) 3941-3994.
- [275] D. Klemm, F. Kramer, S. Moritz, T. Lindström, M. Ankerfors, D. Gray, A. Dorris, Nanocelluloses: A New Family of Nature-Based Materials, *Angewandte Chemie International Edition* 50(24) (2011) 5438-5466.



- [276] C. Zinge, B. Kandasubramanian, Nanocellulose based biodegradable polymers, *European Polymer Journal* 133 (2020) 109758.
- [277] H.V. Lee, S.B.A. Hamid, S.K. Zain, Conversion of Lignocellulosic Biomass to Nanocellulose: Structure and Chemical Process, *The Scientific World Journal* 2014 (2014) 631013.
- [278] H. Kargarzadeh, M. Mariano, D. Gopakumar, I. Ahmad, S. Thomas, A. Dufresne, J. Huang, N. Lin, Advances in cellulose nanomaterials, *Cellulose* 25(4) (2018) 2151-2189.
- [279] K. Nelson, T. Retsina, M. Iakovlev, A. van Heiningen, Y. Deng, J.A. Shatkin, A. Mulyadi, American Process: Production of Low Cost Nanocellulose for Renewable, *Advanced Materials Applications*, in: L.D. Madsen, E.B. Svedberg (Eds.), *Materials Research for Manufacturing: An Industrial Perspective of Turning Materials into New Products*, Springer International Publishing, Cham, (2016), 267-302.
- [280] H. Xie, H. Du, X. Yang, C. Si, Recent Strategies in Preparation of Cellulose Nanocrystals and Cellulose Nanofibrils Derived from Raw Cellulose Materials, *International Journal of Polymer Science* 2018 (2018) 7923068.
- [281] M. Jonoobi, R. Oladi, Y. Davoudpour, K. Oksman, A. Dufresne, Y. Hamzeh, R. Davoodi, Different preparation methods and properties of nanostructured cellulose from various natural resources and residues: a review, *Cellulose* 22(2) (2015) 935-969.
- [282] J. Xie, C.-Y. Hse, C.F. De Hoop, T. Hu, J. Qi, T.F. Shupe, Isolation and characterization of cellulose nanofibers from bamboo using microwave liquefaction combined with chemical treatment and ultrasonication, *Carbohydrate Polymers* 151 (2016) 725-734.
- [283] L.P. Novo, J. Bras, A. García, N. Belgacem, A.A.d.S. Curvelo, A study of the production of cellulose nanocrystals through subcritical water hydrolysis, *Industrial Crops and Products* 93 (2016) 88-95.
- [284] L.P. Novo, J. Bras, A. García, N. Belgacem, A.A.S. Curvelo, Subcritical Water: A Method for Green Production of Cellulose Nanocrystals, *ACS Sustainable Chemistry & Engineering* 3(11) (2015) 2839-2846.
- [285] E.M. de Melo, J.H. Clark, A.S. Matharu, The Hy-MASS concept: hydrothermal microwave assisted selective scissoring of cellulose for in situ production of (meso)porous nanocellulose fibrils and crystals, *Green Chemistry* 19(14) (2017) 3408-3417.
- [286] A.S. Matharu, E.M. de Melo, Processing of Citrus Nanostructured Cellulose: A Rigorous Design-of-Experiment Study of the Hydrothermal Microwave-Assisted Selective Scissoring Process, *ChemSusChem* 11(8) (2018) 1344-1353.
- [287] Y. Gao, M.Z. Ozel, T. Dugmore, A. Sulaeman, A.S. Matharu, A biorefinery strategy for spent industrial ginger waste, *Journal of Hazardous Materials* 401 (2021) 123400.
- [288] Y. Gao, H. Xia, A.P. Sulaeman, E.M. de Melo, T.I.J. Dugmore, A.S. Matharu, Defibrillated Celluloses via Dual Twin-Screw Extrusion and Microwave Hydrothermal Treatment of Spent Pea Biomass, *ACS Sustainable Chemistry & Engineering* 7(13) (2019) 11861-11871.
- [289] I. Iliyini, H. Purwaningsih, T. Irawadi, Isolation and Characterization of Cellulose from Banana Stems using Microwave Heating, *Jurnal Kimia Valensi* 6 (2021) 169-176.

- [290] K. Harini, K. Ramya, M. Sukumar, Extraction of nano cellulose fibers from the banana peel and bract for production of acetyl and lauroyl cellulose, *Carbohydrate Polymers* 201 (2018) 329-339.
- [291] N. Lavoine, I. Desloges, A. Dufresne, J. Bras, Microfibrillated cellulose – Its barrier properties and applications in cellulosic materials: A review, *Carbohydrate Polymers* 90(2) (2012) 735-764.
- [292] A. García, A. Gandini, J. Labidi, N. Belgacem, J. Bras, Industrial and crop wastes: A new source for nanocellulose biorefinery, *Industrial Crops and Products* 93 (2016) 26-38.
- [293] J. Gustavsson, C. Cederberg, U. Sonesson, R. Otterdijk, A. McYbeck, Global food losses and food waste: extent, causes and prevention. Food and Agriculture Organization of the United Nations, Rome (2011).
- [294] A.S. Matharu, E.M. de Melo, J.A. Houghton, Opportunity for high value-added chemicals from food supply chain wastes, *Bioresource Technology* 215 (2016) 123-130.
- [295] A.P. Sulaeman, Y. Gao, T. Dugmore, J. Remón, A.S. Matharu, From unavoidable food waste to advanced biomaterials: microfibrillated lignocellulose production by microwave-assisted hydrothermal treatment of cassava peel and almond hull, *Cellulose* 28 (2021) 7687-7705.
- [296] C.E. Wyman, Potential synergies and challenges in refining cellulosic biomass to fuels, chemicals, and power, *Biotechnology progress* 19(2) (2003) 254-62.
- [297] J.J. Bozell, R. Landucci, Alternative Feedstocks Program Technical and Economic Assessment: Thermal/Chemical and Bioprocessing Components, Department of Energy, United States, (1993).
- [298] N. Reddy, Y. Yang, Biofibers from agricultural byproducts for industrial applications, *Trends in Biotechnology* 23(1) (2005) 22-27.
- [299] Nagy, D.H. Kim, C.A. Eckert, C. Liotta, A. Ragauskas, From Wood to Fuels: Integrating Biofuels and Pulp Production, *Industrial Biotechnology* 2 (2006) 55-56.
- [300] L.J. Konwar, R. Kataki, J.P. Mikkola, N. Bordoloi, R. Saikia, R. Chutia, Side-streams from bioenergy and biorefinery complexes as a resource for circular bio-economy, (Chapter 3) in: *Waste Biorefinery: Potential and Perspectives*, Elsevier, United States (2018) 85-125.
- [301] P. Chen, Y. Cheng, S. deng, X. Lin, G. Huang, R. Ruan, Utilization of almond residues, *International Journal of Agricultural and Biological Engineering* 3 (2010) 1-18.
- [302] I. Prgomet, B. Gonçalves, R. Domínguez-Perles, N. Pascual-Seva, Valorization Challenges to Almond Residues: Phytochemical Composition and Functional Application, *Molecules* 22(10) (2017) 1774.
- [303] M. Schirra, Postharvest Technology and Utilization of Almonds, *Horticultural Reviews* 20 (1997), 267-311.
- [304] Y. Li, Y. Liu, W. Chen, Q. Wang, Y. Liu, J. Li, H. Yu, Facile extraction of cellulose nanocrystals from wood using ethanol and peroxide solvothermal pretreatment followed by ultrasonic nanofibrillation, *Green Chemistry* 18(4) (2016) 1010-1018.
- [305] Z. Hu, Z. Wen, Enhancing enzymatic digestibility of switchgrass by microwave-assisted alkali pretreatment, *Biochemical Engineering Journal* 38(3) (2008) 369-378.

- [306] M. Li, Y.-L. Cheng, N. Fu, B. Adhikari, X. Chen, Isolation and Characterization of Corn cob Cellulose Fibers using Microwave-Assisted Chemical Treatments, *International Journal of Food Engineering* 10 (2014) 427-436.
- [307] Y. Gao, J. Remón, A.S. Matharu, Microwave-assisted hydrothermal treatments for biomass valorisation: a critical review, *Green Chemistry* 23(10) (2021) 3502-3525.
- [308] H.H. Strain, Sources of d-Sorbitol, *Journal of the American Chemical Society* 59(11) (1937) 2264-2266.
- [309] P. Barbaro, F. Liguori, C. Moreno-Marrodan, Selective direct conversion of C5 and C6 sugars to high added-value chemicals by a bifunctional, single catalytic body, *Green Chemistry* 18(10) (2016) 2935-2940.
- [310] D. Scholz, C. Aellig, C. Mondelli, J. Pérez-Ramírez, Continuous Transfer Hydrogenation of Sugars to Alditols with Bioderived Donors over Cu–Ni–Al Catalysts, *ChemCatChem* 7(10) (2015) 1551-1558.
- [311] B. García, J. Moreno, G. Morales, J. Melero, J. Iglesias, Production of Sorbitol via Catalytic Transfer Hydrogenation of Glucose, *Applied Sciences* 10 (2020) 1843.
- [312] A. Shrotri, H. Kobayashi, A. Tanksale, A. Fukuoka, J. Beltrami, Transfer Hydrogenation of Cellulose-based Oligomers over Carbon-supported Ruthenium Catalyst in a Fixed-bed Reactor, *ChemCatChem* 6(5) (2014) 1349-1356.
- [313] R. Taylor, L. Natrass, G. Alberts, P. Robson, C. Chudziak, A. Bauen, I. Libelli, G. Lotti, M. Prussi, R. Nistri, D. Chiamonti, A. López-Contreras, H. Bos, G. Eggink, J. Springer, R. Bakker, R. van, From the Sugar Platform to biofuels and biochemicals: Final report for the European Commission Directorate-General Energy, (2015).
- [314] J.A. Dávila, V. Hernández, E. Castro, C.A. Cardona, Economic and environmental assessment of syrup production. Colombian case, *Bioresource Technology* 161 (2014) 84-90.
- [315] S. Ren, X.P. Ye, A.P. Borole, Separation of chemical groups from bio-oil water-extract via sequential organic solvent extraction, *Journal of Analytical and Applied Pyrolysis* 123 (2017) 30-39.
- [316] R.B. Madsen, R.Z.K. Bernberg, P. Biller, J. Becker, B.B. Iversen, M. Glasius, Hydrothermal co-liquefaction of biomasses – quantitative analysis of bio-crude and aqueous phase composition, *Sustainable Energy & Fuels* 1(4) (2017) 789-805.
- [317] C. Sabot, E. Oueis, X. Brune, P.-Y. Renard, Synthesis of polysubstituted 3-hydroxypyridines via the revisited hetero-Diels–Alder reaction of 5-alkoxyoxazoles with dienophiles, *Chemical Communications* 48(5) (2012) 768-770.
- [318] S. Zhao, C. Hu, L. Guo, K. Li, H. Yu, Isolation of a 3-hydroxypyridine degrading bacterium, *Agrobacterium* sp. DW-1, and its proposed degradation pathway, *AMB Express* 9(1) (2019) 65-65.
- [319] G. García Liñares, G. Parraud, C. Labriola, A. Baldessari, Chemoenzymatic synthesis and biological evaluation of 2- and 3-hydroxypyridine derivatives against *Leishmania mexicana*, *Bioorganic & Medicinal Chemistry* 20(15) (2012) 4614-4624.
- [320] K. Yoshida, F. Kawagoe, K. Hayashi, S. Horiuchi, T. Imamoto, A. Yanagisawa, Synthesis of 3-Hydroxypyridines Using Ruthenium-Catalyzed Ring-Closing Olefin Metathesis, *Organic Letters* 11(3) (2009) 515-518.

- [321] J. Wildschut, F.H. Mahfud, R.H. Venderbosch, H.J. Heeres, Hydrotreatment of Fast Pyrolysis Oil Using Heterogeneous Noble-Metal Catalysts, *Industrial & Engineering Chemistry Research* 48(23) (2009) 10324-10334.
- [322] S. Ahmadi, E. Reyhanitash, Z. Yuan, S. Rohani, C. Xu, Upgrading of fast pyrolysis oil via catalytic hydrodeoxygenation: Effects of type of solvents, *Renewable Energy* 114 (2017) 376-382.
- [323] S. Xiu, A. Shahbazi, Bio-oil production and upgrading research: A review, *Renewable and Sustainable Energy Reviews* 16(7) (2012) 4406-4414.
- [324] T. Shan Ahamed, S. Anto, T. Mathimani, K. Brindhadevi, A. Pugazhendhi, Upgrading of bio-oil from thermochemical conversion of various biomass – Mechanism, challenges and opportunities, *Fuel* 287 (2021) 119329.
- [325] R.J. French, J. Stunkel, R.M. Baldwin, Mild Hydrotreating of Bio-Oil: Effect of Reaction Severity and Fate of Oxygenated Species, *Energy & Fuels* 25(7) (2011) 3266-3274.
- [326] R.J. French, J. Hrdlicka, R. Baldwin, Mild hydrotreating of biomass pyrolysis oils to produce a suitable refinery feedstock, *Environmental Progress & Sustainable Energy* 29(2) (2010) 142-150.
- [327] D.C. Elliott, G.G. Neuenschwander, Liquid Fuels by Low-Severity Hydrotreating of Biocrude, in: A.V. Bridgwater, D.G.B. Boocock (Eds.), *Developments in Thermochemical Biomass Conversion: Volume 1/Volume 2*, Springer Netherlands, Dordrecht, (1997), 611-621.
- [328] R.H. Venderbosch, A.R. Ardiyanti, J. Wildschut, A. Oasmaa, H.J. Heeres, Stabilization of biomass-derived pyrolysis oils, *Journal of Chemical Technology & Biotechnology* 85(5) (2010) 674-686.
- [329] Y. Han, M. Gholizadeh, C.-C. Tran, S. Kaliaguine, C.-Z. Li, M. Olarte, M. Garcia-Perez, Hydrotreatment of pyrolysis bio-oil: A review, *Fuel Processing Technology* 195 (2019) 106140.
- [330] M.V. Olarte, A.H. Zacher, A.B. Padmaperuma, S.D. Burton, H.M. Job, T.L. Lemmon, M.S. Swita, L.J. Rotness, G.N. Neuenschwander, J.G. Frye, D.C. Elliott, Stabilization of Softwood-Derived Pyrolysis Oils for Continuous Bio-oil Hydroprocessing, *Topics in Catalysis* 59(1) (2016) 55-64.
- [331] J. Gagnon, S. Kaliaguine, Catalytic hydrotreatment of vacuum pyrolysis oils from wood, *Industrial & Engineering Chemistry Research* 27(10) (1988) 1783-1788.
- [332] S. Kim, E.E. Kwon, Y.T. Kim, S. Jung, H.J. Kim, G.W. Huber, J. Lee, Recent advances in hydrodeoxygenation of biomass-derived oxygenates over heterogeneous catalysts, *Green Chemistry* 21(14) (2019) 3715-3743.
- [333] D.A. Ruddy, J.A. Schaidle, J.R. Ferrell Iii, J. Wang, L. Moens, J.E. Hensley, Recent advances in heterogeneous catalysts for bio-oil upgrading via “ex situ catalytic fast pyrolysis”: catalyst development through the study of model compounds, *Green Chemistry* 16(2) (2014) 454-490.
- [334] Z. Li, S. Kelkar, L. Raycraft, M. Garedew, J.E. Jackson, D.J. Miller, C.M. Saffron, A mild approach for bio-oil stabilization and upgrading: electrocatalytic hydrogenation using ruthenium supported on activated carbon cloth, *Green Chemistry* 16(2) (2014) 844-852.
- [335] J. Wildschut, M. Iqbal, F.H. Mahfud, I.M. Cabrera, R.H. Venderbosch, H.J. Heeres, Insights in the hydrotreatment of fast pyrolysis oil using a ruthenium on carbon catalyst, *Energy & Environmental Science* 3(7) (2010) 962-970.



- [336] S. Brand, R.F. Susanti, S.K. Kim, H.-s. Lee, J. Kim, B.-I. Sang, Supercritical ethanol as an enhanced medium for lignocellulosic biomass liquefaction: Influence of physical process parameters, *Energy* 59 (2013) 173-182.
- [337] T. Yang, Y. Jie, B. Li, X. Kai, Z. Yan, R. Li, Catalytic hydrodeoxygenation of crude bio-oil over an unsupported bimetallic dispersed catalyst in supercritical ethanol, *Fuel Processing Technology* 148 (2016) 19-27.
- [338] S. Ahmadi, Z. Yuan, S. Rohani, C. Xu, Effects of nano-structured CoMo catalysts on hydrodeoxygenation of fast pyrolysis oil in supercritical ethanol, *Catalysis Today* 269 (2016) 182-194.
- [339] J. Peng, P. Chen, H. Lou, X. Zheng, Catalytic upgrading of bio-oil by HZSM-5 in sub- and super-critical ethanol, *Bioresource Technology* 100(13) (2009) 3415-3418.
- [340] W. Chen, Z. Luo, Y. Yang, G. Li, J. Zhang, Q. Dang, Upgrading of Bio-oil in Supercritical Ethanol: Using Furfural and Acetic Acid as Model Compounds, *BioResources* 8 (2013) 3934-3952.
- [341] R.W. Jenkins, C.D. Bannister, C.J. Chuck, The emissions and the performance of diethyl succinate in a diesel fuel blend, *Proceedings of the Institution of Mechanical Engineers, Part D: Journal of Automobile Engineering* 231(14) (2017) 1889-1899.